

Acknowledgement

I wish to express my gratitude to both my supervisors, Prof. *Herman Deconinck* and Prof. *Jaroslav Fořt*, for their invaluable support during the entire period when this work has been elaborated. They both supported me enormously during the beginning of my professional career, which emphasizes the importance of their help.

Regarding this work, I would like to thank all my colleagues who have contributed with useful comments, objections and advices.

Although not belonging to the official achievements, I am thankful this work brought my steps to pathways on which I met my beloved wife

Romana

a wonderful person, to whom this work is dedicated.

Summary

Keywords: fluid dynamics, CFD, in-house numerical code, finite volume method, turbulence modelling, ALE formulation, reciprocating engine, exhaust system

The main target of this work is to simulate and describe the flow around the exhaust valve of a reciprocating engine during an exhaust stroke. The computations are performed with two independent in-house numerical codes. Both the codes are based on the finite volume method, using the modern numerical schemes and the Arbitrary Lagrangian-Eulerian formulation for the simulations with moving geometries. In order to perform the simulations, some substantial developments (with the main focus on the turbulence modelling) were necessary and have been accomplished within the scope of this work. Some one- and two-equations turbulence models of the first and second order closure have been taken from the literature and implemented. The properties of the mathematical model are tested together with the sensitivity analysis of the simulation parameters (including geometry changes) on the results obtained, respectively on the processes over the exhaust stroke.

Anotace

Klíčová slova: mechanika tekutin, CFD, vlastní numerický program,
metoda konečných objemů, modelování turbulence,
ALE formulace, spalovací motor, výfukový systém

Cílem této práce je modelovat a popsat proudění okolo výfukového ventilu čtyřdobého spalovacího motoru během jeho pracovního cyklu. Presentované výpočty jsou získány pomocí dvou nezávislých (nekomerčních) numerických programů. Oba tyto programy jsou založeny na metodě konečných objemů, využívají moderní numerická schémata, případně ALE formulaci pro výpočty proudění na pohybujících se geometriích. Pro realizaci těchto výpočtů bylo zapotřebí vyvinout (naprogramovat) určité části obou programů, zejména doplnit modely turbulence. Tento úkol byl plněn v rámci zpracovávání této práce. Postupně bylo do programů doplněno několik jedno- a dvou-rovnicových modelů turbulence 1. a 2. řádu převzatých z literatury. Presentované výsledky zkoumají vlastnosti sestaveného matematického modelu a odhalují citlivost výsledků (respektive dějů ve válci a výfukovém potrubí během výfukové fáze) na vstupní parametry simulace, včetně geometrických úprav.

Contents

1	Introduction	1
2	Motivation	5
2.1	Reciprocating Engines	6
2.2	Flow Inside a Combustion Engine	10
3	Flow Model	15
3.1	Conservation Laws	15
3.2	Constitutive Relations	17
3.3	Initial and Boundary Conditions	19
4	Turbulence	21
4.1	Physical Properties	21
4.2	Turbulence Averaging	25
4.3	U-RANS Equations	28
4.4	Hierarchy of Turbulence Models	33
4.5	Models Used	37
5	Numerics	45
5.1	Mathematical Formulation	45
5.2	Spatial Discretization Methods	46
5.3	Numerical Codes Used	49
5.4	Inviscid Fluxes	50
5.5	Accuracy Improvement	58
5.6	Viscous Fluxes	63
5.7	Source Terms	65
5.8	Time Integration	66
5.9	Moving Geometries	69
5.10	Boundary Conditions	74
5.11	Computation Parallelization	75
6	Reference Test Cases	77
6.1	Inviscid Flow Model	77
6.2	Laminar Flow Model	95
6.3	Turbulent Flow Model	102

7	Flow around an Exhaust Valve	117
7.1	Test Matrix	117
7.2	Exhaust Channel Geometry	117
7.3	Inviscid Flow Model	119
7.4	Laminar Flow Model	135
7.5	Turbulent Flow Model	140
8	Conclusions	183
8.1	Findings on the Exhaust Channel	184
8.2	Future Work	186
A	Laval Nozzle - 1D Analysis	195
B	Exhaust Channel Geometry	197

List of Figures

2.1	Absolute number of the double-track vehicles registered in the Czech Republic . . .	5
2.2	Scheme of the reciprocating engine	6
2.3	General thermodynamic cycle in a temperature-entropy diagram	7
2.4	The Carnot cycle in <i>a)</i> pressure-volume chart <i>b)</i> temperature-entropy chart	7
2.5	The pressure-volume charts of <i>a)</i> Brayton <i>b)</i> Diesel <i>c)</i> Otto operating cycles	8
2.6	Operating cycle of a four-stroke engine	9
2.7	Operating cycle of a two-stroke engine	10
2.8	Basic geometry of the reciprocating internal combustion engine, a figure from [41] .	12
2.9	Intake/exhaust valve nomenclature	13
4.1	Examples of turbulent motions: sea waves (left), re-entry of the Apollo module to the atmosphere (right)	21
4.2	Example of energy spectrum for a turbulent flow, figure from [103]	23
4.3	Detail of the vortex core discretization	24
4.4	Time averaging for non-stationary turbulence, figure from [103]	26
4.5	Development of time-scale ratio inside the combustion chamber during the compression and expansion strokes, for different turbulence models (left-right) in three fixed spatial points, figure from [98]	27
4.6	Methods of RANS equations closure	33
4.7	Blending functions behaviour, a figure from [75]	40
5.1	The most frequent planar and spatial volumes	47
5.2	The flux between neighbouring cells	48
5.3	The COOLFluiD solver	49
5.4	Splitting polynoms of the Mach number (left), pressure (right)	52
5.5	Local indexing of a quad within structured grid	58
5.6	Limiter impact on the higher order reconstruction	59
5.7	Computational stencils for unstructured grids	61
5.8	Different approaches of 2D dual grids	64
5.9	1D example of <i>a)</i> Eulerian, <i>b)</i> Lagrangian, <i>c)</i> ALE grid and particle motion, fig. from [28].	70
5.10	Mesh around the NACA0012 profile: <i>a)</i> original, <i>b)</i> deformed using the spring analogy, fig. from [105].	72
5.11	Deformed mesh around the NACA0012 profile using the elastic body analogy: <i>a)</i> , <i>b)</i> homogeneous, <i>c)</i> volume based, <i>d)</i> distance based stiffness, fig. from [105].	73
5.12	Exhaust valve at the TDC (left) and BDC (right) positions.	73

5.13	1D scheme of the ghost state adaptation to avoid negative ghost state pressure; <i>a)</i> before, <i>b)</i> after adaptation.	74
5.14	Scheme of the OpenMP parallelization, figure from [18].	75
6.1	The Laval nozzle.	77
6.2	The Mach number evolution for typical regimes of the Laval nozzle.	78
6.3	Contours of the Mach number in a transonic regime of the Laval nozzle.	79
6.4	The Mach number distribution for different variants of the AUSM scheme.	80
6.5	The detailed view of the shock-wave resolution for different variants of the AUSM scheme.	80
6.6	The transonic channel.	80
6.7	The reference solution on the transonic channel. Flow topology with highlighted sonic line (upper), Mach number distribution along lower and upper wall. Figures from [10].	81
6.8	Computational grids of channel with 10% bump (coarse and fine) and 4% bump	82
6.9	Transonic channel, $M_{2,i} = 0.675$, different numerical schemes. Iso-Mach lines (upper), distribution of M along the upper (lower left) and lower (lower right) wall.	82
6.10	Detail of a shock wave, $M_{2,i} = 0.675$, different numerical schemes.	83
6.11	Reference grid and solution for $M_{2,i} = 1.40$, contours of the Mach number, figure from [82].	83
6.12	Channel with 4% bump, $M_{2,i} = 1.40$, different numerical schemes. Iso-Mach lines (upper), distribution of M along the upper (lower left) and lower (lower right) wall.	84
6.13	The reference subsonic solution on the channel with a circular bump, figure from [10].	84
6.14	Channel with 10% bump, $M_{2,i} = 0.200$, different numerical schemes. Iso-Mach lines (upper), distribution of M along the upper (lower left) and lower (lower right) wall.	85
6.15	Channel with 10% bump, $M_{2,i} = 0.020$, different numerical schemes. Distribution of the Mach number.	85
6.16	Mach number distribution along a lower wall, the MUSA solver, AUSM+up scheme, different limiters.	86
6.17	Mach number distribution along a lower wall, the COOLfluid solver, AUSM+up scheme, different limiters.	87
6.18	$M_{2,i} = 0.675$, Mach number distribution along an upper wall (left) and a lower wall, different numerical codes.	88
6.19	$M_{2,i} = 0.200$, Mach number distribution along an upper wall (left) and a lower wall, different numerical codes.	88
6.20	$M_{2,i} = 0.020$, Mach number distribution along an upper wall (left) and a lower wall, different numerical codes.	88
6.21	Various modifications of a transonic channel in 3D.	89
6.22	Pure extrusion. Contours of the Mach number, different channel planes. <i>a)</i> reference solution, <i>b)</i> MUSA, <i>c)</i> COOLfluid	90
6.23	Pure extrusion. Mach number distribution along an upper wall and a lower wall, different numerical codes. <i>a)</i> reference solution, <i>b)</i> MUSA, <i>c)</i> COOLfluid	90
6.24	Sweep shift. Contours of the Mach number, different channel planes. <i>a)</i> reference solution, <i>b)</i> MUSA, <i>c)</i> COOLfluid	91
6.25	Sweep shift. Mach number distribution along an upper wall and a lower wall, different numerical codes. <i>a)</i> reference solution, <i>b)</i> MUSA, <i>c)</i> COOLfluid	92

6.26	Variable bump height. Contours of the Mach number, different channel planes. <i>a)</i> reference solution, <i>b)</i> MUSA, <i>c)</i> COOLFluiD	93
6.27	Variable bump height. Mach number distribution along an upper wall and a lower wall, different numerical codes. <i>a)</i> reference solution, <i>b)</i> MUSA, <i>c)</i> COOLFluiD	93
6.28	Variable bump length and height. Contours of the Mach number, different channel planes. <i>a)</i> reference solution, <i>b)</i> MUSA, <i>c)</i> COOLFluiD	94
6.29	Variable bump length and height. Mach number distribution along an upper wall and a lower wall, different numerical codes. <i>a)</i> reference solution, <i>b)</i> MUSA, <i>c)</i> COOLFluiD	95
6.30	The laminar boundary layer scheme.	96
6.31	The flat plate.	97
6.32	The laminar flow over a flat plate, code comparison. <i>a)</i> velocity profile, <i>b)</i> distribution of the skin friction coefficient.	98
6.33	Scheme of imposed heaving and pitching motions. Evolution in time (figure from [46]).	98
6.34	The computational grid for an oscillating airfoil. Left: initial state, right: deformed state.	99
6.35	Contours of the pressure coefficient ($\Delta c_P = 0.05$) for different regimes: <i>a)</i> R1, <i>b)</i> R2, <i>c)</i> R3. Solution in time $t/T = 0; 0.25; 0.50; 0.75$	100
6.36	Pressure coefficient distribution ($\Delta c_P = 0.05$) <i>a)</i> ref. solution (figure from [46]), <i>b)</i> solution by COOLFluiD. Regime R1, solution time $t/T = 0.25$	101
6.37	Forces coefficients over a periodic cycle, regime R1, <i>a)</i> ref. solution (figure from [46]), <i>b)</i> solution by COOLFluiD.	102
6.38	Different regions of the turbulent boundary layer.	103
6.39	Adimensional velocity profile. Comparison of different turbulent models with a theoretical profile.	104
6.40	Distribution of the skin friction coefficient. Comparison of different turbulent models with a theoretical curve.	105
6.41	The computational grid of the NACA 0012. Details of the grid around the profile (upper) and detail of structured triangular grid (lower).	105
6.42	Contours of pressure coefficient (left) and isolines of velocity (right). Different turbulence model: <i>a)</i> BSL, <i>b)</i> SST.	106
6.43	Contours of pressure coefficient (left) and isolines of velocity (right). Different turbulence model: <i>a)</i> Wilcox, <i>b)</i> TNT, <i>c)</i> EARSM.	107
6.44	Distribution of the pressure coefficient along the profile for different turbulence models.	107
6.45	The profile RAE 2822.	108
6.46	The computational grid of the RAE 2822. Details of the grid around the profile (upper) and detail of structured triangular grid (lower).	108
6.47	Contours of pressure coefficient (left) and isolines of the Mach number (right) for a subsonic regime. Different turbulence model: <i>a)</i> BSL, <i>b)</i> Wilcox, <i>c)</i> EARSM.	109
6.48	Distribution of the pressure coefficient for a subsonic regime. Different turbulence models.	110
6.49	Contours of pressure coefficient (left) and isolines of the Mach number (right) for a transonic regime. Different turbulence model: <i>a)</i> BSL, <i>b)</i> Wilcox, <i>c)</i> EARSM.	111
6.50	Distribution of the pressure coefficient for a transonic regime. Different turbulence models.	111

6.51	Convergence plot for different turbulence models. <i>a)</i> subsonic regime, <i>b)</i> transonic regime.	112
6.52	Geometry of the Deléry channel (figure from [95])	113
6.53	Computational grid for the Deléry channel	113
6.54	Interferogram in the region of interest - lambda shock (figure from [95])	113
6.55	Isolines of the Mach number. Different outlet pressure $p_{out} = \{40; 60; 65\}$ kPa (top to bottom)	114
6.56	Deléry channel, isolines of the Mach number ($\Delta M = 0.025$). Solution from [95]	114
6.57	Comparison of different turbulence models: <i>a)</i> BSL, <i>b)</i> SST. Whole channel - isolines of the Mach number ($\Delta M = 0.025$). Detail of the lambda shock - isolines of density ($\Delta\rho = 0.015$).	115
6.58	Comparison of different turbulence models: <i>a)</i> Wilcox, <i>b)</i> TNT, <i>c)</i> EARSM. Whole channel - isolines of the Mach number ($\Delta M = 0.025$). Detail of the lambda shock - isolines of density ($\Delta\rho = 0.015$).	115
6.59	Comparison of pressure distribution along the lower wall of the channel.	116
6.60	Comparison of pressure distribution along the lower wall of the channel.	116
7.1	Scheme of the region of interest.	118
7.2	Different construction approaches of the computational domain.	118
7.3	Scheme of a 3D grid construction.	119
7.4	Different exhaust valve geometries: <i>a)</i> G1, <i>b)</i> original, <i>c)</i> G2.	119
7.5	First structured multi-block grid on the exhaust channel: <i>a)</i> overview, <i>b)</i> zoom of the seat region.	120
7.6	Refined structured multi-block grid on the exhaust channel: <i>a)</i> overview, <i>b)</i> zoom of the seat region.	121
7.7	Unstructured grid on the exhaust channel: <i>a)</i> overview, <i>b)</i> zoom of the seat region.	121
7.8	Inviscid flow simulation on the coarse mesh, the MUSA solver, $p_2/p_0 = 0.896$. <i>a)</i> Isolines of the Mach number, <i>b)</i> velocity streamlines.	122
7.9	Inviscid flow simulation on the fine mesh, the MUSA solver, $p_2/p_0 = 0.896$. <i>a)</i> Isolines of the Mach number, <i>b)</i> velocity streamlines.	122
7.10	Inviscid flow simulation on the triangular mesh, the COOLFluid solver, $p_2/p_0 = 0.896$. <i>a)</i> Isolines of the Mach number, <i>b)</i> velocity streamlines.	122
7.11	Inviscid flow simulation on the coarse mesh, the MUSA solver, $p_2/p_0 = 0.559$. <i>a)</i> Isolines of the Mach number, <i>b)</i> velocity streamlines.	123
7.12	Inviscid flow simulation on the fine mesh, the MUSA solver, $p_2/p_0 = 0.559$. <i>a)</i> Isolines of the Mach number, <i>b)</i> velocity streamlines.	123
7.13	Detail of the channel throat on <i>a)</i> coarse mesh, <i>b)</i> fine mesh. Isolines of the Mach number.	124
7.14	Inviscid flow simulation, the MUSA solver, $p_2/p_0 = 0.250$. <i>a)</i> isolines of the Mach number, <i>b)</i> velocity streamlines. <i>a1), b1)</i> AUSM scheme, <i>a2), b2)</i> AUSM+up scheme.	125
7.15	Inviscid flow simulation, the COOLFluid solver, $p_2/p_0 = 0.250$, AUSM+up scheme. <i>a)</i> isolines of the Mach number, <i>b)</i> velocity streamlines.	125
7.16	The Mach number distribution along the central streamline for different numerical schemes and different numerical codes.	126

7.17	Inviscid flow simulation on the elongated geometry, the MUSA solver, $p_2/p_0 = 0.559$. a) Elongated domain, b) isolines of the Mach number, c) velocity streamlines, detail of the backflow.	127
7.18	Inviscid flow simulation on the elongated geometry, the MUSA solver, $p_2/p_0 = 0.559$. a) isolines of the Mach number, b) velocity streamlines.	128
7.19	Scheme of the inlet wall inclination.	128
7.20	Inviscid flow simulation, the MUSA solver, $p_2/p_0 = 0.250$, velocity streamlines. In- fluence of the inlet wall inclination a) 0 degrees (original), b) 5 degrees, c) 10 degrees.	129
7.21	The effect of the inlet wall inclination on the recirculation length.	129
7.22	3D Inviscid flow simulation, the MUSA solver, $p_2/p_0 = 0.784$. Solution cut at $Z = 0$. a) isolines of the Mach number, b) velocity streamlines.	130
7.23	3D Inviscid flow simulation, the MUSA solver, $p_2/p_0 = 0.559$. Solution cut at $Z = 0$. a) isolines of the Mach number, b) velocity streamlines.	130
7.24	3D Inviscid flow simulation on a smoothed geometry, the MUSA solver, $p_2/p_0 =$ 0.559 . Solution cut at $Z = 0$. a) isolines of the Mach number, b) velocity streamlines.	130
7.25	Inviscid flow simulation, the MUSA solver, $p_2/p_0 = 0.784$. a) isolines of the Mach number, b) velocity streamlines. a1), b1) 2D model, a2), b2) 3D model, cut at $Z=0$.	131
7.26	Inviscid flow simulation, the MUSA solver, $p_2/p_0 = 0.591$. a) isolines of the Mach number, b) velocity streamlines. a1), b1) 2D model, a2), b2) 3D model, cut at $Z=0$.	132
7.27	The Mach number distribution along the central streamline. Pressure ratio: a) $p_2/p_0 = 0.784$, b) $p_2/p_0 = 0.591$	132
7.28	The plot of an active area within the exhaust channel. a) the scheme of the values extraction, b1) pressure ratio $p_2/p_0 = 0.784$, b2) pressure ratio $p_2/p_0 = 0.591$	133
7.29	A structured multi-block grid on the exhaust channel: a) overview, b) zoom of the block connection and the seat region.	135
7.30	Laminar flow simulation, the MUSA solver, $Re/L=1500$. a) isolines of the Mach number, b) velocity streamlines. The pressure ratio a1), b1) $p_2/p_0 = 0.656$, a2), b2) $p_2/p_0 = 0.250$	136
7.31	Laminar flow simulation, the MUSA solver, $p_2/p_0 = 0.656$. a) isolines of the Mach number, b) velocity streamlines. The viscosity parameter a1), b1) $Re/L=800$, a2), b2) $Re/L=1500$, a3), b3) $Re/L=10\ 000$	137
7.32	Laminar flow simulation, the MUSA solver, $p_2/p_0 = 0.250$, $Re/L = 800$. a) isolines of the Mach number, b) velocity streamlines. a1), b1) geometry without valve casing, a2), b2) complete geometry.	138
7.33	Laminar flow simulation, the MUSA solver, $p_2/p_0 = 0.250$, $Re/L = 1\ 500$, isolines of the Mach number. Gradient discretization a1) approximate method, a2) exact method, b) isolines overlay.	139
7.34	Sensitivity to grid coarseness. Turbulent flow simulation, SST turbulence model, $L = 7\ \text{mm}$, $p_2/p_0 = 0.400$. a) isolines of the Mach number, b) velocity streamlines; According to the table 7.13: a1) b1) grid 1, a2) b2) grid 2, a3) b3) grid 3.	141
7.35	Sensitivity to numerical scheme parameter. Turbulent flow simulation, SST turbu- lence model, $L = 4\ \text{mm}$, $p_2/p_0 = 0.400$. Isolines of the Mach number a) $M_\infty = 0.01$, b) $M_\infty = 0.10$, c) $M_\infty = 0.30$	142
7.36	Influence of the turbulence model. $L = 4\ \text{mm}$, $p_2/p_0 = 0.400$. a) isolines of the Mach number, b) velocity streamlines, a1, b1) Spalart-Allmaras, a2, b2) BSL, a3, b3) SST.	143

7.37	Influence of the turbulence model. $L = 4$ mm, $p_2/p_0 = 0.400$. <i>a)</i> isolines of the Mach number, <i>b)</i> velocity streamlines, <i>a1, b1)</i> Wilcox, <i>a2, b2)</i> TNT, <i>a3, b3)</i> EARSM.	143
7.38	Scheme of the main recirculation zones, 2D model.	144
7.39	Distribution of the pressure and the Mach number along the central streamline for different turbulence models.	145
7.40	Influence of the turbulence model. $L = 4$ mm, $p_2/p_0 = 0.250$. <i>a)</i> isolines of the Mach number, <i>b)</i> velocity streamlines, <i>a1, b1)</i> SST, <i>a2, b2)</i> EARSM.	146
7.41	Influence of the turbulence model. Simplified geometry without the casing. $L = 4$ mm, $p_2/p_0 = 0.250$. <i>a)</i> isolines of the Mach number, <i>b)</i> velocity streamlines, <i>a1, b1)</i> SST, <i>a2, b2)</i> EARSM.	146
7.42	Influence of the valve geometry. $L = 10$ mm, $p_2/p_0 = 0.400$. <i>a)</i> isolines of the Mach number, <i>b)</i> velocity streamlines. Valve geometry <i>a1, b1)</i> original, <i>a2, b2)</i> G1, <i>a3, b3)</i> G2.	148
7.43	3D grid. Planes for solution extraction.	149
7.44	Sensitivity to grid coarseness. 3D turbulent flow simulation, SST turbulence model, $L = 10$ mm, $p_2/p_0 = 0.400$, contours of the Mach number, two longitudinal perpendicular cuts. According to the table 7.21: <i>a)</i> grid 1, <i>b)</i> grid 2, <i>c)</i> grid 3.	150
7.45	Sensitivity to grid coarseness. 3D turbulent flow simulation, SST turbulence model, $L = 10$ mm, $p_2/p_0 = 0.400$, isolines of the Mach number, outlet transverse cut. According to the table 7.21: <i>a)</i> grid 1, <i>b)</i> grid 2, <i>c)</i> grid 3.	150
7.46	Influence of the turbulence model. $L = 4$ mm, $p_2/p_0 = 0.400$. <i>a)</i> isolines of the Mach number, <i>b)</i> velocity streamlines, <i>a1, b1)</i> SST, <i>a2, b2)</i> Wilcox, <i>a3, b3)</i> EARSM.	151
7.47	Scheme of the main recirculation zones, 3D model.	152
7.48	Detail of the throat zone. <i>a)</i> 2D model, <i>b)</i> 3D model.	152
7.49	Influence of the inclined inlet wall. $L = 4$ mm, $p_2/p_0 = 0.400$. <i>a)</i> isolines of the Mach number, <i>b)</i> velocity streamlines, <i>a1, b1)</i> 0 degrees (original), <i>a2, b2)</i> 5 degrees, <i>a3, b3)</i> 10 degrees.	153
7.50	Schematic view of different inlet boundary conditions: <i>a)</i> radial inlet, <i>b)</i> tangential inlet.	154
7.51	Influence of the inlet boundary condition, SST model, $p_2/p_0 = 0.400$. Contours of the Mach number. <i>a)</i> $L=4$ mm, <i>b)</i> $L=10$ mm; <i>a1, b1)</i> radial inlet, <i>a2, b2)</i> tangential inlet.	154
7.52	Influence of the valve geometry. $L = 10$ mm, $p_2/p_0 = 0.400$. <i>a)</i> isolines of the Mach number, <i>b)</i> velocity streamlines. Valve geometry <i>a1, b1)</i> original, <i>a2, b2)</i> G1, <i>a3, b3)</i> G2.	156
7.53	Setup of the boundary conditions and the valve movement for an initial unsteady simulation.	157
7.54	Influence of the unsteady approach, $L = 10$ mm, $p_2/p_0 = 0.500$. <i>a)</i> isolines of the Mach number, <i>b)</i> velocity streamlines, <i>a1, b1)</i> steady state solution, <i>a2, b2)</i> unsteady (opening stage), <i>a3, b3)</i> unsteady (closing stage).	158
7.55	Evolution of the Mach number and the mass flow rate with time.	159
7.56	Setup of the boundary conditions and the valve movement for a closing stage simulation.	159
7.57	Solution interpolation. <i>a)</i> $L=6$ mm, <i>b)</i> $L=3$ mm. Left: detail of the original (deformed) grid and solution, Right: detail of the new grid, interpolated solution.	160

7.58	Closing stage. Solution development along time. <i>a)</i> isolines of the Mach number, <i>b)</i> velocity streamlines.	161
7.59	Evolution of the Mach number and the mass flow rate with time, closing stage. . .	161
7.60	Influence of the grid deformation. <i>a)</i> detail of a proper grid and solution in the throat region; <i>b)</i> detail of an excessively deformed grid and its impact on the solution.	162
7.61	Evolution of the Mach number and the mass flow rate with time, closing stage. Inlet wall inclination <i>a)</i> 5°, <i>b)</i> 10°.	162
7.62	Evolution of the Mach number and the mass flow rate with time, closing stage. Influence of the Inlet wall inclination.	163
7.63	Closing stage. Influence of the valve geometry. L=4 mm. <i>a)</i> isolines of the Mach number, <i>b)</i> velocity streamlines; Valve shape <i>a1)</i> <i>b1)</i> original; <i>a2)</i> <i>b2)</i> G1; <i>a3)</i> <i>b3)</i> G2.	164
7.64	Closing stage. Influence of the valve geometry. L=2 mm. <i>a)</i> isolines of the Mach number, <i>b)</i> velocity streamlines; Valve shape <i>a1)</i> <i>b1)</i> original; <i>a2)</i> <i>b2)</i> G1; <i>a3)</i> <i>b3)</i> G2.	164
7.65	Evolution of the Mach number and the mass flow rate with time, closing stage. Influence of the valve geometry.	165
7.66	The valve lift evolution during a real cycle of a reciprocating engine.	166
7.67	The evolution of the pressure in the cylinder and in the exhaust pipe during a real cycle of a reciprocating engine.	166
7.68	Numerical realization of the valve motion.	167
7.69	Real cycle simulation, SI inlet condition, contours of the Mach number. Valve lift: <i>a)</i> 3 mm, <i>b)</i> 7 mm, <i>c)</i> 11 mm; <i>a1)</i> <i>b1)</i> opening stage, <i>a2)</i> <i>b2)</i> closing stage.	167
7.70	Real cycle simulation, CI inlet condition, contours of the Mach number. Valve lift: <i>a)</i> 3 mm, <i>b)</i> 7 mm, <i>c)</i> 11 mm; <i>a1)</i> <i>b1)</i> opening stage, <i>a2)</i> <i>b2)</i> closing stage.	168
7.71	Evolution of the Mach number and the mass flow rate with time, closing stage. Real cycle simulation. Influence of the inlet boundary condition.	168
7.72	Influence of the unsteady approach, CI inlet condition, opening stage, L=7 mm. <i>a)</i> contours of the Mach number, <i>b)</i> velocity streamlines; <i>a1)</i> <i>b1)</i> unsteady, <i>a2)</i> <i>b2)</i> steady.	169
7.73	Influence of the unsteady approach, CI inlet condition, closing stage, L=7 mm. <i>a)</i> contours of the Mach number, <i>b)</i> velocity streamlines; <i>a1)</i> <i>b1)</i> unsteady, <i>a2)</i> <i>b2)</i> steady.	170
7.74	Real cycle simulation, CI inlet condition, G1 geometry, contours of the Mach number. Valve lift: <i>a)</i> 3 mm, <i>b)</i> 7 mm, <i>c)</i> 11 mm; <i>a1)</i> <i>b1)</i> opening stage, <i>a2)</i> <i>b2)</i> closing stage.	170
7.75	Real cycle simulation, CI inlet condition, G2 geometry, contours of the Mach number. Valve lift: <i>a)</i> 3 mm, <i>b)</i> 7 mm, <i>c)</i> 11 mm; <i>a1)</i> <i>b1)</i> opening stage, <i>a2)</i> <i>b2)</i> closing stage.	171
7.76	Evolution of the Mach number and the mass flow rate with time, closing stage. Real cycle simulation. Influence of the valve geometry. <i>a)</i> SI regime, <i>b)</i> CI regime. . . .	171
7.77	Real cycle simulation, CI inlet condition, EARSM turbulence model, contours of the Mach number. Valve lift: <i>a)</i> 3 mm, <i>b)</i> 7 mm, <i>c)</i> 11 mm; <i>a1)</i> <i>b1)</i> opening stage, <i>a2)</i> <i>b2)</i> closing stage.	172
7.78	Evolution of the Mach number and the mass flow rate with time, closing stage. Real cycle simulation. Influence of the turbulence model.	173

7.79	Real cycle simulation, original valve shape, SI inlet condition, contours of the Mach number. Solution cut $Z = 0$. Valve lift: <i>a)</i> 3 mm, <i>b)</i> 7 mm, <i>c)</i> 11 mm; <i>a1, b1)</i> opening stage, <i>a2, b2)</i> closing stage.	175
7.80	Real cycle simulation, G1 valve shape, SI inlet condition, contours of the Mach number. Solution cut $Z = 0$. Valve lift: <i>a)</i> 3 mm, <i>b)</i> 7 mm, <i>c)</i> 11 mm; <i>a1, b1)</i> opening stage, <i>a2, b2)</i> closing stage.	176
7.81	Real cycle simulation, G2 valve shape, SI inlet condition, contours of the Mach number. Solution cut $Z = 0$. Valve lift: <i>a)</i> 3 mm, <i>b)</i> 7 mm, <i>c)</i> 11 mm; <i>a1, b1)</i> opening stage, <i>a2, b2)</i> closing stage.	177
7.82	Evolution of the Mach number and the mass flow rate with time. Real cycle simulation. SI regime. Influence of the valve geometry.	177
7.83	Real cycle simulation, original valve shape, CI inlet condition, contours of the Mach number. Solution cut $Z = 0$. Valve lift: <i>a)</i> 3 mm, <i>b)</i> 7 mm, <i>c)</i> 11 mm; <i>a1, b1)</i> opening stage, <i>a2, b2)</i> closing stage.	178
7.84	Real cycle simulation, G1 valve shape, CI inlet condition, contours of the Mach number. Solution cut $Z = 0$. Valve lift: <i>a)</i> 3 mm, <i>b)</i> 7 mm, <i>c)</i> 11 mm; <i>a1, b1)</i> opening stage, <i>a2, b2)</i> closing stage.	179
7.85	Real cycle simulation, G2 valve shape, CI inlet condition, contours of the Mach number. Solution cut $Z = 0$. Valve lift: <i>a)</i> 3 mm, <i>b)</i> 7 mm, <i>c)</i> 11 mm; <i>a1, b1)</i> opening stage, <i>a2, b2)</i> closing stage.	180
7.86	Evolution of the Mach number and the mass flow rate with time. Real cycle simulation. CI regime. Influence of the valve geometry.	180
A.1	Scheme of a Laval nozzle.	195
B.1	Technical drawing of the cylinder head and the exhaust channel.	198
B.2	Technical drawing of the exhaust valve.	199

List of Tables

2.1	State changes for ideal and some real heat engines	8
5.1	Comparison of solvers used	50
6.1	The Laval nozzle, shock-wave characteristics	79
6.2	Flow regimes for the channel test case	81
6.3	Description of computational grids	82
6.4	Benchmark regime, maximal Mach number, quality of the Zierep singularity capturing (1-excellent, 2-very good, 3-good, 4-inaccurate, 5-inacceptable)	87
6.5	Setup of 3D transonic channel	89
6.6	Pure extrusion. Maximal Mach number on the lower wall.	91
6.7	Sweep shift. Maximal Mach number on the lower wall.	92
6.8	Variable bump height. Maximal Mach number on the lower wall.	94
6.9	Variable bump length and height. Maximal Mach number on the lower wall.	95
6.10	Blasius laminar velocity profile	96
6.11	Comparison of numerical results against theoretical profiles.	98
6.12	Oscillation regimes.	100
6.13	Comparison with the referential data.	102
6.14	Freestream regimes.	108
7.1	Test matrix of the test case of the exhaust valve	117
7.2	Computational grids for 2D Inviscid flow simulations.	121
7.3	Inviscid flow simulation, $p_2/p_0 = 0.896$. Influence of the grid coarseness.	123
7.4	Inviscid flow simulation, $p_2/p_0 = 0.559$. Influence of the grid coarseness.	124
7.5	Inviscid flow simulation, $p_2/p_0 = 0.559$. Comparison with the elongated domain (the average outlet Mach number has been extracted at the conventional outlet position).	127
7.6	The influence of the inclination angle on the flow characteristics.	128
7.7	3D Inviscid flow simulation. Comparison of the different regimes and geometries.	131
7.8	Reduction of the active channel cross-section due to recirculations.	133
7.9	Laminar flow simulation, $Re/L = 1500$. Influence of the pressure ratio.	136
7.10	Laminar flow simulation, $p_2/p_0 = 0.656$. Influence of the viscosity parameter.	137
7.11	Laminar flow simulation, $p_2/p_0 = 0.656$, $Re/L = 800$. Influence of the geometry.	138
7.12	Laminar flow simulation, $p_2/p_0 = 0.250$, $Re/L = 1500$. Influence of the discretization method for the variable gradients.	139
7.13	Computational grids for 2D turbulent simulations.	140
7.14	Turbulent flow simulation. Sensitivity to grid coarseness.	141
7.15	Turbulent flow simulation. Sensitivity to the parameter of the AUSM+up scheme.	142

7.16	Influence of the turbulence model.	144
7.17	Influence of the turbulence models on the size of recirculation zones.	145
7.18	Influence of the turbulence model, $p_2/p_0 = 0.250$	147
7.19	Influence of the turbulence models on the size of recirculation zones, $p_2/p_0 = 0.250$	147
7.20	Influence of the valve geometry.	148
7.21	Computational grids for 3D turbulent simulations. *) Grid file in a neutral (solution-free, ASCII) format <i>.neu</i>	149
7.22	3D turbulent flow simulation. Sensitivity to grid coarseness.	151
7.23	Influence of the turbulence model.	152
7.24	The influence of the inclination angle.	153
7.25	The influence of the inlet boundary condition.	155
7.26	Influence of the valve geometry.	156
7.27	Influence of the unsteady approach.	158
7.28	Influence of the valve geometry.	165
7.29	Period of aerodynamical blockage for different inlet boundary conditions.	169
7.30	Differences between steady state and unsteady solutions.	170
7.31	Influence of the valve geometry on the total mass flow over one cycle.	172
7.32	Period of aerodynamical blockage for different turbulence models.	173
7.33	Influence of the turbulence model on the total mass flow over one cycle.	174
7.34	Period of aerodynamical blockage for different inlet boundary conditions. 3D simulation, CI regime.	181
7.35	Influence of the turbulence model on the total mass flow over one cycle.	181

List of Symbols

Symbol	Meaning	Unit
a	local speed of sound	$[m \cdot s^{-1}]$
c_p	specific heat at constant pressure	$[J \cdot mol^{-1} \cdot K^{-1}]$
c_v	specific heat at constant volume	$[J \cdot mol^{-1} \cdot K^{-1}]$
C	generic constant	
C_D	cross diffusion	
C_{ij}	tensor of viscous diffusion	
D_{ij}	tensor of Reynolds stress diffusion	
e	specific internal energy	$[J \cdot kg^{-1}]$
E	internal energy	$[J]$
f	frequency	$[Hz]$
F^I	vector of convective (inviscid) fluxes	
F^V	vector of diffusive (viscous) fluxes	
F_1, F_2	blending functions between $k - \omega$ and $k - \epsilon$ models	
g	gravitational acceleration	$[m \cdot s^{-2}]$
h	specific total enthalpy	$[J \cdot kg^{-1}]$
H	total enthalpy	$[J]$
J	Jacobian matrix	
k	turbulent kinetic energy	$[m^2 \cdot s^{-2}]$
l	integral length scale of the turbulence	$[m]$
L	valve lift	$[mm]$
M	Mach number	$[-]$
\vec{n}	normal vector	
p	static pressure	$[Pa]$
P	general property	
P_{ij}	tensor of Reynolds stress production	
Pr	Prandtl number	$[-]$
\dot{q}	local heat flux	$[W \cdot m^{-2}]$
Q	heat	$[J]$
\dot{Q}	heat flux	$[W]$
Q	vector of source terms	
\vec{r}	displacement vector	
R	specific heat constant	$[J \cdot kg^{-1} \cdot K^{-1}]$
\mathcal{R}	residual vector	
R_{ij}	two-point velocity correlation tensor	

Re	Reynolds number	[-]
s	entropy	$[J \cdot kg^{-1} \cdot K^{-1}]$
S	constitutive air constant (Sutherland's law)	[K]
S_P	general surface source of property P	
S_{ij}	strain rate tensor	
t	time	[s]
T	absolute temperature	[K]
U	internal energy	[J]
v	volume	$[m^3]$
V_P	general volume source of property P	
\vec{w}	vector of fluid velocity	
\vec{w}_B	vector of boundary velocity	
w_1, w_2, w_3	velocity along x, y and z direction	$[m \cdot s^{-1}]$
W	vector of conservative unknowns	
W	thermodynamical work	[J]
\vec{x}	vector of spatial coordinates	

Greek Symbols

Symbol	Meaning	Unit
δ	Kronecker's delta	
η	efficiency	[-]
γ	Poisson's constant (ratio of specific heats)	[-]
ϵ	dissipation rate of the turbulent kinetic energy	$[m^2 \cdot s^{-3}]$
ϵ_{ij}	tensor of Reynolds stress dissipation	
λ	thermal conductivity	$[W \cdot m^{-1} \cdot K^{-1}]$
λ_S	Stokes viscosity	
Λ	linear slope	
μ	dynamic viscosity	$[Pa \cdot s]$
ν	kinematic viscosity	$[m^2 \cdot s]$
Π_{ij}	tensor of Reynolds stress redistribution	
Φ	vector of conservative variables	
ρ	density	$[kg \cdot m^{-3}]$
τ_l	integral time scale of the turbulence	[s]
τ_{ij}	viscous stress tensor	
τ_{ij}^R	Reynolds stress tensor	
χ	turbulent Reynolds number	[-]
ω	specific dissipation rate of the turbulent kinetic energy	$[s^{-1}]$
ω_i	i -th finite volume	
Ω	control volume	
Ω_{ij}	vorticity tensor	
$\partial.$	boundary of a control volume	
$\frac{\partial.}{\partial.}$	partial derivative	
∇	Hamilton's nabla operator	

Indices

\cdot_0	reservoir or initial value
\cdot_2	outlet value
\cdot_{init}	initial value
$\cdot_{L/R}$	belongs to the left / right
\cdot_t ; \cdot_{turb}	turbulent
\cdot_{wall}	value on the (wall) boundary
$\cdot' ; \cdot''$	fluctuation (time-weighted; density-weighted)
$\bar{\cdot} ; \tilde{\cdot}$	average value (time-weighted; density-weighted)

Abbreviations

ALE	Arbitrary Lagrangian-Eulerian
AUSM	Advection Upstream Splitting Method
BDC	Bottom-Dead-Center (piston position with the largest cylinder volume)
BC	Boundary Condition
BDF2	2-steps Backward Difference Formula
BE	Backward Euler formula
BSL	Menter's Baseline turbulence model
CE	Combustion Engine
C-N	Crank-Nicolson
CFD	Computational Fluid Dynamics
COOLFluid	Computational Object Oriented Library for Fluid Dynamics
CPU	Central Processing Unit
DNS	Direct Numerical Simulation
EARSM	Explicit Algebraic Reynolds Stress Model
ECE	External Combustion Engine
FVM	Finite Volume Method
GMRES	Generalized Minimal Residual
ICE	Internal Combustion Engine
MPI	Message Passing Interface
MUSA	name of an in-house CFD code
MUSCL	Monotone Upstream-centered Schemes for Conservation Laws
NS	Navier-Stokes equations
PETSc	Portable Extensive Toolkit for Scientific calculations
RANS	Reynolds-Averaged Navier-Stokes equations
RPM	Revolutions Per Minute
RS	Reynolds stress
RSM	Reynolds Stress Model
SA, S-A	Spalart-Allmaras turbulence model
SST	Menter's Shear Stress Transport turbulence model
TDC	Top-Dead-Center (piston position with the smallest cylinder volume)

Chapter 1

Introduction

This doctoral work focuses on the application of fluid dynamics on a real industrial problem. Since its origin, fluid dynamics has been both a theoretical and experimental discipline of general physics. While the experimental branch has gained in popularity by providing respectable descriptions of dynamics of fluids, its theoretical sibling has been left in shade for long decades.

The first mathematical equations describing the fluid motion have been known since the 18th century, by *D. Bernoulli* and *L. Euler*. Their substantial extension is dated to the 19th century, acknowledging mainly the works of *A. Cauchy*, *C. Navier*, *S. Poisson*, *O. Reynolds*, *B. de Saint-Venant*, *G. Stokes* and others. The mathematical properties of the equations derived have been however, far beyond the limits of the then computational power (usually just a pen & paper).

The real breakthrough came in 1940's when a series of mechanical counters and multipliers to automatize the computations have been used for the first time, by *R. Feynman*. This algorithmization principle together with the development of the transistor gave birth to the numerical branch of fluid dynamics. Its evolution then directly mirrors the enormous progress in the computer engineering over the past years.

The original rivalry between the experimental and numerical branches about the verity of results has recently turned into a synergy, establishing a discipline called Computational Fluid Dynamics (CFD).

From the long term perspective, aeronautics has been the main customer to CFD. Nonetheless, with the apparent rise in computational power, the numerical methods and models have been extended to a wide range of applications. More and more industries appreciate the advantages of an accurate numerical simulation of the flow fields in industrial processes. As a part of an integrated design tool, CFD can help reducing the development time together with the simultaneous increase of its efficiency, leading to obvious resource savings.

Today's CFD therefore links: any *industrial domain* interested (whoever dealing with fluids in any form), *physics* (providing the rules/equations of fluid behaviour) and *mathematics* (providing the tools and methods to solve efficiently the equations given).

General Objectives

This work applies CFD on the automotive industry issue. The main target is to reveal and describe the fluid behaviour over an exhaust stroke of a four-stroke internal combustion engine.

So far, the flow under our consideration has only been approached by roughly simplified models/estimates. The programs designed for the simulation of the complete cycle (of the internal combustion engine) often use too coarse discretization around valves, which causes serious inaccuracies of the flow parameters during the scavenging strokes (intake and exhaust).

The commercial CFD codes are usually also not suitable for the exhaust flow. The main reason is the wide velocity range (most of the flow is deeply subsonic, whereas for the small valve lifts the velocity turns to supersonics and expands down the exhaust channel) and its steep gradients, which most of the softwares fail to model properly. Hence, the merit of the thesis is an accurate insight into the processes affecting the exhaust flow. Due to lack of sufficiently detailed explorations on the domain of interest, the novel work does not relate to any previous research.

The general objective is to develop a numerical method capable of a reliable prediction of the (time-dependent) flow field characteristics over the stroke chosen.

The research has been accomplished in several consecutive steps, ordered and executed in a logical sequence. After a literature survey it has been decided to develop an own numerical code that would use the state-of-art physical models and numerical methods and allow a flexible and wide code customization. It was crucial that this code remains as transparent and open source as possible. This numerical code should also be sufficiently robust and easy to apply (not only for the exhaust channel problem, but) for other CFD test cases.

An in-house numerical code *MUSA* (coded by M. Žaloudek) has been used as an initial platform. In order to carry out realistic simulations on the test case chosen, the code has required several substantial changes and extensions.

Within the scope of cooperation with the von Kármán Institute for Fluid Dynamics (Rhode St. Genèse, Belgium) an opportunity to participate on the development of the large CFD framework *COOLFluiD* (Computational Object Oriented Library for Fluid Dynamics) has been utilised - this code has also been used for the purposes of this thesis.

In order to perform the simulations on the exhaust channel, *COOLFluiD* has required code extensions, namely supplying the code with new turbulence models, their extension to 3D and further implementations related to the unsteady approach. Therefore a subsidiary target of the thesis has been to make a review of current turbulence models and to select those, suitable for the subject solved, for the code framework (regarding its internal structure) and with affordable CPU demands. The models selected have then been implemented into the code.

The reliability and properties of both numerical codes used have been tested, debugged and tuned on several reference test cases. Having this validation finished the solvers have been used on the exhaust channel test case. Next objective of this work has been to cross-validate the results obtained by these fundamentally different CFD codes.

After gaining confidence in the reliability of the results, the influence of various simulation parameters has been analyzed.

From the *numerical* point of view, over a progressive development of the codes, the influence of the ascending flow model complexity (inviscid / laminar / turbulent) has been studied and appraised regarding the respective suitability of the models. The influence of particular turbulence models has also been tested. Lastly, the effect of steady and unsteady approach to the problem simulation has been investigated.

From the *technical* point of view, an impact of (technologically affordable) geometrical changes to the exhaust channel has been studied. On the fixed part of the channel, the angle between

the plane of a chamber top and the valve axis has been altered in order to better cast the flow direction. On the moving part, three different profiles of the exhaust valve stem have been tested, observing their influence on the mass flow rate through a channel during the exhaust stroke.

Goals of the Thesis

The general objectives have been concretized into the following goals:

- model and describe the flow field around the exhaust valve during the exhaust stroke; describe the characteristic flow properties and dependencies;
- assess the aerodynamical properties of the geometry of the valve and the exhaust channel;
- ascertain the limits of the contemporary numerical methods for simulations of the flow around the exhaust valve regarding the turbulence modelling and the numerical scheme used;
- implement the modern numerical schemes and turbulence models into the numerical methods with an emphasis on the computations on a moving domain.

Structure of the Thesis

Due to the scope of the subject, the thesis is structured into eight chapters.

The second chapter contextualizes the work among the up-to-date research topics and extracts the respective motivation. A broader technical and physical background of the problem to be solved is also presented in this chapter.

The third chapter describes the governing equations of the flow under the consideration. The mathematical model is based on a general conservation equation for a moving control volume. Necessary constitutive relations, initial and boundary conditions are presented creating altogether the so-called well-posed problem (having same number of unknowns and equations, allowing a numerical solution).

The fourth chapter is dedicated to the turbulence. Its general characteristics are outlined together with a method of describing the turbulence with mathematical equations. Next section presents the assembly of the turbulence transport equations with the original equations of fluid motion from the chapter 3. This chapter also contains a review of current turbulence models, followed by a detailed description of the models selected for implementation,

The fifth chapter focuses on the numerical methods used across the whole work. Both the numerical codes employed are introduced here, with an emphasis on their common and diverse aspects.

The sixth chapter presents numerical results on the reference test cases. The goal has been to prove the suitability of both codes for the exhaust channel test case. The accuracy and reliability of both numerical codes have been assessed by the differences measured from the reference solution. After tuning the codes so to have the best agreement possible, the solvers have been used on the target test case.

The seventh chapter shows, analyzes and discusses the numerical results obtained on the exhaust channel. The novel results and main achievements of this work are concentrated here.

The final chapter brings the conclusions gathered over the entire work and suggests possible directions for an eventual sequel.

The last pages belong to the annexes containing useful analysis and derivations and related technical drawings.

Chapter 2

Motivation

Up to present days, internal combustion engines are the most frequently used sources of mechanical energy. They play a dominant role in the means of ground transport, such as motorbikes, cars, buses, as well as in many other industrial applications. To make the image more concrete, the figure 2.1 presents the absolute number of registered vehicles in the Czech Republic during the past decade. Data has been extracted from [6] and the Central Vehicle Registry of the Czech Republic.

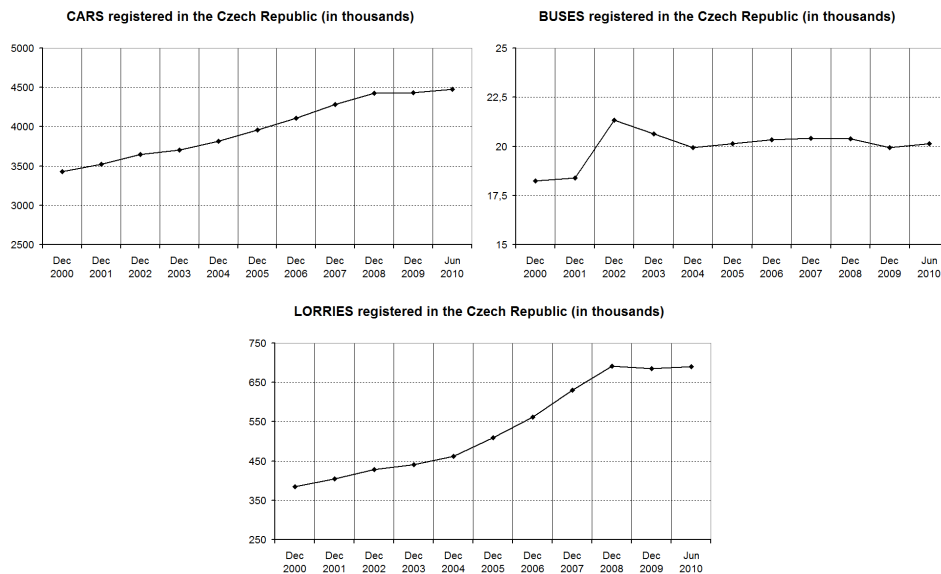


Figure 2.1: Absolute number of the double-track vehicles registered in the Czech Republic

The recent year-to-year growth has slowed down due to the economic crisis of last years, nevertheless the long term trends have remained positive for all the categories observed¹. Also to emphasize the importance of motor vehicles let us mention that the today's Czech Republic is a country with roughly ten million inhabitants and with more than seven million motor vehicles registered. Because their absolute majority is being powered with an internal combustion engine, its mechanical reliability, economical operation and ecological friendliness is highly required.

In order to reduce any inconvenient sequels of the usage of the combustion engines, the transformation process of the chemical energy of the fuel into the mechanical energy must be completely

¹The peak in the buses' chart in 2002 is caused by the legislative change to the classification of vehicles of this type.

understood.

Combustion Engines

In general terms, the combustion engine (CE) represents any heat engine, whose purpose is to produce mechanical energy from chemical energy of (usually fossil) fuel. Two main families of CE can be distinguished:

- external combustion engine (ECE) - the working medium is heated by the combustion of an external source. The heating is then made through the heat exchanger or through the wall.
- internal combustion engine (ICE) - here the combustion of the (most often) fuel-air mixture happens directly inside the engine. The mixture plus its burned products are then the actual working medium.

By these definitions, the gas turbines also belong to the family of ICE. However, their working principles are too different from the common car engines and will therefore not be considered as an ICE in the scope of this work.

The term *internal combustion engine*, if mentioned here, will stand for a reciprocating engine. It is a unit with one or more reciprocating pistons. The reciprocation is then actuated by the combustion, whereas the output energy is mechanically extracted from the moving pistons, see the figure 2.2.

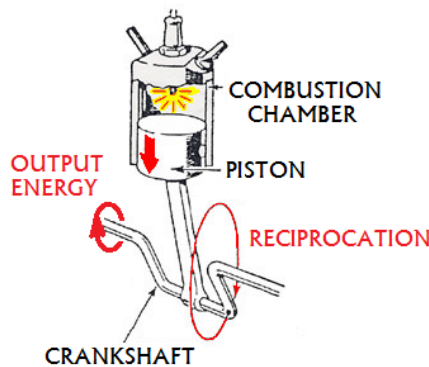


Figure 2.2: Scheme of the reciprocating engine

2.1 Reciprocating Engines

The first reciprocating engine has been developed already in the 18th century, but its real boom started together with the beginning of the commercial production of petroleum in the middle of the 19th century. Despite its respectable age, the technology of reciprocating engines is still actual and its current research focuses on the increase of the overall efficiency with simultaneous decrease of air and noise pollution.

Ideal Operating Cycle

Suppose a heat engine at a concrete thermodynamic state. A thermodynamic (operating) cycle arises, if this engine undergoes a series of different states and finally returns to its initial state (see

the figure 2.3). A Carnot heat engine is a system following an ideal thermodynamic cycle, the so-called Carnot cycle (the figure 2.4 b).

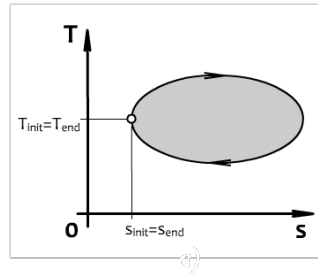


Figure 2.3: General thermodynamic cycle in a temperature-entropy diagram

This cycle represents an ideal reversible heat machine. Due to the reversibility it can be seen either as a heat engine (following the state changes in a clock-wise manner) or a heat pump (following the state changes in a counter-clock-wise manner).

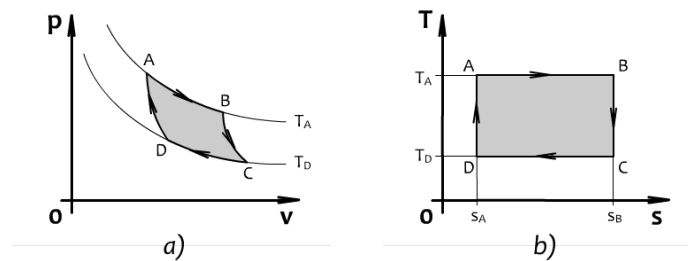


Figure 2.4: The Carnot cycle in a) pressure-volume chart b) temperature-entropy chart

As depicted in p - v and T - s diagrams in the figure 2.4, the cycle consists of four state changes:

1. isothermal expansion (step A-B) - the absorption of heat Q_{AB} induces the gas expansion, which provides work W_{AB} .
2. isentropic expansion (step B-C) - all the acting parts of engine are assumed to be thermally insulated and therefore neither gaining nor losing heat. The gas however continues expanding, which leads to a decrease of its temperature from T_B to T_C .
3. isothermal compression (step C-D) - the surroundings perform work on the gas. This work is released from the system in a form of heat Q_{CD} .
4. isentropic compression (step D-A) - all the acting parts are assumed to be thermally insulated again. The surroundings perform work on the gas, causing an increase of its temperature to T_D , with a simultaneous decrease of the volume.

The overall work gained during such cycle can be computed (according to the first law of thermodynamics) as

$$W = \oint p dv = \oint (dQ - dU) . \quad (2.1)$$

The integral of an internal energy $\oint dU$ is zero for any closed cycle and therefore the work provided by the cycle only depends on the heat difference

$$W = Q_{AB} - Q_{CD} . \quad (2.2)$$

The efficiency of a thermodynamic cycle η is expressed as a ratio of the work done and the energy provided. Respecting the second law of thermodynamics and equalities $T_{A/C} = T_{B/D}$, $s_{A/B} = s_{D/C}$, the Carnot cycle efficiency therefore is

$$Q_{AB} = T_A(s_B - s_A), \quad Q_{CD} = T_D(s_B - s_A)$$

$$\eta_{Carnot} = \frac{W}{Q} = \frac{Q_{AB} - Q_{CD}}{Q_{AB}} = 1 - \frac{T_D(s_B - s_A)}{T_A(s_B - s_A)} = 1 - \frac{T_D}{T_A}. \quad (2.3)$$

It can be shown that the Carnot cycle efficiency (2.3) is the theoretical maximal efficiency of a cycle which operates between T_A and T_D . Furthermore (*Carnot's theorem*) it can be proved (see [68]) that any irreversible thermodynamic cycle has smaller efficiency than η_{Carnot} .

Real Operating Cycles

Any real operating cycle is irreversible due to thermodynamic losses. The isothermal and isentropic state changes of the Carnot cycle are therefore substituted by other mechanisms, as shown in the table 2.1. The p - v charts of these engines are shown in the figure 2.5.

step	A-B	B-C	C-D	D-A
Cycle	heat addition	expansion	heat rejection	compression
Carnot	isothermal	isentropic	isothermal	isentropic
Brayton	isobaric	adiabatic	isobaric	adiabatic
Diesel	isobaric	adiabatic	isochoric	adiabatic
Otto	isochoric	adiabatic	isochoric	adiabatic

Table 2.1: State changes for ideal and some real heat engines

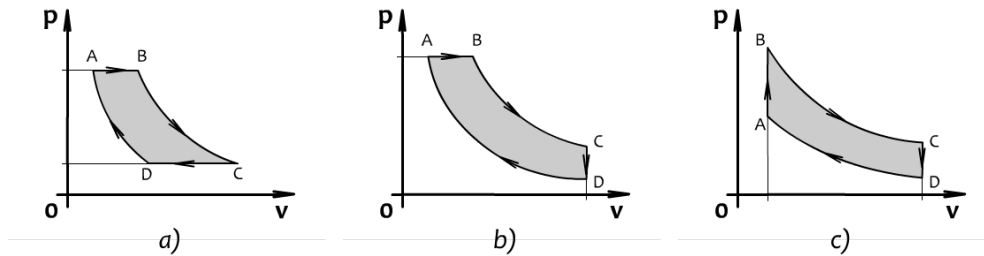


Figure 2.5: The pressure-volume charts of a) Brayton b) Diesel c) Otto operating cycles

- the Brayton cycle describes the work of the gas turbine engine.
- the Diesel cycle is an ideal model of a compression-ignition engine, therefore called a diesel engine.
- the Otto cycle describes the work of the spark-ignition engine, also called a gasoline or a petrol engine.

The last two cycles represent the most frequent engines of the today's car industry.

Four-Stroke Engine

All the cycles mentioned consist of four state changes, which is why they are often realized by four-stroke engines - each cycle step represented by one stroke. Each cylinder needs two revolutions of

the crankshaft (720 degrees) in order to undergo a whole cycle, i.e. to produce one power stroke. Both spark-ignition and compression-ignition engines follow the scheme shown in the figure 2.6, passing the strokes in a following order:

1. an *intake* stroke ($0^\circ - 180^\circ$) - the piston travels from its top to the bottom position, drawing fresh mixture into the cylinder.
2. a *compression* stroke ($180^\circ - 360^\circ$) - the both valves are closed and the mixture inside the cylinder is compressed by the piston moving upwards.
3. a *power* stroke ($360^\circ - 540^\circ$) - the mixture ignition leads to a sudden increase of the temperature and pressure, which pushes the piston downwards, forcing the crank to rotate.
4. an *exhaust* stroke ($540^\circ - 720^\circ$) - the exhaust valve opens, so that the mixture burnt can leave the cylinder and the whole cycle can be restarted.

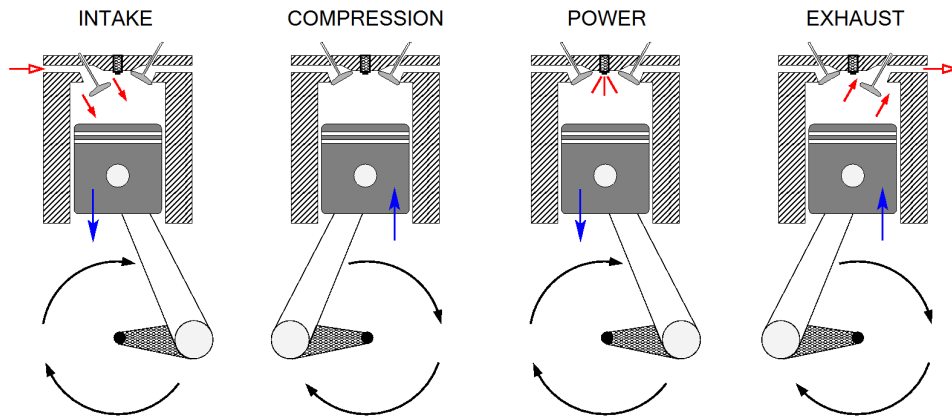


Figure 2.6: Operating cycle of a four-stroke engine

Two-Stroke Engine

In order to obtain a higher power output from a given engine size as well as a simpler valve design, the two-stroke engines have been developed, linking some stages of the operating cycle together, see the figure 2.7. The two strokes usually are

1. a *compression* stroke - the piston travels upwards, closes the inlet and exhaust ports and compresses the mixture inside the cylinder with a simultaneous draw of fresh mixture into the crankcase. When the piston reaches the top position, the combustion is initiated.
2. a *power* stroke - this stroke is similar to the four-stroke engine until the moment, when the piston uncovers the exhaust port (first), allowing the burnt mixture to exit the cylinder and the inlet port (second) allowing to refresh the mixture.

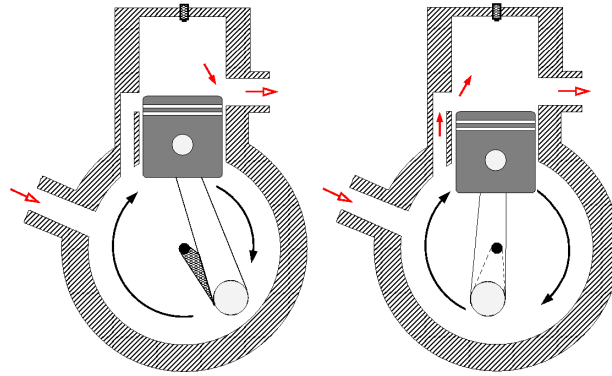


Figure 2.7: Operating cycle of a two-stroke engine

The advantage of a two-stroke engine is the higher frequency of power strokes (one power stroke each crankshaft revolution), but it is more difficult to fill completely the displaced volume with the fresh mixture on the other hand. Its primary drawback however is, that some mixture of fresh fuel and air flows directly out of the cylinder during the scavenging process.

Other Internal Combustion Engines

The list of internal combustion engines should be completed also mentioning the Wankel engine, gas turbine and jet engine. This work is however focused on piston engines (in a four-strokes regime only), into which group none of the engines listed belongs to.

- a Wankel engine is a rotary machine operating in a four-stroke manner. The strokes take place in separate locations of the engine, producing one power stroke per crankshaft revolution. Due to the eccentric shaft it gives better power-to-weight ratio than piston engines, but also creates much higher technological demands on the manufacturing process.
- a gas turbine is also a rotary machine consisting of a compressor, a combustion chamber and a turbine. The air, after being compressed, is heated by burning fuel in it. The burnt mixture then expands in the turbine resulting in work output, which partly also actuates back the compressor.
- a jet engine requires a large volume of hot gas from a combustion process (typically a gas turbine), which is then accelerated inside a jet nozzle. This effect provides a thrust and work output to the moving vehicle.

For detailed information about the Wankel engine see [107], for further details of a gas turbine and a jet engine see [87].

2.2 Flow Inside a Combustion Engine

If not specifically mentioned, only the *four-stroke internal combustion engine* (its basic version has been depicted in the figure 2.6) will be discussed from here on. Moreover, the main focus of this work is on the flow through the combustion chamber.

It is the most important domain which governs the output parameters of whole engine, such as its efficiency, the emission of pollution, the lifespan etc.

According to the literature [61, 80], the flowfield in a combustion chamber is claimed to depend on the geometry of the interior and on turbulent and chemical processes inside the chamber. The flowfield structure has been found responsible for the quality of the combustion, for the wall heat transfer and also for the ease of scavenging processes. Altogether it answers the question, why the proper modelling of the flow inside a combustion engine plays so important role.

The characteristics of the flowfield can be found in [72]: it is a complicated unsteady turbulent flow of interacting boundary layers, shear stress and recirculation zones, with both small and large turbulent timescales of the same importance.

From the turbulence point of view the processes inside the engine can be splitted in two categories:

1. Scavenging strokes, when either the intake or the exhaust valve is opened. The turbulence is generated by the shear stress zones, which appear due to the flow around the valve (channel with a narrow throat). The intake stroke strongly affects the flowfield inside the chamber, which then becomes a source of turbulence during the high-pressure strokes.
2. High-pressure strokes, when the air mixture works in a closed volume. Here the turbulence arises due to the piston movement, due to the mixture movement (initiated during the intake stroke), due to geometry of the chamber, due to ignition and combustion of the fuel. Large pressure, velocity and temperature gradients are present here, together with the intensive heat transfer to the walls.

The first group of processes impacts the engine power (intake) and the efficiency of the turbocharger (exhaust), whereas the second group affects the efficiency of the whole thermodynamic cycle and the production of pollution. These high-pressure processes have been described in [98], where the effect of turbulence on the compression and the expansion stroke has been studied. The numerical results have been obtained with an in-house developed CFD solver, based on the finite volume method solving an unsteady 3D flow. Its results have been compared to the experimental measurements with a qualitative agreement observed for carefully tuned turbulence models. Strong correlation among the turbulence model chosen, the initial layout of the air mixture, the grid size on the agreement with experiments have been found.

The numerical results have also proved the independence of the turbulent variables on the temperature and therefore not affecting the solution with or without considering the heat transfer to the wall. However, serious disproportions have been captured for the non-diagonal Reynolds stresses and integral scales of the engine when compared to the experimental data.

The scavenging processes have mainly been simulated by 0D or 1D models as described in [62] (solver OBEH) and [2] (solver GT-Power), empirically (and roughly) estimating the influence of the turbulence and other factors. Within last years these scavenging processes are also modelled with more advanced methods, usually provided by commercial solvers as Fluent or StarCD. Their focus is mainly bounded to the intake stroke [12, 63] and only few recent works simulate the processes during an exhaust stroke [36].

This work is focused especially on this last stroke of the engine cycle and brings first explorations of the problem.

Experimental Results

More than hundred years after the first combustion engine has been constructed, there is still a big lack of experimental data from the combustion chamber and the intake/exhaust channels.

This is mainly due to the complicated (and expensive) instrumentation required (moving parts at high speeds and pressures, large volume displacements, non-symmetric geometry etc.) or a strict policy of the industrial company performing the experimental measurements. For this work, no publishable experimental data have been available.

Engine Terminology Used

According to the literature [41] the engine parts around the combustion chamber (with importance to this work) use a nomenclature shown in the figure 2.8, with

TDC the top dead center, a position with the smallest cylinder volume and with zero instantaneous velocity of the piston.

BDC the bottom dead center, a position with the largest cylinder volume and with zero instantaneous velocity of the piston.

V_c , V_d , V_t the clearance, displacement and total cylinder volume.

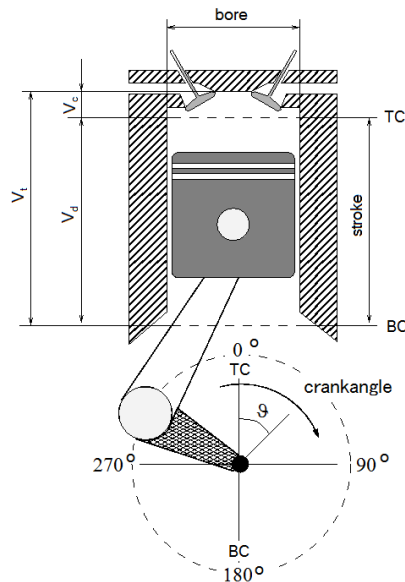


Figure 2.8: Basic geometry of the reciprocating internal combustion engine, a figure from [41]

The nomenclature of the intake/exhaust valve is shown in the figure 2.9. As the valve and flow around it belong to the main target of this work, it will often be displayed with a horizontal alignment of the valve axis.

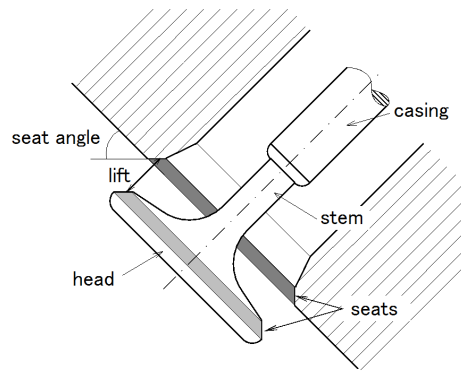


Figure 2.9: Intake/exhaust valve nomenclature

Chapter 3

Flow Model

This chapter will present the mathematical model of the flow inside a combustion chamber. This model is based on the integral balance of the basic conservation laws of mass, momentum and energy over an arbitrary control volume. Such systems generally contain more unknowns than the actual number of equations. Therefore, in order to have a solvable system, several constitutive relations, initial and boundary conditions must also be provided.

3.1 Conservation Laws

Any conservation law on a bounded domain can be expressed with a following equation

$$[\text{accumulation}] = [\text{inflow}] - [\text{outflow}] + [\text{creation}]. \quad (3.1)$$

When balancing a property P , all possible mechanisms of right hand side terms must be considered. Assume a control volume Ω with a surface $\partial\Omega$ and \vec{w} the velocity vector. Because of many moving parts inside the engine (i.e. moving boundaries of the control volume) the following formulation has been chosen

$$\frac{d}{dt} \int_{\Omega} P d\Omega = - \int_{\partial\Omega} P (\vec{w} - \vec{w}_B) \cdot \vec{n} d\partial\Omega + \int_{\Omega} V_P d\Omega + \int_{\partial\Omega} \vec{S}_P \cdot \vec{n} d\partial\Omega, \quad (3.2)$$

with \vec{w} the convective velocity of P , \vec{w}_B the boundary movement, \vec{n} the outward unit normal, V_P the volume source and S_P the surface source of P . The equation (3.2) is also known as the *Leibnitz-Reynolds transport theorem*.

Integral Form of Conservation Laws

By substituting the property P with a suitable physical variable, the equation (3.2) turns to a conservation law of mass, momentum or energy. The detailed expansion can be found in [68, 110], with the resulting equations:

- continuity equation (conservation of mass):

$$P = \rho, V_P = 0, \vec{S}_P = 0, \quad (3.3)$$
$$\frac{d}{dt} \int_{\Omega} \rho d\Omega = - \int_{\partial\Omega} \rho (\vec{w} - \vec{w}_B) \cdot \vec{n} d\partial\Omega$$

- momentum equation (conservation of momentum):

$$P = \rho w_i, V_P = \rho g_i, \left[\vec{S}_P \cdot \vec{n} \right]_i = \left[-p \cdot \vec{n} + \vec{\tau} \cdot \vec{n} \right]_i,$$

$$\begin{aligned} \frac{d}{dt} \int_{\Omega} \rho w_i d\Omega &= - \int_{\partial\Omega} \rho w_i (\vec{w} - \vec{w}_B) \vec{n} d\partial\Omega + \int_{\Omega} \rho g_i d\Omega \\ &+ \int_{\partial\Omega} (-p\delta_{ij} + \tau_{ij}) n_j d\partial\Omega, \end{aligned} \quad (3.4)$$

with g the gravitational acceleration, p the pressure and τ the stress tensor. The volume source due to gravity $\int_{\Omega} \rho g_i d\Omega$ can be neglected for most of the applications of internal aerodynamics as its size becomes negligible compared to other terms of the equation.

- energy equation (conservation of energy):

$$P = \rho e, V_P = \rho g_i w_i + \dot{Q} - W, \vec{S}_P = \left(-p \cdot \vec{n} + \vec{\tau} \right) (\vec{w} - \vec{w}_B) - \vec{q},$$

$$\begin{aligned} \frac{d}{dt} \int_{\Omega} \rho e d\Omega &= - \int_{\partial\Omega} \rho E (\vec{w} - \vec{w}_B) \vec{n} d\partial\Omega \\ &+ \int_{\Omega} \rho g_i w_i d\Omega + \int_{\Omega} \dot{Q} d\Omega - \int_{\Omega} W d\Omega \\ &+ \int_{\partial\Omega} (-p\delta_{ij} + \tau_{ij}) (\vec{w} - \vec{w}_B) \vec{n} d\partial\Omega - \int_{\partial\Omega} \dot{q} \vec{n} d\partial\Omega, \end{aligned} \quad (3.5)$$

with \dot{Q} , W the heat flux and the work corresponding to the first law of thermodynamics (2.1) and \dot{q} the surface source.

As mentioned hereabove, the gravitational terms do not play important role for applications with characteristic length of centimeters and therefore are neglected in both equations (3.4) and (3.5). The closed thermodynamic cycle allows the substitution

$$- \int_{\Omega} W d\Omega = \int_{\partial\Omega} (-p\delta_{ij} + \tau_{ij}) \vec{w}_B \vec{n} d\partial\Omega, \quad (3.6)$$

because the work can only be provided through pressure or viscous forces.

Due to historical reasons, the conservation law of momentum, equation (3.4), is often called the *Navier-Stokes equation*. The same terminology is however also being used for the whole set of equations (3.3), (3.4) and (3.5), mainly in Anglo-Saxon literature. This work employs the second approach, with the term *Navier-Stokes equations* denoting all three conservation laws.

Differential Form of Conservation Laws

The original equation (3.1) can be differentiated using *the Gauss theorem*

$$\int_{\Omega} \nabla \mathbf{F} d\Omega = \oint_{\partial\Omega} \mathbf{F} \cdot \vec{n} d\partial\Omega. \quad (3.7)$$

The boundary movement does not need to be considered in the differential form ($\vec{w}_B = 0$) and so the equation (3.1) transforms into

$$\frac{\partial P}{\partial t} = -\vec{\nabla} P \vec{w} + V_P + \vec{\nabla} \vec{S}_P. \quad (3.8)$$

The analogous substitutions of the property P as for the integral form lead to conservation laws in differential form

$$\frac{\partial \rho}{\partial t} + \frac{\partial \rho w_j}{\partial x_j} = 0, \quad (3.9)$$

$$\frac{\partial (\rho w_i)}{\partial t} + \frac{\partial (\rho w_i w_j)}{\partial x_j} = \frac{\partial}{\partial x_j} (-p \delta_{ij} + \tau_{ij}), \quad (3.10)$$

$$\frac{\partial (\rho E)}{\partial t} + \frac{\partial (\rho e w_j)}{\partial x_j} = \frac{\partial}{\partial x_j} [(-p \delta_{ij} + \tau_{ij}) w_i] - \frac{\partial \dot{q}_j}{\partial x_j} + \dot{Q}. \quad (3.11)$$

The Euler Equations

The complete Navier-Stokes equations describe the behaviour of a viscous fluid. However, in many applications the viscous effects can be neglected outside the boundary layer: e.g. high Reynolds-number flows, where a boundary layer is very thin compared to the dimension of the body, the effect of the boundary layer on the pressure field is very small. In such case the right hand side of the equations (3.10) and (3.11) simplifies by assuming

$$\tau_{ij} \equiv 0 \quad (3.12)$$

and transforms the whole system into

$$\frac{\partial \rho}{\partial t} + \frac{\partial \rho w_j}{\partial x_j} = 0, \quad (3.13)$$

$$\frac{\partial (\rho w_i)}{\partial t} + \frac{\partial (\rho w_i w_j)}{\partial x_j} + \delta_{ij} \frac{\partial p}{\partial x_j} = 0, \quad (3.14)$$

$$\frac{\partial (\rho E)}{\partial t} + \frac{\partial (\rho e w_j)}{\partial x_j} + \frac{\partial}{\partial x_j} (p w_i \delta_{ij}) = 0. \quad (3.15)$$

This simplified form of the governing equations is called the *Euler equations*. They describe the pure convection of flow quantities in a compressible inviscid flow.

The Euler equations serve as the basis for the development of discretisation methods and boundary conditions. However, due to the growth of the computational power and due to the increased demands on the quality of the simulations (mainly the accurate prediction of the losses, drag, friction, position of separation, turbulence effects, etc.), the Euler equations are increasingly less employed for flow computations.

3.2 Constitutive Relations

These relations arise from physical assumptions about the problem solved and create a solvable set of equations out of the system (3.9)-(3.11). As a working medium the choice of single phase air has been considered, obeying the state equation

$$p = \rho R T, \quad (3.16)$$

with R the specific heat constant, see the equation (3.25). The internal energy e is defined as

$$e = c_v T, \quad (3.17)$$

with c_v the specific heat at constant volume. Similarly for the enthalpy

$$h = e + \frac{p}{\rho} = c_p T. \quad (3.18)$$

With the knowledge of relation between c_p , c_v and, R

$$R = c_p - c_v = \frac{\gamma - 1}{\gamma} c_p \quad (3.19)$$

the equation of state (3.16) can be rewritten into

$$p = (\gamma - 1) \rho \left[E - \frac{|\vec{w}|^2}{2} \right]. \quad (3.20)$$

Here γ denotes the ratio of specific heats (so-called the *Poisson's constant*), see the equation (3.25). The viscous stresses which originate from a friction between the fluid and the surface of an element are described by the symmetric stress tensor τ

$$\tau_{ij} = \mu \left(\frac{\partial w_i}{\partial x_j} + \frac{\partial w_j}{\partial x_i} \right) + \left(\lambda_S - \frac{2}{3} \mu \right) \frac{\partial w_k}{\partial x_k} \delta_{ij}. \quad (3.21)$$

The *Stokes viscosity* λ_S has been neglected and the dynamic viscosity has been computed by *Sutherland's law*

$$\mu = \frac{C_1 T^{3/2}}{T + S}, \quad (3.22)$$

with C_1 and S the constitutive air constants, shown in (3.25) and the temperature calculated from equation (3.16). Such fluid for which the shear stress τ is linearly related to the velocity gradients is called a *Newtonian fluid*.

The kinetic theory of gases, supported by experimental observations, indicates that the heat flux by thermal conduction in a fluid depends linearly on the temperature gradient. This is expressed by *Fourier's law*

$$\dot{q}_i = -\lambda \cdot \frac{\partial T}{\partial x_i}, \quad (3.23)$$

$$\lambda = \frac{c_p \mu}{\text{Pr}} \quad (3.24)$$

where the thermal conductivity λ is computed from the specific heat at constant pressure c_p and the laminar *Prandtl number*, see (3.25). This *Prandtl number* is assumed constant over the entire flow field.

$$\begin{aligned} R &= 286.9 \frac{\text{J}}{\text{kg} \cdot \text{K}}, & \gamma &= 1.4, \\ c_p &= 29.19 \frac{\text{J}}{\text{mol} \cdot \text{K}}, & c_v &= 20.85 \frac{\text{J}}{\text{mol} \cdot \text{K}}, \\ C_1 &= 1.458 \cdot 10^{-6} \frac{\text{kg}}{\text{m} \cdot \text{s} \cdot \sqrt{\text{K}}}, & S &= 110,4\text{K}, \text{Pr} = 0.72. \end{aligned} \quad (3.25)$$

3.3 Initial and Boundary Conditions

In order to solve the system (3.9)-(3.11) some suitable initial and boundary conditions have to be specified. Their number and character must reflect the mathematical properties of the system solved.

Mathematical Character of the Governing Equations

The character is best explained on the quasi-linear second order equation

$$a \frac{\partial^2 U}{\partial x_i^2} + b \frac{\partial^2 U}{\partial x_i \partial x_j} + c \frac{\partial^2 U}{\partial x_j^2} = d, \quad (3.26)$$

with U the general scalar function and a , b , c , d the general coefficients (constants, non-linear functions of coordinates, functions of U or functions of first derivatives of U). Depending on the sign of the discriminant function $D = (b^2 - 4ac)$ three different classes can be defined:

- hyperbolic, $D > 0$, such equation (3.26) has two real characteristics. Any solution point X then depends exclusively on the part of the boundary intersected by characteristics which are triggered from the point X . Therefore the conditions must be specified only at part of the boundary representing an initial-value problem.
- elliptic, $D < 0$, such equation (3.26) has two complex characteristics. Any solution point X depends completely on the surrounding domain, i.e. on all the boundaries. Therefore the boundary conditions must be defined everywhere, representing a boundary-value problem.
- parabolic, $D = 0$, such equation (3.26) has one real characteristic. It is a mixture between previous cases, representing a mixed initial- boundary-value problem.

The complete mathematical analysis can be found in [14, 35].

Unfortunately, the classification of the Navier-Stokes equations (3.9), (3.10), (3.11) can not be determined uniquely. In fact, they are in general a mixture of all three classes, depending on the flow conditions and on the geometry of the problem. The detailed description must therefore be presented in a particular relation to the problem solved. Hence only the general conditions are presented here.

Initial Conditions

The initial condition determines the fluid state at the initial time $t = 0$ or at the first step of an iterative scheme. For the steady state problem, the closer the initial guess is, the faster the final solution will be obtained, together with the reduced probability of the computation breakdown.

Regarding the usual fact that the solution is unknown, it is important that the initial solution satisfies at least the governing equations and the additional thermodynamic relations. A common practice consists of imposing freestream values of pressure, velocity and temperature components in the whole flowfield.

$$\begin{aligned} p(0, \vec{x}) &= p_{init} \\ \vec{w}(0, \vec{x}) &= \vec{w}_{init} \\ T(0, \vec{x}) &= T_{init} \end{aligned} \quad (3.27)$$

Boundary Conditions

Different conditions can be found on places where the boundary is exposed to the fluid. For a viscous flow governed by the Navier-Stokes equations (3.9)-(3.11), the appropriate boundary condition is the zero velocity on the surface

$$\vec{w}(t, \vec{x})|_{\Theta_1} = 0, \quad (3.28)$$

if the surface Θ_1 is at rest and

$$\vec{w}(t, \vec{x})|_{\Theta_2} = \vec{w}_B, \quad (3.29)$$

if the surface Θ_2 is moving at speed \vec{w}_B . Such conditions, directly imposing the value of the variable, are called *Dirichlet* boundary conditions.

The conditions for the variables remaining are represented by *Neumann* boundary conditions prescribing the variable's gradient. Based on the analysis of the two-dimensional boundary layer at high Reynolds number, see [93], the pressure boundary condition reads

$$\left. \frac{\partial p(t, \vec{x})}{\partial n} \right|_{\Theta_1 \cup \Theta_2} = 0. \quad (3.30)$$

According to Fourier's law (3.23) the condition for temperature is

$$\left. \frac{\partial T(t, \vec{x})}{\partial n} \right|_{\Theta_1 \cup \Theta_2} = -\frac{\dot{q}_{wall}}{\lambda(T)}, \quad (3.31)$$

for the computations including the wall heat transfer. If the heat transfer is neglected (adiabatic condition), the equation (3.31) simplifies to

$$\left. \frac{\partial T(t, \vec{x})}{\partial n} \right|_{\Theta_1 \cup \Theta_2} = 0. \quad (3.32)$$

For an inviscid flow governed by the Euler equations (3.13)-(3.15), the appropriate wall boundary condition is to require tangential flow to the surface

$$\vec{w} \cdot \vec{n}|_{\Theta_1 \cup \Theta_2} = 0. \quad (3.33)$$

Compatibility Constrains

In order to fulfill this constraint, in zones where the initial condition interferes with the boundary conditions the actual value imposed by both conditions must be identical. This is usually accomplished via a well-fitted initial condition.

Chapter 4

Turbulence

All the equations previously mentioned describe either *an inviscid* (equations (3.13)-(3.15)) or a *laminar* (equations (3.9)-(3.11)) flow model, with all their constitutive relations. Such systems of equations create solvable sets, but due to the physical assumptions they have arisen from, they unfortunately have very strong limitation for practical use. Most flows in nature as well as many real applications require a *turbulent* flow model, which adds more transport equations and constitutive relations to the current system.

The physical background of turbulent flow, differences compared to the laminar flow and new demands caused by various turbulent models are explained in this chapter.

4.1 Physical Properties

Turbulence appears in all fluids and all velocity ranges: from a subsonic speed of the sea water ($|\vec{w}| \approx 1 \text{ m/s}$) to a hypersonic speed of air in many aeronautical applications ($|\vec{w}| \approx 1000 \text{ m/s}$), see examples in the figure 4.1. Turbulence comes into play anytime when the inertia or the volume forces have grown sufficiently, with respect to the viscous forces.

When the critical ratio of inertia and viscous forces (the so called *Reynolds* number, $\text{Re} = \frac{w \cdot L}{\nu}$) is exceeded, the current laminar flow that has been dumping the respective flow instabilities turns into turbulent, which is characterized by rotational and vorticular movements.



Figure 4.1: Examples of turbulent motions: sea waves (left), re-entry of the Apollo module to the atmosphere (right)

Despite more than a century lasting research of turbulence, a clear and unique definition of this phenomenon has not been found yet. A question still to be answered is also the description and understanding of all turbulent mechanisms, which task can only be resolved by both theoretical and experimental observations.

Turbulence is not a property of a fluid (such as temperature, dynamic viscosity, etc.), but it

rather is a property of the flow. It is affected by the geometry of the domain, by the initial state, by the boundaries and also by the nature of the fluid. Turbulence can be characterized by terms as instability, unsteadiness, spatiality, nonlinearity, inordinance, rotation or diffusivity. The aim of this work however is not to rigorously define these terms or to build up a new turbulence theory. Therefore references as [75, 103] are offered for closer explanations.

Regarding to the general observations, turbulence consists of a continuous spectrum of vortices (eddies) ranging from largest to smallest. A turbulent vortex can be thought of as a local swirling motion whose characteristic dimension is the local turbulence scale. Large eddies carry the smaller ones, featuring a cascade process, whereby as the turbulence decays, its kinetic energy is transferred from larger to smaller eddies. Ultimately, the smallest eddies dissipate into heat through the action of molecular viscosity, concluding that any turbulent flow is always dissipative.

From an engineering point of view the most important property of turbulence is the enhanced diffusivity - often several orders of magnitude larger than in corresponding laminar flows. It greatly increases the transfer of mass, momentum and energy.

The large turbulent eddies have a relatively long lifespan inside the flowfield, which is why they depend both on the local flow parameters and also on their own history. The dissipation of the turbulent energy is realized in smallest vortices, in which the molecular viscosity plays a major role. The energy of these vortices is usually consumed within a single revolution and therefore the rate of the dissipation is mainly driven by the speed of the energy relegation from large to smaller eddies.

Scales of Turbulent Vortices

The turbulent eddies can be characterized by a size measure l , the so-called integral length scale (of turbulence). Unfortunately, this scale can not be directly measured and must be extracted from the following relation (see [103])

$$l(x, t) = \frac{3}{16} \int_0^\infty \frac{R_{ii}(\vec{x}, t; \vec{r})}{k(\vec{x}, t)} dr, \quad (4.1)$$

with \vec{x} the position vector, \vec{r} the displacement vector, R_{ij} the two-point velocity correlation tensor

$$R_{ij}(\vec{x}, t; \vec{r}) = \overline{w'_i(\vec{x}, t) w'_j(\vec{x} + \vec{r}, t)}, \quad (4.2)$$

and k the total kinetic energy per unit mass of the fluctuating turbulent velocity

$$k = k(\vec{x}, t) = \frac{1}{2} R_{ii}(\vec{x}, t; 0). \quad (4.3)$$

The time averaging operator \bar{X} on the right hand side and the velocity fluctuations w'_i are explained below by the equation (4.26). The integral time scale τ_l is defined analogically

$$\tau_l(\vec{x}, t) = \frac{1}{2} \int_0^\infty \frac{R_{ii}^r(\vec{x}, t; t')}{k(\vec{x}, t)} dt', \quad (4.4)$$

$$R_{ij}^r(\vec{x}, t; t') = \overline{w'_i(\vec{x}, t) w'_j(\vec{x}, t + t')}. \quad (4.5)$$

The total kinetic energy per unit mass of the fluctuating turbulent velocity can now be expressed as Considering that turbulence has a continuous spectrum of scales, it is also possible to perform a quantitative analysis via the spectral distribution of energy. In general, a spectral representation is

a Fourier decomposition into wavenumbers κ , or wavelengths λ . If $E_k d\kappa$ is the turbulence kinetic energy between wavenumbers κ and $\kappa + d\kappa$, then the equation (4.3) can also be written

$$k = \int_0^{\infty} E(\kappa) d\kappa. \quad (4.6)$$

With the definition made, the reciprocal of κ corresponds to the vortex size. An example of the energy spectrum of the homogeneous turbulent flow (balanced production and dissipation) is shown in the figure 4.2.

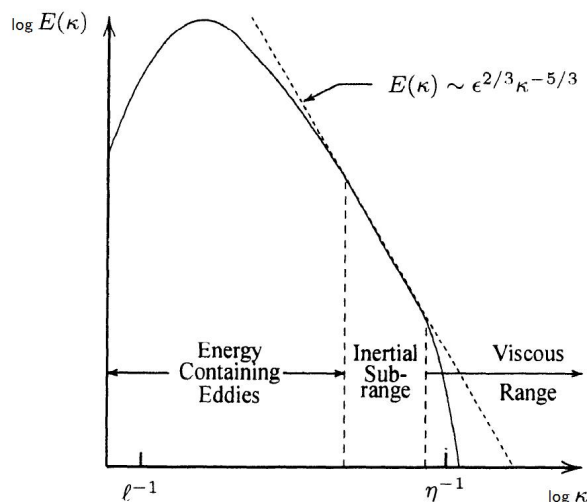


Figure 4.2: Example of energy spectrum for a turbulent flow, figure from [103]

Smallest Scales

The smallest eddies are responsible for the dissipation of the turbulent kinetic energy into heat (through the molecular viscosity). Because this process occurs on a short time scale, it can be reasonably assumed independent of the dynamics of the large eddies and of the mean flow. Therefore the motion at smallest scales depends only on the rate at which the larger eddies supply the energy, $\epsilon = -\frac{dk}{dt} = [m^2 \cdot s^{-3}]$, and on the kinematic viscosity $\nu = [m^2 \cdot s^{-1}]$.

According to *Kolmogorov's* universal equilibrium theory (viz. [48]) the following (smallest) length-, time- and velocity-scales are defined

$$\eta \equiv \left(\frac{\nu^3}{\epsilon}\right)^{1/4}, \quad \tau \equiv \left(\frac{\nu}{\epsilon}\right)^{1/2}, \quad v \equiv (\nu\epsilon)^{1/4}. \quad (4.7)$$

By means of these scales it can be shown that for the majority of engineering applications the Kolmogorov length is much larger than the mean free path of the fluid particles and therefore the turbulence can be assumed as a continuum phenomenon.

Large Scales

The relation between large eddies (integral lengthscale) and small eddies (Kolmogorov scale) can be estimated with the relation

$$\frac{\eta}{l} \approx \text{Re}_T^{-1/4}, \quad (4.8)$$

where the *turbulent Reynolds number* Re_T is defined

$$Re_T = \frac{\sqrt{k}l}{\nu}. \quad (4.9)$$

Further on, the energy dissipated can be approximated as

$$\epsilon = -\frac{dk}{dt} \approx \frac{\sqrt{k^3}}{l}. \quad (4.10)$$

The relations (4.7) have presented the smallest scales which need to be captured for the complete turbulent computations. Such solution is based only on the governing equations of the chapter 3 and therefore called the *Direct Numerical Simulation* (DNS). The advantage of the smaller number of equations (compared to conventional turbulence models, see below) is balanced by the enormous demands on computer resources.

The computational grid must capture even the smallest eddies, whose size is given by the length-scale η . At least two computational cells are needed to describe any vortex, see the figure 4.3, therefore the grid size is proportional to the Reynolds number. According to [75] the number of grid elements scales with the power $Re^{9/4}$.

Regarding that also the time-stepping must fulfill the time-scale criteria, $\Delta t < \tau$, only the (clusters of) super-computers are able to resolve turbulent flows with DNS. Despite the annual increase of the computers' power, the current limits of DNS simulations lie around $Re \approx 10^5$, which is still insufficient for most technical applications.

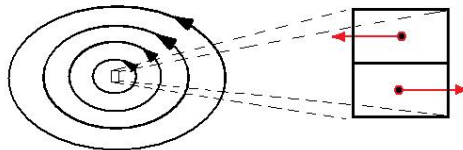


Figure 4.3: Detail of the vortex core discretization

The direct numerical simulation is also complicated in terms of formulation of the initial and boundary conditions, failures of any symmetry assumptions, careful numerical discretization (the artificial viscosity of an inappropriate numerical scheme can completely ruin the result), etc. DNS is however very useful for basic research, providing extremely detailed information about flow parameters, which are unavailable from any experiment otherwise.

Another approach to turbulence modelling is the statistical one. The foundational idea has been introduced by O. Reynolds [79], who expressed all flow quantities as the sum of mean and fluctuating parts

$$A(\vec{x}, t) = \bar{A}(\vec{x}) + a'(\vec{x}, t). \quad (4.11)$$

When all the unknowns of the governing and their constitutive equations are replaced by (4.11), the nonlinearity of the momentum equation causes the appearance of some new terms, acting as apparent stresses throughout the flow. These terms are unknown a priori and so the goal of all turbulence models is to establish a sufficient number of equations for all of the unknowns. As will be shown later, such equations use only the *mean* parts \bar{A} (even to derive relations for fluctuations a'). It creates a solvable system only for mean values of the flow, filtering out all information about the fluctuations in fact. This price is paid as a trade off for larger grid spacing and bigger time steps, allowing to use current CPU power also for real engineering applications.

4.2 Turbulence Averaging

The averaging concept for turbulent flows has also been introduced by O. Reynolds in [79] (therefore named *Reynolds Averaging*). The concept involves a variety of forms in general. The three most frequent forms used for turbulence modelling are the *time*-averaging, equation (4.12), the *spatial*-averaging, equation (4.13) and the *ensemble*-averaging, equation (4.14). According to the ergodic hypothesis, the resulting values of these averages for a stationary and homogeneous turbulence are equal and represent the mean value \bar{A} of the equation (4.11).

$$F_t(\vec{x}) = \lim_{T \rightarrow \infty} \frac{1}{T} \int_t^{t+T} f(\vec{x}, t) dt \quad (4.12)$$

$$F_v(t) = \lim_{V \rightarrow \infty} \frac{1}{V} \int_V f(\vec{x}, t) dV \quad (4.13)$$

$$F_e(\vec{x}, t) = \lim_{N \rightarrow \infty} \frac{1}{N} \sum_{n=1}^N f_n(\vec{x}, t) \quad (4.14)$$

The time averaging is appropriate for stationary turbulence. Such flows do not vary with time on the average. The definition of the spatial averaging is suitable for homogeneous turbulence, where the average values are uniform in all directions (for a detailed description see [73]). The last ensemble approach is the most general type of Reynolds averaging. It is mainly used for the processing of many experimental measurements f_n of a single phenomenon with identical initial and boundary conditions¹.

Since the flow inside the combustion engine strongly varies with time and space neither time- nor spacial- averaging could be used in their original form (4.12) or (4.13). The ensemble approach is not suitable, as the turbulence model would also include the intercycle variations (low frequency fluctuations of all mean values, with the period of the order of several working cycles), which are not considered of a turbulent nature, viz [80].

For applications like a combustion engine the averaging needs therefore to be modified, in order to accommodate non-stationary effects of mean variables. The equation (4.12) is replaced by

$$\bar{F}(\vec{x}, t) = \frac{1}{T} \int_t^{t+T} f(\vec{x}, t) dt, \quad (4.15)$$

with a time-scale constrain

$$\tau \sim T_1 \ll T \ll T_2. \quad (4.16)$$

As illustrated in the figure 4.4, T_1 is the time scale of the instantaneous fluctuation and T_2 the time scale characteristic of the slow variations in the flow, not to be regarded as belonging to the turbulence. The assumption of T_1 and T_2 differing by several orders of magnitude is very strong and regrettably most of the engineering applications do not satisfy this condition (4.16). The values of turbulent time scales in an internal combustion engine (with focus to the exhaust stroke) are presented in the following subsection.

¹As in the experiments it is difficult to hold all parameters constant, the term *identical* represents close values which statistical average ideally equals the mean value.

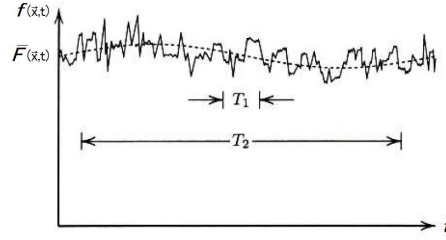


Figure 4.4: Time averaging for non-stationary turbulence, figure from [103]

Time Scale Estimation

The condition (4.16) can be rewritten and converted to

$$\frac{T_2}{T_1} \gg 1 \quad \rightarrow \quad \frac{f_1}{f_2} \gg 1, \quad (4.17)$$

where $f_{1,2}$ represents the frequency of the corresponding time scale

$$T = \frac{1}{f}. \quad (4.18)$$

According to [98], the lowest frequency of non-turbulent motions f_2 for a four-stroke engine can be estimated from the engine revolutions n (in RPM) as

$$f_2 = \frac{n}{4 \cdot 60}. \quad (4.19)$$

The frequency of a turbulent time scale f_1 is estimated from the size of large-scale eddies with size comparable to an integral scale l . The circumferential speed of such vortex can be approximated by the fluctuating velocity component w' , see equation (4.11), and therefore

$$w' = 2\pi f_1 l. \quad (4.20)$$

The approximation of turbulent variables is done through equations

$$\frac{3}{2}w' = \frac{1}{2}C_k w_v, \quad (4.21)$$

$$l = C_l L, \quad (4.22)$$

with L the valve lift. The mean valve speed w_v , according to the literature [41], can be defined as

$$w_v = 2L f_2. \quad (4.23)$$

The order of magnitude of the proportionality constants can be found in literature $C_k \approx 10^{-1} \div 10^0$ and $C_l \approx 10^{-2}$. The frequency ratio is then expressed and evaluated

$$\frac{f_1}{f_2} = \sqrt{\frac{C_k}{3}} \frac{1}{\pi C_l} \approx 5.81 \div 18.38. \quad (4.24)$$

Although the ratio fulfils the inequality (4.17), the order of magnitude of the resulting ratio is not very significant ($10^{0 \div 1}$). The more accurate estimation can be extracted from particular numerical

simulations, by evaluating the equation

$$\frac{f_1}{f_2} = \frac{1}{2\pi} \sqrt{\frac{2}{3}} k \frac{60}{n \cdot l}. \quad (4.25)$$

From the precedent numerical studies of the high-pressure strokes [98], the development of $\frac{f_1}{f_2}$ inside the combustion chamber during the compression and exhaust stroke is observed. Some of the typical results are shown in the figure 4.5.

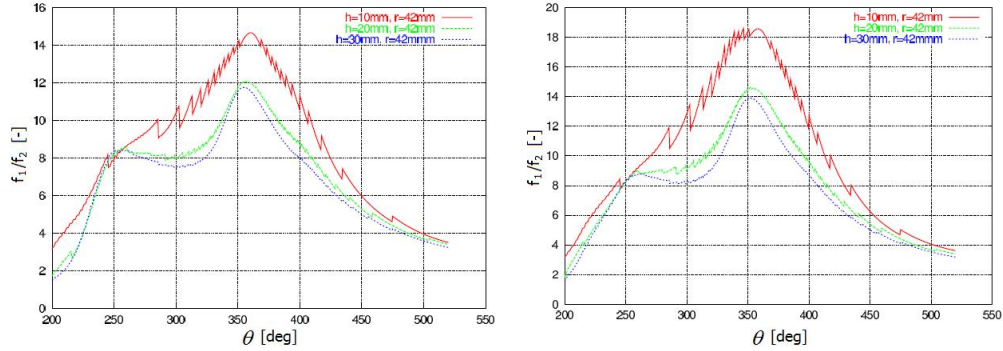


Figure 4.5: Development of time-scale ratio inside the combustion chamber during the compression and expansion strokes, for different turbulence models (left-right) in three fixed spatial points, figure from [98]

Suitable Averaging for Compressible Flows

For the conventional Reynolds averaging one reads

$$A = \bar{A} + a', \quad (4.26)$$

with the mean value \bar{A} computed as (4.15) and with the above discussed assumption (4.16). Further important relations are:

$$\overline{a'} = 0, \quad (4.27)$$

$$\overline{A_1 + A_2} = \bar{A}_1 + \bar{A}_2, \quad (4.28)$$

$$\overline{A_1 \cdot A_2} = \bar{A}_1 \cdot \bar{A}_2 + \overline{a'_1 a'_2}, \quad (4.29)$$

$$\overline{\bar{A}_1 \cdot a'_2} = 0. \quad (4.30)$$

The original equations (3.3)-(3.5), with unknowns replaced by their average (4.26), are then understood as transport equations of actual values. This approach however does not lead to a substantial simplification for the compressible flows, due to non-vanishing density-related fluctuations $\overline{\rho w'_i} \neq 0$. Therefore a density-weighted averaging has been defined by A. Favre in [30]. The decomposition into mean and fluctuation part denotes

$$A = \tilde{A} + a'', \quad (4.31)$$

with the mean value defined through

$$\begin{aligned}\tilde{F}\bar{\rho} &= \frac{1}{T} \int_t^{t+T} f \cdot \rho dt = \overline{F\rho}, \\ \tilde{F} &= \frac{\overline{F\rho}}{\bar{\rho}},\end{aligned}\tag{4.32}$$

implying similar important relations

$$\overline{\rho a''} = 0,\tag{4.33}$$

$$\overline{\rho(A_1 + A_2)} = \rho(\tilde{A}_1 + \tilde{A}_2),\tag{4.34}$$

$$\overline{\rho \cdot A_1 \cdot A_2} = \bar{\rho} \cdot \tilde{A}_1 \cdot \tilde{A}_2 + \overline{\rho a_1'' a_2''},\tag{4.35}$$

$$\overline{\rho \tilde{A}_1 \cdot a_2''} = 0.\tag{4.36}$$

Also Favre's averaging relies on the validity of the time scales difference (4.26). The quotable differences of these approaches are summarized:

$$\begin{aligned}\bar{a}' = 0, \overline{\rho a'} \neq 0 &\quad \dots \quad \text{for conventional averaging,} \\ \overline{a''} \neq 0, \overline{\rho a''} = 0 &\quad \dots \quad \text{for density weighted averaging.}\end{aligned}$$

4.3 U-RANS Equations

The acronym U-RANS stands for the *unsteady Reynolds-averaged Navier-Stokes* equations, which describe an arbitrary turbulent flow of a compressible fluid upon a moving domain. The system has arisen from the original equations (3.3), (3.4) and (3.5). The decomposition (4.37) has been applied first, followed by the averaging (4.15).

$$\begin{aligned}\rho &= \bar{\rho} + \rho', \\ p &= \bar{p} + p', \\ w_i &= \tilde{w}_i + w_i'', \\ T &= \tilde{T} + T'', \\ \overline{\rho e} &\equiv \bar{\rho} \tilde{e} = \bar{\rho} \tilde{u} + \bar{\rho} \frac{\tilde{w}_i \tilde{w}_i}{2} + \frac{\overline{\rho w_i'' w_i''}}{2}.\end{aligned}\tag{4.37}$$

The above mentioned operations lead to²

- averaged continuity equation. Except formal notation, the equation holds the original form, with no new terms appeared.

$$\frac{d}{dt} \int_{\Omega} \bar{\rho} d\Omega = - \int_{\partial\Omega} \bar{\rho} (\tilde{w} - w_B) \vec{n} d\partial\Omega.\tag{4.38}$$

- averaged momentum equation. The turbulent stress tensor $-\overline{\rho w_i'' w_j''}$ appears on the right

²For an easier reading of averaged values, the vectorial mark $\vec{\cdot}$ will be skipped for the velocity vector. The variable meaning remains untouched.

hand side, due to the averaging.

$$\begin{aligned} \frac{d}{dt} \int_{\Omega} \bar{\rho} \tilde{w}_i d\Omega &= - \int_{\partial\Omega} \bar{\rho} \tilde{w}_i (\tilde{w} - w_B) \vec{n} d\partial\Omega + \int_{\Omega} \bar{\rho} g_i d\Omega \\ &+ \int_{\partial\Omega} \left(-\bar{p} \delta_{ij} + \bar{\tau}_{ij} - \overline{\rho w_i'' w_j''} \right) \vec{n} d\partial\Omega. \end{aligned} \quad (4.39)$$

The tensor involves the product of velocity fluctuations, which by the definition (4.11) can not be expressed by any combination of conservative variables. The tensor must therefore be modelled separately, as described in the following subsection 4.3.2.

- averaged energy equation. Nonlinear terms of the original right hand side cause several correlation of fluctuations to appear.

$$\begin{aligned} \frac{d}{dt} \int_{\Omega} \bar{\rho} \tilde{E} d\Omega &= - \int_{\partial\Omega} \bar{\rho} \tilde{e} (\tilde{w} - w_B) \vec{n} d\partial\Omega + \int_{\Omega} \bar{\rho} g_i \tilde{w}_i d\Omega \\ &+ \int_{\partial\Omega} \left(-\bar{p} \delta_{ij} + \bar{\tau}_{ij} - \overline{\rho w_i'' w_j''} \right) (\tilde{w} - w_B) \vec{n} d\partial\Omega \\ &- \int_{\partial\Omega} \left(\bar{q}_j + \overline{\rho w_j'' h''} \right) \vec{n} d\partial\Omega \\ &+ \int_{\partial\Omega} \left(\overline{\tau_{ij} w''} - \frac{1}{2} \overline{\rho w_i'' w_i'' w_j''} \right) \vec{n} d\partial\Omega \\ &+ \int_{\Omega} \bar{Q} d\Omega - \int_{\Omega} \bar{W} d\Omega. \end{aligned} \quad (4.40)$$

Note that for $\vec{w}_B \equiv 0$ the so-called *steady* Reynolds-averaged Navier-Stokes equations can be recovered.

4.3.1 Constitutive Relations

Analogically to section 3.1, also the equations (4.38), (4.39) and (4.40) must be completed by a set of constitutive relations. For $R=const.$ the state equation can be derived (after decomposition and averaging)

$$\bar{p} = \bar{\rho} R \bar{T}. \quad (4.41)$$

The internal energy \tilde{e} has already been defined by the equation (4.37). Other relations are derived analogically to their non-averaged templates

$$\bar{\tau}_{ij} = \mu \left(\bar{T} \right) \left(\frac{\partial \tilde{w}_i}{\partial x_j} + \frac{\partial \tilde{w}_j}{\partial x_i} \right) + \left(\lambda_S - \frac{2}{3} \mu \left(\bar{T} \right) \right) \frac{\partial \tilde{w}_k}{\partial x_k} \delta_{ij}, \quad (4.42)$$

$$\bar{q}_i = -\lambda \left(\bar{T} \right) \cdot \frac{\partial \bar{T}}{\partial x_i}, \quad (4.43)$$

although the validity of these new relations can not be proven in general. The original relations (3.21), (3.23) are defined for the instantaneous values (see the equation (4.11)) and only by the analogy assumption they are said valid also for the average values. This analogy has been assumed both for the remaining constitutive relations (section 3.2) and for the initial and boundary conditions (section 3.3). All the equations involved hold the formal notation, with the instantaneous values just substituted by their averages.

On the contrary to section 3.1, these relations do not turn the original set of equations into a

solvable system, because of the turbulent correlations which still remain unknown.

4.3.2 Turbulent Correlation Terms

The most important correlation term is the Reynolds stress tensor

$$\tau_{ij}^R = -\overline{\rho w_i'' w_j''}, \quad (4.44)$$

which represents the influence of turbulent fluctuations on the momentum balance. Analogically to the molecular heat flux \dot{q} , the corresponding correlation term in the energy equation (4.40) is called the turbulent heat flux

$$\dot{q}_i^{turb} = \overline{\rho w_i'' h''}. \quad (4.45)$$

The terms $\overline{\tau_{ij} w''}$ and $\frac{1}{2} \overline{\rho w_i'' w_i'' w_j''}$ represent the molecular and turbulent transport of energy. As the original energy equation (3.5) has been modified with the equation (3.6), an analogical relation is found for the turbulent case

$$-\int_{\Omega} \bar{W} d\Omega = \int_{\partial\Omega} (-\bar{p}\delta_{ij} + \bar{\tau}_{ij} + \tau_{ij}^R) w_B \vec{n} d\partial\Omega. \quad (4.46)$$

Hence, the averaged energy equation reads

$$\begin{aligned} \frac{d}{dt} \int_{\Omega} \bar{\rho} \bar{e} d\Omega &= - \int_{\partial\Omega} \bar{\rho} \bar{e} (\tilde{w} - w_B) \vec{n} d\partial\Omega + \int_{\Omega} \bar{\rho} g_i \tilde{w}_i d\Omega \\ &+ \int_{\partial\Omega} (-\bar{p}\delta_{ij} + \bar{\tau}_{ij} + \tau_{ij}^R) \tilde{w} \vec{n} d\partial\Omega \\ &- \int_{\partial\Omega} (\bar{q}_j + \dot{q}_j^{turb}) \vec{n} d\partial\Omega + \int_{\Omega} \bar{Q} d\Omega \\ &+ \int_{\partial\Omega} \left(\overline{\tau_{ij} w''} - \frac{1}{2} \overline{\rho w_i'' w_i'' w_j''} \right) \vec{n} d\partial\Omega. \end{aligned} \quad (4.47)$$

This equation (4.47), together with (4.38) and (4.39), provides the system of governing equations, based on the time averaging, for modelling turbulent flows in the combustion engine.

Namely the terms (4.44) and (4.45) increase the transport properties (momentum and energy) against the laminar system. The turbulent terms τ_{ij}^R and \dot{q}_i^{turb} are usually larger (sometimes by several orders of magnitude) than their molecular counterparts τ_{ij} and \dot{q}_i . This fact firstly confirms the dominant role of the inertial forces to the viscous ones, secondly emphasizes the importance of careful modelling of these turbulent terms.

4.3.3 Turbulent Transport Equations

Equation of the Kinetic Energy of Mean Motion

Assume the steady averaged momentum equation (eq. (4.39) with $\vec{w}_B \equiv 0$). The equation of the i^{th} momentum component is multiplied by \tilde{w}_j and vice versa. The sum of these cross-multiplied equations gives

$$\begin{aligned} \frac{\partial}{\partial t} (\bar{\rho} \tilde{w}_i \tilde{w}_j) + \frac{\partial}{\partial x_k} (\bar{\rho} \tilde{w}_i \tilde{w}_j \tilde{w}_k) &= -\tilde{w}_j \frac{\partial \bar{p}}{\partial x_i} - \tilde{w}_i \frac{\partial \bar{p}}{\partial x_j} \\ &+ \tilde{w}_j \frac{\partial}{\partial x_k} \left(\bar{\tau}_{ik} - \overline{\rho w_i'' w_k''} \right) + \tilde{w}_i \frac{\partial}{\partial x_k} \left(\bar{\tau}_{jk} - \overline{\rho w_j'' w_k''} \right). \end{aligned} \quad (4.48)$$

For $i=j$ the relation (4.48) turns into the equation of the kinetic energy of the mean motion

$$\frac{\partial}{\partial t} \left(\bar{\rho} \frac{\tilde{w}_i \tilde{w}_i}{2} \right) + \frac{\partial}{\partial x_k} \left(\tilde{w}_k \bar{\rho} \frac{\tilde{w}_i \tilde{w}_i}{2} \right) = -\tilde{w}_i \frac{\partial \bar{p}}{\partial x_i} + \tilde{w}_i \frac{\partial \bar{\tau}_{ik}}{\partial x_k} - \tilde{w}_i \frac{\partial}{\partial x_k} \left(\overline{\rho w_i'' w_k''} \right), \quad (4.49)$$

where the left-hand-side terms represent the time change and advection, term I the work provided by pressure forces and II the dissipation due to viscosity. The term III can be splitted into

$$-\tilde{w}_i \frac{\partial}{\partial x_k} \left(\overline{\rho w_i'' w_k''} \right) = -\frac{\partial}{\partial x_k} \left(\tilde{w}_i \overline{\rho w_i'' w_k''} \right) + \overline{\rho w_i'' w_k''} \frac{\partial \tilde{w}_i}{\partial x_k}, \quad (4.50)$$

with $IIIa$ the energy transport via turbulent fluctuations and $IIIb$ the energy production at the expense of the mean motion.

Transport Equation of Reynolds Stresses

This equation is derived from the momentum conservation law (3.10). Here the sum of the cross-multiplied equations gives

$$\frac{\partial}{\partial t} (\rho w_i w_j) + \frac{\partial}{\partial x_k} (\rho w_i w_j w_k) = -w_j \frac{\partial p}{\partial x_i} - w_i \frac{\partial p}{\partial x_j} + w_j \frac{\partial \tau_{ik}}{\partial x_k} + w_i \frac{\partial \tau_{jk}}{\partial x_k}. \quad (4.51)$$

The density-weighted decomposition (4.31) and time averaging (4.15) leads to

$$\begin{aligned} & \frac{\partial}{\partial t} \left(\bar{\rho} \tilde{w}_i \tilde{w}_j + \overline{\rho w_i'' w_j''} \right) \\ & + \frac{\partial}{\partial x_k} \left(\bar{\rho} \tilde{w}_i \tilde{w}_j \tilde{w}_k + \tilde{w}_k \overline{\rho w_i'' w_j''} + \tilde{w}_i \overline{\rho w_j'' w_k''} + \tilde{w}_j \overline{\rho w_i'' w_k''} + \overline{\rho w_i'' w_j'' w_k''} \right) = \\ & -\tilde{w}_j \frac{\partial \bar{p}}{\partial x_i} - \tilde{w}_i \frac{\partial \bar{p}}{\partial x_j} - \tilde{w}_i \frac{\partial \bar{p}}{\partial x_j} - \tilde{w}_j \frac{\partial \bar{p}}{\partial x_i} + \tilde{w}_j \frac{\partial \bar{\tau}_{ik}}{\partial x_k} + \tilde{w}_i \frac{\partial \bar{\tau}_{jk}}{\partial x_k} + \tilde{w}_i \frac{\partial \bar{\tau}_{jk}}{\partial x_k} + \tilde{w}_j \frac{\partial \bar{\tau}_{ik}}{\partial x_k}. \end{aligned} \quad (4.52)$$

The tranport equations of Reynolds stresses (RS) is found when the equation (4.48) is subtracted from (4.52)

$$\frac{\partial}{\partial t} \left(\overline{\rho w_i'' w_j''} \right) + \frac{\partial}{\partial x_k} \left(\tilde{w}_k \overline{\rho w_i'' w_j''} \right) = P_{ij} + D_{ij} + \Pi_{ij} + C_{ij} + \bar{\rho} \epsilon_{ij}. \quad (4.53)$$

The left-hand-side terms represent the time change and advection of RS. Other terms correspond to

- production P_{ij} - generation of the RS by the interaction with the mean flow

$$P_{ij} = -\overline{\rho w_i'' w_k''} \frac{\partial \tilde{w}_j}{\partial x_k} - \overline{\rho w_j'' w_k''} \frac{\partial \tilde{w}_i}{\partial x_k}. \quad (4.54)$$

- turbulent diffusion D_{ij} - tranport of the RS through the pressure and velocity fluctuations

$$D_{ij} = -\frac{\partial}{\partial x_k} \overline{\rho w_i'' w_j'' w_k''} - \frac{\partial}{\partial x_k} \left[\overline{p' (\delta_{jk} w_i'' + \delta_{ik} w_j'')} \right]. \quad (4.55)$$

- redistribution Π_{ij} - equalizing the normal components of the RS

$$\Pi_{ij} = \overline{p' \left(\frac{\partial w_j''}{\partial x_i} + \frac{\partial w_i''}{\partial x_j} \right)}. \quad (4.56)$$

- viscous diffusion C_{ij} - transport of the RS through the molecular viscosity. This term is negligible for high Reynolds number flows.

$$C_{ij} = \frac{\partial}{\partial x_k} \left[\frac{\mu}{\bar{\rho}} \frac{\partial}{\partial x_k} \left(\overline{\rho w_i'' w_j''} \right) \right]. \quad (4.57)$$

- dissipation ϵ_{ij} - destruction of the RS due to the molecular viscosity.

$$\epsilon_{ij} = 2\mu \overline{\frac{\partial w_i''}{\partial x_k} \frac{\partial w_j''}{\partial x_k}} \quad (4.58)$$

Other terms, which has arisen due to the density weighted averaging, are not shown as they are generally negligible, viz. [75].

Transport Equation of Turbulent Kinetic Energy

The importance of the equation (4.53) consists in its form for $i=j$ which derives the transport equation of the turbulent kinetic energy

$$k = \frac{1}{2} \frac{\overline{\rho w_i'' w_i''}}{\bar{\rho}}. \quad (4.59)$$

This variable is computed as the sum of the normal components of the RS tensor. With some algebra involved, the final equation reads

$$\begin{aligned} \frac{\partial}{\partial t} \left(\frac{1}{2} \overline{\rho w_i'' w_i''} \right) + \frac{\partial}{\partial x_j} \left(\tilde{w}_j \frac{1}{2} \overline{\rho w_i'' w_i''} \right) &= - \overline{\rho w_i'' w_j''} \frac{\partial \tilde{w}_i}{\partial x_j} - \frac{\partial}{\partial x_j} \left(\overline{w_j'' \frac{1}{2} \rho w_i'' w_i''} + \delta_{ij} \overline{p' w_i''} \right) \\ &+ \frac{\partial}{\partial x_j} \left[\frac{\mu}{\bar{\rho}} \frac{\partial}{\partial x_j} \left(\frac{1}{2} \overline{\rho w_i'' w_i''} \right) \right] - \mu \overline{\frac{\partial w_i''}{\partial x_j} \frac{\partial w_i''}{\partial x_j}}. \end{aligned} \quad (4.60)$$

The redistribution term Π_{ii} does not appear in (4.60), hence it only affects the redistribution of k among the normal components of the tensor (tendency of isotropy).

Because the dissipation happens exclusively in the smallest (isotropic) turbulent vortices the tensor ϵ_{ij} is often replaced by

$$\epsilon_{ij} = \delta_{ij} \epsilon, \quad (4.61)$$

with ϵ the turbulent dissipation rate.

Transport Equation of Turbulent Dissipation Rate

For compressible flows the turbulent dissipation rate ϵ is expressed

$$\bar{\rho} \epsilon = \mu \overline{\frac{\partial w_i''}{\partial x_j} \frac{\partial w_i''}{\partial x_j}}. \quad (4.62)$$

The exact transport equation for ϵ can be derived from the transport equation of the instantaneous fluctuation velocity. The final equation is however quite complex, involving many unknown terms.

In [38] the simpler form of the transport equation of ϵ for the incompressible flow has been published

$$\begin{aligned} \frac{\partial \rho \epsilon}{\partial t} + \frac{\partial \bar{w}_k \rho \epsilon}{\partial x_k} = & -\frac{\partial}{\partial x_k} \left(\overline{\mu w'_k \frac{\partial w'_i}{\partial x_j} \frac{\partial w'_i}{\partial x_j}} + \frac{2\mu}{\rho} \overline{\frac{\partial p}{\partial x_i} \frac{\partial w'_i}{\partial x_k}} - \mu \frac{\partial \epsilon}{\partial x_k} \right) \\ & -2\mu \frac{\partial \bar{w}_i}{\partial x_k} \left(\overline{\frac{\partial w'_i}{\partial x_j} \frac{\partial w'_k}{\partial x_j}} + \overline{\frac{\partial w'_j}{\partial x_i} \frac{\partial w'_j}{\partial x_k}} \right) + 2\mu \overline{w'_k \frac{\partial w'_i}{\partial x_j} \frac{\partial^2 \bar{w}_i}{\partial x_j \partial x_k}} \\ & -2\mu \overline{\frac{\partial w'_i}{\partial x_j} \frac{\partial w'_k}{\partial x_j} \frac{\partial w'_i}{\partial x_k}} - 2\frac{\mu^2}{\rho} \overline{\left(\frac{\partial^2 w'_i}{\partial x_k \partial x_j} \right)}, \end{aligned} \quad (4.63)$$

with many unknown turbulent correlations which are difficult to model.

Based on the dimensional analysis and empirical presumptions, the simplified transport equation of ϵ is constructed as an analogy to the transport equation of the turbulent energy, viz [37].

4.4 Hierarchy of Turbulence Models

The system of U-RANS equations can not be directly completed by the transport equation of the Reynolds stresses, as this equation (4.53) contains other unknown pressure and velocity fluctuations. Therefore it is essential also to model these fluctuation terms remaining. The general method of the RANS closure is shown in the figure 4.6, on which basis the turbulence models can be divided into

1st order turbulence model - approximates directly the Reynolds stresses, subsection 4.4.1,

2nd order turbulence model - approximates the correlations inside the RS transport equations, subsection 4.4.2.

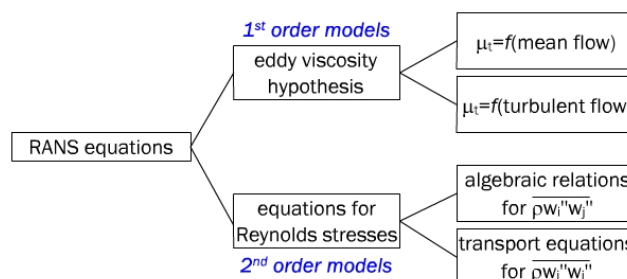


Figure 4.6: Methods of RANS equations closure

Based on section 4.2, it can be deduced that a universal turbulence model which would fit all the regimes and flow conditions cannot be constructed. Despite this, each turbulence model shall fulfill at least the following conditions (viz. [98])

- all the approximations of compressible flow tend to corresponding incompressible terms as the Mach number tends to zero,
- all the density fluctuations tend to zero as the Mach number tends to zero,
- the approximation terms are domain (geometry) independent,
- all the approximations are dimensionally consistent and invariant against a Galileo transformation.

4.4.1 1st Order Turbulence Models

These models are based on the analogy between molecular and turbulent transport of momentum. Similarly to *Newton's law* (its generalized form written in the equation (3.21)), J. Boussinesq has proposed in [15] a relation between the velocity gradient and the Reynolds stresses of a 2D incompressible boundary layer

$$-\overline{\rho w'_i w'_j} = \mu_t \frac{\partial \bar{w}_i}{\partial x_j}. \quad (4.64)$$

The parameter μ_t is the so-called turbulent (eddy) viscosity. This original Boussinesq hypothesis (4.64) has been extended by Harlow and Nakayama in [?, ?] to a general multi-dimensional turbulent flow

$$-\overline{\rho w''_i w''_j} = \mu_t \left(\frac{\partial \tilde{w}_i}{\partial x_j} + \frac{\partial \tilde{w}_j}{\partial x_i} - \frac{2}{3} \delta_{ij} \frac{\partial \tilde{w}_k}{\partial x_k} \right) - \frac{1}{3} \delta_{ij} \overline{\rho w''_k w''_k}. \quad (4.65)$$

For transparency purposes, equation (4.65) can be written in terms of the mean-strain-rate tensor S_{ij} and the mean-rotation tensor Ω_{ij} , respectively defined by

$$S_{ij} = \frac{1}{2} \left(\frac{\partial \tilde{w}_i}{\partial x_j} + \frac{\partial \tilde{w}_j}{\partial x_i} \right), \quad \Omega_{ij} = \frac{1}{2} \left(\frac{\partial \tilde{w}_i}{\partial x_j} - \frac{\partial \tilde{w}_j}{\partial x_i} \right). \quad (4.66)$$

The Reynolds stress tensor (4.44) then reads

$$\tau_{ij}^R \equiv -\overline{\rho w''_i w''_j} = 2\mu_t \left(S_{ij} - \frac{1}{3} \delta_{ij} \frac{\partial \tilde{w}_k}{\partial x_k} \right) - \frac{2}{3} \delta_{ij} \bar{\rho} k. \quad (4.67)$$

Even the last relation does not close the system of equation, as the unknown *tensor* τ_{ij}^R has only been replaced by the unknown *scalar* μ_t . According to the dimensional analysis the eddy viscosity shall be expressed as a product of a velocity term and a length term - often called the velocity and the length *scale*.

Algebraic Models

The simplest turbulence models contain only transport equations of the conservative variables and relates the eddy viscosity with the values of the mean flow. The relations are often based on the Prandtl mixing layer theory, published in [74]

$$\mu_t = C \rho l_{mix}^2 \left| \varepsilon_{ijk} \frac{\partial w_k}{\partial x_j} \right|, \quad (4.68)$$

where C , l_{mix} are model constants and $\left| \varepsilon_{ijk} \frac{\partial w_k}{\partial x_j} \right|$ is the size of the vorticity vector. Although it might be shown that the analogy between molecular and turbulent transport (that mostly arises from the formal analogy of the terms involved) is not physically correct, the constants C and l_{mix} could be tuned so that the computational results correspond to experimental ones. Such agreement is found mainly (only) for the equilibrium turbulent flows with weak fluctuations and small changes in time.

One Equation Models

Such models use only one transport equation for a suitable turbulent variable. The most often quantity balanced is the turbulent kinetic energy k , because its square root can directly be used as a velocity scale. The length scale is then usually determined by an algebraic relation $l_t = l_t(x_j)$, which limits the use of such models rather to the equilibrium turbulent flows.

A general k transport equation and the eddy viscosity can be written as

$$\frac{\partial}{\partial t} (\bar{\rho}k) + \frac{\partial}{\partial x_j} (\tilde{w}_j \bar{\rho}k) = \tau_{ij}^R \frac{\partial \tilde{w}_i}{\partial x_j} - \bar{\rho}\epsilon + \frac{\partial}{\partial x_j} \left[\left(\mu + \frac{\mu_t}{\sigma_k} \right) \frac{\partial k}{\partial x_j} \right], \quad (4.69)$$

$$\mu_t = \bar{\rho} \frac{\sqrt{k}}{l_t}. \quad (4.70)$$

The turbulent dissipation rate is settled by dimensional analysis

$$\epsilon = C_D \frac{k^{3/2}}{l_t}. \quad (4.71)$$

In order to build up an efficient and robust model, the parameters C_D , σ_k were suggested constant, which often turns insufficient and unacceptable in practice.

Models with Transport Equation for Eddy Viscosity

In a strict sense these models still belong to the previous group. Nonetheless they are usually excluded due to their different nature. The models have been developed following the concept of a simple and robust tool for many aerodynamic applications. The original model has been derived by B. S. Baldwin and T. J. Barth in [8] from the $k - \epsilon$ model (see below). Later it has been modified by P. R. Spalart and S. R. Allmaras in [90], supplying the equation with some additional diffusive terms.

Despite μ_t or ν_t , respectively are the fictitious (directly immeasurable) variables, their empirical transport equation recognizes advection, production, diffusion and dissipation terms, similarly to the other transport equations. Currently, there are several classes of this equation, corresponding to the target application of the simulation. Although infringing its original idea, the S-A model provides better robustness and accuracy among the one-equation models together with lower demands compared to the two-equations models.

Two Equations Models

Most models of the statistical approach belong to the family of two transport equations, each one characterizing a different turbulence scale. The velocity scale is again extracted from the transport equation of the turbulent kinetic energy, such as equation (4.69). The second transport equation characterizes the length scale or its equivalent.

With the assumption of local isotropy of the smallest vortices, the length scale can be extracted from equation (4.71), with the balanced variable the turbulent dissipation rate ϵ . This approach has founded the family of $k - \epsilon$ turbulence models. The later research suggested the transport equations for another preferable variable balanced:

- the length scale l_t , or its product $k \cdot l_t$. Published by [85], the so-called $k - l$ models.
- the specific dissipation rate $\omega = \epsilon/k$. Published by [49], the $k - \omega$ models.
- the turbulent dissipation time τ . Published by [91], the $k - \tau$ models.

Depending on the variable chosen, the eddy viscosity μ_t is recovered from

$$\mu_t \sim \bar{\rho} \frac{k^2}{\epsilon} \sim \bar{\rho} \sqrt{k} l_t \sim \bar{\rho} \frac{k}{\omega} \sim \bar{\rho} k \tau. \quad (4.72)$$

Although the two-equations models have proven large improvements against the one-equation models, there is still no fundamental reason why μ_t should depend only upon turbulence parameters such as k , l , ϵ or ω . In general, the ratio of the individual Reynolds stresses to mean strain rate components, depends on both the mean-flow and the turbulence scales. Thus, these models can still perform inaccurately for many non-equilibrium turbulent flows.

4.4.2 2nd Order Turbulence Models

RSM

For complex non-equilibrium turbulent flows the turbulence models with equations for Reynolds stresses are assumed more suitable than the 1st order models. Recall the transport equation of the Reynolds stresses, which has already been shown above in the equation (4.53)

$$\begin{aligned} \frac{\partial}{\partial t} \left(\overline{\rho w_i'' w_j''} \right) + \frac{\partial}{\partial x_k} \left(\tilde{w}_k \overline{\rho w_i'' w_j''} \right) &= - \overline{\rho w_i'' w_k''} \frac{\partial \tilde{w}_j}{\partial x_k} - \overline{\rho w_j'' w_k''} \frac{\partial \tilde{w}_i}{\partial x_k} \\ &\quad - \frac{\partial}{\partial x_k} \overline{\rho w_i'' w_j'' w_k''} - \frac{\partial}{\partial x_k} \left[p' \left(\delta_{jk} w_i'' + \delta_{ik} w_j'' \right) \right] \\ &\quad + p' \left(\frac{\partial w_j''}{\partial x_i} + \frac{\partial w_i''}{\partial x_j} \right) + 2 \bar{\rho} \mu \frac{\partial w_i''}{\partial x_k} \frac{\partial w_j''}{\partial x_k}, \end{aligned}$$

with the right-hand side terms describing in turn the production, diffusion, redistribution and dissipation. Note that only the production term can be solved directly, whereas the other terms require next approximations.

Further transport equations can be derived for each particular correlation term in theory, but such equations contain correlations of higher order, which does not allow the closure desired. Therefore the transport equations for the Reynolds stresses, eq. (4.53), are used at the most in practice. Hence, the 2nd order models are called the *Reynolds Stress Models (RSM)*.

The unknown correlations are approximated by means of the average values, Reynolds stresses $\overline{\rho w_i'' w_j''}$ and turbulence scales. The characteristic scales are again computed from the transport equations for the turbulent kinetic energy and a suitable length scale equivalent.

ARSM

Beyond the conservation laws of density (1 equation), momentum (2-3) and energy (1), the full RSM requires another 5-8 partial differential equations to be solved, which notably increases the memory demands as well as prolongates the computational time.

Therefore the full RSM are sometimes simplified, substituting the differential equations for the Reynolds stresses by algebraic relations (the *Algebraic Reynolds Stress Models, ARSM*). Based on the observation of (nearly) constant ratio of a turbulent shear stress to a turbulent kinetic energy across a thin shear layer, the original transport equations can be transformed into algebraic relations for an anisotropy tensor

$$a_{ij} = \frac{\overline{\rho w_i'' w_j''}}{\bar{\rho} k} - \frac{2}{3} \delta_{ij}. \quad (4.73)$$

A universal relation has been derived in [83] in a shortened form

$$\frac{\partial}{\partial t} \left(\overline{\rho w_i'' w_j''} \right) + \frac{\partial}{\partial x_k} \left(\tilde{w}_k \overline{\rho w_i'' w_j''} \right) = P_{ij} + D_{ij} + \Pi_{ij} - \epsilon_{ij}, \quad (4.74)$$

$$\frac{\partial}{\partial t} (\bar{\rho} k) + \frac{\partial}{\partial x_k} (\tilde{w}_k \bar{\rho} k) = P_k + D_k - \epsilon. \quad (4.75)$$

The weak equilibrium assumption is expressed as

$$\frac{\partial}{\partial t} \left(\frac{\overline{\rho w_i'' w_j''}}{\bar{\rho} k} \right) + \frac{\partial}{\partial x_k} \left(\tilde{w}_k \frac{\overline{\rho w_i'' w_j''}}{\bar{\rho} k} \right) \approx 0,$$

which turns into an implicit algebraic relation for the anisotropy tensor

$$\frac{\overline{\rho w_i'' w_j''}}{\bar{\rho} k} (P_k - \epsilon) = P_{ij} + \Pi_{ij} - \epsilon_{ij}. \quad (4.76)$$

EARSM

After the approximation of Π_{ij} and ϵ_{ij} , equation (4.76) leads to an implicit nonlinear set of equations. Due to the lack of any diffusive and/or damping terms the whole system is numerically unstable and unusable for cases with complex boundary conditions. The way out is through an explicit relation for the entries of a_{ij} , as published in [99], leading to the class of Explicit Algebraic Reynolds Stress Models (*EARSM*).

This class requires only two extra differential equations (for turbulent scales) beside the conservation laws, thus having a potential of an accurate and efficient model which disposes the linear dependency between the turbulent stresses and the strain rate tensor, without an enormous increase in the CPU demands or the model complexity.

4.4.3 Recapitulation

The current development of fluid dynamics is strongly conditioned by the development of CPU technologies. The more powerful processors and larger memories allow to capture enhanced mathematical models and more complex geometries.

The models of turbulence are however limited by their physical nature, preferring simpler and concrete correlations rather than series of equations for abstract variables. As mentioned above the transport equations for turbulent correlations are not able to close the entire system themselves, always needing some empirical approximations, likely based on experimental observations.

A proper turbulence model is therefore a *compromise* between the number of equations employed and a rational chance to approximate the unknown correlations contained inside.

4.5 Models Used

This section describes all the turbulence models used within this work. For transparency reasons the models are presented in a differential form, together with all the constitutive relations required for their numerical realization.

Because the goal of this work is not to develop an own turbulence model, all the models presented have been taken up from the literature. The initial and boundary conditions are described in the last part of this section, in 4.5.6.

4.5.1 One Equation *Spalart-Allmaras* Model

This model has been published in [90] and belongs to the group of the models with the transport equation for the eddy viscosity, introduced in section 4.4.1. This model has been implemented for

2D and its only transport equation defined for the turbulent kinetic viscosity $\nu_t = \mu_t/\bar{\rho}$ reads

$$\frac{D\tilde{\nu}_t}{Dt} = C_{b1}\tilde{\nu}_t\tilde{S} + C_{b2}\frac{1}{\sigma}\frac{\partial\tilde{\nu}_t}{\partial x_j}\frac{\partial\tilde{\nu}_t}{\partial x_j} + \frac{1}{\sigma}\frac{\partial}{\partial x_j}\left[(\nu + \tilde{\nu}_t)\frac{\partial\tilde{\nu}_t}{\partial x_j}\right] - C_{w1}f_w\left(\frac{\tilde{\nu}_t}{d}\right)^2. \quad (4.77)$$

The left hand side uses the so-called substantial derivation

$$\frac{D}{Dt} = \frac{\partial}{\partial t} + w_i\frac{\partial}{\partial x_i} \quad (4.78)$$

The correction

$$\nu_t = \tilde{\nu}_t f_{\nu 1}, \quad f_{\nu 1} = \frac{\chi^3}{\chi^3 + C_{\nu 1}^3}, \quad (4.79)$$

is used for the low Reynolds number (near wall) regions. The damping function $f_{\nu 1}$ defined by the equation (4.79) tends to 1, with increasing distance from the wall, causing the modified viscosity $\tilde{\nu}_t$ to tend to ν_t . The parameter $\chi = \tilde{\nu}_t/\nu$ defines the turbulent Reynolds number. Similarly the production term uses the modified vorticity

$$\tilde{S} = S + \frac{\tilde{\nu}_t}{\kappa^2 d^2} f_{\nu 2}, \quad S = \sqrt{2\Omega_{ij}\Omega_{ij}}, \quad (4.80)$$

$$f_{\nu 2} = 1 - \frac{\chi}{1 + \chi f_{\nu 1}} \quad (4.81)$$

with the original vorticity Ω_{ij} defined by the equation (4.66) and d the wall distance. The damping function f_w for the dissipation term has been chosen

$$f_w = g\left(\frac{1 + C_{w3}^6}{g^6 + C_{w3}^6}\right)^{1/6}, \quad g = r + C_{w2}(r^6 - r), \quad (4.82)$$

$$r = \frac{\tilde{\nu}_t}{\tilde{S}\kappa^2 d^2}, \quad (4.83)$$

using the mixing length $L \equiv \sqrt{\tilde{\nu}_t/\tilde{S}}$ as the length scale for the inner part of the boundary layer. In the logarithmic layer $r = f_w = 1$ and for the outer regions r decreases to 0. The model constants used are

$$\begin{aligned} C_{\nu 1} &= 7.1, \quad C_{b1} = 0.1355, \quad C_{b2} = 0.622 \\ C_{w1} &= 3.238, \quad C_{w2} = 0.3, \quad C_{w3} = 2, \\ \sigma &= 0.667. \end{aligned} \quad (4.84)$$

4.5.2 Two Equations *Menter's Models*

After many two equations models tested, F. Menter has designed and published [64] two universal models which combine the advantages of the precedent two equations models. Namely, he combines the $k - \omega$ models near the surfaces and the $k - \epsilon$ model in rest of the domain.

For an easier numerical realization, the $k - \epsilon$ model is rewritten to a form of the $k - \omega$ model, with the ϵ -terms plugged throughout a function F_1 . This blending function then takes the value

$F_1 = 1$ in the near wall regions and $F_1 = 0$ outside. The transport equations are given by

$$\frac{D(\bar{\rho}k)}{Dt} = \tau_{ij} \frac{\partial \tilde{w}_i}{\partial x_j} - \beta^* \bar{\rho} k \omega + \frac{\partial}{\partial x_j} \left[(\mu + \sigma^* \mu_t) \frac{\partial k}{\partial x_j} \right], \quad (4.85)$$

$$\begin{aligned} \frac{D(\bar{\rho}\omega)}{Dt} &= \frac{\gamma}{\nu_t} \tau_{ij} \frac{\partial \tilde{w}_i}{\partial x_j} - \beta \bar{\rho} \omega^2 + \frac{\partial}{\partial x_j} \left[(\mu + \sigma \mu_t) \frac{\partial \omega}{\partial x_j} \right] \\ &\quad + 2\bar{\rho}(1 - F_1) \frac{\sigma_2}{\omega} \frac{\partial k}{\partial x_j} \frac{\partial \omega}{\partial x_j}. \end{aligned} \quad (4.86)$$

The blending function is used also for the model constants

$$\phi = F_1 \phi_1 + (1 - F_1) \phi_2, \quad (4.87)$$

with $\phi_{1/2}$ corresponding constants of the $k - \omega/k - \epsilon$ model. The eddy viscosity is then computed from

$$\mu_t = \bar{\rho} \frac{k}{\omega}. \quad (4.88)$$

Baseline Model

The baseline model (*BSL*) was designed to perform like the $k - \omega$ model without the strong freestream sensitivity. The blending takes place in the wake region of the boundary layer through the function

$$F_1 = \tanh(\Gamma_{BSL}^4). \quad (4.89)$$

with

$$\Gamma_{BSL} = \min(\max(\Gamma_1; \Gamma_3); \Gamma_2), \quad (4.90)$$

$$\Gamma_1 = \frac{500\nu}{\omega d^2}, \quad \Gamma_2 = \frac{4\rho\sigma_2 k}{d^2 C_D}, \quad \Gamma_3 = \frac{\sqrt{k}}{\beta_1^* \omega d}. \quad (4.91)$$

The variable d represents the wall distance and the cross-diffusion term C_D is defined as

$$C_D = \max\left(\rho \frac{2\sigma_2}{\omega} \frac{\partial k}{\partial x_j} \frac{\partial \omega}{\partial x_j}; 10^{-20}\right). \quad (4.92)$$

The inner/outer model constants are

$$\begin{aligned} \beta_{1/2}^* &= 0.09, & \sigma_{1/2}^* &= 0.5/1.0, & \kappa &= 0.41 \\ \gamma_{1/2} &= \frac{5}{9}/0.44, & \sigma_{1/2} &= 0.5/1.0, & \beta_{1/2} &= \left(\gamma_{1/2} + \frac{\sigma_{1/2} \kappa^2}{\sqrt{\beta_{1/2}^*}} \right) \beta_{1/2}^* \end{aligned} \quad (4.93)$$

Shear Stress Transport Model

Numerous experiments have proven that the turbulent shear stress τ_{ij}^R is proportional to the turbulent energy k in a dominant part of the boundary layer. Nevertheless the classical formulation of the eddy viscosity, see the equation (4.88), does not take the shear stress transport (*SST*) into account.

Bradshaw [16] has therefore used a relation

$$\frac{\tau_{ij}^R}{\rho} = a_1 k, \quad (4.94)$$

and Menter [64] has lately suggested a modified eddy viscosity definition

$$\nu_t = \min \left(\frac{a_1 k}{F_2 \Omega}; \frac{k}{\omega} \right). \quad (4.95)$$

The first term arises from the assumption

$$\tau_{ij}^R = \nu_t \left| \frac{\partial \tilde{\omega}}{\partial x_j} \right|, \quad (4.96)$$

with the velocity gradient being substituted by the absolute value of vorticity Ω for more general cases. The term required is then recovered from the equation (4.94) and the blending function

$$\begin{aligned} F_2 &= \tanh(\Gamma_{SST}^2), \\ \Gamma_{SST} &= \max(\Gamma_1; 2 \cdot \Gamma_3). \end{aligned} \quad (4.97)$$

The second term of the equation (4.95) prevents the model from singular behaviour for $\Omega = 0$. The model constants are

$$\begin{aligned} \beta_{1/2}^* &= 0.09, & \sigma_{1/2}^* &= 0.85/1.0, & \kappa &= 0.41, & a_1 &= 0.31, \\ \gamma_{1/2} &= \frac{5}{9}/0.44, & \sigma_{1/2} &= 0.5/0.857, & \beta_{1/2} &= \left(\gamma_{1/2} + \frac{\sigma_{1/2} \kappa^2}{\sqrt{\beta_{1/2}^*}} \right) \beta_{1/2}^*. \end{aligned} \quad (4.98)$$

The figure 4.7 shows the behaviour of the blending functions F_1 , F_2 across the boundary layer for various velocity profiles. The variable U represents the velocity component in x direction, U_e the shear-layer edge velocity and δ the boundary layer thickness.

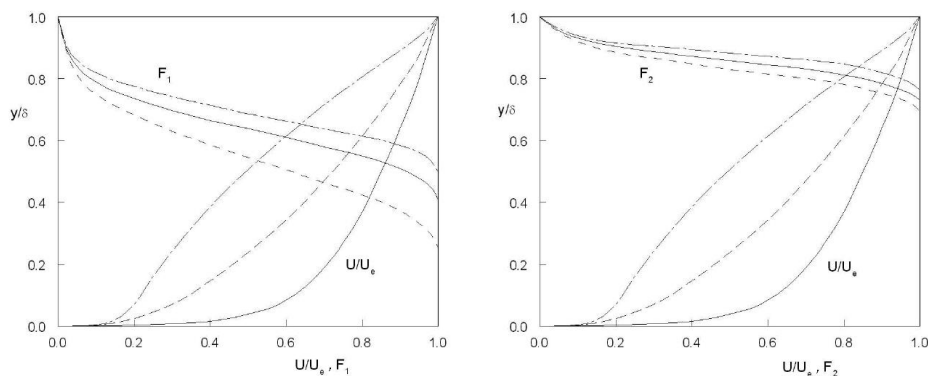


Figure 4.7: Blending functions behaviour, a figure from [75]

4.5.3 Two Equations *Wilcox* $k - \omega$ Model

The original $k - \omega$ model proposed by D. Wilcox has been published in [102] in 1988. This work deals with its revised version [104], published in November 2008. The new model incorporates two key modifications

- the addition of a cross-diffusion term,
- a built-in stress-limiter modification.

The transport equations for the k and ω are

$$\frac{D(\bar{\rho}k)}{Dt} = \bar{\rho}\tau_{ij}\frac{\partial\tilde{w}_i}{\partial x_j} - \beta^*\bar{\rho}k\omega + \frac{\partial}{\partial x_j}\left[\left(\mu + \sigma^*\frac{\bar{\rho}k}{\omega}\right)\frac{\partial k}{\partial x_j}\right], \quad (4.99)$$

$$\frac{D(\bar{\rho}\omega)}{Dt} = \alpha\frac{\omega}{k}\bar{\rho}\tau_{ij}\frac{\partial\tilde{w}_i}{\partial x_j} - \beta\bar{\rho}\omega^2 + \sigma_d\frac{\bar{\rho}}{\omega}\frac{\partial k}{\partial x_j}\frac{\partial\omega}{\partial x_j} + \frac{\partial}{\partial x_j}\left[\left(\mu + \sigma\frac{\bar{\rho}k}{\omega}\right)\frac{\partial\omega}{\partial x_j}\right], \quad (4.100)$$

with the eddy viscosity defined as

$$\mu_t = \frac{\bar{\rho}k}{\tilde{\omega}}, \quad \tilde{\omega} = \max\left(\omega; C_{lim}\sqrt{\frac{2\bar{S}_{ij}\bar{S}_{ij}}{\beta^*}}\right). \quad (4.101)$$

The constitutive relations and closure coefficients are

$$\bar{S}_{ij} = S_{ij} - \frac{1}{2}\frac{\partial w_k}{\partial x_k}\delta_{ij}, \quad C_{lim} = \frac{7}{8},$$

$$\alpha = \frac{13}{25}, \quad \beta^* = \frac{9}{100}, \quad \sigma = \frac{1}{2}, \quad \sigma^* = \frac{3}{5}, \quad \text{Pr}_T = \frac{8}{9}, \quad (4.102)$$

$$\sigma_d = \begin{cases} 0, & \text{for } \frac{\partial k}{\partial x_j}\frac{\partial\omega}{\partial x_j} \leq 0 \\ \sigma_{do}, & \text{for } \frac{\partial k}{\partial x_j}\frac{\partial\omega}{\partial x_j} > 0 \end{cases}, \quad \sigma_{do} = \frac{1}{8}, \quad (4.103)$$

$$\beta = \beta_o f_\beta, \quad \beta_o = 0.0708, \quad f_\beta = \frac{1 + 85\chi_\omega}{1 + 100\chi_\omega}, \quad (4.104)$$

$$\chi_\omega \equiv \left|\frac{\Omega_{ij}\Omega_{jk}\hat{S}_{ki}}{(\beta^*\omega)^3}\right|, \quad \hat{S}_{ki} = S_{ki} - \frac{1}{2}\frac{\partial w_m}{\partial x_m}\delta_{ki}. \quad (4.105)$$

Note that the diffusion terms in the equations (4.99) and (4.100) (terms multiplied by σ^* and σ) are proportional to $\bar{\rho}k/\omega$ rather than to the eddy viscosity.

The term proportional to σ_d in the equation (4.100) is called the cross-diffusion. In free shear flows the cross-diffusion term enhances production of ω , which in turn reduces the net production of k . Close to the solid surface boundary (k increases, while ω decreases) the cross-diffusion term is suppressed because of the splitting (4.103). The new model therefore simplifies the complicated blending functions (4.89), (4.97) of the Menter models to a necessary minimum.

The stress limiter (4.101) makes the eddy viscosity a function of k , ω and the ratio of the turbulence-energy production to the turbulence-energy dissipation, resolving also the shear stress transport. In [43] it has been shown, that by limiting the magnitude of μ_t when the energy production exceeds the dissipation, a strong improvement for incompressible and transonic flows predictions is acquired.

4.5.4 Two Equations *Kok's TNT* Model

Another member of the family of the $k - \omega$ models, has been published by J. Kok in [47]. His advantage is the insensitivity to the turbulent variables of the mean flow and the new model

constants. The transport equations are

$$\frac{D(\bar{\rho}k)}{Dt} = P - \beta^* \bar{\rho}k\omega + \frac{\partial}{\partial x_j} \left[(\mu + \sigma^* \mu_t) \frac{\partial k}{\partial x_j} \right], \quad (4.106)$$

$$\frac{D(\bar{\rho}\omega)}{Dt} = \alpha \frac{\omega}{k} P - \beta \bar{\rho}\omega^2 + \frac{\partial}{\partial x_j} \left[(\mu + \sigma \mu_t) \frac{\partial \omega}{\partial x_j} \right] + C_D, \quad (4.107)$$

with P the production and C_D the cross-diffusion term

$$P = \tau_{ij} \frac{\partial u_i}{\partial x_j}, \quad C_D = \frac{1}{2} \frac{\rho}{\omega} \left(\frac{\partial k}{\partial x_j} \frac{\partial \omega}{\partial x_j}; 0 \right). \quad (4.108)$$

The eddy viscosity and the model constants are

$$\begin{aligned} \mu_t &= \alpha^* \frac{\bar{\rho}k}{\omega}, \\ \alpha &= 0.553, \quad \alpha^* = 1.0, \quad \beta = 0.075, \quad \beta^* = 0.09, \\ \sigma &= 0.5, \quad \sigma^* = \frac{2}{3}, \quad \text{Pr}_t = 0.9. \end{aligned} \quad (4.109)$$

The transport equations (4.106), (4.107) have mainly been used for the velocity and time scale extraction, required by the following EARS model.

4.5.5 EARSM

This model, based on [99] disposes the linear dependency between the turbulent stresses and the strain rate tensor by introducing the anisotropy tensor (4.73) in a form

$$a_{ij} = \beta_4 (S_{ik}^* \Omega_{kj}^* - \Omega_{ik}^* S_{kj}^*). \quad (4.110)$$

The Reynolds stresses and the eddy viscosity are then computed as

$$\tau_{ij}^R = 2\mu_t S_{ij} - \frac{2}{3} \delta_{ij} \bar{\rho}k - \bar{\rho}k a_{ij}, \quad (4.111)$$

$$\mu_t = -\frac{1}{2} \beta_1 \bar{\rho}k \tau. \quad (4.112)$$

The deformation and rotation tensors S_{ij} , Ω_{ij} are defined by the equations (4.66), with their normalized clones S_{ij}^* , Ω_{ij}^*

$$S_{ij}^* = \tau S_{ij}, \quad \Omega_{ij}^* = \tau \Omega_{ij}, \quad (4.113)$$

with τ the turbulent time scale

$$\tau = \max \left(\frac{1}{\beta^* \omega}; C_\tau \sqrt{\frac{\mu}{\beta^* \bar{\rho}k\omega}} \right). \quad (4.114)$$

The coefficients β_1 in the equation (4.112) and β_4 in the equation (4.110) are computed from

$$\beta_1 = -\frac{6}{5} \frac{N}{N^2 - 2II_\Omega}, \quad (4.115)$$

$$\beta_4 = \frac{\beta_1}{N}, \quad (4.116)$$

with II_Ω the invariant of the rotation tensor () and the parameter N

$$N = \begin{cases} \frac{C'_1}{3} + (P_1 + \sqrt{P_2})^{\frac{1}{3}} + \text{sign}(P_1 - \sqrt{P_2}) (|P_1 - \sqrt{P_2}|)^{\frac{1}{3}} & \text{for } P_2 \geq 0 \\ \frac{C'_1}{3} + 2(P_1^2 - P_2)^{\frac{1}{6}} \cos \left[\frac{1}{3} \arccos \left(\frac{P_1}{\sqrt{P_1^2 - P_2}} \right) \right] & \text{for } P_2 < 0 \end{cases} \quad (4.117)$$

$$P_1 = \left(\frac{C'_1}{27} + \frac{9}{20} II_S - \frac{2}{3} II_\Omega \right) C'_1 \quad (4.118)$$

$$P_2 = P_1^2 - \left(\frac{C'^2_1}{9} + \frac{9}{10} II_S + \frac{2}{3} II_\Omega \right)^3 \quad (4.119)$$

The invariants II_S and II_Ω and the model constants are

$$II_S = \text{tr} \{ S_{ik}^* S_{kj}^* \} \quad , \quad II_\Omega = \text{tr} \{ \Omega_{ik}^* \Omega_{kj}^* \} . \quad (4.120)$$

$$C'_1 = 1.8 \quad , \quad C_\tau = 6.0 . \quad (4.121)$$

For determination of the velocity and the time scales this model uses the above shown transport equations of the TNT turbulence model (4.106) and (4.107).

4.5.6 Initial and Boundary Conditions

Transport Equation of ν_t

According to [75] the Spalart-Allmaras model, which uses a transport equation for the eddy viscosity, is insensitive to the initial value of ν_t , therefore the initial flowfield has been filled with one of these options

$$\nu_t^{init} = \begin{cases} 0 \\ \nu_t^\infty \end{cases} \quad (4.122)$$

The inlet condition is defined

$$\nu_t^{inlet} = C_\nu \nu_t^\infty , \quad (4.123)$$

with the model constant $C_\nu = 10^{-(1 \div 3)}$. The outlet condition (as for all other models used) does not require any value prescribed. The condition for the solid surfaces is realized by

$$\nu_t^{wall} = 0 . \quad (4.124)$$

Transport Equation of k

The flowfield gets initialized by the value k^{init} defined by the equation (4.125) for the velocity w^{inlet} . The inlet value is related to the inlet velocity as

$$k^{inlet} = C_k \nu_t^\infty \frac{w^{inlet}}{L} . , \quad (4.125)$$

where L is the reference length, ν_t the eddy viscosity given by (4.123) and $C_k = 10^{0 \div 1}$ the constant chosen. The condition for the solid surfaces is again trivial

$$k^{wall} = 0 . \quad (4.126)$$

Transport Equation of ω

The initial value ω^{init} is set to

$$\omega^{init} = \frac{w^{inlet}}{L}, \quad (4.127)$$

with an identical meaning to the equation (4.125). The inlet value uses w^{inlet} with the same equation (4.127). According to [65], the condition for solid surfaces is modeled by

$$\omega^{wall} = C_\omega \cdot \frac{6\nu}{\beta_1^* d^2}, \quad (4.128)$$

with the constant $\beta_1^* = 0.09$, d the distance to the first gridpoint and $C_{\omega 0} = 10$ the adjustable constant.

In [102] it is pointed out that the $k-\omega$ models give the correct smooth wall sublayer behaviour if

$$\omega^{wall} > \frac{100 \cdot u_\tau^2}{\nu}, \quad (4.129)$$

which is satisfied due to the equation (4.128) as long as $y^+ < (\sim 3)$.

Chapter 5

Numerics

Although the Navier-Stokes (resp. RANS, resp. U-RANS) equations are investigated by mathematicians for many decades, any analytical solution have not been obtained due to their complexity yet, except for the most simple cases. Thus, the numerical mathematics must be introduced to the problem, in order to acquire a relevant and physically acceptable result.

As there is a large variety of numerical methods, this chapter will introduce the numerical procedures and numerical tools particularly used for the sake of this work.

5.1 Mathematical Formulation

The system of U-RANS equations (4.38), (4.39), (4.40) can be written in a vectorial form for an arbitrary volume Ω with a surface $\partial\Omega$

$$\frac{d}{dt} \int_{\Omega} W \, d\Omega = - \oint_{\partial\Omega} (F_j^I - F_j^V) n_j \, d\partial\Omega + \int_{\Omega} Q \, d\Omega. \quad (5.1)$$

W is the vector of conservative unknowns, $F^{I/V}$ the inviscid/viscous fluxes and Q the source term. The general form of the vectors mentioned for a general 3D unsteady compressible flow on a moving domain with the Spalart-Allmaras turbulence model 4.5.1 follows

$$W = \left[\bar{\rho}; \bar{\rho}\tilde{w}_1; \bar{\rho}\tilde{w}_2; \bar{\rho}\tilde{w}_3; \bar{\rho}\tilde{E}; \tilde{v}_t \right]^T, \quad (5.2)$$

$$F_j^I = \begin{bmatrix} \bar{\rho}(\tilde{w}_j - w_{Bj}) \\ \bar{\rho}\tilde{w}_1(\tilde{w}_j - w_{Bj}) + (\bar{p} + \frac{2}{3}\bar{\rho}k) \delta_{1j} \\ \bar{\rho}\tilde{w}_2(\tilde{w}_j - w_{Bj}) + (\bar{p} + \frac{2}{3}\bar{\rho}k) \delta_{2j} \\ \bar{\rho}\tilde{w}_3(\tilde{w}_j - w_{Bj}) + (\bar{p} + \frac{2}{3}\bar{\rho}k) \delta_{3j} \\ \bar{\rho}\tilde{e}(\tilde{w}_j - w_{Bj}) + (\bar{p} + \frac{2}{3}\bar{\rho}k) \tilde{w}_i \delta_{ij} \\ \tilde{v}_t(\tilde{w}_j - w_{Bj}) \end{bmatrix}, \quad (5.3)$$

$$F_j^V = \begin{bmatrix} 0 \\ (\mu + \mu_t) \left(\frac{\partial \tilde{w}_1}{\partial x_j} + \frac{\partial \tilde{w}_j}{\partial x_1} - \frac{2}{3} \frac{\partial \tilde{w}_k}{\partial x_k} \delta_{1j} \right) \\ (\mu + \mu_t) \left(\frac{\partial \tilde{w}_2}{\partial x_j} + \frac{\partial \tilde{w}_j}{\partial x_2} - \frac{2}{3} \frac{\partial \tilde{w}_k}{\partial x_k} \delta_{2j} \right) \\ (\mu + \mu_t) \left(\frac{\partial \tilde{w}_3}{\partial x_j} + \frac{\partial \tilde{w}_j}{\partial x_3} - \frac{2}{3} \frac{\partial \tilde{w}_k}{\partial x_k} \delta_{3j} \right) \\ (\mu + \mu_t) \left[\left(\frac{\partial \tilde{w}_i}{\partial x_j} + \frac{\partial \tilde{w}_j}{\partial x_i} \right) \tilde{w}_i - \frac{2}{3} \frac{\partial \tilde{w}_k}{\partial x_k} \delta_{ij} \right] + \left(\mu + \frac{\mu_t}{\sigma_k} \right) \frac{\partial k}{\partial x_j} + \left(\lambda + \frac{\mu_t c_v + r}{\text{Pr}_t} \right) \frac{\partial \tilde{T}}{\partial x_j} \\ \frac{1}{\sigma} (\nu + \tilde{\nu}_t) \frac{\partial \tilde{\nu}_t}{\partial x_j} \end{bmatrix} \quad (5.4)$$

$$Q = \begin{bmatrix} 0 \\ \bar{\rho} g_1 \\ \bar{\rho} g_2 \\ \bar{\rho} g_3 \\ \bar{\rho} g_k \tilde{w}_k + \bar{Q} \\ C_{b1} \tilde{\nu}_t \tilde{S} + C_{b2} \frac{1}{\sigma} \frac{\partial \tilde{\nu}_t}{\partial x_j} \frac{\partial \tilde{\nu}_t}{\partial x_j} - C_{w1} f_w \left(\frac{\tilde{\nu}_t}{d} \right)^2 \end{bmatrix}. \quad (5.5)$$

The respective modifications for other turbulence models or simplifications for 2D, laminar or inviscid flow model are straight forward. The set of equations (5.1) is appended by the equation of state (3.20), the Sutherland resp. Fourier law (3.22), resp. (3.23) and the last equation of (4.37). Together with a proper initial condition of a type (3.27) and boundary conditions of type (3.29), (3.30) and (3.31) a complete system is created, containing sufficient number of equations.

Despite a persistent mathematical effort, the existence and the uniqueness of solution of such system has not been proven yet. Nonetheless all the numerical computations performed and presented here have assumed such solution to exist and to be uniquely determined by the choice of the flow model, initial and boundary conditions.

5.2 Spatial Discretization Methods

Any computational domain Ω has been discretized by a finite number of disjoint volumes ω_i , such that

$$\begin{aligned} \bigcup_i \omega_i &= \Omega, \\ \omega_i \cap \omega_j &= 0, \quad \forall i, j : i \neq j. \end{aligned} \quad (5.6)$$

Depending on the dimension, each volume consists of several *nodes* which are connected by *faces* creating together an *element*. In the figure 5.1 the most frequent elements are shown.

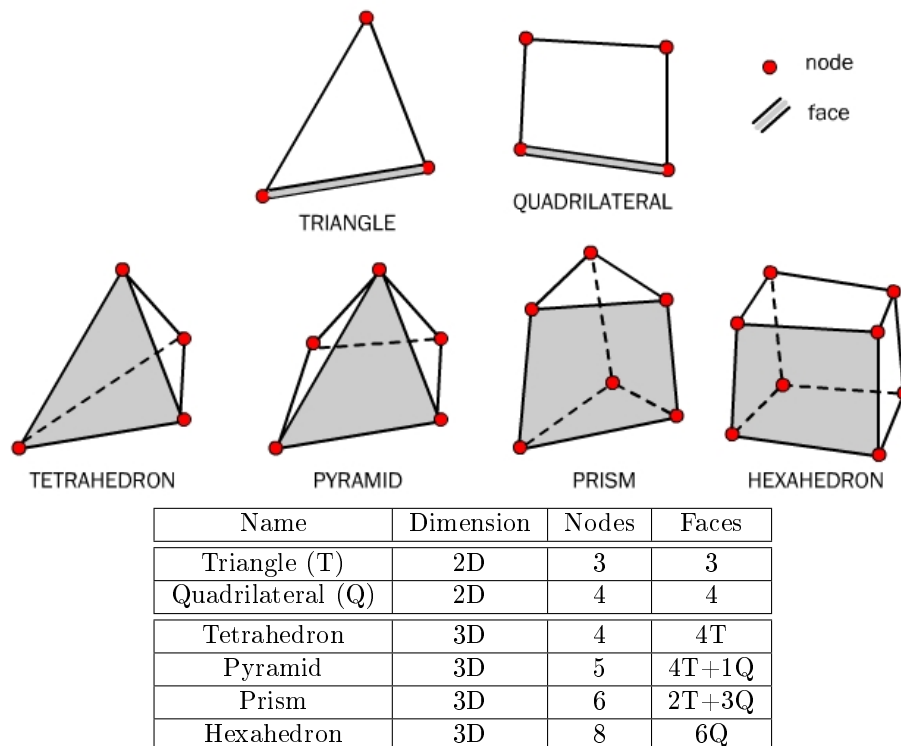


Figure 5.1: The most frequent planar and spatial volumes

For the above-constructed *computational grid*, three main spatial discretization methods can be distinguished for most of the CFD simulations.

5.2.1 Finite Difference Method (FDM)

The computational domain is filled with regularly spaced grid points and the derivatives are approximated using Taylor series expansion. The higher order of accuracy can be obtained from the extended Taylor expansions, but these require extended stencils and have a tendency to an oscillatory behaviour.

The main advantage of the FDM is its simplicity. On the other hand, the computational domains are limited to simple geometries, restraining the use of FDM for complex applications.

5.2.2 Finite Element Methods (FEM)

The solution is approximated using a continuous function belonging to a finite element space, defined on the computational domain. The solution is assumed in a form

$$W(t, \vec{x}) = \sum_{i \in \text{nodes} \in \omega} N_i W_i, \quad (5.7)$$

with N_i the nodal shape function defined at node i and W_i the solution at node i . The shape functions are either defined locally for each element (Galerkin method) or globally (collocation method). The method can be easily extended to higher accuracy orders by increasing the order of the shape functions.

For the advection (-dominated) flows oscillatory solutions can appear. In order to overcome these instability problems, the streamline-upwind Petrov-Galerkin (SUPG) methods (see [70], [95]) and

residual distribution (RD) methods (see [27], [81]) have been developed.

5.2.3 Finite Volume Method (FVM)

Nowadays, this method is probably the most widely used for solving high-Reynolds number flows and complex flow problems. This work is based on the FVM, thus it will describe the method in more detail. Out of many references on the FVM, the works by [14] and [54] are considered particularly complete.

In the cell-centered finite volume framework, the discrete solution is defined at the centroid of the element and remains constant over the element. The solution field is therefore discontinuous on the computational domain. The balance equation (5.1) is constructed for each volume ω_i and due to its (relatively) small size, the mean value theorem (5.8) is applied on the original integral equation. The fluxes over the cell faces and the volume sources by approximated by

$$F_{mean} = \frac{\int_{\partial\omega_{i,f}} F d\omega_{i,f}}{\int_{\partial\omega_{i,f}} d\omega_{i,f}}, \quad Q_{mean} = \frac{\int_{\omega_i} Q d\omega_i}{\int_{\omega_i} d\omega_i}. \quad (5.8)$$

The subscript f represents a face of the volume ω_i . The equation (5.1) is then transformed into

$$\frac{d}{dt} (W_{mean}\omega) = - \sum_f \left(F_j^I|_{mean,f} - F_j^V|_{mean,f} \right) n_{j,f} S_f + Q_{mean}\omega, \quad (5.9)$$

where

$$\omega = \int_{\omega_i} d\omega_i, \quad S_f = \int_{\partial\omega_{i,f}} d\omega_{i,f}. \quad (5.10)$$

The spatial discretization residual is computed by summing the contributions of the fluxes¹ along the faces of the element. The inviscid and viscous fluxes F are described by the physical model, see equations (5.3) and (5.4). In the FV approach the so-called numerical fluxes \tilde{F} have to be evaluated at the element faces, using the information from the neighbouring cells, leading to

$$\sum_f F_j \cdot n_j|_{mean,f} = \sum_f \tilde{F}_j \cdot n_j|_f. \quad (5.11)$$

In the simplest case, the numerical flux through a face f is obtained by an arithmetic averaging of the physical fluxes F_L and F_R that are computed from the cell values on both sides of the face, see the figure 5.2,

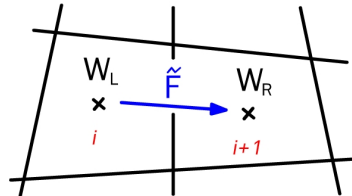


Figure 5.2: The flux between neighbouring cells

¹Note, that the Einstein sum rule does not apply to the subscript f here.

$$\begin{aligned} F_{L/R} &= F(W_{L/R}) \\ \tilde{F} &= \frac{F_L + F_R}{2}. \end{aligned} \quad (5.12)$$

Similarly to FDM, this centered flux is however known to be oscillatory for advection flows, viz. [77], [95] and requires a stabilization term and/or algorithms (e.g. blending with other numerical fluxes). The numerical fluxes at the cell interfaces are therefore often computed using exact or approximate mono-dimensional Riemann solvers along the face normal, see [54]. Among the schemes used for computation of compressible flows, the van Leer scheme [97], the Roe scheme [84], and the family of AUSM schemes [55], [57], [60] must be mentioned at minimum. The flux used in this work is described in section 5.4.

5.3 Numerical Codes Used

Two different *in-house* numerical codes have been used in this work. Both are based on the FVM but having a completely different internal structure. Their basic description follows.

MUSA

MUSA² is a numerical code being developed exclusively by the author, for the sake of this work. Due to the limited manpower the code features are not as enhanced as in the second solver and therefore the MUSA solver has mainly been used for the lighter computations in order to acquire the reference solutions.

COOLFluiD

COOLFluiD³ is a numerical framework, being developed by a team of engineers centralized at the VKI. The solver deals with many applications related to fluid dynamics. It uses the advantages of unstructured grids, parallel computing and multiphysics modelling. New features can be added to the code through its interfaces and due to high modularity of the code, see the figure 5.3.

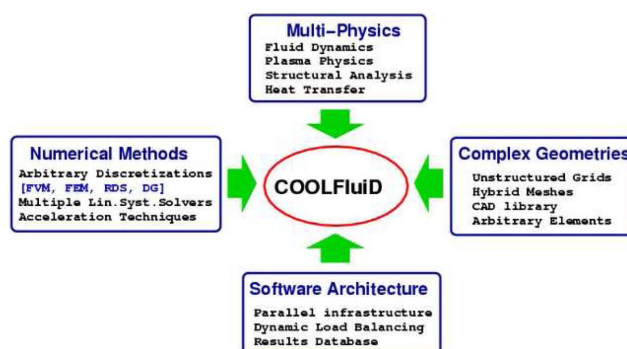


Figure 5.3: The COOLFluiD solver

²Musa is the ancient goddess who inspired the creation of all arts in the greek mythology. The name is also an anagram of the AUSM numerical scheme.

³Computational Object Oriented Library for Fluid Dynamics.

Apart from a perfect gas aerodynamics, the solver can deal with ICP (inductively coupled plasma), MHD (magneto-hydrodynamics), CNEQ (chemical non-equilibrium) flows and others, continuously widening its capabilities. See [1] for precise information about the current state of the solver.

Some general characteristics of both codes are presented in the table 5.1. Note that the following sections 5.4-5.11 belong to both numerical codes if not explicitly said otherwise.

	MUSA	COOLFluiD
Developers	1	>35
Developed since	2003	2001
Dominant programming language	C	C++
Flow models	inviscid, laminar, turbulent	inviscid, laminar, turbulent
Dimensionality	2D (quads), 3D (hexahedrons)	2D, 3D (hybrid)
Grid structure	multi-block, structured	unstructured
Turbulence models	S-A (only 2D)	S-A, $k - \epsilon$, $k - \omega$, BSL, SST, TNT, EARSM
Parallelization	OpenMP	MPI
Time integration	explicit	explicit, implicit

Table 5.1: Comparison of solvers used

5.4 Inviscid Fluxes

The inviscid fluxes F^I can be evaluated using either centered type schemes, based on the equation (5.12), or upwind schemes. The space centered schemes are robust and easy to implement, however as mentioned here-above, these schemes depend on the artificial dissipation coefficients which are necessary to prevent undesired oscillations. Due to this dependence, the centered schemes add an artificial dissipation which deteriorates the quality of the solution.

According to [26], [54] and others the upwind schemes are recommended for advection dominated flows, because of their smaller dissipation in a sense that they do not require the adjunction and tuning of an artificial viscosity. As a matter of fact, the upwind schemes also possess a natural artificial viscosity to avoid oscillations and can also be re-written as a centered scheme with an additional anti-diffusive component. However, compared to the centered schemes, the upwind schemes differentiate the physical propagation of waves which reflects the mathematical properties of the RANS equations.

AUSM scheme

The AUSM⁴ is an upwind-based numerical scheme, developed for compressible flows. According to [13], this scheme is efficient, has a high resolution shock capturing and is enthalpy conservative. Several variations of this scheme have been chosen and tested within this work. The references cite to their original papers, whereas a compact summary of the AUSM-family schemes can be found in [58].

⁴abbreviation of Advection Upstream Splitting Method.

For the sake of clarity, consider the 1D Euler equations in a differential form

$$\begin{aligned}\frac{\partial W}{\partial t} + \frac{\partial F}{\partial x} &= 0, \\ W &= [\rho, \rho w, \rho E]^T, \\ F &= [\rho w, \rho w^2 + p, \rho w H]^T,\end{aligned}\tag{5.13}$$

where $E = e + \frac{1}{2}w^2 = H - \frac{p}{\rho}$. The basic principle of any AUSM scheme is the splitting of an inviscid flux F in two physically distinct parts, namely the convective and the pressure part

$$F = w \cdot \begin{pmatrix} \rho \\ \rho w \\ \rho H \end{pmatrix} + \begin{pmatrix} 0 \\ p \\ 0 \end{pmatrix}.\tag{5.14}$$

The advective term can be considered as passive scalar quantities which are being convected by a suitably defined velocity w at the cell interface. By the contrary, the pressure terms are governed by the acoustic wave speeds.

(original) AUSM scheme, [55]

According to the figure 5.2, $F_I \equiv \tilde{F} \equiv F_{i+1/2}$ denotes a flux across an interface between states L and R . The advective term of the equation (5.14) can be rewritten as

$$F_I = w_I \cdot \begin{pmatrix} \rho \\ \rho w \\ \rho H \end{pmatrix}_{L/R} = M_I \cdot \begin{pmatrix} \rho a \\ \rho a w \\ \rho a H \end{pmatrix}_{L/R} = M_I \cdot \Phi_I,\tag{5.15}$$

with M_I the interface Mach number and a the speed of sound. The convected quantities are upwinded as

$$\Phi_I = \begin{cases} \Phi_L & \text{if } M_I > 0, \\ \Phi_R & \text{if } M_I < 0. \end{cases}\tag{5.16}$$

The subscripts L/R indicate the state the actual value is taken from. The choice of the advective velocity allows to define a whole family of schemes. One option is to represent this velocity as a combination of the wave speeds travelling towards the interface I from the adjacent states L and R , as

$$M_I = M_L^+ + M_R^-.\tag{5.17}$$

The splitting Mach number polynomials are defined as

$$M^\pm = \begin{cases} \pm \frac{1}{4} (M \pm 1)^2 & \text{if } |M| \leq 1, \\ \frac{1}{2} (M \pm |M|) & \text{otherwise.} \end{cases}\tag{5.18}$$

By the same principle, the pressure part is constructed as

$$p_I = p_L^+ + p_R^-.\tag{5.19}$$

The pressure splitting is weighted using the polynomial expansion of the characteristic speeds ($M \pm 1$). The splitting polynomials are expressed as

$$p^\pm = \begin{cases} \frac{p}{4} (M \pm 1)^2 (2 \mp M) & \text{if } |M| \leq 1, \\ \frac{p}{2} \frac{(M \pm |M|)}{M} & \text{otherwise.} \end{cases} \quad (5.20)$$

The Mach number and pressure (for $p = 1$) splitting polynomials are visualized in the figure 5.4.

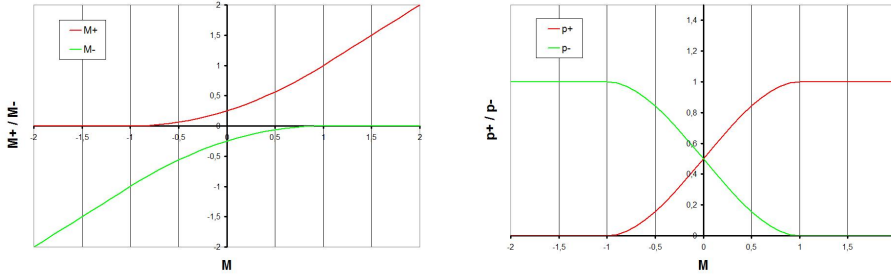


Figure 5.4: Splitting polynomials of the Mach number (left), pressure (right)

Note that the above equations can be cast in a form

$$\begin{pmatrix} \rho w \\ \rho w^2 + p \\ \rho w H \end{pmatrix}_I = M_I \cdot \frac{1}{2} \left[\begin{pmatrix} \rho a \\ \rho a w \\ \rho a H \end{pmatrix}_L + \begin{pmatrix} \rho a \\ \rho a w \\ \rho a H \end{pmatrix}_R \right] \quad (5.21)$$

$$- \frac{1}{2} |M_I| \Delta_I + \begin{pmatrix} 0 \\ p_L^+ + p_R^- \\ 0 \end{pmatrix},$$

$$\Delta_I = \begin{pmatrix} \rho a \\ \rho a w \\ \rho a H \end{pmatrix}_R - \begin{pmatrix} \rho a \\ \rho a w \\ \rho a H \end{pmatrix}_L. \quad (5.22)$$

The first term is an average of L and R states weighted by the Mach number, whereas the second term is the numerical dissipation, rendering the flux formula upwinding.

AUSM-D, AUSM-V, [56]

These variations have been designed in order to remove overshoots behind shocks, with D and V denoting a flux-difference-splitting-biased scheme and a flux-vector-splitting-biased scheme, respectively. Both schemes decompose the inviscid flux as

$$F_I = (\rho w)_I \cdot \begin{pmatrix} 1 \\ w \\ H \end{pmatrix}_{L/R} + \begin{pmatrix} 0 \\ p \\ 0 \end{pmatrix}_I = \dot{m}_I \cdot \Psi_I + p_I, \quad (5.23)$$

allowing to rewrite the equation (5.21) to

$$\begin{pmatrix} \rho w \\ \rho w^2 + p \\ \rho w H \end{pmatrix}_I = \dot{m}_I \cdot \frac{1}{2} (\Psi_L + \Psi_R) - \frac{1}{2} |\dot{m}_I| \hat{\Delta}_I + \begin{pmatrix} 0 \\ p_L^+ + p_R^- \\ 0 \end{pmatrix}, \quad (5.24)$$

$$\hat{\Delta}_I = \Psi_R - \Psi_L.$$

Compared to the original AUSM scheme, the mass flux \dot{m}_I is biasing the L and R values rather than the interface velocity w_I or the Mach number $M_I = \frac{w_I}{a}$ in the equation (5.15). Note that the original AUSM scheme can still be recovered, using the relations

$$\dot{m}_I = \frac{1}{2} [w_I (\rho_L + \rho_R) - |w_I| (\rho_R + \rho_L)], \quad (5.25)$$

$$M_I = \frac{w_L^+}{a_L} + \frac{w_R^-}{a_R} = M^+ + M^-, \quad (5.26)$$

$$w_I = M_I \cdot a_I, \quad (5.27)$$

$$a_I = \frac{1}{2} (a_L + a_R), \quad (5.28)$$

with M^\pm being evaluated from the equations (5.18). The present modifications define the interface mass flux as

$$\dot{m}_I = w_L^+ \rho_L + w_R^- \rho_R, \quad (5.29)$$

where the velocity splittings w^\pm are defined

$$w^\pm = \begin{cases} \alpha \left[\pm \frac{1}{4a_m} (w \pm a_m)^2 - \frac{1}{2} (w \pm |w|) \right] + \frac{1}{2} (w \pm |w|) & \text{if } \frac{|w|}{a_m} \leq 1, \\ \frac{1}{2} (w \pm |w|) & \text{otherwise,} \end{cases} \quad (5.30)$$

$$\alpha_{L/R} = \frac{2(p/\rho)_{L/R}}{(p/\rho)_L + (p/\rho)_R},$$

$$a_m = \max(a_L, a_R).$$

The splitting (5.30) is designed to capture stationary and/or moving contact discontinuities. The pressure flux re-uses the relation (5.19), with

$$p^\pm = \begin{cases} \frac{p}{4} \left(\frac{w}{a_m} \pm 1 \right)^2 \left(2 \mp \frac{w}{a_m} \right) & \text{if } \frac{|w|}{a_m} \leq 1, \\ \frac{p}{2} \frac{\left(\frac{w}{a_m} \pm \left| \frac{w}{a_m} \right| \right)}{\frac{w}{a_m}} & \text{otherwise.} \end{cases} \quad (5.31)$$

Both schemes presented follow the equation (5.24) for the mass and the energy conservation. The difference is found in the formulation of the interface momentum flux $(\rho w^2)_I$, or $(\rho w)_I \cdot w = \dot{m}_I \cdot w$ respectively. For the AUSM- D scheme

$$\dot{m}_I \cdot w|_{AUSM-D} = \frac{1}{2} [\dot{m}_I (w_L + w_R) - |\dot{m}_I| (w_R - w_L)], \quad (5.32)$$

whereas the AUSM- V scheme uses

$$\dot{m}_I \cdot w|_{AUSM-V} = \dot{m}_L \cdot w_L^+ + \dot{m}_R \cdot w_R^-. \quad (5.33)$$

In order to determine whether AUSM-D or AUSM-V was preferable, several numerical experiments have been carried out in [56]. Apparent oscillations have been observed for both the original AUSM and the AUSM-D schemes. The AUSM-V scheme has provided a better shock capturing capability, however in other testcases, this scheme has produced spurious oscillations (especially for contact discontinuities).

Hence a hybrid AUSM-DV scheme has been defined, which blends the previous formulations into

$$\dot{m}_I \cdot w|_{AUSM-DV} = \left(\frac{1}{2} + s\right) (\dot{m}_I \cdot w)_{AUSM-V} + \left(\frac{1}{2} - s\right) (\dot{m}_I \cdot w)_{AUSM-D}, \quad (5.34)$$

with s a switching function, based on the pressure gradient

$$s = \frac{1}{2} \min\left(1, K \frac{|p_R - p_L|}{\min(p_L, p_R)}\right).$$

The parameter K has been taken as 10.

AUSM+, [57]

The previous AUSM-DV scheme improves the robustness in the strong shock capturing, however, it still suffers by the *carbuncle* phenomenon. Moreover, the AUSM-DV scheme does not capture exactly a stationary shock. Hence the AUSM+ scheme is defined, having following properties: exact resolution of a stationary normal shock or contact discontinuity, positivity-preserving, accuracy improvement, simplicity and easy generalization to other conservation laws.

This new algorithm uses

$$M_L = \frac{w_L}{a_I}, \quad (5.35)$$

$$M_R = \frac{w_R}{a_I}, \quad (5.36)$$

In order to unify the velocity and the Mach number splittings, the interface speed of sound has to be unique, rather than using a_L and a_R . Several definitions are suggested in [57, 59], out of which the arithmetic average, eq. (5.37), the geometric average, eq. (5.38), or the relation (5.39) have been used.

$$a_I = \frac{1}{2}(a_L + a_R), \quad (5.37)$$

$$a_I = \sqrt{a_L \cdot a_R}. \quad (5.38)$$

$$a_I = \min(\bar{a}_L, \bar{a}_R) \quad (5.39)$$

$$\bar{a} = \frac{a_{crit}^2}{\max(a_{crit}, |w|)}$$

$$a_{crit} = \sqrt{\frac{2(\gamma - 1)}{\gamma + 1} H}$$

The sensitivity of results to the a_I definition is shown in the figure 6.5.

The inviscid flux F^I is again splitted as in (5.14) and (5.15), with

$$M_I = M_L^+ + M_R^-, \quad (5.40)$$

$$p_I = p_L^+ + p_R^-. \quad (5.41)$$

The splitting polynoms are then

$$M^\pm = \begin{cases} \pm (M \pm 1)^2 \pm \beta (M^2 - 1)^2 & \text{if } |M| \leq 1, \\ \frac{1}{2} (M \pm |M|) & \text{otherwise,} \end{cases} \quad (5.42)$$

$$p^\pm = \begin{cases} \frac{\rho}{4} (M \pm 1)^2 (2 \mp M) \pm \alpha p M (M^2 - 1)^2 & \text{if } |M| \leq 1, \\ \frac{\rho (M \pm |M|)}{2M} & \text{otherwise.} \end{cases} \quad (5.43)$$

The parameters α , β are said to be

$$-\frac{3}{4} \leq \alpha \leq \frac{3}{16}, \quad -\frac{1}{16} \leq \beta \leq \frac{1}{2}. \quad (5.44)$$

From the experimental studies, the values suggested are $\alpha = \frac{3}{16}$ and $\beta = \frac{1}{8}$.

AUSM+up, [60]

This extension allows the compressible flow solver to reliably predict the flows with all speed ranges. The main difficulties occur with the low speed regions that cause an extremely slow or stalled convergence and/or grossly inaccurate solutions.

The slow convergence originates at the continuum level, being associated with the disparity of convective and acoustic speeds as $M \rightarrow 0$. Turkel, Choi and Merkle, Weiss and Smith and Van Leer et al. (citation to be found in [60]) devised a *local preconditioner* which modifies the structure of eigenvalues and alters the characteristics of the governing equations.

The accuracy deficiency is inherently tied to the flux scheme employed. As the speed slows down to zero the pressure term dominates the flow field. Hence, a proper scaling of pressure differences must be reflected by the numerical scheme, so that the small perturbation in the pressure field affects accordingly the velocity field. Such behaviour can be saturated with a *numerical speed of sound* viz. [29]. This concept heals the accuracy problem, but introduces a singularity to the pressure splittings at stagnation point, $M = 0$. This singularity is overcome by the introduction of the cut-off Mach number M_{co} .

Most schemes based on the concept of the numerical speed of sound set the M_{co} empirically, e.g. like

$$M_{co} = \max\left(0.3, \frac{1}{2}M_\infty\right), \quad (5.45)$$

with 0.3 the conventional compressibility limit and M_∞ the freestream Mach number. It is, however, desired to avoid this preset value and to scale the cut-off Mach number directly with the freestream value, $M_{co} = O(M_\infty)$, rather than being bounded from below 0.3. The AUSM+up scheme is therefore based on the asymptotic series expansion for low M to derive proper scales required in the pressure and velocity diffusion terms.

The complete analysis and algebra involved can be found in [60], with an outputting result. The Mach number is defined as

$$M_{L/R} = \frac{w_{L/R}}{a_I}, \quad (5.46)$$

with the interface speed of sound defined by one of the equations (5.37), (5.38), or (5.39). The

mean local Mach number \bar{M} and the reference Mach number M_o are defined as

$$\bar{M}^2 = \frac{w_L^2 + w_R^2}{2a_I^2}, \quad (5.47)$$

$$M_o^2 = \min [1, \max (\bar{M}^2, M_\infty^2)], \quad (5.48)$$

with the scaling factor

$$f_a = M_o (2 - M_o). \quad (5.49)$$

The interface Mach number then consists of splitting contributions and a correction term

$$M_I = M_L^+ + M_R^- + M_{corr}, \quad (5.50)$$

where

$$M^\pm = \begin{cases} \pm \frac{1}{4} (M \pm 1)^2 [1 \mp 4\beta (\mp (M \mp 1)^2)] & \text{if } |M| \leq 1, \\ \frac{1}{2} (M \pm |M|) & \text{otherwise,} \end{cases} \quad (5.51)$$

$$M_{corr} = 2 \cdot K_p \max (1 - \sigma \bar{M}^2, 0) \frac{p_L - p_R}{(\rho_L + \rho_R) a_I^2}. \quad (5.52)$$

Similarly, the p_I reads as

$$p_I = p_L^+ + p_R^- + p_{corr}, \quad (5.53)$$

where

$$p^\pm = \begin{cases} \pm \frac{p}{4} (M \pm 1)^2 [(\pm 2 - M) + 4 \cdot \alpha \cdot M (M \mp 1)^2] & \text{if } |M| \leq 1, \\ \frac{p}{2M} (M \pm |M|) & \text{otherwise,} \end{cases} \quad (5.54)$$

$$p_{corr} = K_u \cdot p^+ \cdot p^- \cdot (\rho_L + \rho_R) \cdot f_a \cdot a_I \cdot (w_L - w_R). \quad (5.55)$$

The parameters α , β , K_p , K_u and σ had to fulfil certain requirements, upon which their values have been set to

$$\begin{aligned} -\frac{3}{4} \leq \alpha \leq \frac{3}{16} &\rightarrow \alpha = \frac{3}{16} (-4 + 5f_a^2), \\ -\frac{1}{16} \leq \beta \leq \frac{1}{2} &\rightarrow \beta = \frac{1}{8}, \\ 0 \leq K_p \leq 1 &\rightarrow K_p = \frac{1}{4}, \\ 0 \leq K_u \leq 1 &\rightarrow K_u = \frac{3}{4}, \\ \sigma \leq 1 &\rightarrow \sigma = 1. \end{aligned}$$

According to upwind principle the interface mass flow is defined

$$\dot{m}_I = a_I M_I \begin{cases} \rho_L & \text{if } M_I \geq 0, \\ \rho_R & \text{otherwise.} \end{cases}$$

The whole flux then reads

$$F_I = \dot{m}_I \begin{cases} \Psi_L & \text{if } \dot{m}_I \geq 0, \\ \Psi_R & \text{otherwise,} \end{cases} + p_I \quad (5.56)$$

using the notation of the equation (5.23). Note, that for $f_a = 1$ the original AUSM+ scheme can be recovered.

AUSM for ALE

The arbitrary Lagrangian-Eulerian formulation (ALE), as it is described later in section 5.9.1, is used for computations on domains with moving boundaries. For completeness sake, the modifications to the AUSM scheme are however presented here. According to [20, 89], the inviscid flux for the ALE is defined

$$F_{I, ALE} = \begin{pmatrix} \rho w_R \\ \rho w_R w + p \\ \rho w_R H + p w_B \end{pmatrix}, \quad (5.57)$$

$$w_R = w - w_B, \quad (5.58)$$

with w the conventional flow velocity, w_B the speed of the boundary movement and w_R the relative velocity. The flux (5.57) is again splitted into a convective and a pressure part, similarly to equations (5.15) and (5.23)

$$F_{I, ALE} = M_R \cdot a \cdot \begin{pmatrix} \rho \\ \rho w \\ \rho H \end{pmatrix} + \begin{pmatrix} 0 \\ p \\ p w_B \end{pmatrix} \quad \text{or} \quad F_{I, ALE} = \dot{m}_R \cdot a \cdot \begin{pmatrix} 1 \\ w \\ H \end{pmatrix} + \begin{pmatrix} 0 \\ p \\ p w_B \end{pmatrix} \quad (5.59)$$

$$F_{I, ALE} = M_{I,R} \cdot a_I \cdot \Phi_I + \begin{pmatrix} 0 \\ 1 \\ w_B \end{pmatrix} p_I \quad \text{or} \quad F_{I, ALE} = \dot{m}_{I,R} \cdot a_I \cdot \Psi_I + \begin{pmatrix} 0 \\ 1 \\ w_B \end{pmatrix} p_I \quad (5.60)$$

The local Mach number, resp. local mass flux, is substituted by the relative local Mach number, resp. relative local mass flux. The pressure part contains an extra term that depends on the mesh velocity.

The interface variables are again expressed as a suitable combination of left/right-hand state values, depending on the AUSM branch selected.

Extension of AUSM to Multi-dimensions

All the AUSM variants have been presented for the case of 1D Euler equations (5.13). Due to the rotation invariance, the 2D and 3D fluxes F_I can be rotated into a normal direction to the interface, re-creating the local 1D flux between left- and right-hand state.

Consider 3D Euler equations

$$\frac{\partial W}{\partial t} + \frac{\partial F_i}{\partial x_i} = 0, \quad (5.61)$$

$$W = [\rho, \rho w_1, \rho w_2, \rho w_3, \rho E]^T,$$

$$F_1 = [\rho w_1, \rho w_1^2 + p, \rho w_1 w_2, \rho w_1 w_3, \rho w_1 H]^T,$$

$$F_2 = [\rho w_2, \rho w_1 w_2, \rho w_2^2 + p, \rho w_2 w_3, \rho w_2 H]^T,$$

$$F_3 = [\rho w_3, \rho w_1 w_3, \rho w_2 w_3, \rho w_3^2 + p, \rho w_3 H]^T,$$

and $\vec{n} = (n_1, n_2, n_3)$ the vector pointing from left to right state and perpendicular to the interface.

Then

$$F_i \cdot n_i = w_i n_i \begin{pmatrix} \rho \\ \rho w_1 \\ \rho w_2 \\ \rho w_3 \\ \rho H \end{pmatrix} + p \begin{pmatrix} 0 \\ n_1 \\ n_2 \\ n_3 \\ 0 \end{pmatrix} = M_n \cdot a \cdot \Phi + p \begin{pmatrix} 0 \\ n_1 \\ n_2 \\ n_3 \\ 0 \end{pmatrix}, \quad (5.62)$$

$$M_n = \frac{w_1 n_1 + w_2 n_2 + w_3 n_3}{a}.$$

Terms M_n , Φ (resp. \dot{m}_n , Ψ), a , p are now subject to the splitting algorithms of the AUSM.

AUSM scheme for RANS

As far as the splitting is concerned, the turbulence quantities are treated in the exactly same way as the flow primary variables. In case of the two-equation $k - \omega$ model

$$\Phi = [\rho, \rho w_i, \rho H, \rho k, \rho \omega]^T,$$

$$\Psi = [1, w_i, H, k, \omega]^T.$$

5.5 Accuracy Improvement

The AUSM scheme presented is first order accurate in space since it only depends on the states of the immediate first neighbours of the interface. The solution is considered piecewise constant on each cell. In order to increase the spatial accuracy, the computational molecule (stencil) needs to be enlarged and the solution to be *reconstructed*. Depending on the solver used (thereby the grid structure), different types of reconstruction are recognized.

5.5.1 Reconstruction on Structured Grids (MUSA)

Each structured grid is characterized with an ordered sequel (1D), pair (2D) or trinity (3D) of indices, describing position of each grid element. Hence the spatial reconstruction can be easily built in several (index-oriented) 1D directions, with no actual computational costs for searching the neighbouring elements.

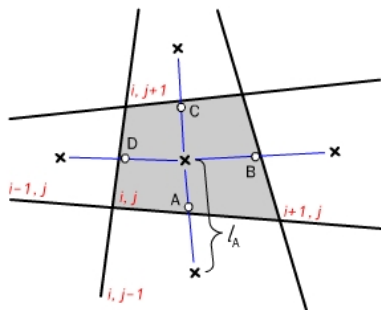


Figure 5.5: Local indexing of a quad within structured grid

The extrapolation of the cell centered values to the interface is often called MUSCL⁵. According

⁵Monotone Upstream-centered Schemes for Conservation Laws.

to [96], the linear extrapolation in one direction on an arbitrary quadrilateral i, j (see the figure 5.5 for schematic description) is defined as

$$\begin{aligned} W_A &= W_{i,j} + \omega_A (W_{i,j} - W_{i,j+1}), \\ W_C &= W_{i,j} + \omega_C (W_{i,j} - W_{i,j-1}), \end{aligned} \quad (5.63)$$

with ω the weighting functions which account the different size of neighbouring cells

$$\omega_A = \frac{|x_A - x_{i,j}|}{l_A}, \quad \omega_C = \frac{|x_C - x_{i,j}|}{l_C}. \quad (5.64)$$

For a regular cartesian grid the weights simplify to $\omega_A = \omega_C = \frac{1}{2}$. The introduction of piecewise linear reconstruction (5.63) generates oscillations near discontinuities and requires reverting the scheme to the first order accuracy near shocks, viz. [40]. This is done through the use of various limiters which bound the overshoots near shocks.

Another approach uses an interpolated slope Λ_{AC} that is computed from both sides of the element as

$$\begin{aligned} \Lambda_{AC} &= \max[0, \min(\Lambda_A; \Lambda_C)], \\ \Lambda_A &= \frac{W_{i,j} - W_{i,j-1}}{l_A}, \quad \Lambda_C = \frac{W_{i,j+1} - W_{i,j}}{l_C}. \end{aligned} \quad (5.65)$$

The equation (5.65) incorporates the *minmod* limiter in fact and can be substituted by any equation (5.67)-(5.69). The interface values are then reconstructed

$$\begin{aligned} W_A &= W_{i,j} - \frac{1}{2} \Lambda_{AC} \frac{l_A + l_C}{2}, \\ W_C &= W_{i,j} + \frac{1}{2} \Lambda_{AC} \frac{l_A + l_C}{2}. \end{aligned} \quad (5.66)$$

Limiters As mentioned above, the limiters prevent the higher order reconstruction to deteriorate the quality of the solution by undesired oscillations. The figure 5.6 demonstrates the behaviour of a linear reconstruction along the 1D discontinuity (between cells i and $i+1$). The sketches shown:

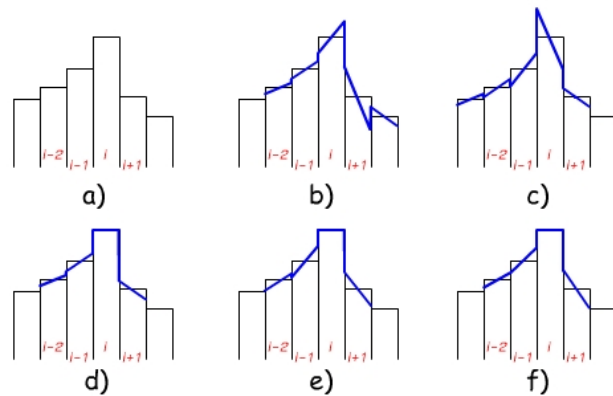


Figure 5.6: Limiter impact on the higher order reconstruction

fig. 5.6 a) piecewise constant (i.e. first order) solution;

fig. 5.6 b) reconstruction ignoring the right neighbouring value. Such approach leads to over-

shoots and oscillations behind a shock;

fig. 5.6 c) reconstruction ignoring the left neighbouring value. Oscillations and an overshoot occur in front of a shock;

fig. 5.6 d) linear reconstruction with a *minmod* limiter. This limiter always chooses the milder reconstruction, or zero.

$$\Lambda^{minmod} = \begin{cases} \Lambda_L & \text{if } |\Lambda_L| \leq |\Lambda_R| \\ \Lambda_R & \text{if } |\Lambda_L| > |\Lambda_R| \\ 0 & \text{if } \Lambda_L \cdot \Lambda_R < 0 \end{cases} \quad (5.67)$$

It is a robust limiter preventing any oscillations, therefore often used in MUSA, for higher order computations.

fig. 5.6 e) linear reconstruction with a *superbee* limiter.

$$\begin{aligned} \Lambda^{superbee} &= \text{maxmod} [\text{minmod} (\Lambda_L, 2 \cdot \Lambda_R), \text{minmod} (2 \cdot \Lambda_L, \Lambda_R)] , \quad (5.68) \\ \text{maxmod} (\Lambda_L, \Lambda_R) &= \begin{cases} \Lambda_L & \text{if } |\Lambda_L| > |\Lambda_R| \\ \Lambda_R & \text{if } |\Lambda_L| < |\Lambda_R| \end{cases} \end{aligned}$$

This reconstruction allows steeper gradients, but can also generate oscillations near inflection points.

fig. 5.6 f) linear reconstruction with a *monotonized-central (MC)* limiter.

$$\begin{aligned} \Lambda^{MC} &= \text{minmod} [\Lambda_C, \text{minmod} (\Lambda_L, \Lambda_R)] , \quad (5.69) \\ \Lambda_C &= \frac{W_{i,j+1} - W_{i,j-1}}{l_A + l_C} . \end{aligned}$$

This limiter incorporates the advantages of *minmod* and *superbee* limiters, allowing steeper gradients but denying any oscillations.

Many other limiters can be found in [9, 52, 54]. Note, that reconstruction in other directions (W_B - W_D , etc.) are defined analogically.

5.5.2 Reconstruction on Unstructured Grids (COOLFluid)

Each element of an unstructured grid is described by a single number i , independently to grid topology and dimension, $i=1, 2, \dots, N$, with N the overall number of elements. The previous reconstruction technique is therefore unacceptable, due to excessive computational demands and universal impracticability (no unique identification of left and right neighbouring elements).

The cellwise gradient ∇W is therefore computed with a least square approach [9, 11], as a result of the linear system

$$L \cdot \nabla W_i = f . \quad (5.70)$$

The matrix L is built as a product of a weight ω_j and a distance between a centroid of the current

cell and centroids of its σ neighbours, belonging to the computational stencil

$$L = \begin{pmatrix} \omega_1 \Delta x_1|_1 & \omega_1 \Delta x_2|_1 & \omega_1 \Delta x_3|_1 \\ \omega_2 \Delta x_1|_2 & \vdots & \vdots \\ \vdots & \vdots & \vdots \\ \omega_\sigma \Delta x_1|_\sigma & \omega_\sigma \Delta x_2|_\sigma & \omega_\sigma \Delta x_3|_\sigma \end{pmatrix}. \quad (5.71)$$

The linear weights are at easiest based on the inverse of distances

$$\omega_j = \frac{1}{|\Delta x_j|}. \quad (5.72)$$

The vector f is computed as

$$f = \begin{pmatrix} \omega_1 (W_1 - W_i) \\ \omega_2 (W_2 - W_i) \\ \vdots \\ \omega_\sigma (W_\sigma - W_i) \end{pmatrix}. \quad (5.73)$$

The equation (5.70) is solved in a least squares sense with an orthogonalization technique

$$\begin{aligned} L^T \cdot L \cdot \nabla W_i &= L^T \cdot f, \\ \nabla W_i &= (L^T \cdot L)^{-1} \cdot (L^T \cdot f). \end{aligned} \quad (5.74)$$

The resulting system (5.74) is not necessarily well-posed and a sufficiently large stencil is needed to prevent singularities. The importance of the computational stencil to the solution accuracy and robustness has been studied in [53].

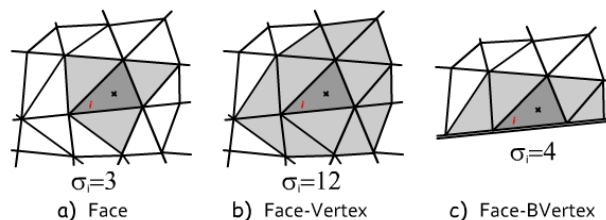


Figure 5.7: Computational stencils for unstructured grids

In the figure 5.7, some of the possibilities are shown.

Face the stencil includes only the face neighbours of each cell, fig. 5.7 a);

Face-Vertex the stencil includes all cells sharing at least one vertex, fig. 5.7 b);

Face-BVertex the stencil includes the face neighbours for internal faces and vertex neighbours for the boundary faces, fig. 5.7 c);

Face-Edge the stencil includes all cell neighbours sharing at least one edge (in 3D).

The *Face* and *Face-BVertex* options are cheap from the computational point of view, but do not provide enough robustness and accuracy, especially in 2D. The remaining options yield the best results and therefore they have been chosen for 2D (*Face-Vertex* approach) and 3D (*Face-Edge* as it avoids excessively large stencils) simulations.

With the knowledge of a cellwise gradient ∇W , the interface values are computed as

$$W_A = W_i + \nabla W_i \cdot (x_A - x_i), \quad (5.75)$$

with x_A the interface mid point and x_i the centroid of the i -th cell. To avoid oscillations caused by the reconstruction (remind the figures 5.6 *b*) or *c*) a suitable limiter is again required. The equation (5.75) therefore changes to

$$W_A = W_i + \psi \cdot \nabla W_i \cdot (x_A - x_i). \quad (5.76)$$

The parameter $\psi \in \langle 0; 1 \rangle$ can be computed according to various recipes.

Barth-Jespersen's limiter, [9]

This multidimensional limiter ensures that all extrapolated interface values fit among the minimal and maximal values of all face neighbours, W_{min} to W_{max} . Denoting the increment (resp. decrement) against the original centered value

$$\Delta W_A = \nabla W_i \cdot (x_A - x_i), \quad (5.77)$$

the parameter ψ is expressed as

$$\psi = \min \begin{cases} \min \left[1, \frac{W_{min} - W_i}{\Delta W_A} \right], & \text{if } \Delta W_A < 0 \\ \min \left[1, \frac{W_{max} - W_i}{\Delta W_A} \right], & \text{if } \Delta W_A > 0 \\ 1, & \text{if } \Delta W_A = 0 \end{cases} \quad (5.78)$$

Venkatkrishnan's limiter, [101]

This limiter overcomes some deficiencies of the previous limiter, namely the degradation of accuracy in nearly smooth flow regions. On the other hand, its implementation becomes more intricate. The limiter is based on the similar splitting equation as (5.78)

$$\psi = \min \begin{cases} \psi_V \left(\frac{W_{min} - W_i}{\Delta W_A} \right), & \text{if } \Delta W_A < 0 \\ \psi_V \left(\frac{W_{max} - W_i}{\Delta W_A} \right), & \text{if } \Delta W_A > 0 \\ 1, & \text{if } \Delta W_A = 0 \end{cases} \quad (5.79)$$

where

$$\psi_V(a) = \frac{a^2 + 2a}{a^2 + a + 2}. \quad (5.80)$$

In order to maintain the accuracy in almost flat regions, where $\Delta W_{min} \approx \Delta W_{max} \approx 0$, the function ψ_V is rewritten to

$$\psi_V(a) = \frac{\Delta W_{max}^2 + 2 \cdot \Delta W_{max} \cdot \Delta W_{min} + \epsilon}{\Delta W_{max}^2 + \Delta W_{max} \cdot \Delta W_{min} + 2 \cdot \Delta W_{min}^2 + \epsilon}. \quad (5.81)$$

The term ϵ requires a scaling from negligible in non-smooth flow regions and dominant in uniform parts. Thus

$$\epsilon = KW_0^2 \left(\frac{h}{L} \right)^3, \quad (5.82)$$

where $W_0 \simeq O(|W|)$ along whole domain, h is a local characteristic length (e.g. the average distance between the neighbouring cells), L is a local characteristic solution length in the smooth flow regions and $K \approx O(1)$ is a user-defined constant.

According to [66] these parameters can corrupt solution if wrongly chosen, therefore the higher order accuracy computations have mainly used the Barth-Jespersen's limiter, that does not require any tuning.

5.5.3 Reconstruction on Boundaries

The boundary faces require a special treatment, due to an incomplete computational stencil. In both codes, the boundary conditions have been realized via the ghost-state approach, creating a virtual cell located symmetrically to each internal boundary state. The ghost-variables W_G are then imposed or extrapolated, depending on the boundary condition type chosen.

For structured grids, (according to the figure 5.5, assuming the edge between cells i, j and $i, j-1$ being the boundary interface) the interface values are computed as

$$W_A = \frac{\omega_A W_{i,j} + \omega_G W_G}{\omega_A + \omega_G}, \quad (5.83)$$

with ω_A and ω_G the distance weights, defined by the equation (5.64). For a symmetric ghost-cell, as the ghost state has been designed, the weights are equal to $\omega_A = \omega_G = \frac{1}{2}$, reducing the previous equation into an arithmetic average. The ghost-cell is however allowed to shrink, in order to maintain the ghost-values in reasonable bounds, e.g. positive pressure. In such cases $\omega_A \neq \omega_G$.

For unstructured grids, the stencil of a cellwise gradient ∇W includes also the face ghost-neighbours.

5.5.4 Historical Modification

For higher order accuracy simulations, the magnitude of the residual tends to drop by few orders and to start oscillating, with no further decrease of the residual. In order to improve such convergence the historical modification, see [23], has been used. The parameter ψ of the equation (5.76) is then chosen from

$$\psi_i^n = \min(\psi_i^{n-1}, \psi_i^n), \quad (5.84)$$

with ψ_i^{n-1} the parameter for a cell i , which has been computed in the previous iteration. This approach improves the convergence nature for many testcases, but requires a sufficiently long starting period without using the equation (5.84) on the other hand. It also increases the memory storage demands that may turn substantive, see [52], for very large grids with complex flow model, e.g. 3D multi-species reactive flow.

5.6 Viscous Fluxes

The viscous terms F^V are usually well-behaved in a scope of computational manipulation. Due to their physical nature, a central difference scheme is usually appropriate in the discretization procedure of those terms. For an arbitrary control volume the average value of the gradient of a scalar quantity can be computed according to the relations (5.8) and (5.9) as

$$\oint_{\partial\Omega} F^V \cdot n \, d\partial\Omega \approx \sum_f F^V|_{mean,f} n_f S_f, \quad (5.85)$$

with various techniques of the computational stencil construction, see the figure 5.8. Any of the stencils shown requires an interpolation of variables onto the face midpoints (and other important locations). Rather than rendering the stencils cell-wise it is more efficient to fill up all the stencil points within one loop. This loop creates a virtual *dual*-computational grid in fact.

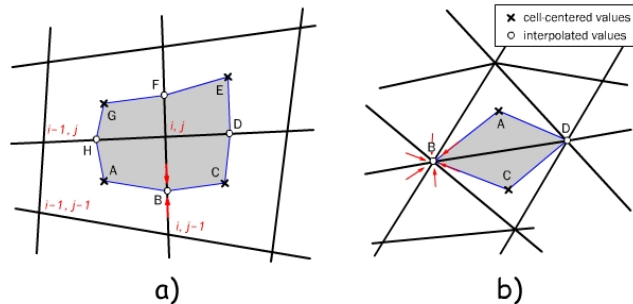


Figure 5.8: Different approaches of 2D dual grids

5.6.1 Structured Dual Grid

The MUSA solver operates on structured grids, hence uses the dual grid from the figure 5.8 a). Each dual element consists of eight edges connecting the centroids and faces' midpoints. Values at nodes A, C, E, G are given directly; their average defines the cell-vertex values. The remaining nodes B, D, F, H are interpolated from these vertex values as indicated in the figure.

The gradient of an arbitrary variable q expressed in this stencil then reads

$$\begin{aligned} \nabla q = \frac{1}{\text{Area}} \left[\frac{1}{2} (q_A + q_B) \vec{n}_1 + \frac{1}{2} (q_B + q_C) \vec{n}_2 + \dots \right. \\ \left. \dots + \frac{1}{2} (q_G + q_H) \vec{n}_7 + \frac{1}{2} (q_H + q_A) \vec{n}_8 \right], \end{aligned} \quad (5.86)$$

with $\vec{n}_{1,2,\dots,8}$ the outward normals to the dual element faces.

A simplified approach replaces the arithmetic averages $\frac{1}{2} (q_A + q_B)$, $\frac{1}{2} (q_B + q_C)$ (and their variations) by one-sided approximations

$$\begin{aligned} \frac{1}{2} (q_A + q_B) &\approx q_A \\ \frac{1}{2} (q_B + q_C) &\approx q_C \end{aligned} \quad (5.87)$$

which transform the equation (5.86) into

$$\begin{aligned} \nabla q = \frac{1}{\text{Area}} [q_A \cdot \vec{n}_1 + q_C \cdot \vec{n}_2 + \dots \\ \dots + q_G \cdot \vec{n}_7 + q_A \cdot \vec{n}_8]. \end{aligned} \quad (5.88)$$

Note, that this equation no longer requires the interpolated values which reduces the computational costs. Furthermore, the usage of the equation (5.88) leads to negligible solution differences even for grids with strongly non-uniform elements, as shown in the later section 7.4.4.

The derivatives (5.86) or (5.88) are then distributed from the dual elements (vertex-points of the primar grid) onto the faces by an arithmetic average. The method can be easily extended to three-dimensional grids.

5.6.2 Unstructured Dual Grid

A popular dual elements on unstructured grids are diamond-shaped volumes, viz [24], as depicted in the figure 5.8 b). They are built around the face considered, involving all face nodes and the left and right state values. The gradient discretized reads similarly to (5.86)

$$\begin{aligned} \nabla q = \frac{1}{\text{Area}} & \left[\frac{1}{2} (q_A + q_B) \vec{n}_1 + \frac{1}{2} (q_B + q_C) \vec{n}_2 \right. \\ & \left. + \frac{1}{2} (q_C + q_D) \vec{n}_3 + \frac{1}{2} (q_D + q_A) \vec{n}_4 \right]. \end{aligned} \quad (5.89)$$

The vertices of the diamond volume are read directly (vertices A, C) or interpolated from all neighbouring states, using the weighted average

$$q_B = \frac{\sum_i q_{B,i} \cdot \omega_i}{\sum_i \omega_i}, \quad (5.90)$$

with i representing all states that share the vertex B (see the figure 5.8 b)). The weights ω_i can be based on the distance (5.91), volume (5.92), or other relations, see [24]

$$\omega_i = \frac{1}{\|x(q_{B,i}) - x_B\|}, \quad (5.91)$$

$$\omega_i = \frac{1}{\Omega(q_{B,i})}. \quad (5.92)$$

Due to a superior robustness, the distance-based approach has been preferred for most simulations. The diamond elements technique is universal, with a straight-forward extension to 3D.

5.6.3 Dual Grid on Boundaries

Because the boundary conditions are realized for both solvers by the ghost-state approach (explained in the section 5.5.3), the internal boundary faces have a complete stencil, not requiring any special modifications.

Problems, however, may occur for border boundary faces which are shared by different topological surfaces, e.g. inlet and wall. In these *corner* vertices the contribution from ghost states of only one boundary is considered, neglecting the ghost states of remaining boundaries. The supremacy of individual boundaries is user defined.

5.7 Source Terms

The last right hand side term of the governing equation (5.1) is the source term (5.5). Its discretization is based on the cell-centered values in a given element

$$\int_{\Omega_i} Q \, d\Omega_i \approx Q(W_i) \cdot \Omega_i. \quad (5.93)$$

The derivatives (if present) are computed with the Gauss theorem (3.7), directly on the cell Ω_i

$$\nabla q = \frac{1}{\Omega_i} \int_{\Omega_i} \nabla q \, d\Omega_i = \frac{1}{\Omega_i} \oint_{\partial\Omega_i} q \cdot \vec{n} \, d\partial\Omega_i.$$

The later approximation of the last integral is identical to the equation (5.85).

5.8 Time Integration

The equation (5.1) can be formally rewritten to

$$\frac{dW}{dt} = -\mathcal{R}(W), \quad (5.94)$$

with W representing the vector of conservative unknowns and $\mathcal{R}(W)$ gathering both inviscid and viscous fluxes and the source terms.

5.8.1 Explicit Scheme

An explicit scheme is a straight forward technique to discretize the equation (5.94). The MUSA solver uses the explicit forward Euler time discretization that reads

$$\frac{W^{n+1} - W^n}{\Delta t} = -\mathcal{R}(W^n). \quad (5.95)$$

The solution in a new time level $n+1$ is thus simply given by

$$W^{n+1} = W^n - \Delta t \cdot \mathcal{R}(W^n). \quad (5.96)$$

This scheme is a first order finite difference scheme in fact and therefore it is only first order accurate in time. Such scheme is suitable for steady flow simulations, for whose

$$\lim_{n \rightarrow \infty} \frac{W^{n+1} - W^n}{\Delta t} = 0. \quad (5.97)$$

Time Step

The simplicity of the scheme is balanced by the limitation on the time step Δt . It has been derived in [110], that the time step of a stable explicit method for Euler equations must fulfill the condition

$$\Delta t_E \leq \min_i \frac{\Omega_i}{\sum_f [(\vec{w} \cdot \vec{n} + a) \cdot \Delta x]_f}, \quad (5.98)$$

with Ω_i the volume of the i -th element, a the speed of sound and Δx the measure of the face. The denominator bracket is summed over faces of the i -th element. For Navier-Stokes equations the condition tightens up to

$$\Delta t_{NS} \leq \min_i \frac{\Omega_i}{\sum_f \left[(\vec{w} \cdot \vec{n} + a) \cdot \Delta x + \left(\frac{\Delta x^2}{\text{Re} \cdot \Omega_i} \right) \right]_f}, \quad (5.99)$$

Both inequalities connect the time step to the size of the smallest face

$$\Delta t_E \sim O\left(\frac{1}{\Delta x}\right), \quad \Delta t_{NS} \sim O\left(\frac{1}{\Delta x^2}\right).$$

which leads to a strong time step limitations and elongation of the overall computational time, especially for refined grids for viscous simulations.

For stability reasons the right hand side expressions are furthermore multiplied by a positive coefficient $C < 1$, typically $C \in (0.01; 0.9)$.

5.8.2 Implicit Scheme

If the right hand side residual of (5.94) is taken from the new time level

$$\frac{W^{n+1} - W^n}{\Delta t} = -\mathcal{R}(W^{n+1}) . \quad (5.100)$$

the relation obtained defines an implicit backward Euler (BE) time stepping. Similarly to (5.95), the backward Euler method is first order accurate in time, thus suitable for the steady flow computations only.

For simulations where the time accuracy is required the *Crank-Nicolson* (C-N) scheme

$$\frac{W^{n+1} - W^n}{\Delta t} = -\frac{1}{2} [\mathcal{R}(W^{n+1}) + \mathcal{R}(W^n)] , \quad (5.101)$$

or the two-step backward differentiation formula (BDF2)

$$\frac{3W^{n+1} - 4W^n + W^{n-1}}{2\Delta t} = -\mathcal{R}(W^{n+1}) , \quad (5.102)$$

are used, as they both yield the second order accuracy. In practise, the simulations usually combine the C-N scheme for the first iteration and the BDF2 scheme, when two consecutive time levels (W^{n-1} , W^n) are known.

In order to evaluate the term $\mathcal{R}(W^{n+1})$, the residual needs to be linearized on the time level n , so that

$$\begin{aligned} \left(\frac{I}{\Delta t} + \frac{\partial \mathcal{R}}{\partial W} \right) \Delta W &= -\mathcal{R}(W^n) , \\ W^{n+1} &= W^n + \Delta W , \end{aligned} \quad (5.103)$$

where $\frac{\partial \mathcal{R}}{\partial W}$ is the Jacobian matrix. In general it is a sparse non-symmetric matrix. Its numerical realization is described in the next subsection. As the time step increases, the term $\frac{I}{\Delta t}$ tends to zero, recovering *Newton's* method in fact. Each linear system arising from (5.103) has been solved in COOLFluid (note that MUSA does not allow implicit time stepping) with a third party mathematical library, such as PETSc, Trilinos or SAMG.

Among several options the generalized minimal residual method (GMRES, viz [86]) has been preferred, together with the restricted additive Schwarz [17] or the incomplete L-U factorization preconditioner. The algorithm approximates the solution of the linear system given by the vector in a Krylov subspace with the minimal residual.

Both the method and preconditioners have been provided by the PETSc library [5], which was incorporated to the solver and treated as a black box.

Numerical Realization of the Jacobian Matrix

According to [52], the equation (5.94) can be transformed to

$$\tilde{\mathcal{R}}(\tilde{W}) = \frac{\partial W}{\partial t} + \mathcal{R}(\tilde{W}) , \quad (5.104)$$

with $\tilde{\mathcal{R}}$ the pseudo-steady residual, W the conservative variables and \tilde{W} the variables in which the solution is stored and updated. The Jacobian matrix then consists of

$$\frac{\partial \tilde{\mathcal{R}}}{\partial \tilde{W}} = J_t + J_x, \quad (5.105)$$

where J_t gathers the time-dependent terms and J_x the terms related to the spatial discretization. Depending on the implicit scheme chosen

$$J_t^{BE} = \frac{\Omega_i}{\Delta t} \frac{\partial W}{\partial \tilde{W}}, \quad J_x^{BE} = \frac{\partial \mathcal{R}}{\partial \tilde{W}}, \quad (5.106)$$

$$J_t^{C-N} = \frac{\Omega_i}{\Delta t} \frac{\partial W}{\partial \tilde{W}}, \quad J_x^{C-N} = \frac{1}{2} \frac{\partial \mathcal{R}}{\partial \tilde{W}}, \quad (5.107)$$

$$J_t^{BDF2} = \frac{3}{2} \frac{\Omega_i}{\Delta t} \frac{\partial W}{\partial \tilde{W}}, \quad J_x^{BDF2} = \frac{\partial \mathcal{R}}{\partial \tilde{W}}, \quad (5.108)$$

where $\partial W / \partial \tilde{W}$ represents the transformer matrix between different variable sets (conservative, primitive, natural, etc.).

Term $\partial \mathcal{R} / \partial \tilde{W}$ is composed of two parts, corresponding to fluxes and sources. The flux part is obtained from a loop over all faces, in order to assemble contributions from the convective and diffusive fluxes, given by equations (5.3) and (5.4). The source part arises from another loop over all cells.

The Jacobian matrix is computed numerically, approximating each partial derivative with a finite difference formula

$$\left. \frac{\partial \mathcal{R}}{\partial \tilde{W}} \right|_i \approx \frac{\mathcal{R}(W + \epsilon_i) - \mathcal{R}(W)}{\epsilon_i}, \quad (5.109)$$

with i referencing the system equation and ϵ_i a perturbation of the current variable. According to [44, 52], the perturbations are computed as

$$\epsilon_i = \text{sign}(W_i) \cdot \max(|W_i|; \hat{W}_i) \cdot \delta, \quad (5.110)$$

where \hat{W}_i is a user-defined value, whose magnitude is of the order $O(W_i)$ and $\delta \leq 10^{-5}$.

On the boundary faces, viz [27], only the internal state is perturbed and the ghost state is recomputed in order to satisfy the numerical boundary condition for the perturbed state. The ghost state entries are therefore not included in the Jacobian matrix.

The source term contribution perturbs only the state value, neglecting the contributions from neighbouring states. Hence, the source term Jacobian part only contributes to the block diagonal of the global matrix and can be easily calculated within a separate loop over cells. According to [100], each source term Q is decomposed into a production and a destruction part, according to its physical meaning, see the section 4.5.

$$Q = Q^+ + Q^-. \quad (5.111)$$

Due to various nature of the source term (especially in the case of stiff behaviour, [95]) the robustness and stability is improved by setting

$$\begin{aligned} \frac{\partial Q^+}{\partial W} &= 0, \\ \frac{\partial Q^-}{\partial W} &= \frac{Q(W + \epsilon) - Q(W)}{\epsilon}. \end{aligned}$$

It means that only the destruction part is treated implicitly and the production part explicitly.

5.8.3 Dual Time Stepping

This approach has been used for all time-accurate computations presented. The idea behind the dual time stepping technique is to have two iteration loops:

outer time stepping loop for a real time-accurate time step Δt using a fully implicit scheme,

inner time stepping loop with a fictitious time step to solve the system at each real time step.

For the BDF2 method (5.102) it can be constructed as

$$\underbrace{\frac{W^{n+1,\alpha+1} - W^{n+1,\alpha}}{\tau}}_{\text{inner loop}} + \underbrace{\frac{3W^{n+1,\alpha+1} - 4W^n + W^{n-1}}{2\Delta t}}_{\text{outer loop}} = -\mathcal{R}(W^n, W^{n+1,\alpha}, W^{n+1,\alpha+1}), \quad (5.112)$$

with τ the fictitious time step and superscript α distinguishing the inner/outer loops.

Due to the A-stability (see [35]) the dual time stepping approach is highly more efficient than other techniques, like an explicit Runge-Kutta scheme. The main benefit is that the time step Δt can be chosen accordingly to the physical problem rather than being governed by a restrictive numerical CFL condition.

5.9 Moving Geometries

The MUSA solver does not have a verified approach to the unsteady simulations on moving grids, thus they have been realized only within the COOLFluid framework. Due to large grid displacements, the Arbitrary Lagrangian-Eulerian (ALE) formulation has been used.

5.9.1 ALE Formulation

The conservative equations are usually solved on a fixed domain where $\Omega(t) \equiv \Omega(t_0)$. This approach is called an *Eulerian* formulation of the equations. If the domain $\Omega(t)$ follows the fluid the formulation is called *Lagrangian*. For the intermediate cases in which the computational domain is deformed independently from the flow pattern, an *arbitrary Lagrangian-Eulerian* formulation [42] is required.

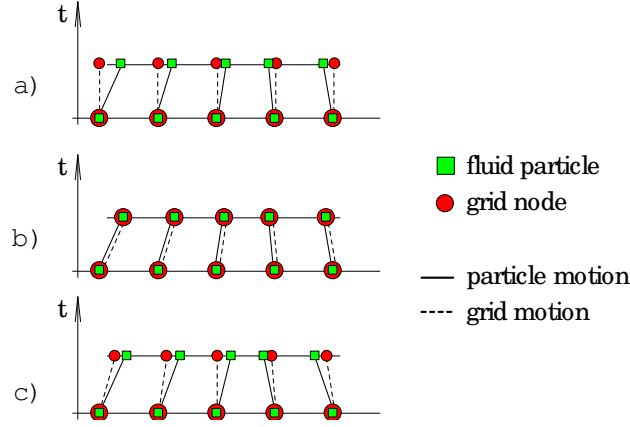


Figure 5.9: 1D example of a) Eulerian, b) Lagrangian, c) ALE grid and particle motion, fig. from [28].

For better transparency, assume Euler equations (3.13)-(3.15). The governing equations in a moving frame can be expressed as

$$\int_{\Omega(t)} \frac{\partial W}{\partial t} d\Omega = - \oint_{\partial\Omega(t)} F_j^I n_j d\partial\Omega + \int_{\Omega(t)} Q d\Omega, \quad (5.113)$$

with

$$W = \begin{bmatrix} \rho \\ \rho \vec{w} \\ \rho E \end{bmatrix}, \quad F^I \cdot \vec{n} = \begin{bmatrix} \rho \cdot \vec{w} \cdot \vec{n} \\ \rho \cdot \vec{w} \cdot (\vec{w} \cdot \vec{n}) + p \cdot \vec{n} \\ \rho \cdot \vec{w} \cdot \vec{n} \cdot H \end{bmatrix} = W \cdot \vec{w} \cdot \vec{n} + \begin{bmatrix} 0 \\ p \cdot \vec{n} \\ p(\vec{w} \cdot \vec{n}) \end{bmatrix}. \quad (5.114)$$

Using the Reynolds transport theorem (3.2), the time derivative is expanded into

$$\int_{\Omega(t)} \frac{\partial W}{\partial t} d\Omega = \frac{d}{dt} \int_{\Omega(t)} W d\Omega - \oint_{\partial\Omega(t)} W \cdot (\vec{w}_B \cdot \vec{n}) d\partial\Omega, \quad (5.115)$$

where \vec{w}_B represents the boundary velocity (velocity of $\partial\Omega(t)$). Hence, the equation (5.113) is transformed to

$$\frac{d}{dt} \int_{\Omega(t)} W d\Omega = - \oint_{\partial\Omega(t)} \left[W (\vec{w} - \vec{w}_B) \cdot \vec{n} + \begin{pmatrix} 0 \\ p \cdot \vec{n} \\ p(\vec{w} \cdot \vec{n}) \end{pmatrix} \right] d\partial\Omega + \int_{\Omega(t)} Q d\Omega. \quad (5.116)$$

The last equation explores that the rate of change of W in $\Omega(t)$ is due to

- convection through $\partial\Omega(t)$ by the relative velocity $\vec{w}_R = \vec{w} - \vec{w}_B$,
- pressure surface terms,
- source terms.

For a fixed $\Omega(t)$ the equation (5.116) reverts into *Eulerian* formulation, when $\Omega(t)$ follows the fluid into *Lagrangian* one. For a finite volume method, the change term is approximated by a sum of

numerical fluxes along the boundaries of the element Ω

$$\oint_{\partial\Omega(t)} \left[W (\vec{w} - \vec{w}_B) \cdot \vec{n} + \begin{pmatrix} 0 \\ p \cdot \vec{n} \\ p (\vec{w} \cdot \vec{n}) \end{pmatrix} \right] d\partial\Omega \approx \sum_{i \in \partial\Omega(t)} F^{I, ALE} \cdot \vec{n}|_i. \quad (5.117)$$

The form and the numerical treatment of the flux $F^{I, ALE}$ has already been described in the section 5.4.

5.9.2 Grid Update Procedures

The main advantage of the ALE formulation is a universal combination of the classical Lagrangian and Eulerian descriptions. The numerical implementation is, however, strongly linked to a grid update procedure that determines the velocity or displacement of each mesh point at each time step. This procedure is user-defined, according to the suitability to the particular test case. Two main strategies may be identified

- a grid regularization - this approach keeps the computational mesh as regular as possible, usually requiring a full or partial remeshing during the computation.
- a grid adaptation - the adaptation consists of movement and/or deformation of the mesh, without changing its structure and connectivity.

Grid Regularization

The objective of the regularization is of a geometrical nature. Its goal is to avoid excessive distortions and squeezing of the computing zones and preventing mesh entanglement. The technique decreases the numerical errors due to mesh distortion, but on the other hand it is therefore limited by small grid deformations, or computational costs of the remeshing algorithm and later the accuracy of the solution interpolation.

In order to avoid a big burden with a manual grid re-creation, the geometry considered shall allow a parameterization. This fact either insulates the regularization technique from complex geometries or puts laboured demands on linkage between an advanced grid generator and the solver.

Grid Adaptation

The adaptation technique optimizes the computational mesh to achieve an improved accuracy, preferably at low computing cost. The total number of elements in a mesh remains constant throughout the computation, as well as the element connectivity. Mesh refinement is typically carried out by moving the nodes towards zones of strong solution gradient.

The simplest approach is a purely algebraic grid deformation [109], that explicitly prescribes a movement of each mesh point. This approach is generally suitable only for very simple geometries or as a pre-processing step to other methods.

Most of the advanced adaptation approaches can be classified as equivalents of mechanical systems.

In the spring analogy approach [108], the grid is considered as a net of interconnected linear springs, represented by the element edges and torsional springs placed in the element nodes. This approach tends to smear the nodes uniformly over the domain, see the figure 5.10. As indicated,

this effect might lead to an inevitable grid deformation for test cases with anisotropic grids (e.g. grid in the boundary layer zone with high aspect ratio).

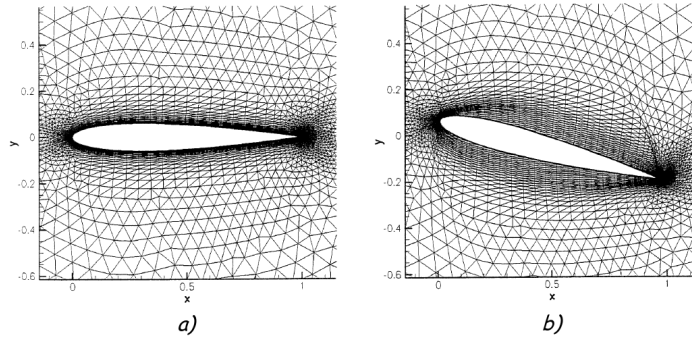


Figure 5.10: Mesh around the NACA0012 profile: a) original, b) deformed using the spring analogy, fig. from [105].

In the solid analogy [92, 105], the mesh is considered as an elastic body. According to the literature this approach is more robust than the spring model and the volume positivity preserving. Thus, it has been used for all test cases which have operated on the moving grids and therefore it will be described in more detail.

Elastic Body Analogy

The mesh is considered to be an elastic body which is deformed accordingly to the displacement imposed at its boundaries. The analogical mechanical system would be described

$$K \cdot \Delta x = F, \quad (5.118)$$

with K the stiffness matrix, Δx the node displacements and F the external forces. This system can be solved using a classical finite element approach. In a mechanical analogy, viz. [67], the deformation is described by means of the Hooke's law

$$\Delta l = \frac{F \cdot l}{E}, \quad (5.119)$$

with Δl the shift of the edge length, l the original length and E the Young modulus. The parameter E then affects the nodal distribution over the domain and allows a preservation of the grid anisotropy. Its magnitude is based on the initial geometry, distinguishing the anisotropic (preferably preserved) and isotropic (free to deform) regions. Generally it is a function depending on a cell volume Ω , a distance to the nearest wall y_0 , a cell quality, etc. However, according to [106, 105], the consideration of just the cell volume or the wall distance

$$E = \frac{1}{\Omega} \quad \text{or} \quad E = \frac{1}{y_0} \quad (5.120)$$

turns out to be sufficiently robust. The figure 5.11 compares the mesh deformation for a homogeneous stiffness 5.11 a), b), the volume based stiffness 5.11 c) and the distance based stiffness 5.11 d). The last two methods have indeed resulted in a satisfactory deformation near the trailing edge with a simultaneous preservation of the grid anisotropy along the profile and therefore they have been used for the test cases presented in the chapters 6 and 7.

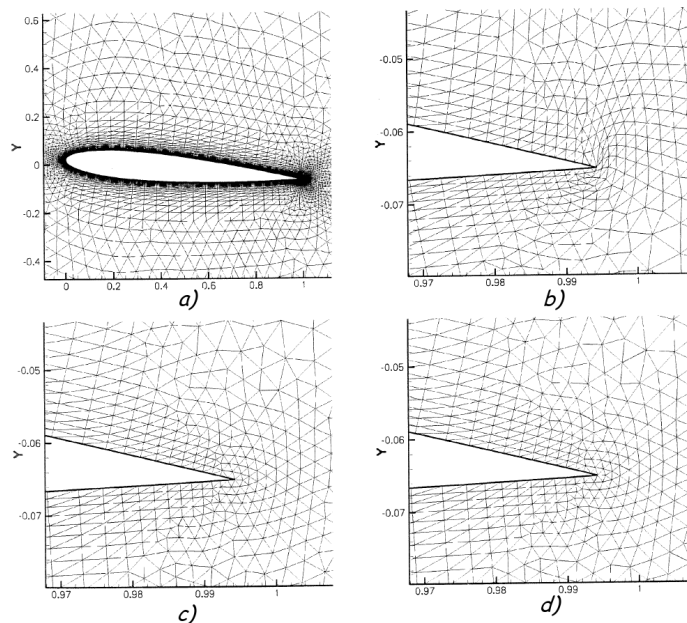


Figure 5.11: Deformed mesh around the NACA0012 profile using the elastic body analogy: a), b) homogeneous, c) volume based, d) distance based stiffness, fig. from [105].

5.9.3 Solution Interpolation

Figure 5.12 shows the contours of the exhaust valve at the TDC and BDC positions. Despite the clearance gap at the TDC, the total displacement is too big to be captured by a single computational mesh of a reasonable quality. Thus, several grids with a successive lift have had to be generated and the current solution has been interpolated among them. This approach links the previously described techniques of a mesh adaptation and regularization in fact.

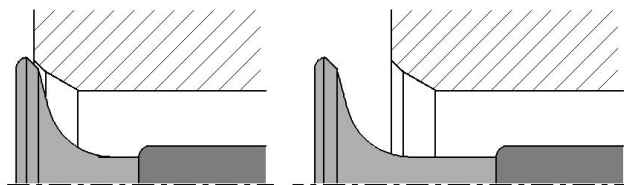


Figure 5.12: Exhaust valve at the TDC (left) and BDC (right) positions.

The interpolation of the solution has been accomplished with *Shepard's* method, viz. [88]. This method interpolates the value at a given position through a distance-weighted average from a cloud of points as

$$W_i = \frac{\sum_{j=1}^N \frac{W_j}{\|x_j - x_i\|_2}}{\sum_{j=1}^N \frac{1}{\|x_j - x_i\|_2}}, \quad (5.121)$$

where W_i is the interpolated value, x_i its position, W_j the old mesh values, x_j their positions and N the number of points in a radius of influence. The main advantage of this technique is the treatment of the mesh as a cloud of disconnected points, not requiring the knowledge of the connectivity neither of the old nor the new mesh. It improves the method robustness and reduces the memory demands, however, the main deficiencies are the smearing of local extremities, appearance of oscillations for a small interpolation stencil and no guarantee of conservation.

5.10 Boundary Conditions

All boundary conditions have been realized by means of the ghost cell approach, in which a virtual cell is created by mirroring the internal cell along the boundary face. The values at the ghost state are prescribed such that the boundary condition is respected, as illustrated in the figure 5.13. The boundary faces are therefore treated identically as the internal ones, with no need of modifications of the numerical scheme on boundaries.

During initiation phase this approach might, however, lead to substantial contradictions. As schematized in the figure 5.13 a), an extrapolation from the internal and boundary value can set a negative value in the ghost state. This causes troubles especially for inherently positive variables, such as pressure, temperature, density, etc. In such cases, following the technique developed in [71], the position of the ghost node is adapted (usually attracted towards the boundary face) in order to maintain the variable positivity, see the figure 5.13 b).

For positive variables requiring zero on the boundary (turbulent kinetic energy k), an arbitrarily small value $\approx 10^{-9}$ is imposed on the boundary face, allowing the ghost state to remain yet positive.

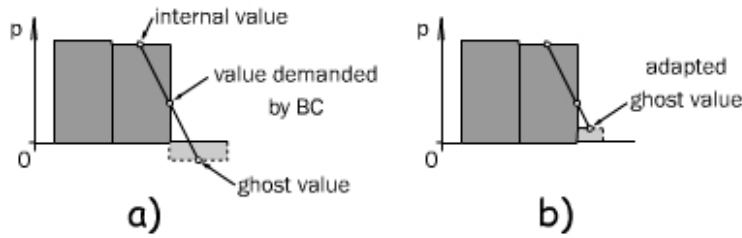


Figure 5.13: 1D scheme of the ghost state adaptation to avoid negative ghost state pressure; a) before, b) after adaptation.

Five different boundary conditions have appeared within all the test cases presented.

Mirror The normal velocity across the boundary is forced to be zero $\vec{w}_n = 0$. All other quantities are extrapolated from the interior cell. This condition can also be called a *non-permeability* condition and is used for inviscid flow models instead of the *wall* condition.

Wall The velocity is set to the speed of the boundary $\vec{w} = \vec{w}_B$ ($\vec{w}_B \equiv 0$ for non-moving boundaries). For an adiabatic wall the temperature gradient along the boundary is set to zero $\partial T / \partial n = 0$. For an isothermal wall the temperature T_{wall} is imposed.

Far-field Depending if the flow is locally subsonic or supersonic and if the flow is entering or leaving the domain, the number of variables to impose for a well-posed problem varies and are determined from the characteristic theory, viz. [76]. The local value of the normal Mach number M_n has been used to distinguish the four different regimes:

- *supersonic outlet*, $M_n < -1$: all characteristics exit the domain, hence all values are extrapolated.
- *subsonic outlet*, $M_n \in \langle -1; 0 \rangle$: one characteristic approaches the boundary from inside, others exit the domain. From here, one value is imposed with the rest being extrapolated. The typically imposed value is pressure.
- *subsonic inlet*, $M_n \in \langle 0; 1 \rangle$: inversely to the subsonic outlet, one value is extrapolated (typically pressure), with the rest being imposed (velocity and temperature).
- *supersonic inlet*, $M_n > 1$: all characteristics enter the domain, hence all values are imposed.

Inlet This condition will appear only in subsonic regimes, thus the total pressure, the total temperature and the incidence angle are imposed.

Outlet Identically to the *far-field* condition, the pressure is either imposed (subsonic) or extrapolated (supersonic). The variables remaining are extrapolated.

The turbulent variables are treated according to the model chosen, as described in the section 4.5.6.

5.11 Computation Parallelization

With increasing complexity of flow models and larger computational grids the demands on the CPU power are increasing. Desktop machines are no longer capable to resolve large scale simulations in a real time horizon. Such simulations require the use of distributed or parallel computing.

The MUSA solver allows the parallelization by means of the OpenMP interface, [18]. The OpenMP works with a shared memory and allows a direct multi-threaded parallel operation, as illustrated in figure 5.14. The approach is therefore suitable for multi-core machines with shared RAM memory, availing more efficiently its resources than a serial job. The main asset is the implementation simplicity and the computational speed-up, while the problem size remains bounded by the size of the shared memory (typically the memory of a single desktop station).

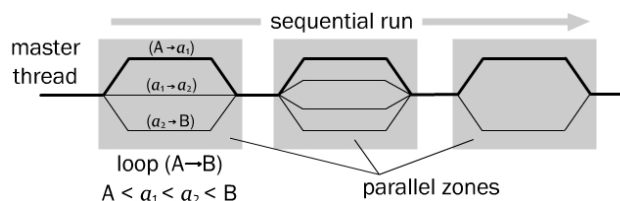


Figure 5.14: Scheme of the OpenMP parallelization, figure from [18].

The COOLfluid framework provides a standard message passing interface, MPI, [69]. It is a communication protocol used for parallel programs running on computer clusters with high costs of accessing the non-local memory. Its assets are the high performance, scalability and portability, thus MPI is suitable for computations on clusters composed of several standalone CPU's. The complete algorithm has been implemented by A. Lani and has not been the subject of this thesis. For further description and implementation details therefore refer to [52, 69].

Chapter 6

Reference Test Cases

As mentioned earlier, previous investigations on the flow around an exhaust valve (as it is the main aim of this thesis) do not provide many data for comparison. Both codes used, section 5.3, have therefore been developed in several successive steps allowing a consecutive control of the correct functionality. The accuracy and the influence of different model formulations have been pursued on several test cases with a reference solution. Some substantial test cases with an increasing complexity are presented in this chapter.

6.1 Inviscid Flow Model

This simplest flow model is described by the Euler equations (3.13), (3.14) and (3.15). This system has no viscous terms (i.e. zero right hand side) and together with the equation of state (3.20) it creates a complete set of equations to be solved. The model does not put any extra demands on the grid fineness near the wall.

6.1.1 Laval Nozzle

A Laval nozzle is a convergent-divergent nozzle that is used for a gas acceleration to a supersonic speed, see its scheme in figure 6.1. The flow-field topology varies according to the ratio of an inlet and an outlet pressure, see the appendix A.

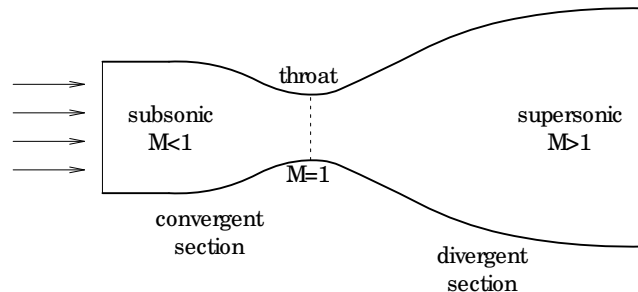


Figure 6.1: The Laval nozzle.

In a design condition the outflow is purely supersonic. For a milder ratio the shock-wave appears in the divergent section or the flow remains entirely subsonic.

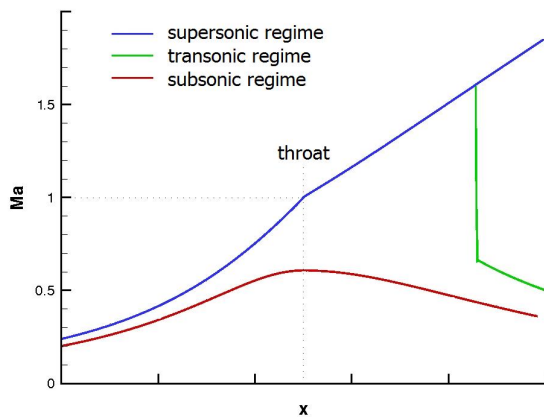


Figure 6.2: The Mach number evolution for typical regimes of the Laval nozzle.

Figure 6.2 shows a usual Mach number evolution along the nozzle axis for each situation. Due to the presence of the shock the transonic regime is convenient for testing the solver accuracy. The differences among the various AUSM schemes, described in the section 5.4, have been studied.

Computation Setup

The results have been acquired by the MUSA code. The pressure ratio has corresponded to an isentropic outlet Mach number $M_{2,i} = 0.5$ as

$$\frac{p_2}{p_0} = \left(1 + \frac{\gamma - 1}{2} M_{2,i}^2\right)^{\frac{\gamma}{1-\gamma}}, \quad (6.1)$$

with p_0 the reservoir and p_2 the outlet pressure. The linear reconstruction with a minmod limiter has been used, together with an explicit time integration.

Results Discussion

Figure 6.3 shows contours of the Mach number for the original AUSM scheme. All the AUSM variants tested converge to a similar solution, with the bigger differences observed on the Mach number distribution along the nozzle axis.

The graph 6.4 compares the results of the AUSM, AUSM+up and AUSM-DV scheme. For the AUSM+up scheme the influence of the choice of the interface speed a_I has been tested. The option A1 corresponds to the choice given by the equation (5.39), A2 to the arithmetic average, eq. (5.37) and A3 to the geometric average, eq. (5.38).

The table 6.1 compares the characteristics of the shock-wave for different schemes, namely the maximal Mach number, the shock-wave position and resolution. The *position* is given by the x -coordinate for which $M=1$. The *resolution* shows the number of grid points required for the shock capturing. Figure 6.5 presents a detailed view on the shocks for different schemes.

AUSM	max M	s-w position	s-w resolution
original	1.3202	0.733267	4
+up	A1	1.2974	0.715247
	A2	1.2898	0.711325
	A3	1.2898	0.711325
D	1.3080	0.733691	5
V	1.2851	0.721183	6
DV	1.2879	0.721501	6

Table 6.1: The Laval nozzle, shock-wave characteristics

Only small differences have appeared in the front part of the convergent section. The subsonic acceleration and later expansion perfectly overlaps for all schemes. The original AUSM scheme predicts the strongest shock, however, it lacks to capture the second local maximum behind the wave. The best performance has been registered for the AUSM+up (A1) scheme, being the only alternative which has computed this extremity. On the other hand, no differences have been found between the choices A2 and A3.

The remaining scheme AUSM-DV has shown an immoderate diffusivity that leads to a smeared shock-wave.

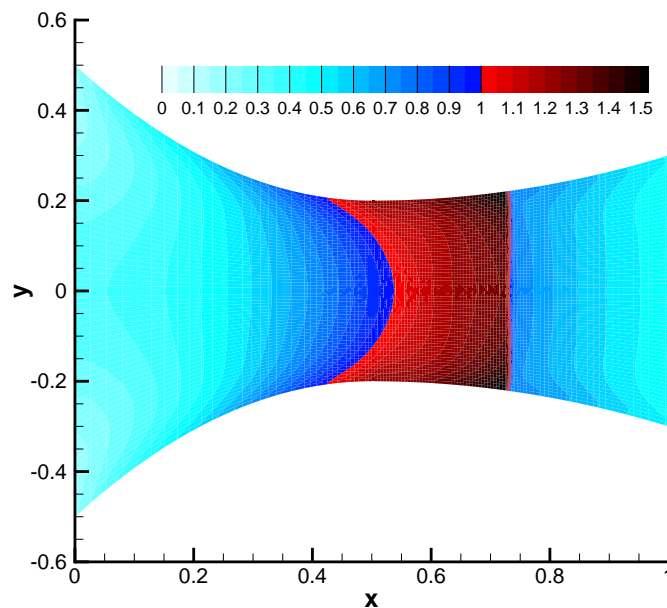


Figure 6.3: Contours of the Mach number in a transonic regime of the Laval nozzle.

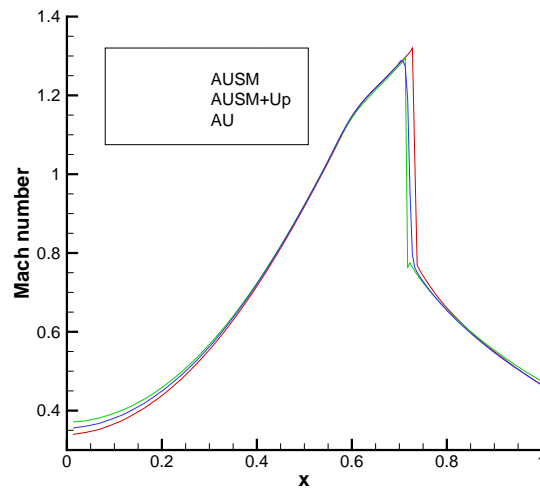


Figure 6.4: The Mach number distribution for different variants of the AUSM scheme.

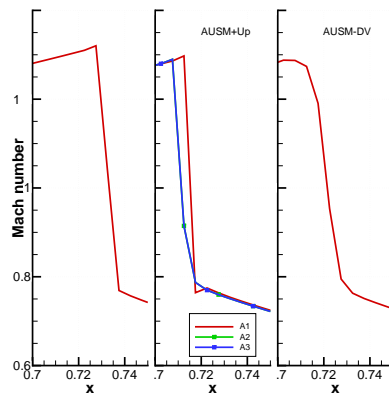


Figure 6.5: The detailed view of the shock-wave resolution for different variants of the AUSM scheme.

6.1.2 Transonic Channel

This test case represents a channel with a circular bump on the lower wall, see figure 6.6.

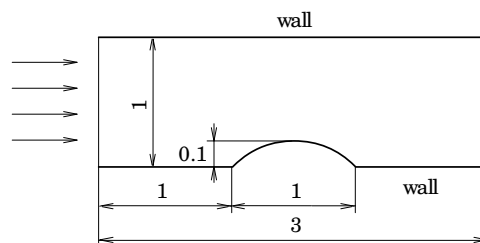


Figure 6.6: The transonic channel.

For a benchmark pressure ratio a supersonic region develops on the bump. The reference solution is then quantified by the flow-field topology and the Mach number profile along the walls; see the reference solution in figure 6.7.

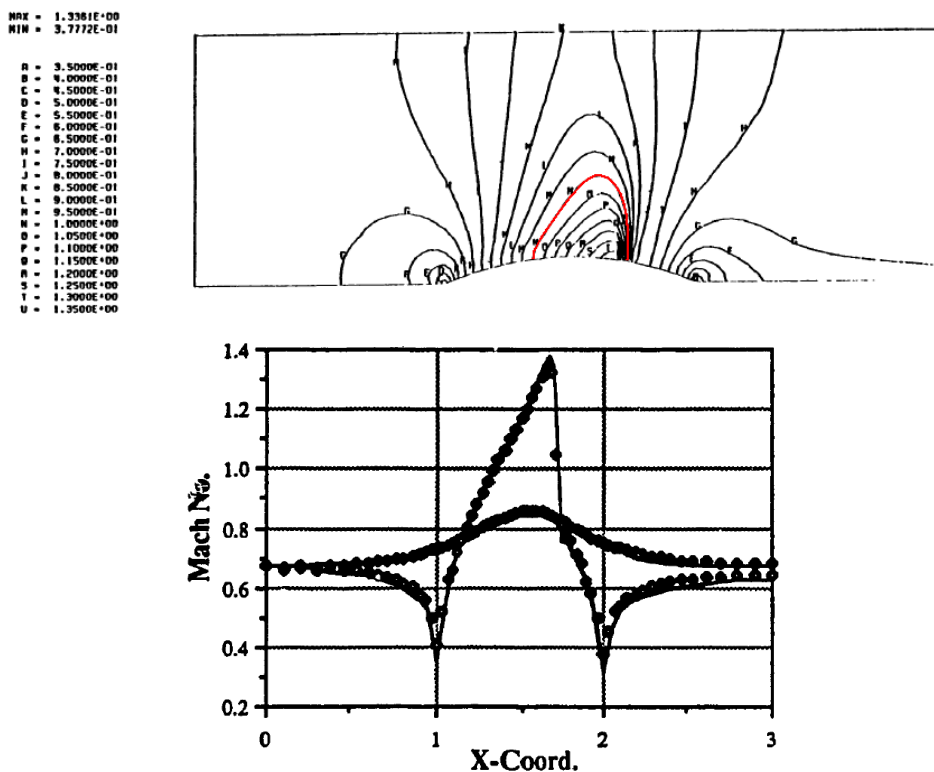


Figure 6.7: The reference solution on the transonic channel. Flow topology with highlighted sonic line (upper), Mach number distribution along lower and upper wall. Figures from [10]

According to the literature (see e.g. [10, 34]) the maximal Mach number on the lower wall should reach $M_{max} \approx 1.36 - 1.38$, with another local maximum appearing behind the shock-wave, the so-called *Zierep* singularity.

Due to the simple geometry, many reference solutions exist also for non-benchmark regimes. Although not explicitly *transonic*, they are also presented within this section.

Computation Setup

The results have been acquired by the MUSA and the COOLfluid codes. As shown in the table 6.2, several pressure ratios have been tested, in order to study the robustness of different schemes, the sensitivity to the grid density and the accuracy of different limiters. The pressure ratio is linked with the isentropic Mach number by the equation (6.1).

	$M_{2,i}$	bump height
deep subsonic	0.020	10%
subsonic	0.200	10%
benchmark	0.675	10%
supersonic	1.400	4%

Table 6.2: Flow regimes for the channel test case

The influence of the grid density has been studied on two grids, noted as coarse and fine, shown in figure 6.8. All the results presented have been obtained by the scheme with a higher order accuracy and a limiter. Depending on the code used the explicit (MUSA) or implicit (COOLfluid) time integration has been used.

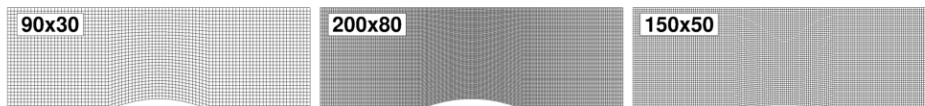


Figure 6.8: Computational grids of channel with 10% bump (coarse and fine) and 4% bump

Bump height	Grid	Size	Elements	Points along bump
10%	coarse	90×30	2 700	30
10%	fine	200×80	16 000	80
4%		150×50	7 500	50

Table 6.3: Description of computational grids

Results Discussion - Benchmark Regime

Figure 6.9 compares the solutions for different numerical schemes. The results have been obtained for the benchmark pressure ratio on fine grid. For this nominal regime, all schemes have converged to a qualitatively identical result which is in an agreement with the reference solution. Minor differences are observed only on the Mach number distributions.

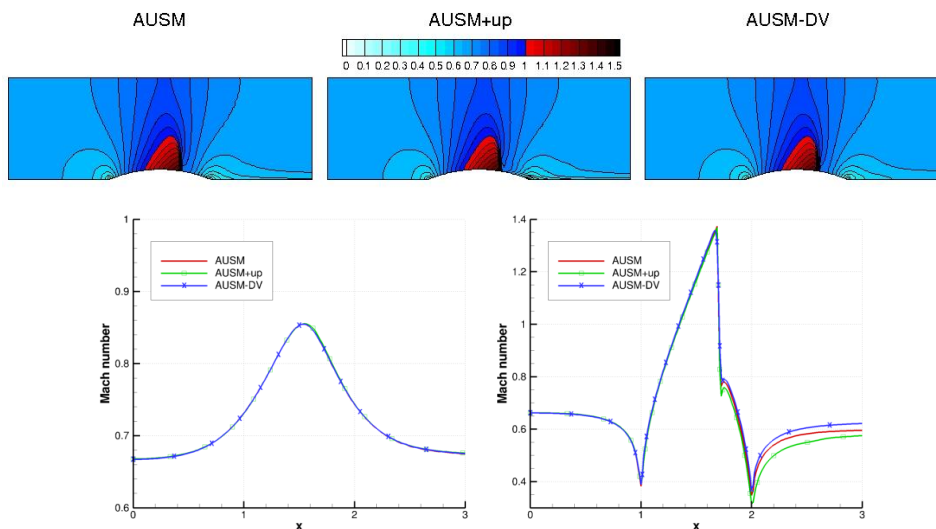


Figure 6.9: Transonic channel, $M_{2,i} = 0.675$, different numerical schemes. Iso-Mach lines (upper), distribution of M along the upper (lower left) and lower (lower right) wall.

A detailed view on the shock-wave structure (figure 6.10) discovers higher accuracy of the AUSM+up scheme, capturing the Zierp singularity even on the coarse mesh. On the other hand the AUSM-DV scheme performs inaccurately in this aspect. This scheme adds excessive numerical dissipation to the regions with steep gradients, leading to the smearing of the shock, similarly to the Laval nozzle test case.

The maximal Mach number for the benchmark regime for all simulations done is summarized in the table 6.4.

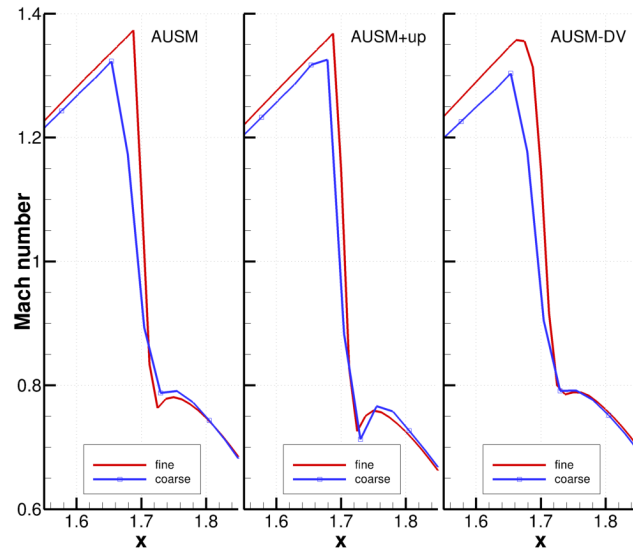


Figure 6.10: Detail of a shock wave, $M_{2,i} = 0.675$, different numerical schemes.

Supersonic Regime

In a supersonic flow, all information propagates only downstream. As mentioned in the section 5.10, it implies a change in the inlet-outlet boundary conditions and it also simplifies the upwind-based numerical schemes (e.g. see the form of splitting polynomials for $|M| > 1$, in section 5.4).

The reference solution [82] has been computed in the channel with 4% bump with the $M_{2,i} = 1.4$. The computational grid (unstructured, 3318 elements) and the solution are shown in figure 6.11.

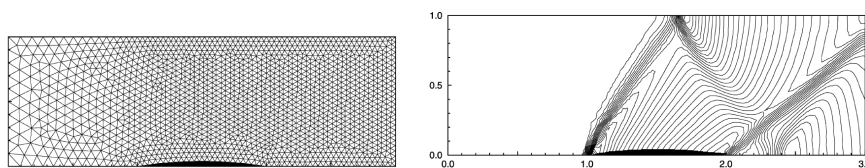


Figure 6.11: Reference grid and solution for $M_{2,i} = 1.40$, contours of the Mach number, figure from [82].

The current numerical codes have been tested on the structured grid with approximately twice more elements, see figure 6.8 right. The solution for different schemes is shown in figure 6.12. The solutions are in excellent agreement with each other and with the reference solution, proving their suitability for supersonic flows.

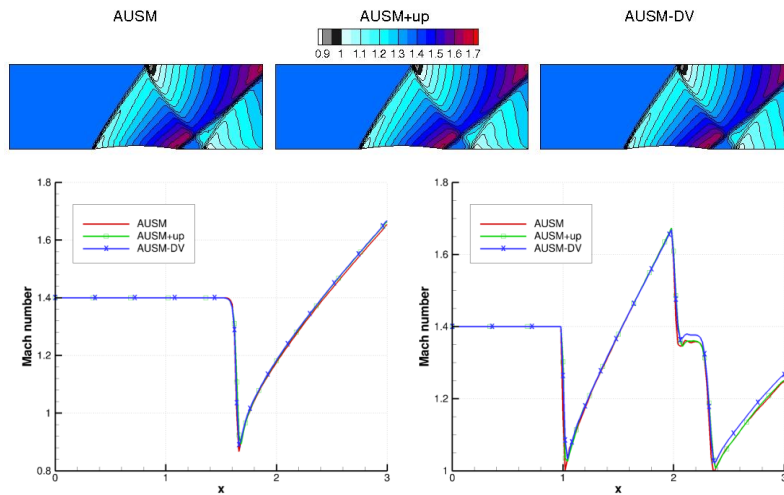


Figure 6.12: Channel with 4% bump, $M_{2,i} = 1.40$, different numerical schemes. Iso-Mach lines (upper), distribution of M along the upper (lower left) and lower (lower right) wall.

Subsonic Regime

In purely subsonic regimes the solution is expected to be symmetric, see the reference solution in figure 6.13, taken from [10].

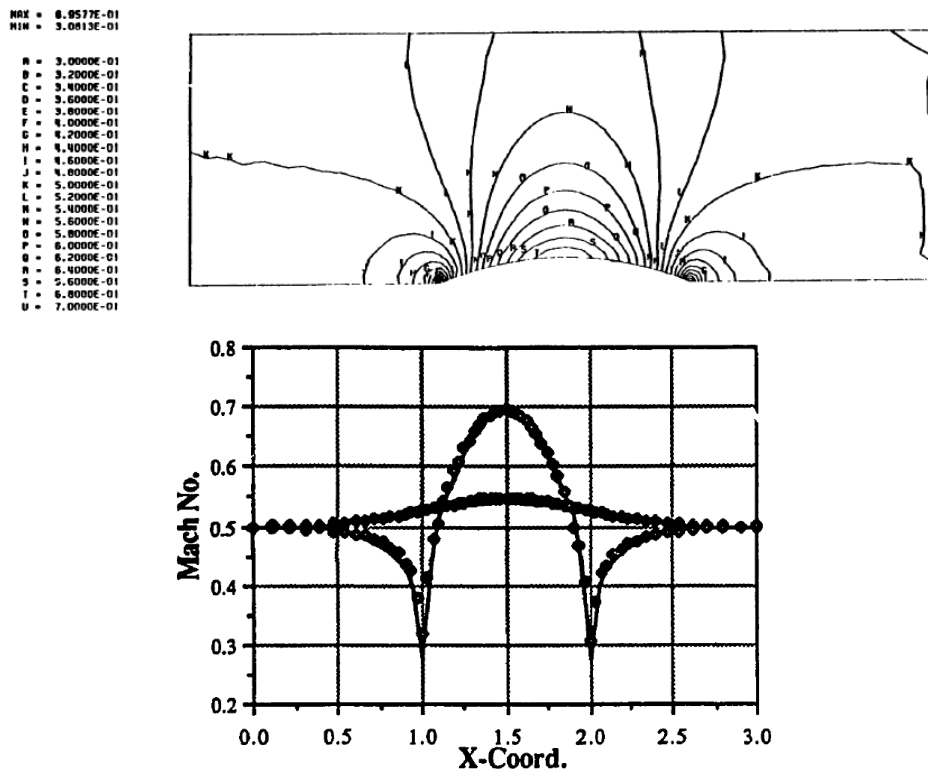


Figure 6.13: The reference subsonic solution on the channel with a circular bump, figure from [10].

However, according to the splitting polynomials (5.18) and (5.20) the convergence properties of the original AUSM scheme deteriorate as $M_\infty \rightarrow 0$. Problems start occurring around the compressibility border, approximately $M_\infty < 0.3$.

Figure 6.14 presents the solution on a channel with 10% bump, at $M_{2,i} = 0.200$ for different AUSM variants. All computations have converged to a nearly symmetric pattern. The AUSM+up scheme has performed the best, with other schemes showing already a visible wake behind the bump.

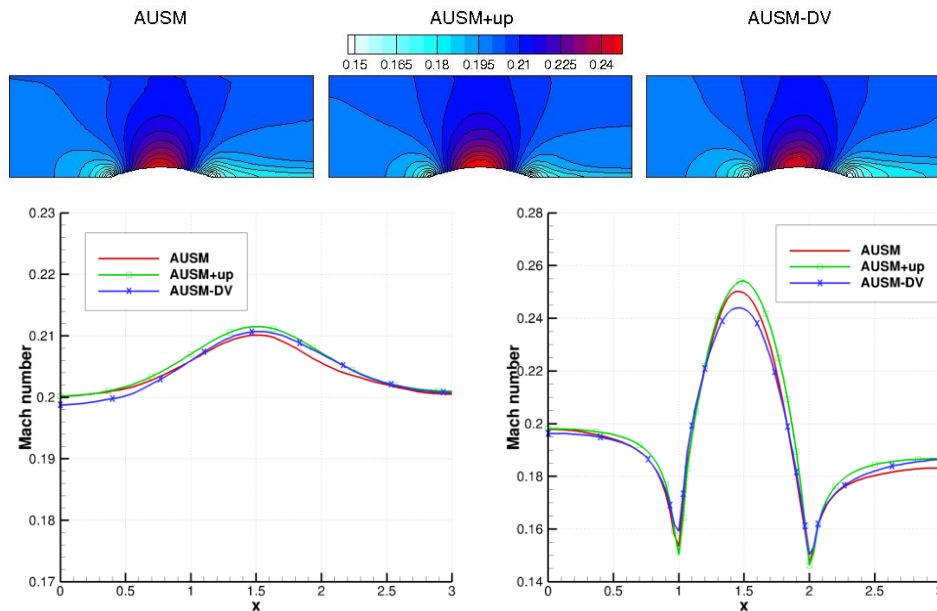


Figure 6.14: Channel with 10% bump, $M_{2,i} = 0.200$, different numerical schemes. Iso-Mach lines (upper), distribution of M along the upper (lower left) and lower (lower right) wall.

The differences are further emphasized for a deep subsonic regime $M_{2,i} = 0.020$ at the same channel. The solution expected is again symmetric, similarly to the reference solution 6.13. The schemes without correction terms for low speed, however, turns into unstable central schemes, as the splitting polynomials of p and M become independent of an actual Mach number. This has been proven by figure 6.15 where the solution for different AUSM schemes is shown. Only the AUSM+up scheme has converged to a reasonable solution, with the rest being inapplicable for the very low speed flows.

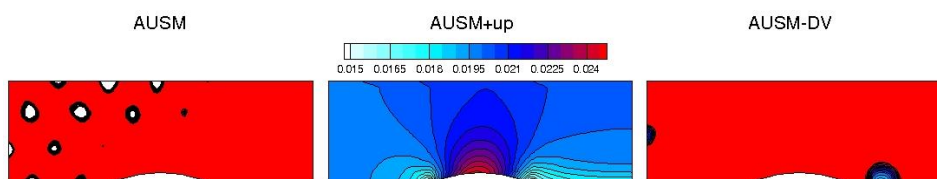


Figure 6.15: Channel with 10% bump, $M_{2,i} = 0.020$, different numerical schemes. Distribution of the Mach number.

Influence of Computational Grid and of Limiter

The accuracy and robustness of different limiters have been tested on a channel with 10% bump at benchmark regime $M_{2,i} = 0.675$. Two different grids have been tested, shown in figure 6.8, described in the table 6.3. Due to previous ascertainments, the AUSM+up scheme has been used for further studies.

As there are only negligible differences in the flow field pattern, the Mach number distribution along the lower wall is only shown for comparison.

The MUSA solver has tested four different limiters, figure 6.16 and COOLFluid has tested two limiters. Note the difference at internal grid handling (structured for MUSA, unstructured for COOLFluid). The accuracy of different limiters is evaluated in the table 6.4.

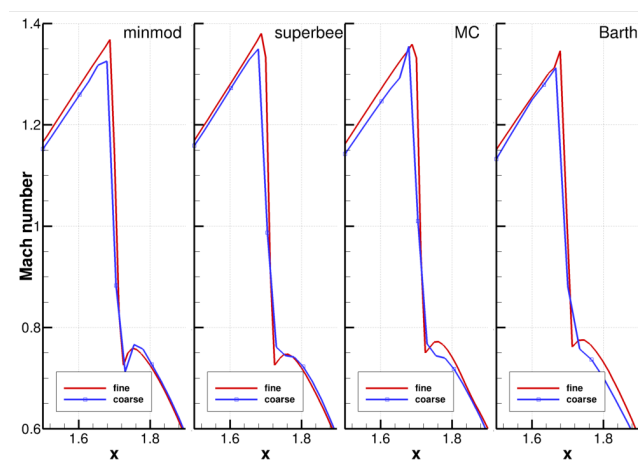


Figure 6.16: Mach number distribution along a lower wall, the MUSA solver, AUSM+up scheme, different limiters.

The *minmod* limiter has shown the best performance, even on the coarse grid. Regarding the maximal Mach number, on the fine grid this limiter has predicted the value expected, $\langle 1.36; 1.38 \rangle$. Other limiters have had difficulties to capture the Zierep singularity on the coarse mesh. The *MC* and *Barth* limiters have also under-estimated the maximal Mach number.

The COOLFluid solver has worked very well on the fine grid. For both limiters tested, the results are in excellent agreement with the reference solution. On the coarse grid they have, however, smeared the shock wave much more than the MUSA solver. Also the resolution of the Zierep singularity is unacceptable (on the coarse grid).

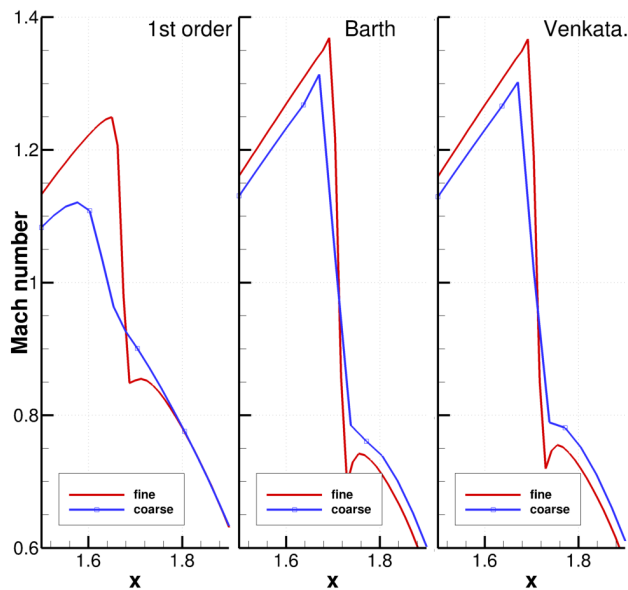


Figure 6.17: Mach number distribution along a lower wall, the COOLFluiD solver, AUSM+up scheme, different limiters.

Solver	Scheme	Limiter	Coarse grid		Fine grid	
			max M	Z. s.	max M	Z. s.
MUSA	AUSM	1 st order	1.1209	5	1.2495	5
	AUSM	minmod	1.3199	3	1.3727	2
	AUSM-DV	minmod	1.3007	4	1.3565	4
	AUSM+up	minmod	1.3255	1	1.3677	1
	AUSM+up	superbee	1.3501	4	1.3807	1
	AUSM+up	MC	1.3587	4	1.3594	1
COOLFluiD	AUSM+up	Barth	1.3128	4	1.3463	2
	AUSM+up	1 st order	1.1211	5	1.2502	5
	AUSM+up	Barth	1.3140	5	1.3673	1
	AUSM+up	Venkata.	1.3024	4	1.3692	1

Table 6.4: Benchmark regime, maximal Mach number, quality of the Zierep singularity capturing (1-excellent, 2-very good, 3-good, 4-inaccurate, 5-inacceptable)

Code Comparison

The results of the numerical codes MUSA and COOLFluiD have been compared to each other for the benchmark, the subsonic and the deep subsonic regimes. The AUSM+up scheme has been used for both codes, with a minmod (MUSA) and a Barth (COOLFluiD) limiter. The results are shown in figures 6.18, 6.19 and 6.20

Small differences have been observed for the deep subsonic regime. In the benchmark and the subsonic regime an excellent agreement has been found. As shown in the table 6.4, the maximal Mach number predicted for the benchmark regime is also nearly identical: 1.3677 (MUSA) and 1.3673 (COOLFluiD).

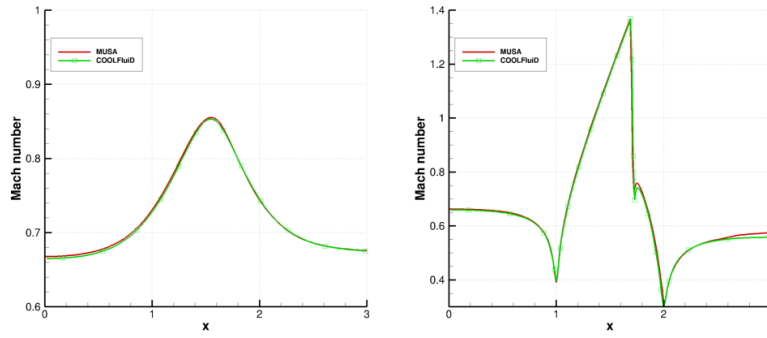


Figure 6.18: $M_{2,i} = 0.675$, Mach number distribution along an upper wall (left) and a lower wall, different numerical codes.

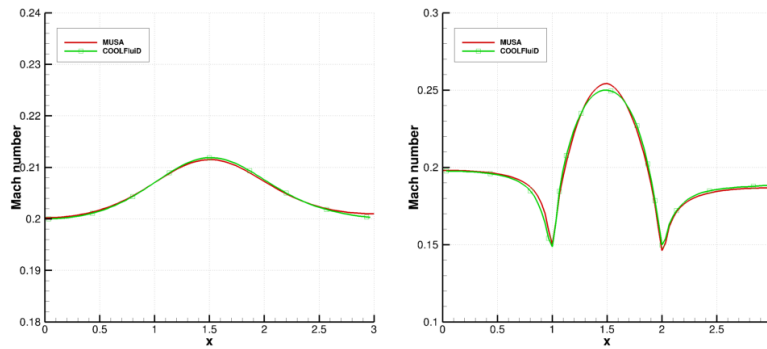


Figure 6.19: $M_{2,i} = 0.200$, Mach number distribution along an upper wall (left) and a lower wall, different numerical codes.

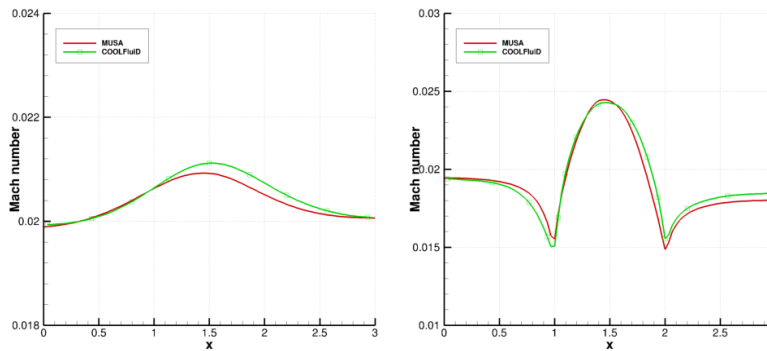


Figure 6.20: $M_{2,i} = 0.020$, Mach number distribution along an upper wall (left) and a lower wall, different numerical codes.

6.1.3 Transonic Channel in 3D

This test case is based on the 2D channel whose contour has been extruded to a third dimension in four different ways:

1. pure extrusion (figure 6.21 a))
2. sweep shift (figure 6.21 b))
3. variable bump height (figure 6.21 c))
4. variable bump length and height (figure 6.21 d))

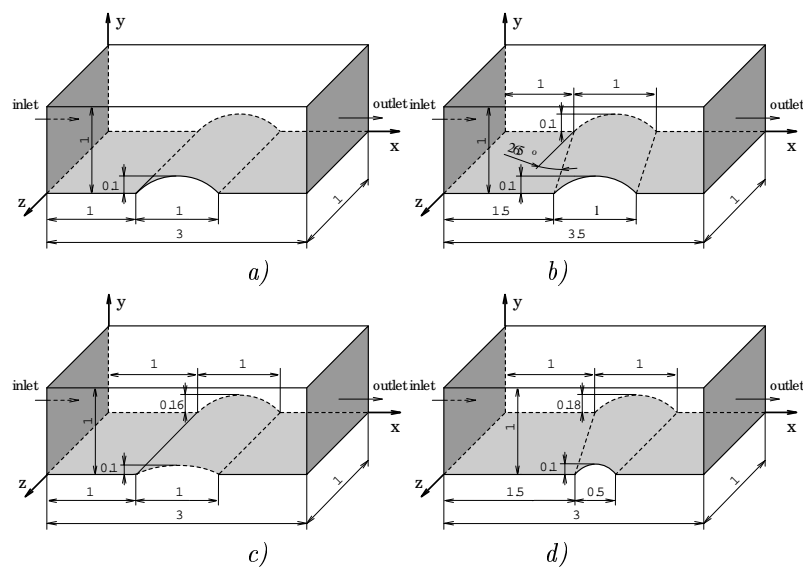


Figure 6.21: Various modifications of a transonic channel in 3D.

Computation Setup

The results have been acquired by the MUSA and the COOLfluid codes and have been compared to a reference solution from [33]. Despite varying geometry the grid topology and regime has been kept constant for all modifications.

	reference	MUSA	COOLfluid
computational grid	180 × 35 × 12		
points along bump	60		
regime	$M_{2,i} = 0.675$		
numerical flux	AUSM	AUSM+up	
limiter	TVD MUSCL	minmod	Barth

Table 6.5: Setup of 3D transonic channel

Results Discussion - Pure Extrusion

The results expected correspond to a 2D reference solution (figure 6.7).

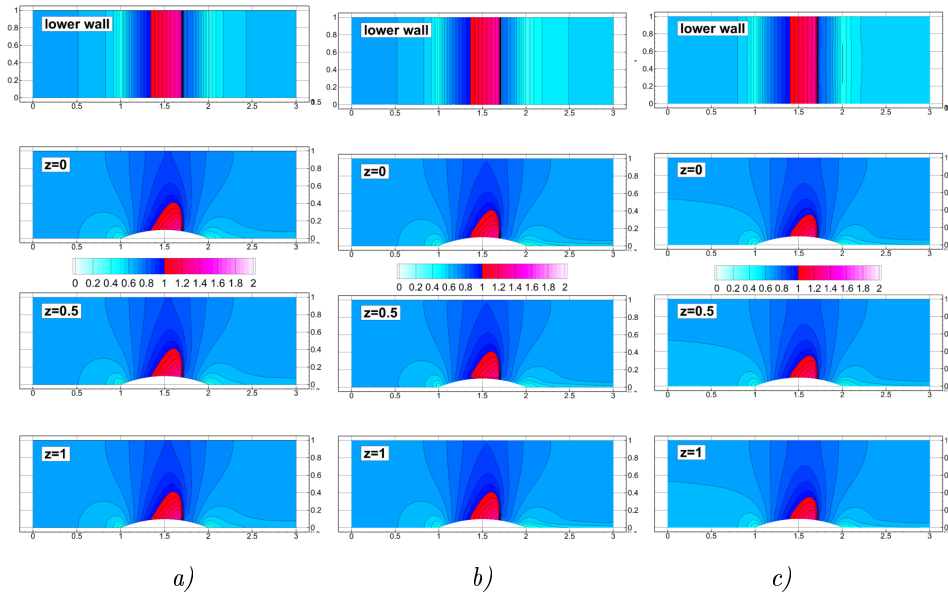


Figure 6.22: Pure extrusion. Contours of the Mach number, different channel planes. *a)* reference solution, *b)* MUSA, *c)* COOLfluid

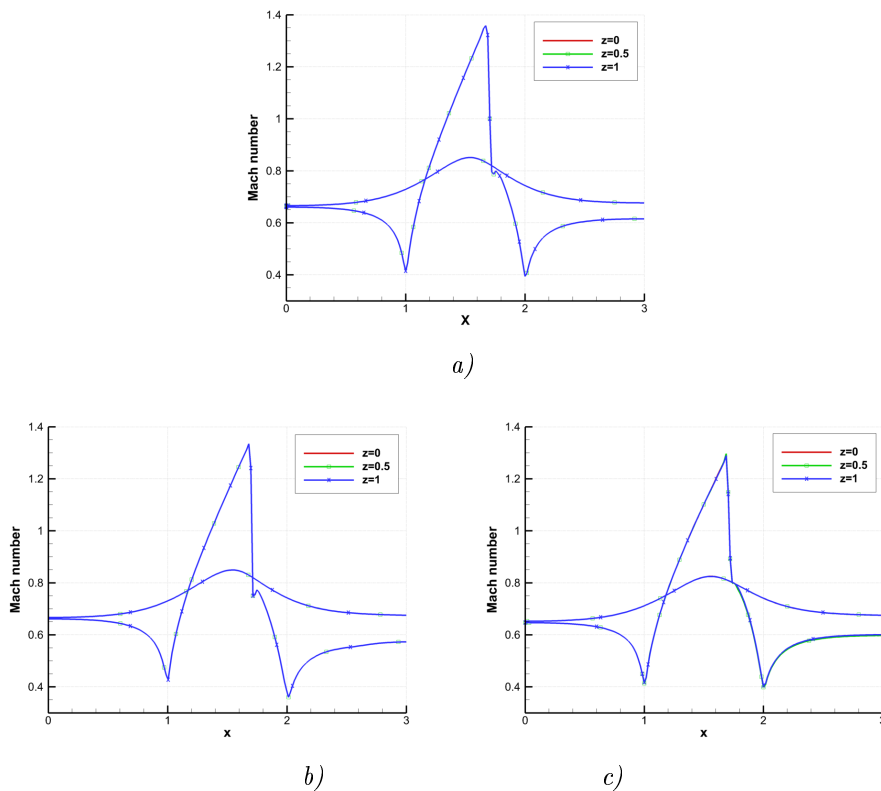


Figure 6.23: Pure extrusion. Mach number distribution along an upper wall and a lower wall, different numerical codes. *a)* reference solution, *b)* MUSA, *c)* COOLfluid

As shown in figure 6.22 all codes used have converged to a quasi-2D solution. The flow field profile in three particular planes ($z=0$, $z=0.5$, $z=1$) perfectly overlaps for each code, which is also demonstrated in the comparison of the Mach number distribution along walls, see figure 6.23.

A numerical dissipation in the transverse direction causes a slightly smaller maximal Mach number on the lower wall than in 2D, see the table 6.6. For the COOLFluid solver, due to the fully spatial reconstruction (the solver handles the computational grid in an unstructured manner, see the section 5.5.2), the maximum has been further lowered. Also the Zierep singularity behind the shock wave has worse resolution, compared to the MUSA solver. Both results are, however, in a good agreement with the reference solution and with each other.

	reference	MUSA	COOLFluid
$z = 0$	1.3587	1.3352	1.2969
$z = 0.5$			
$z = 1$			

Table 6.6: Pure extrusion. Maximal Mach number on the lower wall.

Sweep Shift

At this configuration the circular bump has been extruded and swept with the angle 26.5° . The bump height is constant and the domain has been prolonged by 0.5 length unit. Figure 6.24 compares the flow field and figure 6.25 the Mach number distribution along walls for different codes.

According to the table 6.7, the COOLFluid solver predicts lower maximum of the Mach number on the lower wall. A very good agreement is, however, found in the planar cut $z=0.5$. The differences in the cuts $z=0$ and $z=1$ can be affected by the numerical realization of the boundary condition.

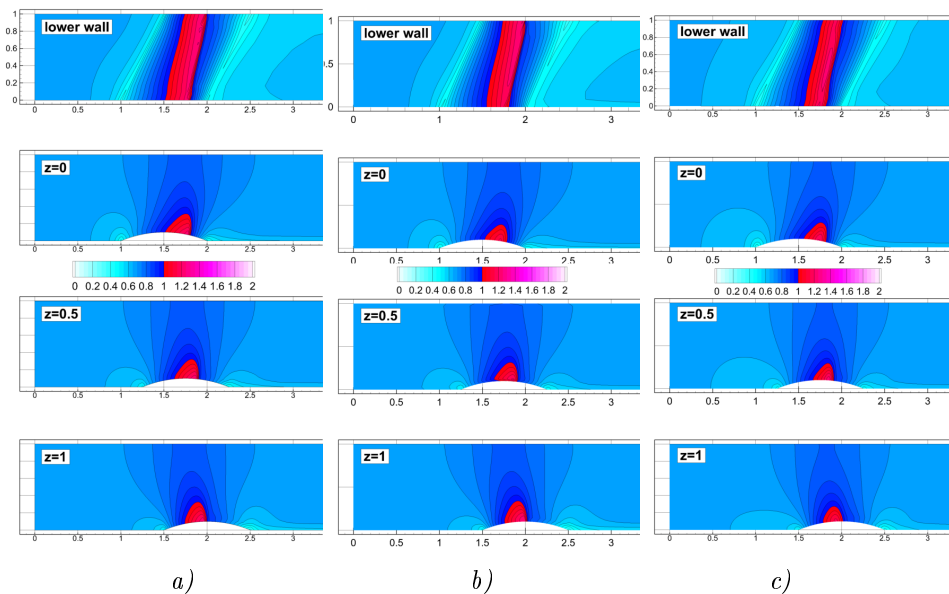


Figure 6.24: Sweep shift. Contours of the Mach number, different channel planes. *a)* reference solution, *b)* MUSA, *c)* COOLFluid

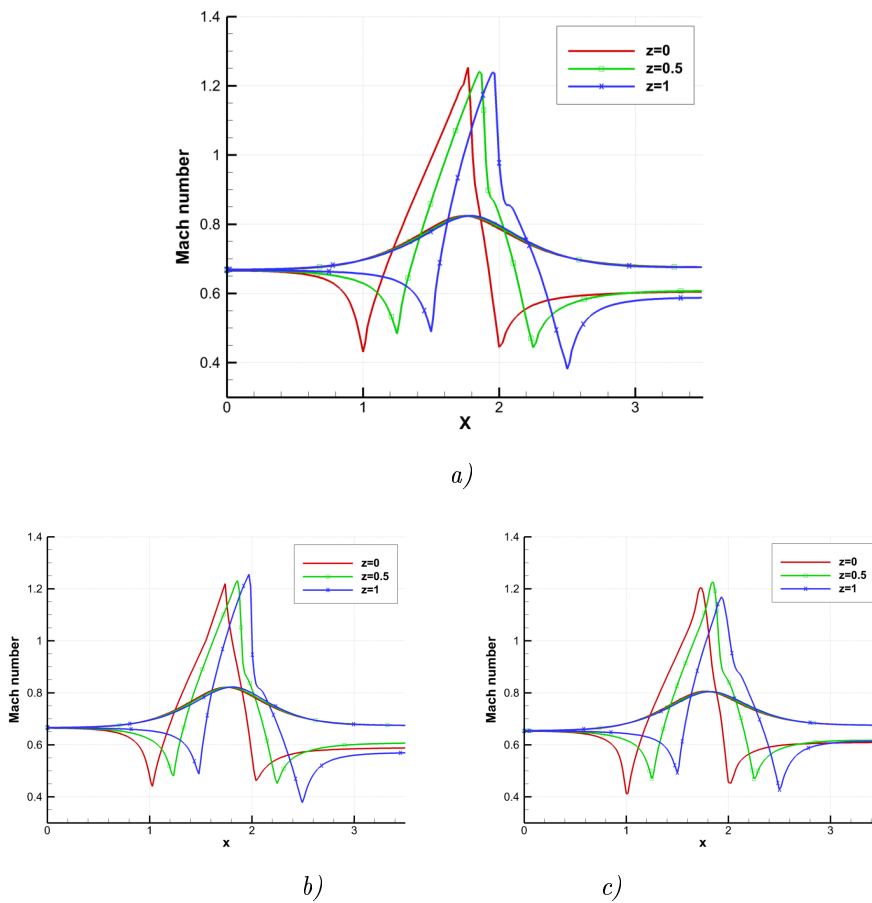


Figure 6.25: Sweep shift. Mach number distribution along an upper wall and a lower wall, different numerical codes. *a)* reference solution, *b)* MUSA, *c)* COOLFluiD

	reference	MUSA	COOLFluiD
$z = 0$	1.2533	1.2564	1.2038
$z = 0.5$	1.2409	1.2249	1.2237
$z = 1$	1.2388	1.2142	1.1693

Table 6.7: Sweep shift. Maximal Mach number on the lower wall.

Variable Bump Height

The height of the circular bump varies from 16% ($z=0$) to 10% ($z=1$) of the channel height. Figure 6.26 compares the flow field and figure 6.27 the Mach number distribution along walls for different codes.

Although the channel profile at $z=1$ corresponds to a benchmark geometry the flow field is affected by the higher bump section, leading to a stronger shock wave and a larger supersonic region, compared to the 2D solution 6.9. The MUSA solver has provided a solution that is in excellent agreement with the referential one and has even better resolution of the Zierep singularity at $z=1$. The solution by the COOLFluiD shows again lower maximums of the Mach number.

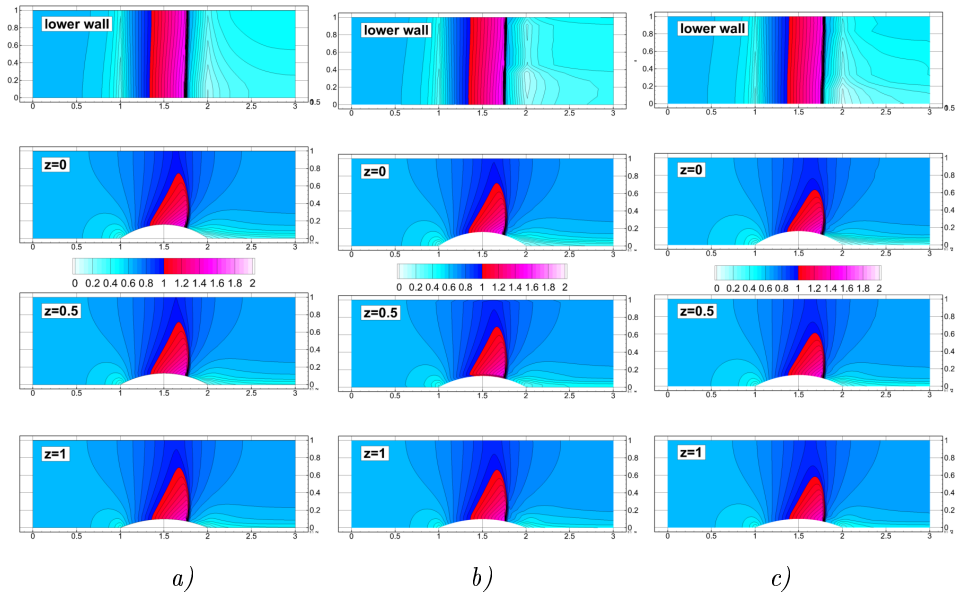


Figure 6.26: Variable bump height. Contours of the Mach number, different channel planes. *a)* reference solution, *b)* MUSA, *c)* COOLfluid

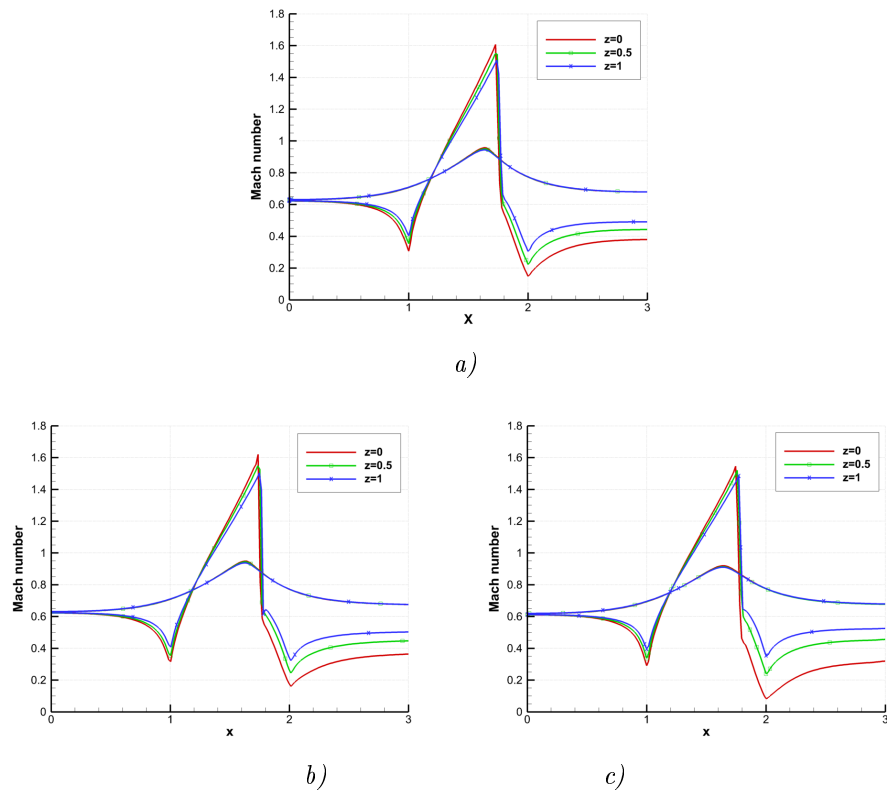


Figure 6.27: Variable bump height. Mach number distribution along an upper wall and a lower wall, different numerical codes. *a)* reference solution, *b)* MUSA, *c)* COOLfluid

	reference	MUSA	COOLfluid
$z = 0$	1.6072	1.6202	1.5460
$z = 0.5$	1.5488	1.5494	1.5204
$z = 1$	1.5099	1.5054	1.4837

Table 6.8: Variable bump height. Maximal Mach number on the lower wall.

Variable Bump Length and Height

The bump shape at this configuration mimics an airplane wing. The bump curvature at $z=1$ is very high which leads to a flow instabilities. Figure 6.28 compares the flow field and figure 6.29 the Mach number distribution along walls for different codes.

The supersonic regions correspond very well to the reference solution and to each other. The distinct differences have only appeared at a plane $z=1$. According to the Mach number distribution each code predicts a completely different wake. The conformity of both codes used on this test case is, however, very satisfying.

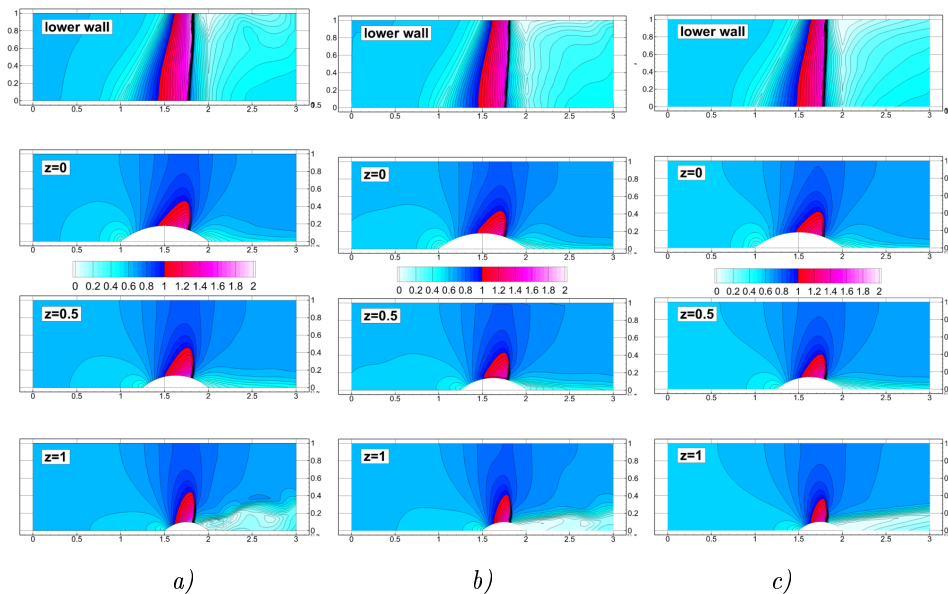


Figure 6.28: Variable bump length and height. Contours of the Mach number, different channel planes. *a)* reference solution, *b)* MUSA, *c)* COOLfluid

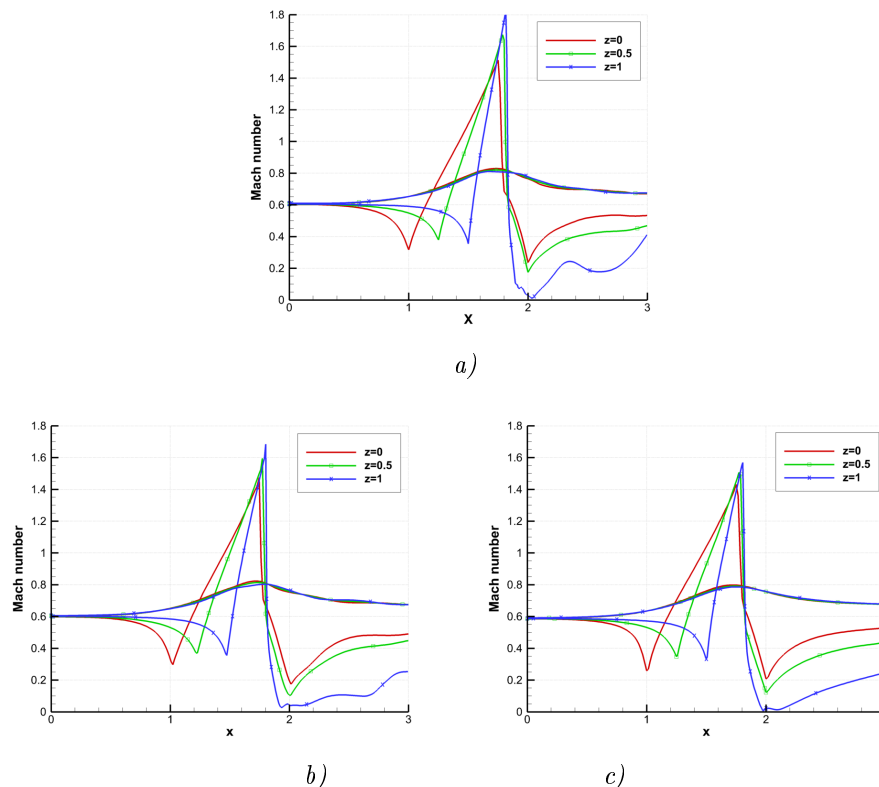


Figure 6.29: Variable bump length and height. Mach number distribution along an upper wall and a lower wall, different numerical codes. *a)* reference solution, *b)* MUSA, *c)* COOLFluid

	reference	MUSA	COOLFluid
$z = 0$	1.5141	1.4733	1.4314
$z = 0.5$	1.6745	1.5952	1.5065
$z = 1$	1.8295	1.6839	1.5694

Table 6.9: Variable bump length and height. Maximal Mach number on the lower wall.

6.2 Laminar Flow Model

This model is described by the Navier-Stokes equations (3.9)-(3.11). A well-posed system of equations is assembled when the equation of state and a relation for a dynamic viscosity (typically the Sutherland's law, eq. (3.22)) are plugged.

Due to the molecular viscosity, the velocity on a (non-moving) wall is equal to zero and fluid next to a boundary is subjected to large shear. The velocity w_1 accelerates to a freestream value w_∞ along a so-called laminar boundary layer profile. This profile is defined with a boundary layer thickness $\delta(x_1)$ for which

$$w_1(x_2) = 0.99 \cdot w_\infty. \quad (6.2)$$

According to [22] the laminar boundary layer growth can be derived as

$$\delta(x_1) = 4.91 \sqrt{\frac{\mu \cdot x_1}{\rho \cdot w_\infty}}, \quad (6.3)$$

as indicated in figure 6.30.

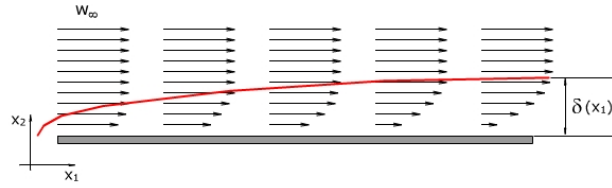


Figure 6.30: The laminar boundary layer scheme.

For a thin boundary layer at steady state the laminar boundary layer equations have been firstly derived by H. Blasius (also demonstrated at [22]), leading to a so-called *Blasius* laminar velocity profile.

$x_2 \sqrt{w_\infty / \nu x_1}$	0.0	1.0	2.0	3.0	4.0	5.0	6.0	7.0
w_1 / w_∞	0.0000	0.3298	0.6298	0.8460	0.9555	0.9915	0.9990	0.9999

Table 6.10: Blasius laminar velocity profile

For such velocity profile the wall shear stress coefficient c_f is expressed as

$$c_f = \frac{\tau_w}{\frac{1}{2} \rho w_\infty^2} = \frac{0.664}{\sqrt{\text{Re}_x}}, \quad (6.4)$$

with the shear stress and the length Reynolds number given by

$$\tau_w = \mu \left. \frac{\partial w_1}{\partial x_2} \right|_{x_2=0} \quad \text{and} \quad \text{Re}_x = \frac{\rho w_\infty x_1}{\mu}. \quad (6.5)$$

The laminar boundary layer growth (6.3) can then be recovered as

$$\delta(x_1) \approx 4.91 \frac{x_1}{\sqrt{\text{Re}_x}}. \quad (6.6)$$

6.2.1 Flat Plate

The basic test case is a boundary layer attached to a flat plate which is held in an oncoming unidirectional flow.

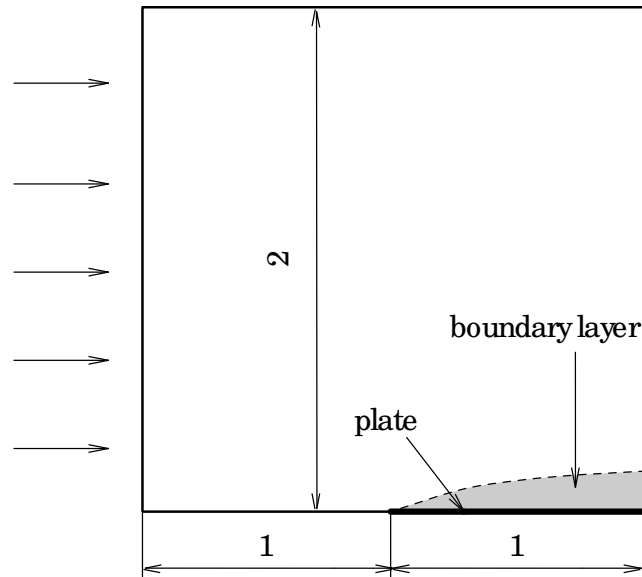


Figure 6.31: The flat plate.

In figure 6.31 the computational domain is shown. In order to overcome the issues with the boundary conditions in the corner (as explained in the section 5.6.3) the domain contains a buffer zone in front of the plate. The height of the domain has been set to a double plate length so to avoid an interference from the upper boundary.

Computation Setup

The boundary condition on the plate has been realized by an adiabatic no-slip condition, the buffer and the upper wall by the mirror condition and the subsonic inlet and outlet on the respective remaining boundaries. The freestream parameters of the working medium have been set to $w_\infty = 70 \text{ m/s}$, $T_0 = 273.15 \text{ K}$, $\text{Re} = 2 \cdot 10^5$, based on the plate length ($L=1$). The results have been acquired by the MUSA and the COOLFluid codes and have been compared to a theoretical Blasius solution.

Results Discussion

Regarding the velocity profile, both codes have shown an excellent agreement with the theoretical Blasius profile, as shown in figure 6.32 a). Some differences are visible from the skin friction distribution along the plate. As shown in figure 6.32 b) both codes overestimate the skin friction near the leading edge and underestimate near the trailing edge. The overall differences are, however, very small, as shown in the table 6.11.

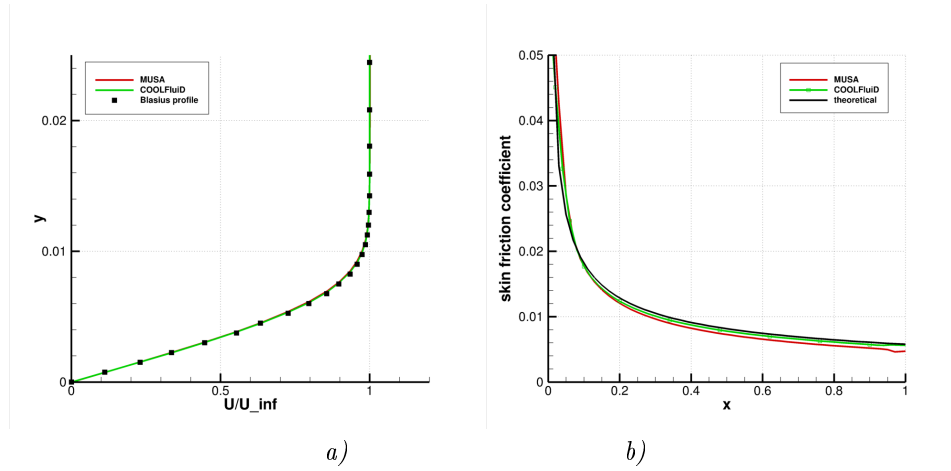


Figure 6.32: The laminar flow over a flat plate, code comparison. *a)* velocity profile, *b)* distribution of the skin friction coefficient.

x_2 [m]	$\Delta \frac{w}{w_\infty}$ [%]		x_1 [m]	Δc_f [%]	
	MUSA vs. Blasius	COOLFluid vs. Blasius		MUSA vs. theory	COOLFluid vs. theory
0.0025	-0.46	0.21	0.25	-7.48	-3.92
0.0050	-1.49	-0.66	0.50	-10.95	-4.53
0.0075	-0.97	-0.29	0.75	-13.46	-5.09

Table 6.11: Comparison of numerical results against theoretical profiles.

6.2.2 Oscillating Airfoil

An impulse to solve this test case has been given by the study [46] (parametric study of an oscillating airfoil). This work provides results of unsteady computations on a (relatively) simple geometry. The oscillating airfoil under investigation is a symmetrical profile of NACA 0015. This is an airfoil with maximum thickness 15% of its chord whose contour is described by the analytical expression (taken from [3])

$$y = \pm \frac{t}{0.2} c \left(0.2969 \cdot \sqrt{\frac{x}{c}} - 0.1260 \cdot \frac{x}{c} - 0.3516 \cdot \left(\frac{x}{c}\right)^2 + 0.2843 \cdot \left(\frac{x}{c}\right)^3 - 0.1015 \cdot \left(\frac{x}{c}\right)^4 \right), \quad (6.7)$$

where c is the chord length, t is the maximum thickness and $x \in \langle 0; c \rangle$.

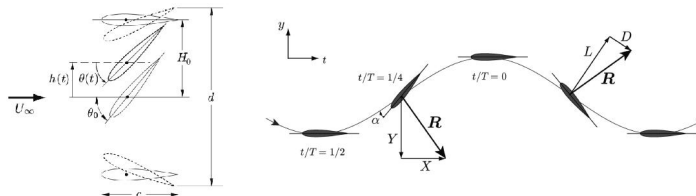


Figure 6.33: Scheme of imposed heaving and pitching motions. Evolution in time (figure from [46]).

According to [46], a flapping wing is an airfoil experiencing simultaneous pitching $\theta(t)$ and heaving $h(t)$ motion, as shown in figure 6.33. Restricting to a pitching axis located on the chord

line at $x_p = \frac{c}{3}$ from the leading edge, the airfoil motion is expressed as

$$\theta(t) = \theta_0 \sin(\gamma t), \quad (6.8)$$

$$h(t) = H_0 \sin(\gamma t + \phi), \quad (6.9)$$

with θ_0 and H_0 the pitching and heaving amplitudes, $\gamma = 2\pi f$ the angular frequency and ϕ the phase difference between the two motions. Later, the adimensional frequency of oscillation (of a period T) has been defined as

$$f^* = \frac{f \cdot c}{U_\infty}, \quad (6.10)$$

$$f = \frac{1}{T}. \quad (6.11)$$

Computation Setup

The computations have been performed only by the COOLFluid solver (the MUSA solver does not contain methods for solving unsteady simulation on moving mesh) using the arbitrary Lagrangian-Eulerian formulation and the dual time-stepping technique.

In figure 6.34 the computational grid is shown. The size of the grid has been $75 \times 70 \cdot c$ and this mesh has consisted of 45 456 triangles (214 points on the profile). Concerning the mesh movement, the grid has been splitted into three zones:

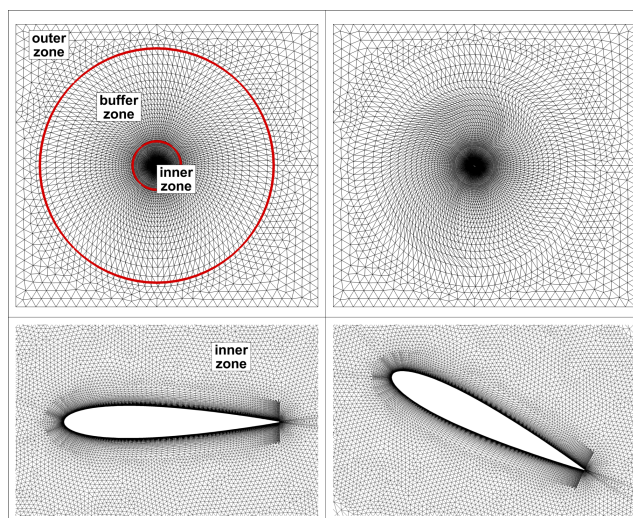


Figure 6.34: The computational grid for an oscillating airfoil. Left: initial state, right: deformed state.

1. inner zone - cells located closer than $8 \cdot c$ from the pitching axis. All cells follow the movement imposed as a rigid body.
2. outer zone - cells located further than $30 \cdot c$ from the pitching axis (at $t = 0$) with no deformation allowed.
3. buffer zone - intermediate zone, accomodating both the pitching and heaving motions of the inner zone.

Due to large airfoil displacements, this strategy has been implemented so as to avoid a degenerative grid quality near the airfoil within several cycles.

According to [46], the flow regime has been defined by the freestream values $M_{in} = 0.3$, $T_{in} = 300$ K, $\alpha = 0^\circ$ and $Re = 1100$. For these parameters, three oscillation regimes have been computed (see the table 6.12).

Regime	θ_0	H_0/c	f^*	ϕ
R1	76.33°	1	0.14	90.0°
R2	60.0°	1	0.18	90.0°
R3	60.0°	1	0.06	90.0°

Table 6.12: Oscillation regimes.

Results Discussion

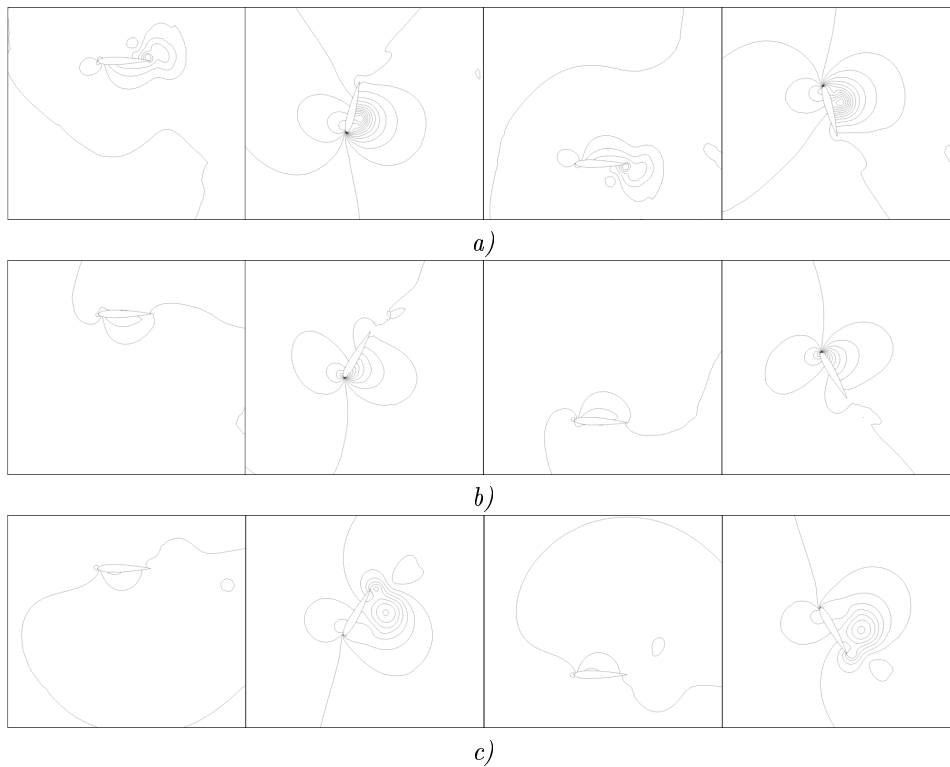


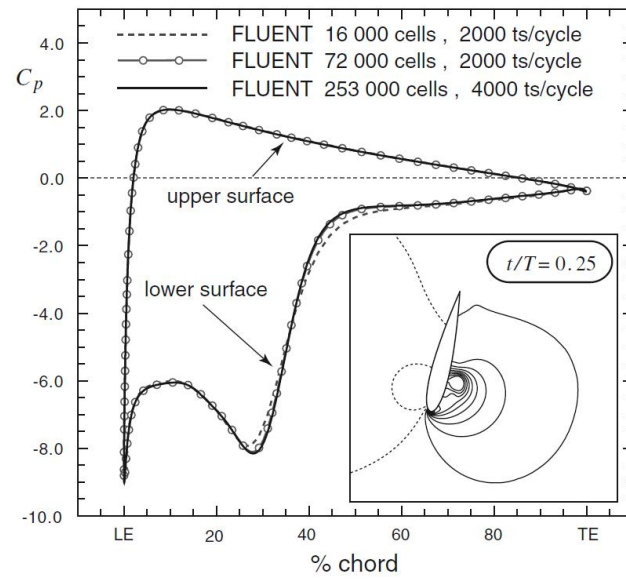
Figure 6.35: Contours of the pressure coefficient ($\Delta c_P = 0.05$) for different regimes: a) R1, b) R2, c) R3. Solution in time $t/T = 0; 0.25; 0.50; 0.75$.

Figure 6.35 shows the results for the regimes R1, R2 and R3. The snapshots have been taken each quarter period and the contours represent the pressure coefficient c_P , where

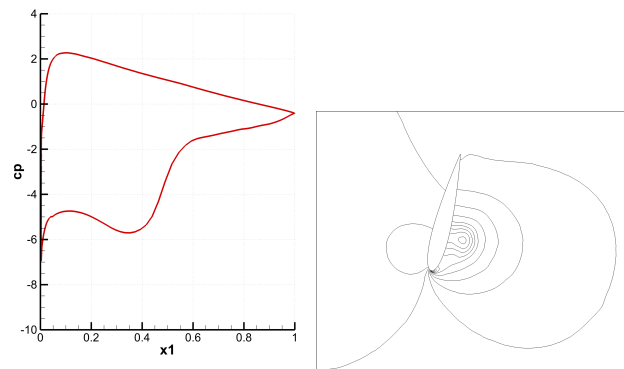
$$c_P = \frac{p - p_\infty}{\frac{1}{2}\rho_\infty w_\infty^2}. \quad (6.12)$$

All the solutions have shown a nearly symmetric behaviour over one period. For the regime R1, the referential paper [46] allows the comparison of pressure coefficient at $t/T = 0.25$ (shown in figure 6.36) and the overall development of the horizontal and vertical force coefficient (shown in figure 6.37).

Regarding the pressure coefficient, the pattern on the lower surface has advanced further along the profile, thus the c_P distribution evinces milder peaks. Similar differences can be found also in the forces distribution. Nevertheless, both result show a good qualitative agreement.



a)



b)

Figure 6.36: Pressure coefficient distribution ($\Delta C_p = 0.05$) a) ref. solution (figure from [46]), b) solution by COOLfluid. Regime R1, solution time $t/T = 0.25$.

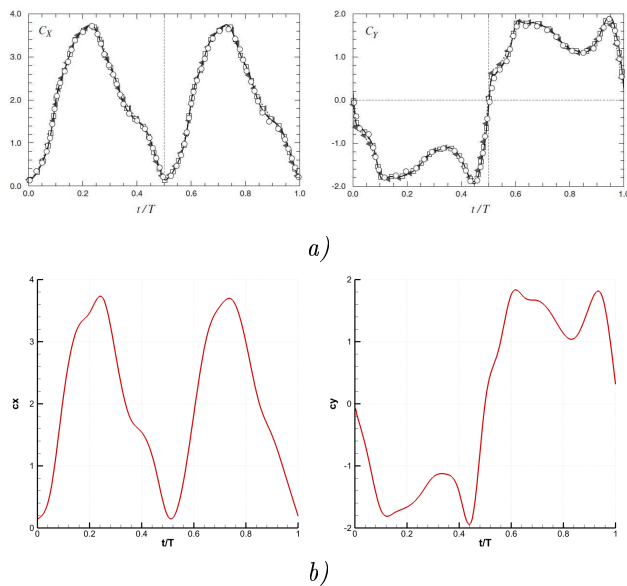


Figure 6.37: Forces coefficients over a periodic cycle, regime R1, *a)* ref. solution (figure from [46]), *b)* solution by COOLFluiD.

	Solver	Cells	Time steps /cycle	c_x [-]	c_y [-]	Δc_x [%]	Δc_y [%]
R1	ad. [46]	253 000	4000	2.019	1.942		
	COOLFluiD	45 456	2000	1.946	1.855	-3.62	-4.48
R2	ad. [46]	253 000	4000	0.692	1.256		
	COOLFluiD	45 456	2000	0.673	1.209	-2.69	-3.70
R3	ad. [46]	253 000	4000	1.257	2.032		
	COOLFluiD	45 456	2000	1.189	1.932	-5.37	-4.94

Table 6.13: Comparison with the referential data.

The table 6.13 compares the mean horizontal force coefficients c_x and peak vertical force coefficient c_y with the values computed in [46]. Upon the computations performed a satisfying agreement has been found, confirming the abilities of the COOLFluiD solver to resolve accurately unsteady problems with moving grids.

6.3 Turbulent Flow Model

The general governing equations are described in the section 4.3. Due to the unbalanced number of unknowns and equations the classical set of conservation laws and constitutive relations (as for the laminar model) is completed by transport equations for various turbulent variables, as described in chapter 4.

The target of the thesis deals mainly with turbulent flow, therefore several reference test cases have been examined for the sake of code verification. It has been mentioned in section 5.3 that the COOLFluiD code uses a wider range of turbulence models. Moreover, thanks to the implicit time integration method it obtains the solution in shorter time and acts in a more stable manner. Therefore all turbulent computations presented beneath have been acquired by the COOLFluiD code, unless indicated otherwise.

Apart from the different mechanisms of momentum and energy transport, the differences be-

tween the turbulent and the laminar flow model can be clearly observed inside the boundary layer. Compared to the laminar boundary layer (BL, described in the section 6.2), the turbulent BL grows with $x_1^{4/5}$ compared to $x_1^{1/2}$ for the laminar BL. Its thickness is defined as

$$\delta(x_1) \approx 0.382 \frac{x_1}{\sqrt[5]{\text{Re}_x}}, \quad (6.13)$$

and also has a different structure, see [94]. By means of an adimensional velocity w_1^+ and an adimensional wall distance x_2^+ three different regions inside the turbulent boundary layer can be distinguished:

1. the laminar sublayer, $x_2^+ < 5$, where $w_1^+ = x_2^+$, i.e. linear behaviour;
2. the turbulent (logarithmic) layer, $x_2^+ > 30$, where $w_1^+ = \frac{1}{\kappa} \ln x_2^+ + B$;
3. the buffer layer, which creates a smooth transition between layers 1 and 2.

The von Kármán constant is $\kappa = 0.41$ and $B = 5.1$.

The adimensional velocity (often called u^+) is defined as

$$\begin{aligned} w_1^+ &\equiv \frac{w_1}{w_*}, \\ w_* &= \sqrt{\frac{\tau_w}{\rho}}, \end{aligned} \quad (6.14)$$

with w_1 the local velocity and w_* the friction velocity. The wall shear stress τ_w is defined by equation (6.5). The adimensional wall distance (often called y^+) is defined as

$$x_2^+ \equiv \frac{w_* x_2}{\nu}, \quad (6.15)$$

with x_2 the distance to the nearest wall and ν the kinematic viscosity. The typical adimensional velocity profile can be seen in figure 6.38.

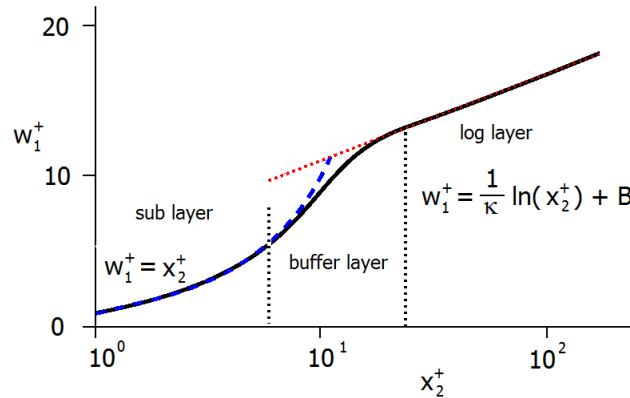


Figure 6.38: Different regions of the turbulent boundary layer.

According to theory (e.g. [94, 103]) a defect layer can be found further from the wall. The velocity profile of the defect layer is defined as

$$\begin{aligned} w_1^+ &= \frac{1}{\kappa} (\ln x_2^+ + 3\eta^2 - 2\eta^3) + B, \\ \eta &= \frac{x_2}{\delta}, \end{aligned} \quad (6.16)$$

where η is the length scale and δ the momentum thickness of the BL. For the turbulent boundary layer, the analytical skin friction coefficient has been derived (e.g. see [103])

$$c_f = \frac{0.0592}{\sqrt[5]{\text{Re}_x}}.$$

6.3.1 Flat Plate

This is again the basic test case to validate the models implemented. The geometry and general setup of the case remains the same as for the laminar flow, see figure 6.31.

Experiments have confirmed that after a certain length of flow a laminar boundary layer turns unstable and becomes turbulent. Although this transition can be modeled nowadays, it significantly increases both the model complexity and the CPU demands. Hence, a fully developed turbulent flow is assumed, for which only a set of RANS equations is used.

Computation Setup

The boundary condition on the plate has been realized by an adiabatic no-slip condition, the buffer and the upper wall boundaries by the mirror condition and the subsonic inlet and outlet on the respective remaining boundaries. The freestream parameters of the working medium have been set to $M_\infty = 0.35$, $T_0 = 273.15 \text{ K}$, $\text{Re} = 7 \cdot 10^7$. The freestream turbulent variables have been acquired from the equations (4.123), (4.125) and (4.127), using the main flow values.

Results Discussion

Figure 6.39 compares the velocity profiles for different turbulence models. All models used fit perfectly in the laminar sublayer, with minor differences in the logarithmic and defect layers. The biggest deflection from the theoretical curves has been observed for the Spalart-Allmaras model, whereas the best agreement has been found for the EARSM model. Only small differences could be found among other models.

Concerning the skin friction coefficient (figure 6.40) most models underestimate the friction in the frontal part of the plate. Due to large pressure gradients at the leading edge a finer grid spacing can improve the agreement. However, at the rear part of the plate all models converge to the value expected. The best fit at the rear part has been found for the S-A model, the overall best performance can possibly be awarded again to the EARSM model.

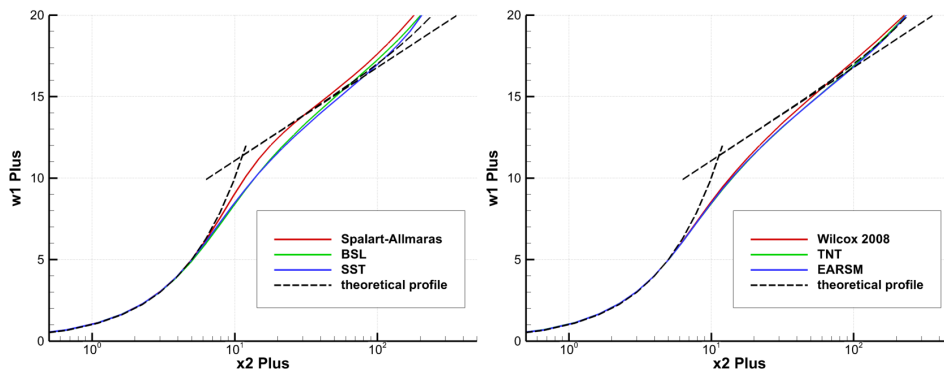


Figure 6.39: Adimensional velocity profile. Comparison of different turbulent models with a theoretical profile.

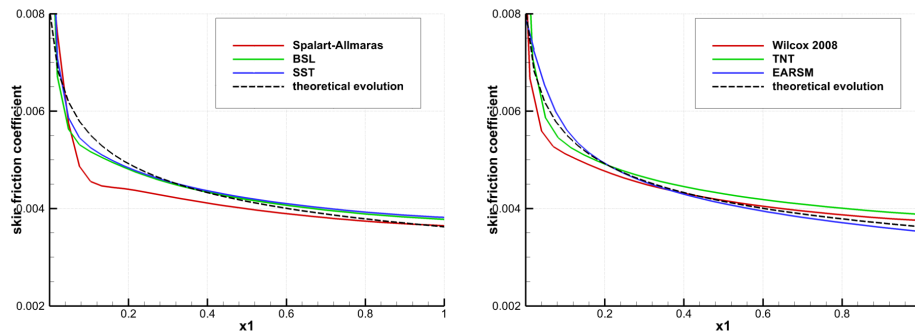


Figure 6.40: Distribution of the skin friction coefficient. Comparison of different turbulent models with a theoretical curve.

6.3.2 Airfoil Profiles

Similarly to the flat plate test case, the purpose here is to provide a validation case for turbulence models. Unlike verification, which seeks to establish that a model has been implemented correctly, validation compares CFD results against data in an effort to establish a model's ability to reproduce physics.

Two widely spread airfoils have been tested in particular: NACA 0012 and RAE 2822. If possible, the results are compared to the data from experiments.

NACA 0012 - Computation Setup

This is a symmetrical airfoil with maximum thickness 12% of its chord. The contour is again given by the analytical expression (6.7). The computational grid has consisted of hybrid triangles, containing $\approx 30\,000$ elements with a profile resolved by 175 points. The size of the domain has been 40×40 chord. Along the airfoil a thin layer of structured triangles has been built, see figure 6.41.

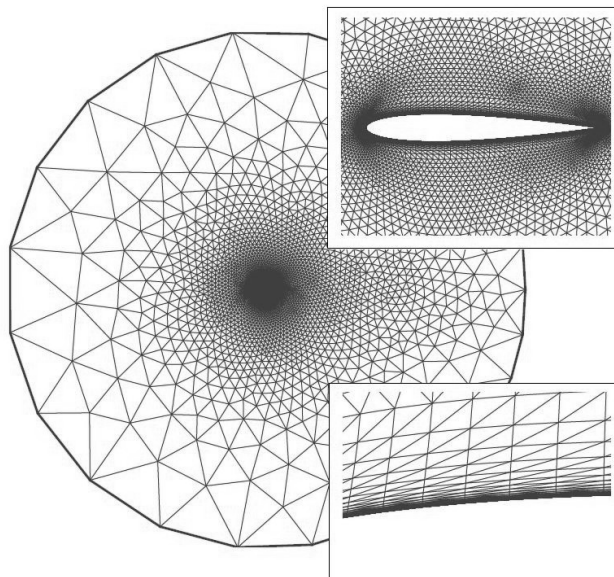


Figure 6.41: The computational grid of the NACA 0012. Details of the grid around the profile (upper) and detail of structured triangular grid (lower).

According to the reference [3], the turbulent NACA 0012 profile should be run at essentially incompressible conditions. Hence, the inflow conditions have been defined by $M_{in} = 0.15$, $T = 288.15\text{ K}$, $\text{Re} = 1.5 \cdot 10^6$ and the angle of incidence $\alpha = 0^\circ$. At this regime, the boundary layers should be fully turbulent over most of the airfoil. The inflow conditions for the turbulence variables have been set by equations (4.125) and (4.127).

The boundary condition on the profile has been realized by an adiabatic no-slip condition, with the rest being treated as a far-field (see the section 5.10).

NACA 0012 - Results Discussion

At the regime given, the solution to expect is smooth and symmetrical. Figures 6.42 and 6.43 show the contours of the pressure coefficient c_P and isolines of velocity. All the turbulence models tested have achieved an identical pattern of the flow field. The only difference can be observed in the wake behind the profile, but in general a very good agreement has been found.

Furthermore, the distribution of c_P has been compared with the experimental data (obtained from [3]) in figure 6.44. Regarding the incidence angle $\alpha = 0^\circ$ (i.e. symmetrical regime) the contours of c_P from lower and upper side perfectly coincide into a single curve. For each turbulence model the distribution of the pressure coefficient matches very well the experimental values.

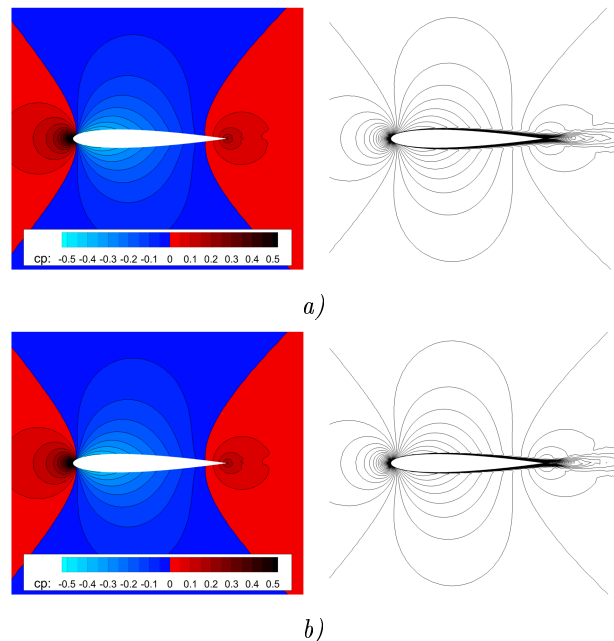


Figure 6.42: Contours of pressure coefficient (left) and isolines of velocity (right). Different turbulence model: *a)* BSL, *b)* SST.

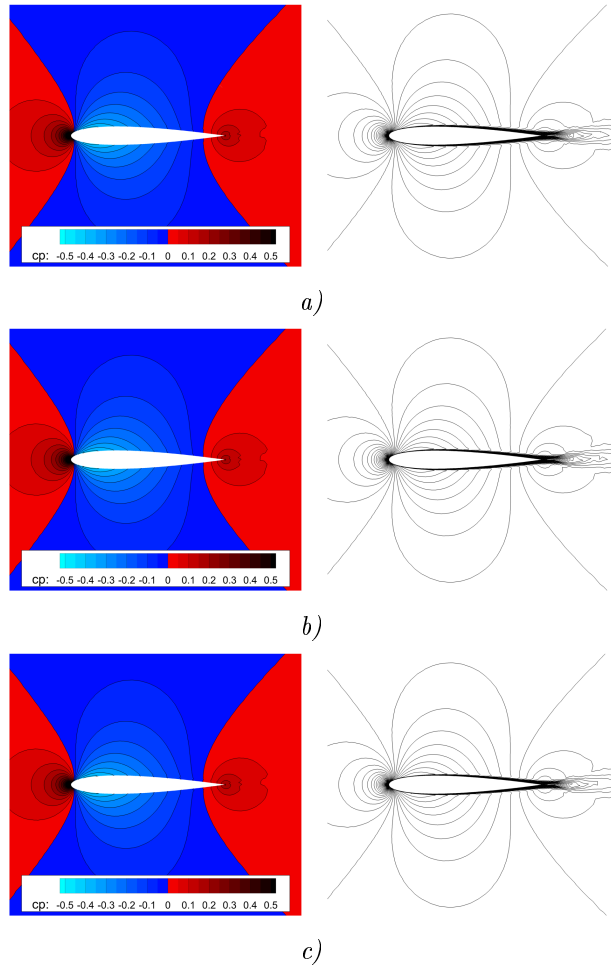


Figure 6.43: Contours of pressure coefficient (left) and isolines of velocity (right). Different turbulence model: a) Wilcox, b) TNT, c) EARSM.

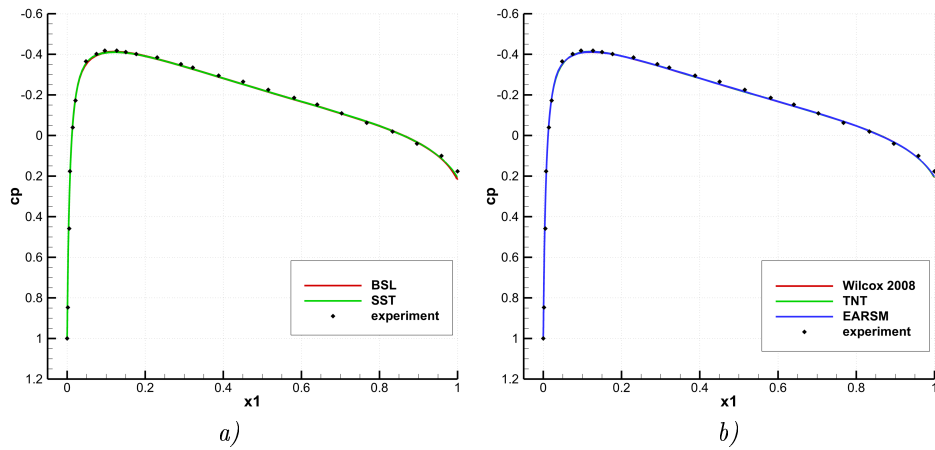


Figure 6.44: Distribution of the pressure coefficient along the profile for different turbulence models.

RAE 2822 - Computation Setup

The second airfoil tested has been a supercritical profile RAE 2822. The coordinates of this profile are defined pointwise (see e.g. [4]), in figure 6.45 the contour is shown. The table 6.14 presents the two flow regimes tested.

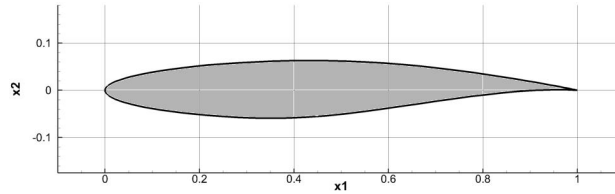


Figure 6.45: The profile RAE 2822.

freestream conditions	M_{in}	T_{in}	Re	α
subsonic	0.604	288.15	$6.0 \cdot 10^6$	2.12°
transonic	0.734	288.15	$6.5 \cdot 10^6$	2.79°

Table 6.14: Freestream regimes.

The results obtained have been compared with the experimental data from [19].

The size of the computational domain has been again 40×40 chord. The computational grid consisted of hybrid triangles, containing $\approx 16\,000$ elements with a profile resolved by 150 points. The grid structure can be seen in figure 6.46.

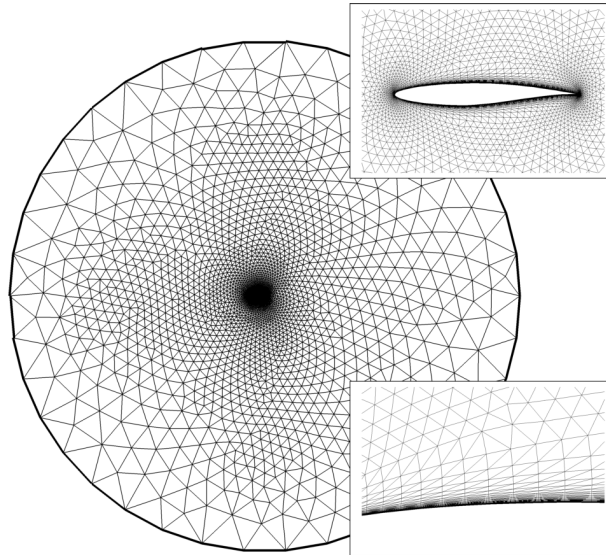


Figure 6.46: The computational grid of the RAE 2822. Details of the grid around the profile (upper) and detail of structured triangular grid (lower).

RAE 2822 - Results Discussion

In figure 6.47 the contours of the pressure coefficient c_P and the Mach number for the subsonic regime is shown. Similarly to the NACA 0012 test case the subsonic regime results in a smooth

solution with no shock-waves. Note that, due to the asymmetrical shape and non-zero angle of incidence the flow is not symmetric any longer.

For all the turbulence models tested the numerical results are in good agreement with each other and with the experimental data. The graph 6.48 compares the distribution of the pressure coefficient along the profile. The biggest differences can be found near the leading edge, however, they all fit into an acceptable range.

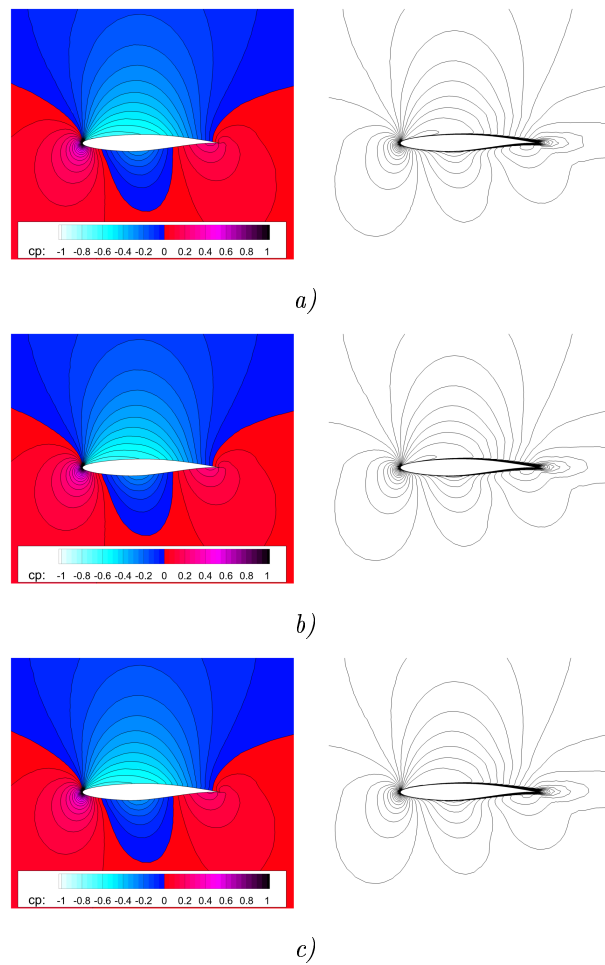


Figure 6.47: Contours of pressure coefficient (left) and isolines of the Mach number (right) for a subsonic regime. Different turbulence model: a) BSL, b) Wilcox, c) EARSM.

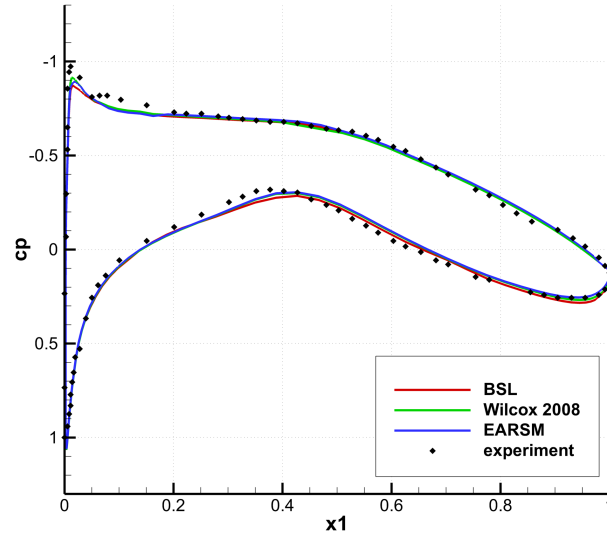


Figure 6.48: Distribution of the pressure coefficient for a subsonic regime. Different turbulence models.

For the transonic regime a shock-wave appears on the upper side of the profile. The position of the wave has been observed, with respect to the turbulence model used. Figures 6.49 and 6.50 present the flow-field contours, respectively the comparison with the experiments. The main flow characteristics have been captured reliably. Some differences against the experiment have occurred near the leading edge and on the c_P magnitude near the shock-wave. Its position has been, however, determined well by all models. The closest agreement has been observed for the EARSM model.

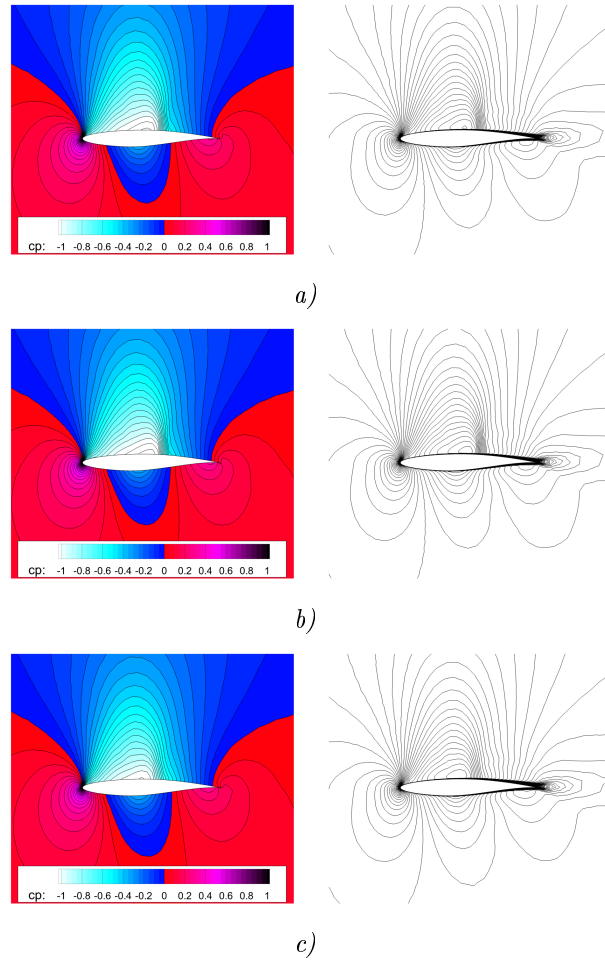


Figure 6.49: Contours of pressure coefficient (left) and isolines of the Mach number (right) for a transonic regime. Different turbulence model: *a)* BSL, *b)* Wilcox, *c)* EARSM.

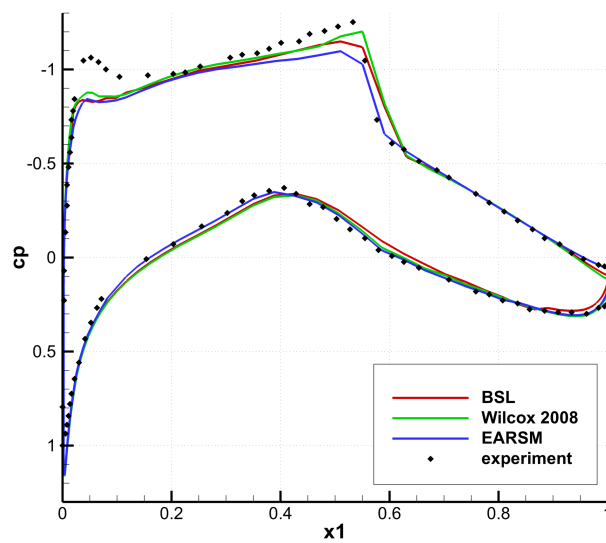


Figure 6.50: Distribution of the pressure coefficient for a transonic regime. Different turbulence models.

The differences observed have been caused by the large grid spacing in a chordwise direction. As distinct from the common practice of refining meshes at steep gradient zones (typically: different regime requires different grid) the grid with a single spacing has been used for both regimes. Regarding the results obtained for this single grid approach, the COOLfluid solver gains very good agreement for shock-free flows and is sufficiently accurate also for the cases involving shocks (despite very few cells across a shock-wave). Considering the target geometry (the exhaust valve) with no obvious shock-wave positioning such a robust tool has been demanded.

Figure 6.51 plots the history of convergence for the regimes and models tested. Although the results obtained by the BSL model evince the biggest errors (still being reasonably accurate though) it usually requires the smallest number of iterations (shortest time) to converge. For the more complicated transonic regime the BSL model claims a quarter-iteration need from other models, nominating itself as an ideal solution initializer for more advanced turbulence models.

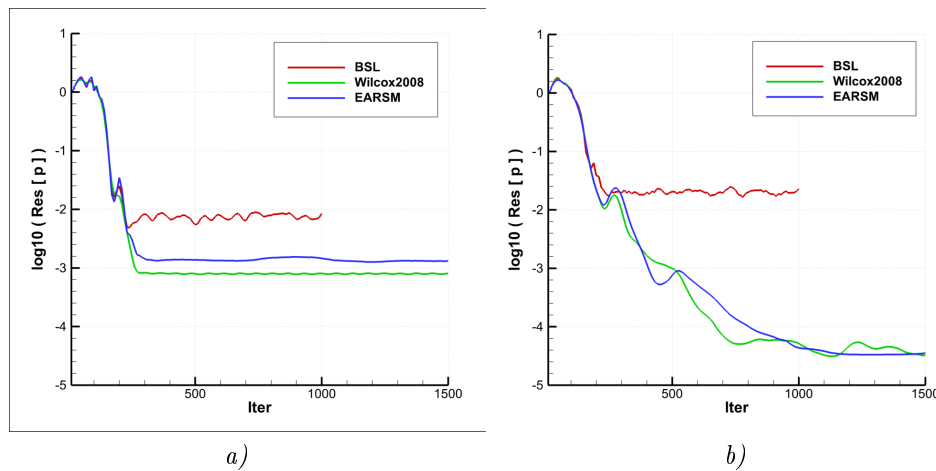


Figure 6.51: Convergence plot for different turbulence models. *a)* subsonic regime, *b)* transonic regime.

6.3.3 Deléry Channel

This test case deals with the shock/boundary layer interaction and has been experimentally realized by J. Deléry, [25]. The goal is again to assess the behaviour of the turbulence models implemented.

Computation Setup

The geometry of the channel is shown in figure 6.52. The flow conditions have been defined by the inlet Mach number $M_{in} = 0,615$, the total inlet pressure $p_{t,in} = 96 \text{ kPa}$, the temperature $T_{in} = 300 \text{ K}$ and the Reynolds number $Re = 10,96 \cdot 10^6$. The computational grid is shown in figure 6.53.

The geometry of the channel is nozzle-like. The convergent part of the channel allows the flow to accelerate to supersonic. The widening behind the throat then induces a separation of the boundary layer, forming a lambda shock structure (see the experimental result in figure 6.54).

In the experiments a second throat has been placed downstream to adjust the position of the shock. For the numerical computations the outlet pressure has been tuned to fit the correct location of the shock. The influence of the outlet pressure is shown in figure 6.55. The final value has been set to $p_{out} = 61.5 \text{ kPa}$.

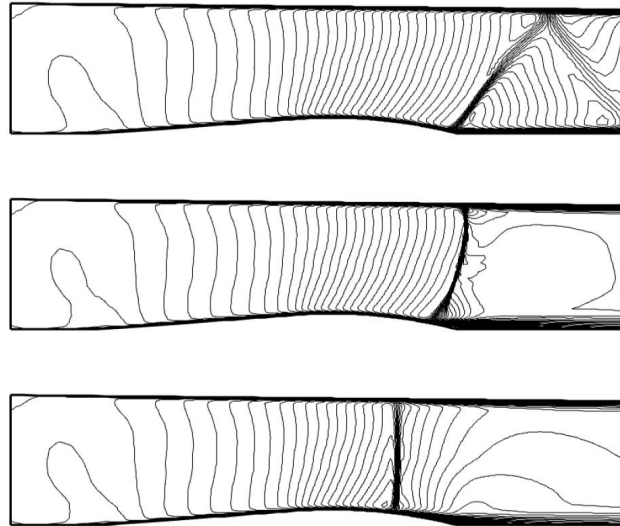


Figure 6.55: Isolines of the Mach number. Different outlet pressure $p_{out} = \{40; 60; 65\}$ kPa (top to bottom)

Results Discussion

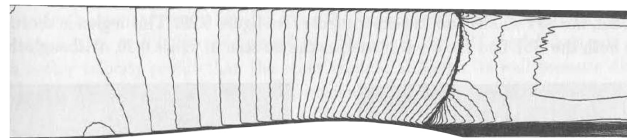


Figure 6.56: Deléry channel, isolines of the Mach number ($\Delta M = 0.025$). Solution from [95]

For the sake of comparison figure 6.56 shows isolines of the Mach number of the numerical solution from [95]. The result has been obtained with the solver THOR, using the BSL turbulence model (see the reference for more details).

Next figures 6.57 and 6.58 show the results of COOLFluiD which have been obtained by different turbulence models. Apart of isolines of the Mach number, the contours of density have been plotted in the area of the lambda shock.

The BSL model predicts the weakest lambda shock. The flowfield, however, corresponds well to the solution in figure 6.56, that has been computed with a different solver but the same turbulence model. Other models have shown a much stronger shock. The closer agreement can be found between SST and EARSM models and between Wilcox and TNT models. Those of the second group model the position of the boundary layer separation slightly further downstream.

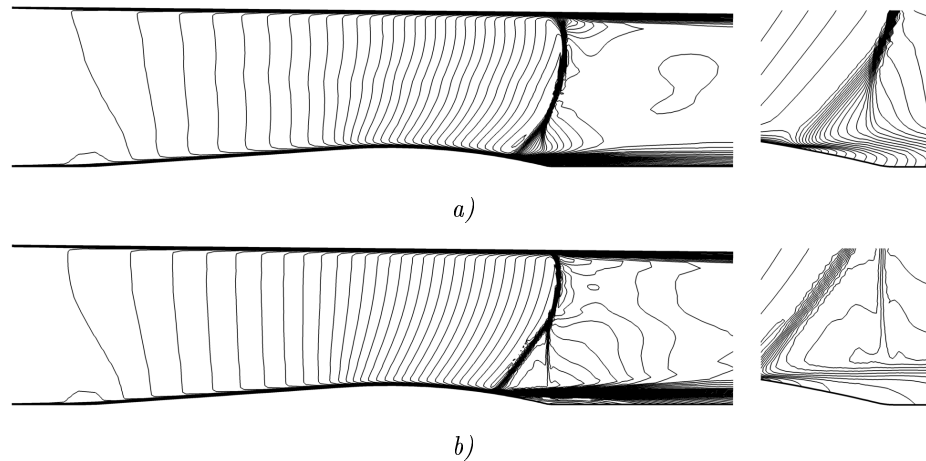


Figure 6.57: Comparison of different turbulence models: *a)* BSL, *b)* SST. Whole channel - isolines of the Mach number ($\Delta M = 0.025$). Detail of the lambda shock - isolines of density ($\Delta \rho = 0.015$).

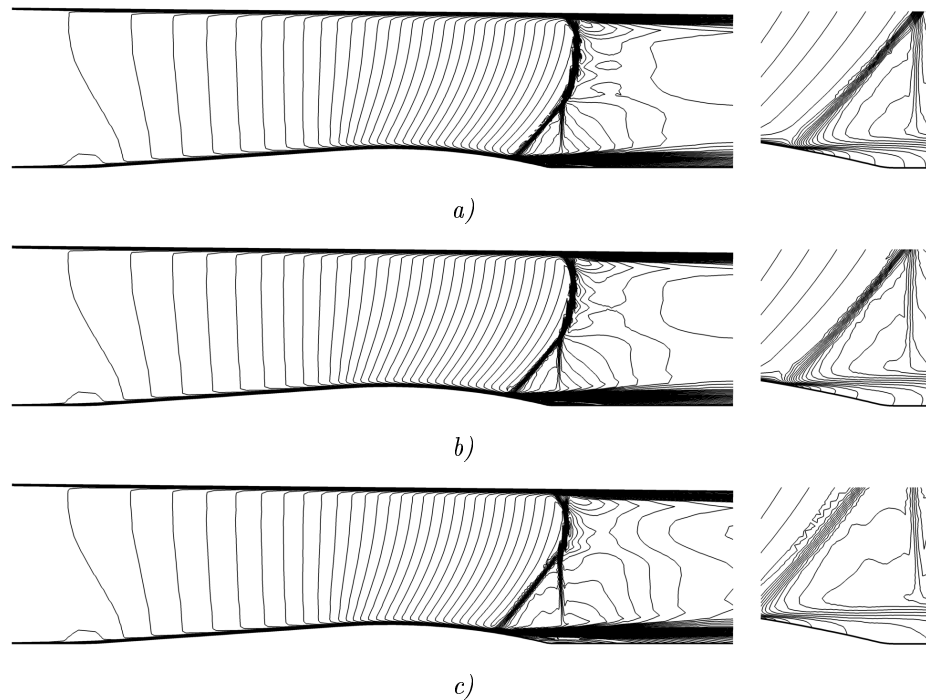


Figure 6.58: Comparison of different turbulence models: *a)* Wilcox, *b)* TNT, *c)* EARSM. Whole channel - isolines of the Mach number ($\Delta M = 0.025$). Detail of the lambda shock - isolines of density ($\Delta \rho = 0.015$).

The experimental data have provided a pressure distribution along the channel walls. Figures 6.59 and 6.60 present the comparison for the lower wall, resp. for the upper wall.

It turns out that the BSL model is unable to capture the inflection point behind the separation (analogy to the Zierp singularity for the GAMM channel) on the lower wall. On the upper wall the BSL model predicts the position of the shock-wave precisely, but suffers by an overshoot downstream.

Both the SST and EARSM models are in best agreement with the experiments out of all models tested. The remaining models, Wilcox and TNT, show inaccuracies in localizing the shock-wave

position on both walls, but capture well main features of the flow. Regarding their offset from the experiment on both sides, the better agreement could potentially be found for a more finely adjusted outlet pressure (this option is possible due to the ambiguous experimental setup).

In front of the shock-wave a very good agreement has been found for all models.

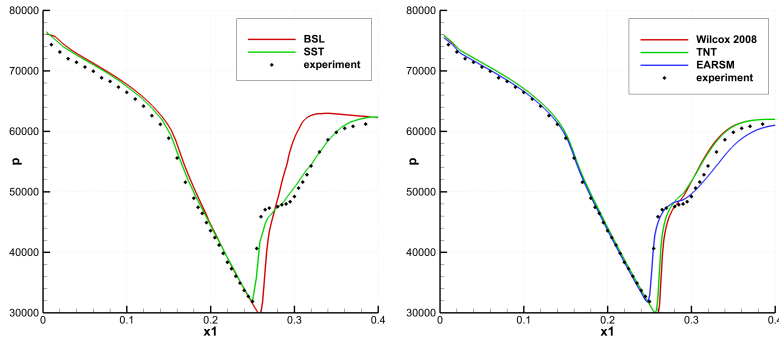


Figure 6.59: Comparison of pressure distribution along the lower wall of the channel.

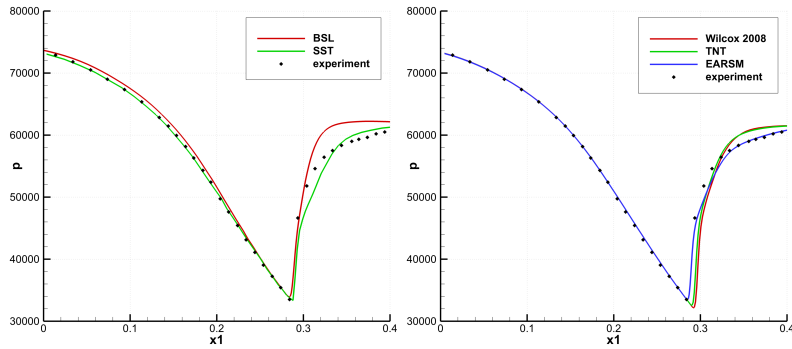


Figure 6.60: Comparison of pressure distribution along the lower wall of the channel.

Chapter 7

Flow around an Exhaust Valve

As mentioned in chapter 2, the main target of this work has been to solve the flow around an exhaust valve inside a reciprocating engine. Chapter 3 describes a mathematical model to be solved. Since no sufficiently robust solver has been available in the initial phase of the project, the development has had to be accomplished in several consecutive steps.

Although the final results comply with the highest complexity demanded, the results of simpler models do not lack an interest. Due to their lower requirements on the grid quality and CPU devices, they have an irreplaceable role in the initial inspection of an a priori unknown phenomenon and in a disclosure of its basic principles.

This chapter will therefore be structured mostly in a chronological order, reproducing the facts and knowledge revealed in the order of their exposure.

7.1 Test Matrix

To give a transparent overview of the work done, the test matrix in the table 7.1 recaps the simulations done. All results have been sorted according to three attributes

- the flow model (inviscid/laminar/turbulent),
- the dimensionality (2D/3D),
- the time resolution (stationary/unsteady).

For each “positive” combination also the solver used (M/CF - MUSA/COOLFluiD) is indicated. Note, that certainly not all results and comparisons available are presented.

INVISCID			LAMINAR			TURBULENT		
	STAT.	UNST.		STAT.	UNST.		STAT.	UNST.
2D	M, CF	CF	2D	M, CF	-	2D	M, CF	CF
3D	M	-	3D	M, CF	-	3D	CF	CF

Table 7.1: Test matrix of the test case of the exhaust valve

7.2 Exhaust Channel Geometry

The original shape of the exhaust channel and the exhaust valve is shown in figures B.1 and B.2. According to the drawings, both components can be considered axisymmetric in the region of

interest, see figure 7.1. For the convenience sake, the original configuration has been rotated (90° clockwise), so that the flow passes the channel from left to right.

Due to the symmetry mentioned all 2D (planar) computations have been solved on one half of the domain. Figure 7.2 shows two alternatives of the computational domain setup.

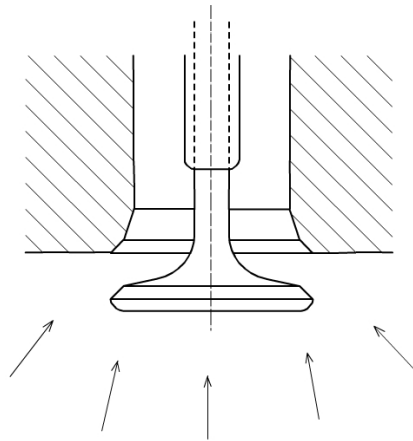


Figure 7.1: Scheme of the region of interest.

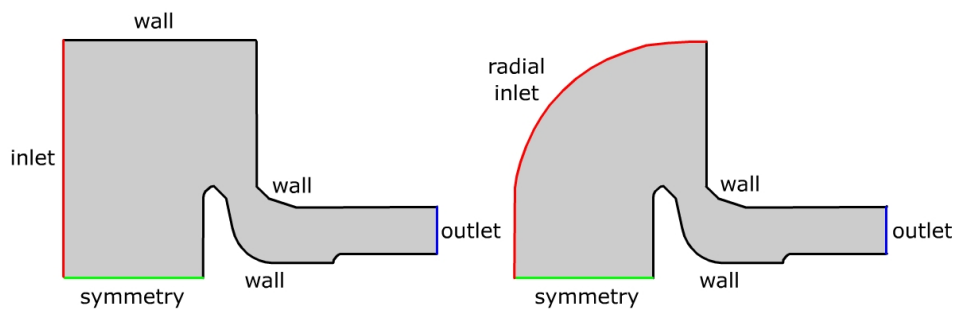


Figure 7.2: Different construction approaches of the computational domain.

The computational domain for a 3D model has been constructed by an axisymmetric extrusion of the planar cut. The mathematical model has, however, stuck to a fully 3D formulation (not axisymmetric) allowing an eventual involvement of other (non-symmetric) parts in the valve vicinity. To prevent mesh singularities near the symmetry axis the extrusion core has been meshed differently, as shown in figure 7.3.

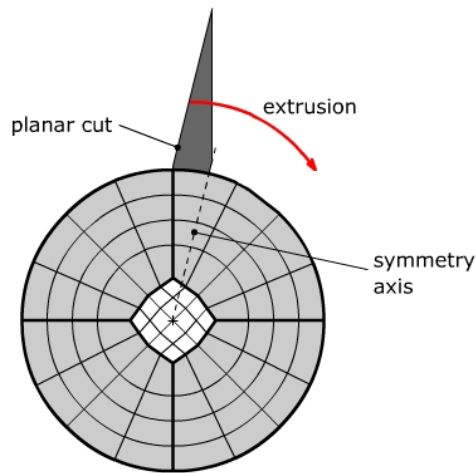


Figure 7.3: Scheme of a 3D grid construction.

Apart from the original geometry, for some flow models two other shapes of the exhaust valve have been tested: *G1* with the bigger curvature and *G2* with milder curvature. All geometries are presented in figure 7.4.

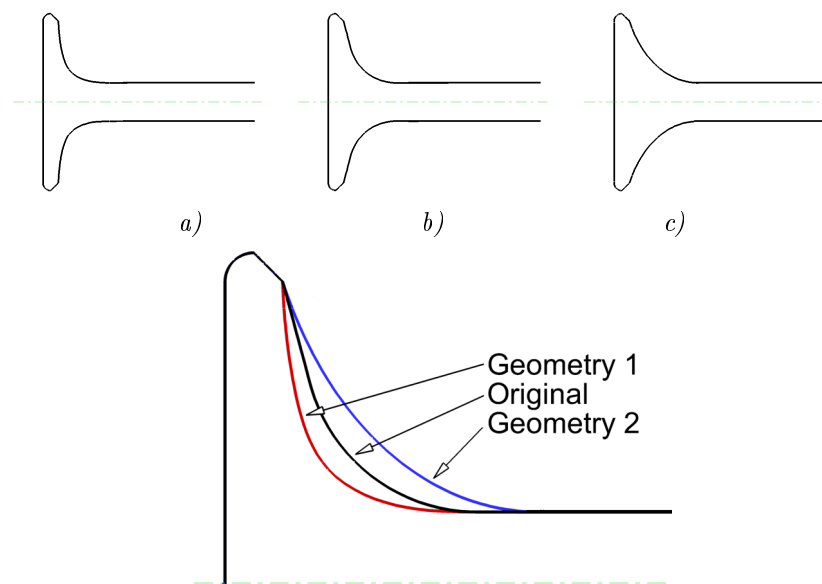


Figure 7.4: Different exhaust valve geometries: a) G1, b) original, c) G2.

7.3 Inviscid Flow Model

The very first simulations have been made using the inviscid flow model. The goal was to explore the flow field characteristics.

The practical experiences have indicated aerodynamically choked flow around the exhaust valve and a subsonic outlet velocity. However, no experimental data could provide the values to get imposed on the boundaries. The initial estimate of an operating regime has therefore been based on the 1D analysis for the Laval nozzle (to be found in [45, 110] or in the appendix A).

From the geometrical size of the throat and outlet sections the isentropic outlet Mach number

$M_{2,i} = 0.4$ has been proposed. The pressure ratio p_2/p_0 has been extracted from equation (6.1).

The numerical results have, however shown an impropriety of this approach, with all solutions standing far from the regime with the aerodynamical blokage (as will be demonstrated later).

The isentropic outlet Mach number has been further increased to $M_{2,i} = 0.95$. Even for this value the transonic regime desired has not been reached. As shown later, the significant non-isentropy of the flow causes the relation (6.1) to be misleading (typical values needed for the transonic regimes would be $M_{2,i} \approx 1.7$). Hence, the regimes computed will be characterized with the pressure ratio p_2/p_0 itself.

Computation Setup

If not stated otherwise, all the results presented have been obtained by the MUSA solver, using the AUSM+up scheme (section 5.4), explicit time integration, piece-wise linear reconstruction of the spatical discretization and the minmod limiter (section 5.5). The valve lift has been fixed to 4 mm. Further specifics will be appended to particular simulations.

The quantitative analysis of results consists of

- the mass flow rate, $\dot{m} = \rho w A$;
- the average outlet Mach number;
- the maximal Mach number in the flow field.

The mass flow rate and the outlet Mach number are the essential values for any further technical analysis. The maximal Mach number then roughly characterizes the flow field. It has also been found the most convenient variable to be used across all the models/regimes/geometries tested.

Computational Grids

The MUSA solver operates exclusively on structured grids. Thus, due to a complex shape of the exhaust channel, the multi-block grid has been used. The initial grid used is shown in figure 7.5. Due to its coarseness (namely in the throat region) a finer mesh has been constructed, see figure 7.6.

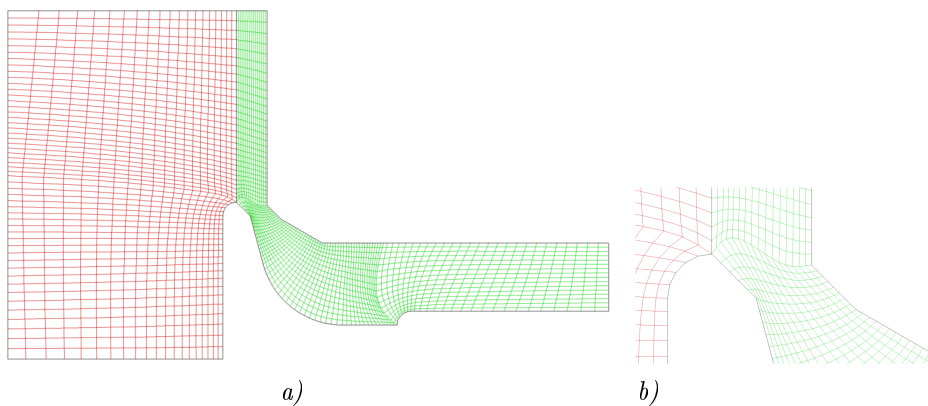


Figure 7.5: First structured multi-block grid on the exhaust channel: *a)* overview, *b)* zoom of the seat region.

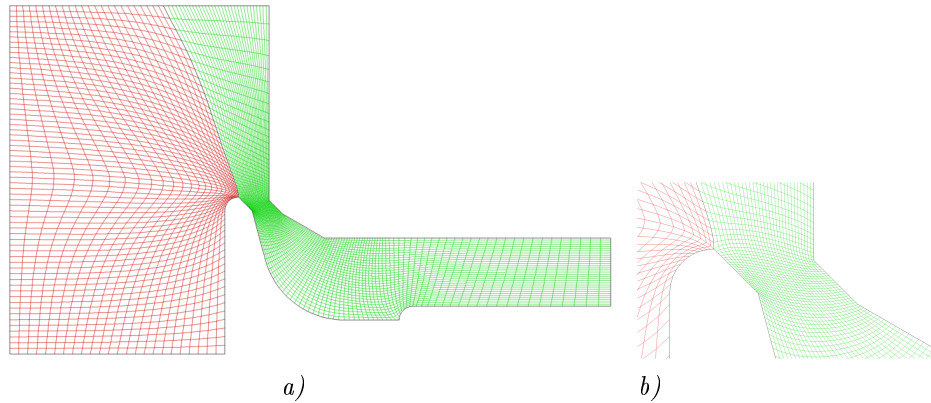


Figure 7.6: Refined structured multi-block grid on the exhaust channel: *a)* overview, *b)* zoom of the seat region.

The COOLFluiD solver operates on unstructured grids, therefore a single block mesh has been used, see figure 7.7. The extra corner in the inlet part has been removed, together with the replacement of the horizontal by the radial inlet boundary condition.

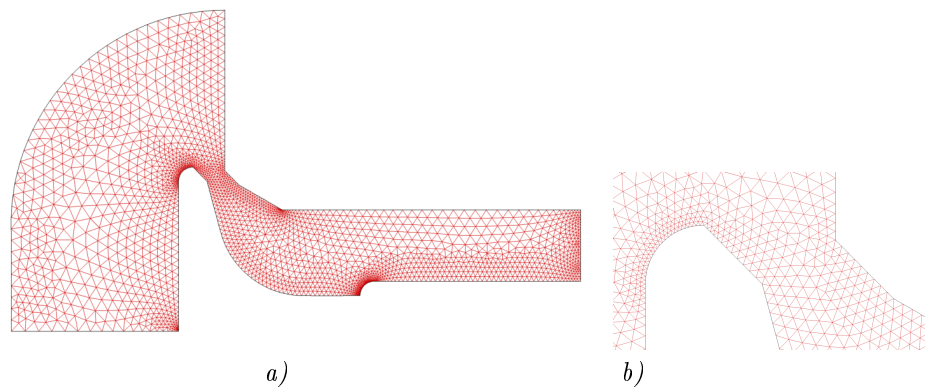


Figure 7.7: Unstructured grid on the exhaust channel: *a)* overview, *b)* zoom of the seat region.

The detailed grid description can be found in the table 7.2.

Grid	Coarse	Fine	Triang
No. of blocks	2	2	1
Size	54×21 107×17	65×25 133×33	4892 elem.
Pts. across throat	16	32	20
Solver	MUSA		COOLFluiD

Table 7.2: Computational grids for 2D Inviscid flow simulations.

7.3.1 2D Geometry, Stationary Simulations

Pressure Ratio 0.896

Based on the 1D analysis, the first simulations have been performed for the pressure ratio $p_2/p_0 = 0.896$ (corresponding to $M_{2,i} = 0.4$). Figures 7.8 and 7.9 show the results obtained on the coarse and fine mesh.

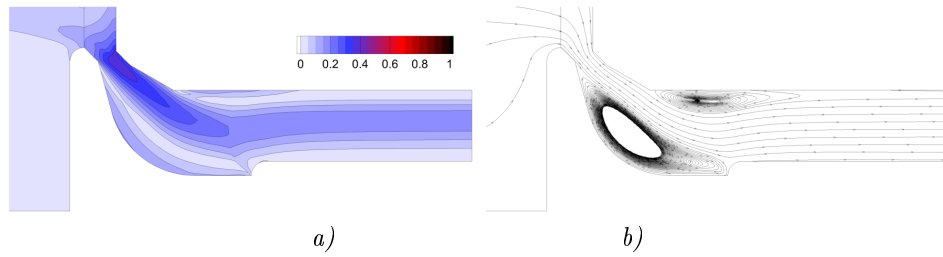


Figure 7.8: Inviscid flow simulation on the coarse mesh, the MUSA solver, $p_2/p_0 = 0.896$. *a)* Isolines of the Mach number, *b)* velocity streamlines.

Figure 7.10 presents the analogous result by the COOLfluid solver on the unstructured grid.

From the streamlines plots two large separation zones can be identified. These zones appear despite their physical unjustification (inviscid flow model very unlikely models recirculation). The flow separates behind sharp corners on both sides of the channel, reducing an actual cross-section. Hence, the supersonic expansion expected is suppressed, dropping the above-mentioned analogy with the Laval nozzle.

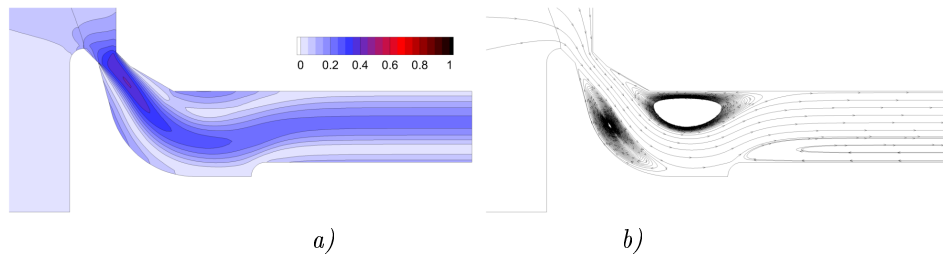


Figure 7.9: Inviscid flow simulation on the fine mesh, the MUSA solver, $p_2/p_0 = 0.896$. *a)* Isolines of the Mach number, *b)* velocity streamlines.

A closer look reveals a strong sensitivity to grid quality. Rough grid spacing for the coarse mesh affects the flow topology behind the throat. This difference also influences the position and the size of the separation zones, together with the structure of the outflow. Comparison between the numerical codes has, however, led to a very good agreement with the fine grid result.

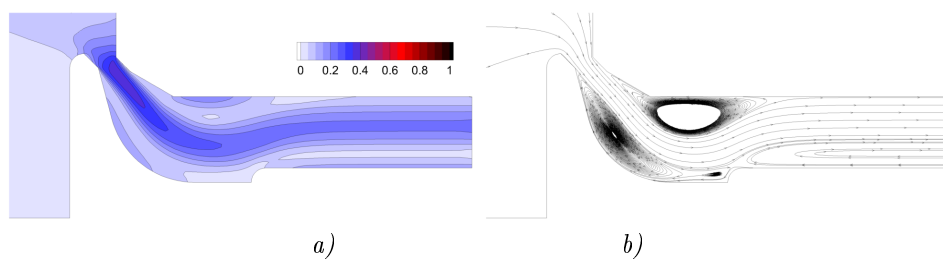


Figure 7.10: Inviscid flow simulation on the triangular mesh, the COOLfluid solver, $p_2/p_0 = 0.896$. *a)* Isolines of the Mach number, *b)* velocity streamlines.

Despite the significant grid topology differences, the quantitative comparison (table 7.3) has detected only minor changes among all results. The result on the fine grid has been assumed as referential. The difference in the outlet Mach number for the coarse mesh is caused by the strong recirculation zone, passing the outlet boundary.

Grid	Fine		Coarse		Triang	
	Abs.	Diff [%]	Abs.	Diff [%]	Abs.	Diff [%]
Max. Mach number	0.403	0.0	0.391	-3.0	0.388	-3.7
Avg. outlet Mach number	0.120	0.0	0.098	-18.3	0.116	-3.3
Mass flow rate	1.028	0.0	1.025	-0.3	1.026	-0.2

Table 7.3: Inviscid flow simulation, $p_2/p_0 = 0.896$. Influence of the grid coarseness.

Pressure Ratio 0.559

Since the first simulations did not reach the transonic regime, the pressure ratio has been intuitively decreased to $p_2/p_0 = 0.559$ (corresponding to $M_{2,i} = 0.95$). The results are presented analogically to the first pressure ratio. Figures 7.11 and 7.12 present the contours of the Mach number and the velocity streamlines. The next figure 7.13 compares the flow fields in the critical throat section.

The quantitative comparison is tabulated in the table 7.4.

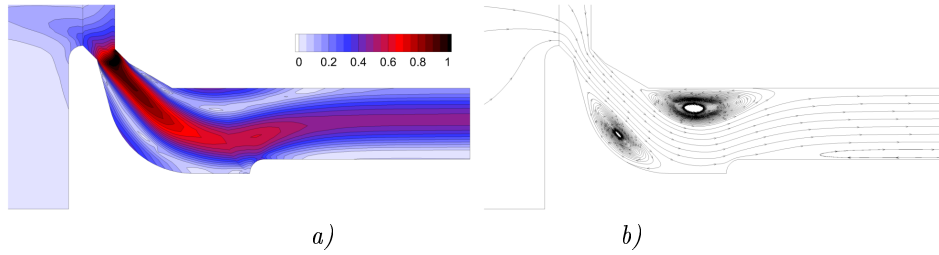


Figure 7.11: Inviscid flow simulation on the coarse mesh, the MUSA solver, $p_2/p_0 = 0.559$. *a)* Isolines of the Mach number, *b)* velocity streamlines.

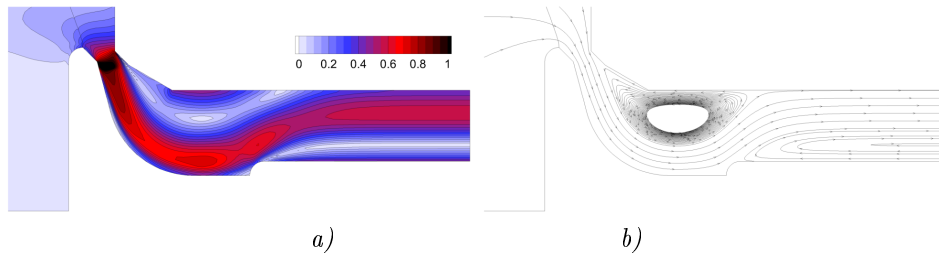


Figure 7.12: Inviscid flow simulation on the fine mesh, the MUSA solver, $p_2/p_0 = 0.559$. *a)* Isolines of the Mach number, *b)* velocity streamlines.

Having an identical setup for both simulations, the strong sensitivity to the grid coarseness has again been noticed. The discretization of the throat section affects the flow resolution, which is then crucial for the entire downstream flow.

Furthermore, with a decreased pressure ratio (i.e. increased mean velocity) the differences in the mass flow rate become bigger and non-negligible. As for the other quantities monitored, the differences are much stronger due to the notably different flow fields.

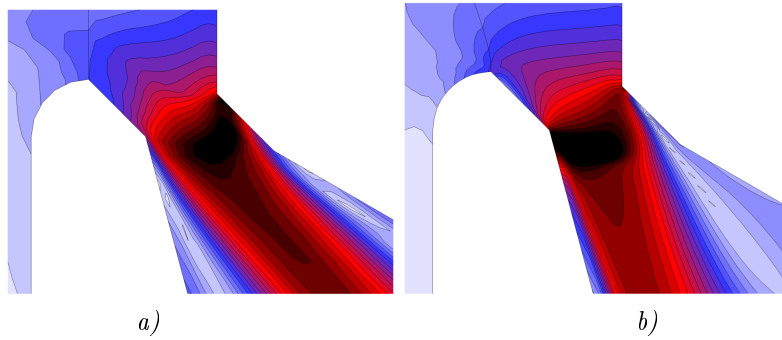


Figure 7.13: Detail of the channel throat on *a)* coarse mesh, *b)* fine mesh. Isolines of the Mach number.

Grid	Fine		Coarse	
	Abs.	Diff [%]	Abs.	Diff [%]
Max. Mach number	1.378	0.0	1.160	-15.8
Avg. outlet Mach number	0.362	0.0	0.283	-21.8
Mass flow rate	1.913	0.0	1.856	-2.9

Table 7.4: Inviscid flow simulation, $p_2/p_0 = 0.559$. Influence of the grid coarseness.

Figure 7.13 also shows that the solution on the coarse mesh is unable to capture correctly the separation on the upper¹ seat. Same behaviour is observed also for the pressure ratio 0.896.

The solutions on both grids evince the backflow through an outlet boundary. This phenomenon is examined in one of the next subsections.

Pressure Ratio 0.250

With a further decrease of the pressure ratio, a strong aerodynamical choking has been expected. Such a transonic flow is very sensitive to both the geometry of the channel and the numerical methods used. On that account this regime has been selected for examination of the influence of the numerical scheme and to measure differences between the codes used.

Figure 7.14 compares the results obtained by the MUSA solver for the original *AUSM* and the *AUSM+up* scheme. Figure 7.15 shows the result obtained by the COOLFluid, using the *AUSM+up* scheme.

¹Regarding the picture orientation: *upper* seat is located on the channel wall, *lower* seat on the valve.

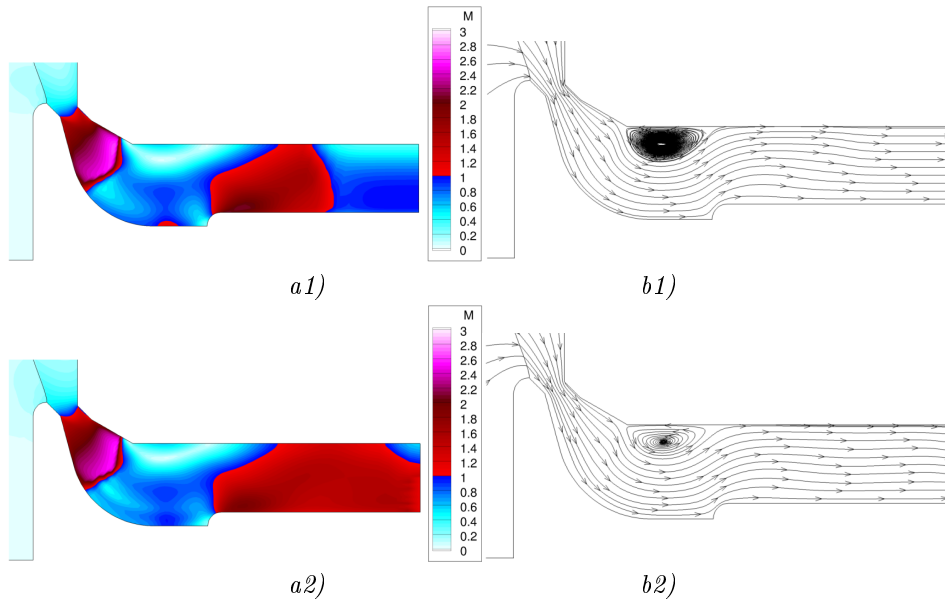


Figure 7.14: Inviscid flow simulation, the MUSA solver, $p_2/p_0 = 0.250$. *a)* isolines of the Mach number, *b)* velocity streamlines. *a1)*, *b1)* AUSM scheme, *a2)*, *b2)* AUSM+up scheme.

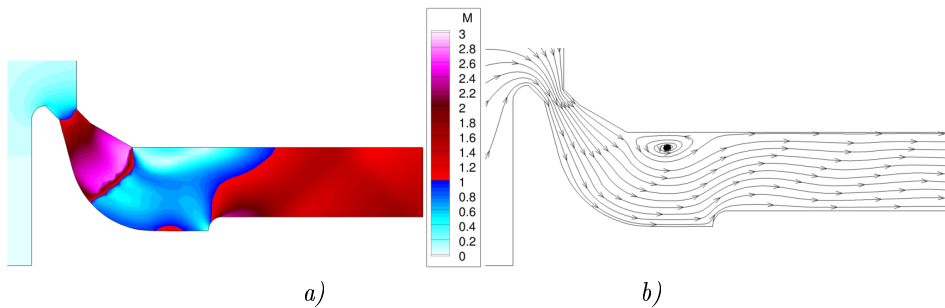


Figure 7.15: Inviscid flow simulation, the COOLfluid solver, $p_2/p_0 = 0.250$, AUSM+up scheme. *a)* isolines of the Mach number, *b)* velocity streamlines.

In order to compare the flow fields (due to the complicated geometry) the variables along a central streamline² have been extracted. The development of the Mach number along the streamline is shown in figure 7.16.

²The central streamline is released from the geometrical mid-point of the throat.

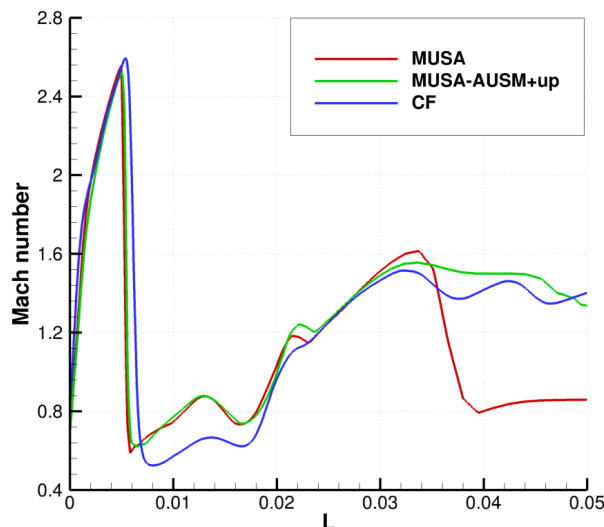


Figure 7.16: The Mach number distribution along the central streamline for different numerical schemes and different numerical codes.

For all three alternatives tested a similar supersonic expansion behind the throat has been observed. The solution by the COOLFluid solver has predicted a later recirculation near the upper wall and therefore a slightly stronger expansion. This expansion has been terminated by a normal shock-wave. Due to the recirculation zone mentioned, the actual cross-section has been converging-diverging again, creating a second throat and allowing the flow to re-accelerate to supersonic.

The original AUSM scheme has predicted a larger recirculation zone, leading to a smaller throat, earlier acceleration to supersonic (mind the supersonic pocket on the valve stem in figure 7.14 *a1*). Also the expansion around the valve casing has appeared the strongest, causing a later drop through the normal shock-wave, whereas the other solutions have remained supersonic.

On the basis of the flow fields comparison, the qualitative agreement (apart from the outlet part for the AUSM scheme) has been found among all the solutions. For the AUSM+up scheme a very good agreement has been observed for both the codes used.

The quantitative comparison (based on the graph 7.16) has shown differences, caused primarily by the position and the size of the recirculation zone. However, for this low pressure ratio, no result has suffered by the backflow problem of the previous regimes.

Although being still far from the flow model in a real engine a general concluding remark has turned up from the simulations performed: in order to obtain a reliable solution the grid in a throat section must be sufficiently fine and a special attention must be paid to a proper modelling of the recirculations.

Artificial Geometries to Control Recirculations

Due to the lack of physical dissipation, the inviscid flow model is not suitable for flows with recirculations. However, all the results have contained large recirculation zones that have been forming an artificial channel inside the real one. It is shown later in the table 7.8 that these zones restrict the active cross-section of the channel up to 74%.

The impropriety of the inviscid model has been demonstrated on an artificial geometry with an elongated outlet part of the channel, see figure 7.17. Despite the massive elongation, the solution

obtained still contains the backflow along the valve casing. The overall solution is otherwise in an excellent agreement with the solution on a conventional geometry.

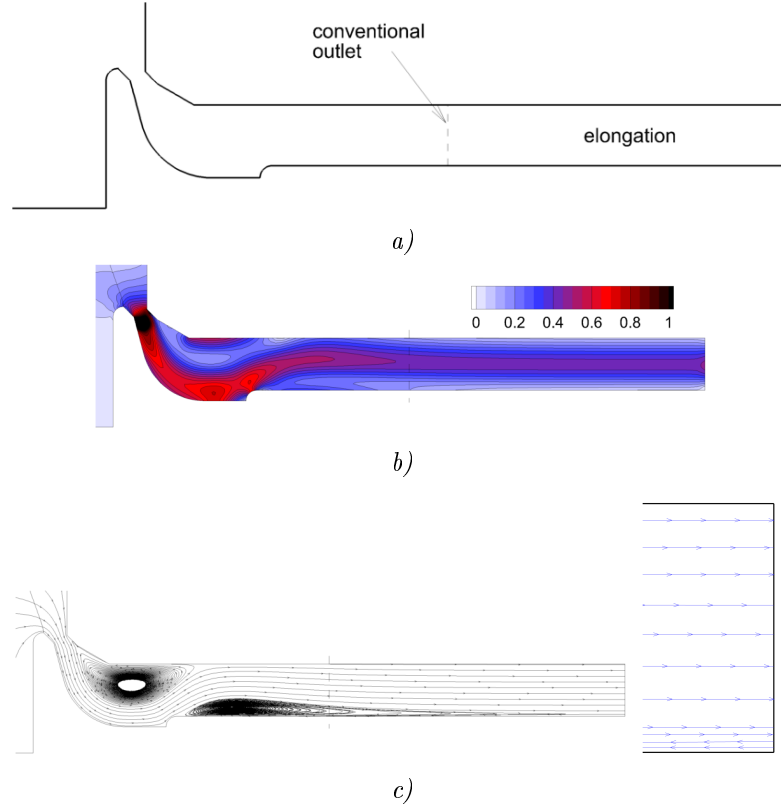


Figure 7.17: Inviscid flow simulation on the elongated geometry, the MUSA solver, $p_2/p_0 = 0.559$. *a)* Elongated domain, *b)* isolines of the Mach number, *c)* velocity streamlines, detail of the backflow.

Geometry	Original		Elongated	
	Abs.	Diff [%]	Abs.	Diff [%]
Max. Mach number	1.378	0.0	1.391	0.9
Avg. outlet Mach number	0.362	0.0	0.349	-3.6
Mass flow rate	1.913	0.0	1.906	-0.4

Table 7.5: Inviscid flow simulation, $p_2/p_0 = 0.559$. Comparison with the elongated domain (the average outlet Mach number has been extracted at the conventional outlet position).

Controlling (avoiding) the recirculations can therefore enhance the model suitability on one hand and improve the parameters of the exhaust process on the other hand. Two artificial geometrical modifications have been tested:

1. a smoothed shape transition between the valve stem and its casing at $p_2/p_0 = 0.559$;
2. an inclination of the inlet wall by 5 and 10 degrees at $p_2/p_0 = 0.250$.

The first modification should reduce the separation along the valve casing (and respective backflow). Although this target has been fulfilled (see figure 7.18), the backflow region has only been displaced on the upper wall of the channel. At the same time a big recirculation has appeared along the valve stem. The mass flow rate has slightly increased by 5.6%, but unfortunately the expected reduction of the recirculations' size has not been achieved.

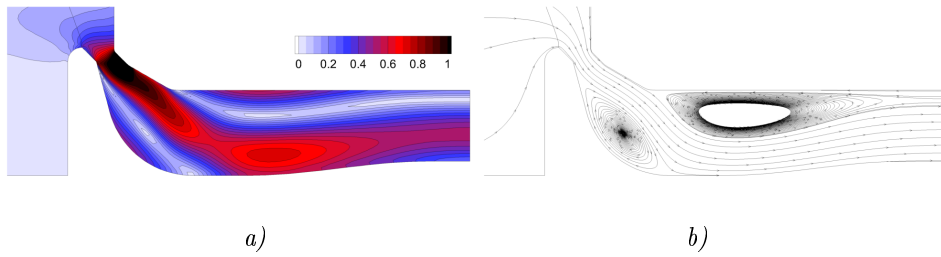


Figure 7.18: Inviscid flow simulation on the elongated geometry, the MUSA solver, $p_2/p_0 = 0.559$.
a) isolines of the Mach number, *b)* velocity streamlines.

The second modification should decrease the turning angle³ of the flow around the seat, so to reduce the flow inertia causing the separation. The modification is schematized in figure 7.19. The table 7.6 presents the influence on the flow characteristics (recirculation length, mass flow rate). The impact on the recirculation length is captured in the graph 7.21.

For the convenient valve lift of 4 mm no significant effect has been observed (see figure 7.20), thus the same strategy has been tested also for the lift 7 mm that converges to an entirely subsonic flow field.

Although the dependencies assessed follow the trends expected, for the flow with a dominant supersonic region behind the throat (lift 4 mm - see figure 7.14) the alternation of an inlet wall occurs inefficient for the recirculation control. For the subsonic regime (lift 7 mm) the impact of the inclination is bigger, however the overall effect within the available technological limits is very low.

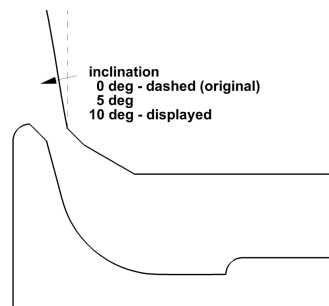


Figure 7.19: Scheme of the inlet wall inclination.

Recirculation length [mm]				Mass flow rate gain [%]			
valve lift	inclination angle			valve lift	inclination angle		
	0°	5°	10°		0°	5°	10°
4 mm	10.4	10.4	10.5	4 mm	0.00	0.01	0.04
7 mm	22.8	24.9	29.1	7 mm	0.00	0.15	1.02

Table 7.6: The influence of the inclination angle on the flow characteristics.

³The outer angle (i.e. $>180^\circ$) between the vertical inlet wall and the seat.

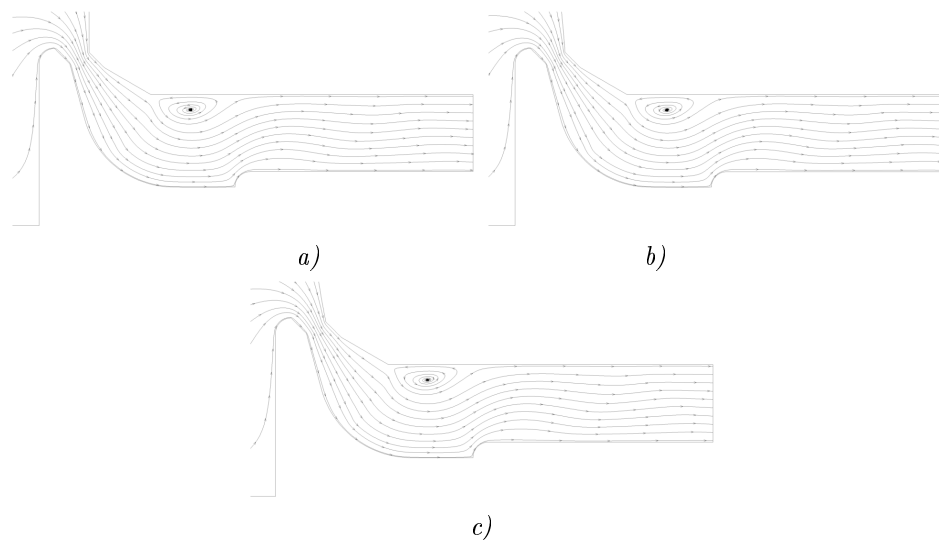


Figure 7.20: Inviscid flow simulation, the MUSA solver, $p_2/p_0 = 0.250$, velocity streamlines. Influence of the inlet wall inclination a) 0 degrees (original), b) 5 degrees, c) 10 degrees.

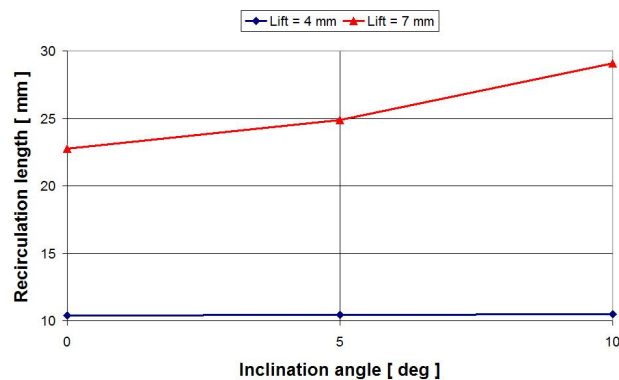


Figure 7.21: The effect of the inlet wall inclination on the recirculation length.

7.3.2 3D Geometry, Stationary Simulations

By the same analogy with the Laval nozzle which was used for the 2D computations, the initial regime has been derived from the equation (A.1) and has led to $p_2/p_0 = 0.784$. Similarly to the planar computations, this pressure ratio hasn't provided an aerodynamically choked flow. The pressure ratio has therefore been decreased to $p_2/p_0 = 0.559$. The influence of the recirculations has again been studied.

As a separate topic the comparison of 2D and 3D solutions for identical computation setup is presented in the later subsection 7.3.3.

Pressure Ratio 0.784

The results of the initial 3D simulation is shown in figure 7.22. The solution contains three strong recirculations, one of them passing the outlet boundary. Due to non-isentropy of these zones, the equation (A.1) fails at its initial premise and thus the regime tested cannot lead the aerodynamical blockage. Remind, that the aerodynamical blockage is the assumption based on a practical experience.

The quantitative analysis is summarized in the table 7.7. As stated above, the comparison with the 2D alternative is discussed in subsection 7.3.3.

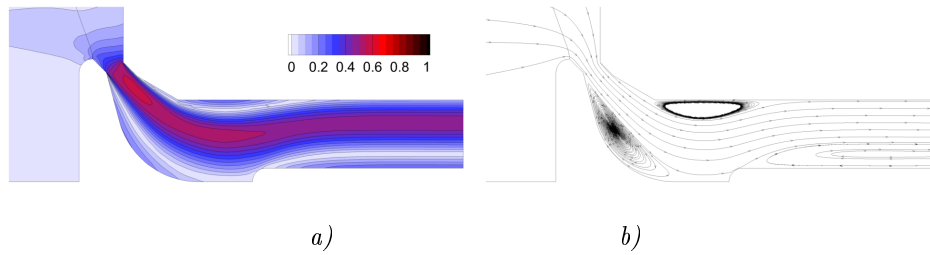


Figure 7.22: 3D Inviscid flow simulation, the MUSA solver, $p_2/p_0 = 0.784$. Solution cut at $Z = 0$. *a)* isolines of the Mach number, *b)* velocity streamlines.

Pressure Ratio 0.559

For a lowered pressure ratio the flow accelerates, but does not exceed the sonic speed, $M=1$, as shown in figure 7.23. Along the channel the main flow beam stays compact and slightly widens. The void regions around the beam again contain recirculations.

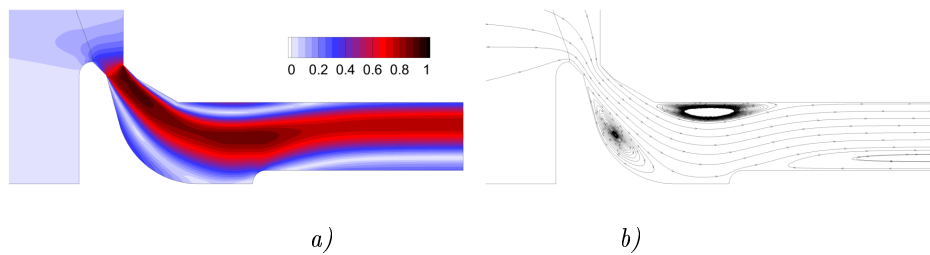


Figure 7.23: 3D Inviscid flow simulation, the MUSA solver, $p_2/p_0 = 0.559$. Solution cut at $Z = 0$. *a)* isolines of the Mach number, *b)* velocity streamlines.

Artificial Geometry to Avoid Recirculations

Compared to the planar computations, only one artificial geometry has been tested here, in order to prevent the flow recirculation. The result on a smoothed geometry (between the valve stem and its casing) is shown in figure 7.24.

The artificial contour of the stem causes the Coanda effect, with the flow beam remaining attached to the lower wall. By that, the recirculation zone passing the outlet boundary is reduced. Having smaller void regions the dominant flow beam widens, leading to a gain of 7.6% in the mass flow rate against the original geometry. The backflow, however only displaces to the upper wall.

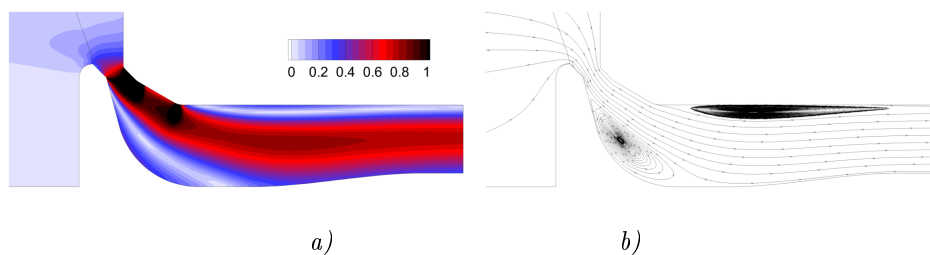


Figure 7.24: 3D Inviscid flow simulation on a smoothed geometry, the MUSA solver, $p_2/p_0 = 0.559$. Solution cut at $Z = 0$. *a)* isolines of the Mach number, *b)* velocity streamlines.

Regime p_2/p_0	0.784		0.559	
Geometry	original		original	
	Abs.	Diff [%]	Abs.	Diff [%]
Max. Mach number	0.565	0.0	0.944	67.1
Avg. outlet Mach number	0.282	0.0	0.467	65.5
Mass flow rate	2.326	0.0	3.011	29.4
Regime p_2/p_0	0.559		0.559	
Geometry	original		smoothened	
	Abs.	Diff [%]	Abs.	Diff [%]
Max. Mach number	0.944	0.0	1.444	34.6
Avg. outlet Mach number	0.467	0.0	0.547	17.8
Mass flow rate	3.011	0.0	3.258	7.6

Table 7.7: 3D Inviscid flow simulation. Comparison of the different regimes and geometries.

This artificial geometry therefore seems efficient in 3D. Remind that the applicability of this geometrical change into practice is still conditioned by the ability of the flow model to capture the recirculation.

Despite this general weak-point of the inviscid flow model the interactions of the flow beam and the recirculations have turned up to be a key issue to control the flow inside the exhaust channel.

7.3.3 Stationary Simulations, Comparison of 2D and 3D Solutions

Two regimes have been selected for the comparison of 2D and 3D solutions, $p_2/p_0 = 0.784$ and 0.591. The respective results are shown in figures 7.25 and 7.26. For all the results a dominant flow beam can be identified, surrounded by three large recirculation zones. The planar model predicts an earlier and larger separation on the upper wall. Furthermore, the graph 7.28 shows that the active area (i.e. the dominant beam versus the recirculations) is always wider for the 3D geometry.

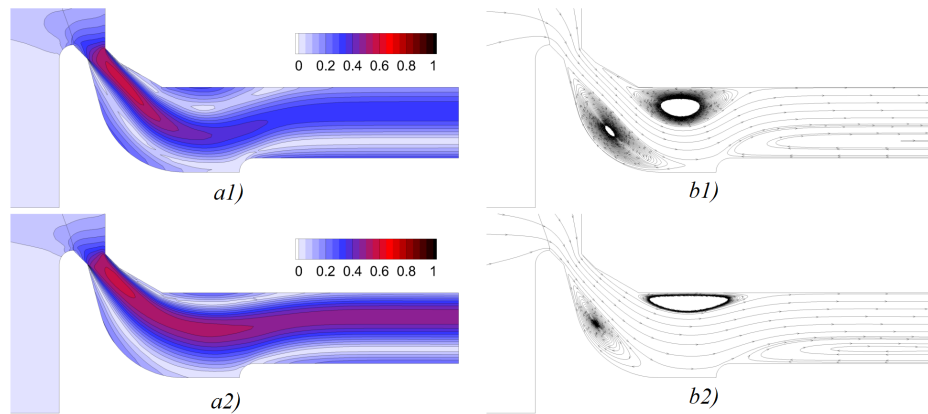


Figure 7.25: Inviscid flow simulation, the MUSA solver, $p_2/p_0 = 0.784$. a) isolines of the Mach number, b) velocity streamlines. a1), b1) 2D model, a2), b2) 3D model, cut at $Z=0$.

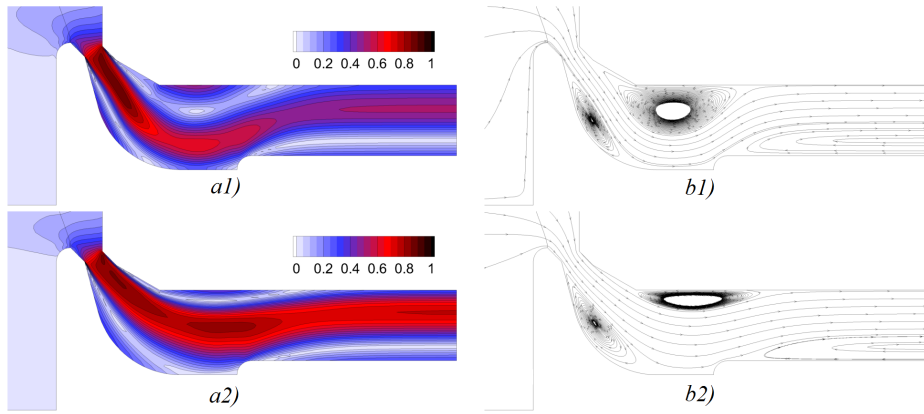


Figure 7.26: Inviscid flow simulation, the MUSA solver, $p_2/p_0 = 0.591$. *a)* isolines of the Mach number, *b)* velocity streamlines. *a1)*, *b1)* 2D model, *a2)*, *b2)* 3D model, cut at $Z=0$.

Using the table 7.8, with the planar model the active area is reduced approximately by 50% with a maximum reduction of up to 74.4%. For the more realistic 3D model on average 38% of the channel remains void.

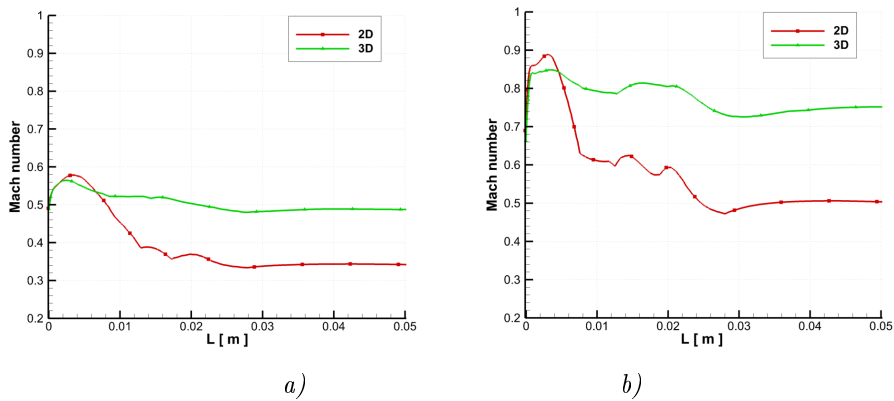


Figure 7.27: The Mach number distribution along the central streamline. Pressure ratio: *a)* $p_2/p_0 = 0.784$, *b)* $p_2/p_0 = 0.591$.

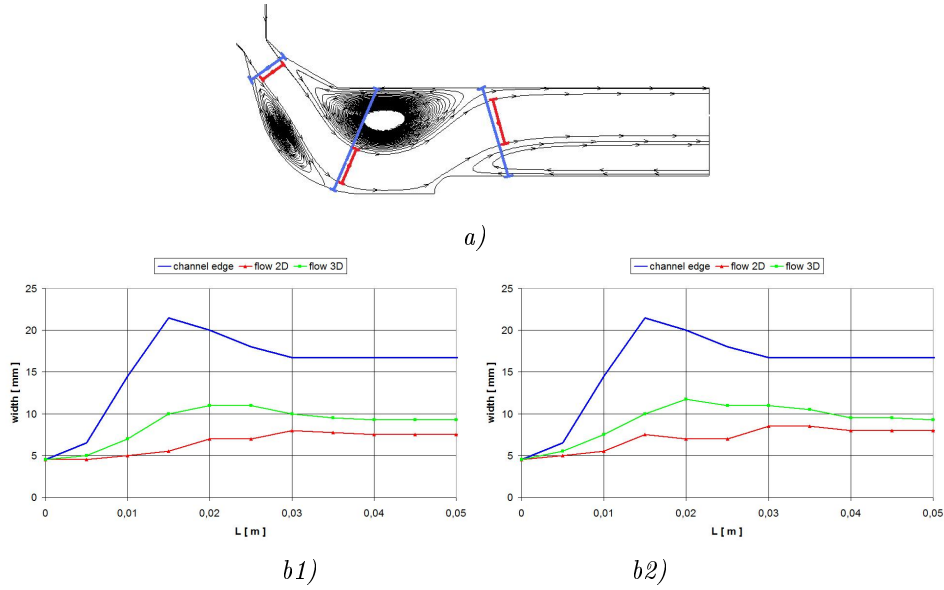


Figure 7.28: The plot of an active area within the exhaust channel. *a)* the scheme of the values extraction, *b1)* pressure ratio $p_2/p_0 = 0.784$, *b2)* pressure ratio $p_2/p_0 = 0.591$.

None of the results compared is aerodynamically choked. The graph 7.27 indicates the higher maximal Mach number for the planar simulations, whereas the average Mach number is higher for the 3D cases. Besides, the contour trends are significantly different - the planar case predicts faster velocity drop, while the spatial case moreless “fluctuates” around a mean value.

Regime p_2/p_0	0.784		0.591	
	Avg [%]	Max [%]	Avg [%]	Max [%]
2D	52.0	74.4	49.9	67.6
3D	39.6	53.3	37.5	53.8

Table 7.8: Reduction of the active channel cross-section due to recirculations.

7.3.4 Summary for Inviscid Flow Model

With respect to all the simplifications assumed, several concluding remarks could still be gathered along the initial explorations with the inviscid flow model:

- The flow field for all configurations contains non-negligible recirculation zones. Therefore an inviscid flow model cannot be used for reliable simulations, as the model does not contain any physical dissipation, crucial for modelling of the recirculation structures.
- Very good agreement has been found between both the numerical codes used, cross-validating both the codes and the results.
- Two key issues have been identified in order to perform proper computations on the exhaust channel: sufficiently fine grid in a throat section and a proper modelling of the recirculations.
- The strong interaction between the main flow beam and recirculations has been observed.
- Most of the results have contained a backflow, entering the domain through an outlet boundary.

- A smoother shape of the valve stem has a potential to positively influence the performance of the exhaust process.
- The significant differences have been observed between the 2D and 3D geometrical models. Almost no quantitative predictions can be extrapolated from the planar to the spatial (and vice versa) cases. From the qualitative point of view the 3D cases are usually less sensitive to the problematic issues identified on the 2D geometry (3D: smaller recirculations, more uniform flow, milder variable gradients).

7.4 Laminar Flow Model

This flow model represents a transition step in the code development between the initial *inviscid* and the target *turbulent* flow model. The explorations made have therefore been more modest, being dedicated mainly to the testing of the numerical methods developed.

If not stated otherwise, all the results presented have been obtained by the MUSA solver, using the AUSM+up scheme, explicit time integration, piece-wise linear reconstruction of the spatical discretization and the minmod limiter. Further specifics will be appended to particular simulations.

The valve lift has been fixed to 4 mm and a modified planar geometry without the valve casing has mainly been used.

Computation Setup

The laminar flow model is determined by (at least) three parameters. For the simulations presented the Mach number, the Reynolds number and the freestream temperature have been chosen.

The Mach number is connected with the pressure ratio across the domain through equation (A.2). For obvious reasons (stated in the section 7.3) the pressure ratio is preferably used.

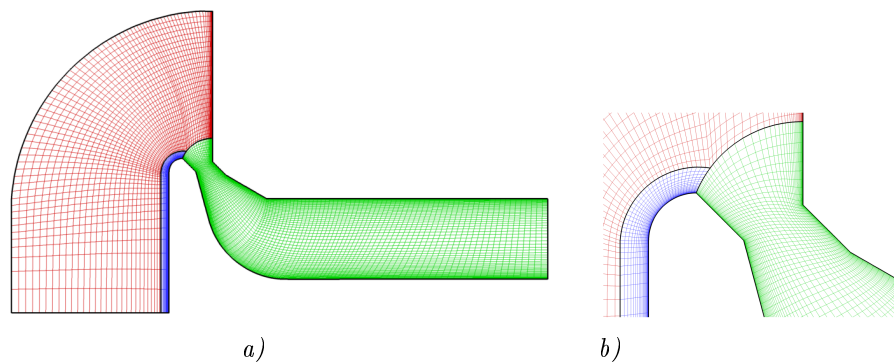
The Reynolds number characterizes the ratio between the dynamic and viscous forces. Its reciprocal then scales the dissipation terms. To characterize the flow regime the Reynolds number on a unit length $Re/L = \rho w/\mu$ has been used.

The freestream temperature has been chosen 500 K for all the simulations.

For the sake of completeness, the quantitative analysis has been recorded in an identical way as for the inviscid flow model.

Computational Grids

Because of the indispensable grid refinement along the walls the multi-block grid consists of three parts. The composition and the detail of the blocks seal is shown in figure 7.29. Compared to the inviscid geometry (figure 7.9), the inlet section has been rounded to have the similar exterior shape to the geometry for unstructured grids.



Size of the grid blocks			
Block	1	2	3
Size	84×30	49×25	117×60
Pts. across throat	60		
(color)	red	blue	green

Figure 7.29: A structured multi-block grid on the exhaust channel: *a)* overview, *b)* zoom of the block connection and the seat region.

7.4.1 Influence of Pressure Ratio

Two pressure ratios $p_2/p_0 = 0.656$ and 0.250 have been used to observe an impact on the flow structure. The viscosity coefficient used has been set to $Re/L = 1500$. The comparisons of the flow field and the streamlines are shown in figure 7.30.

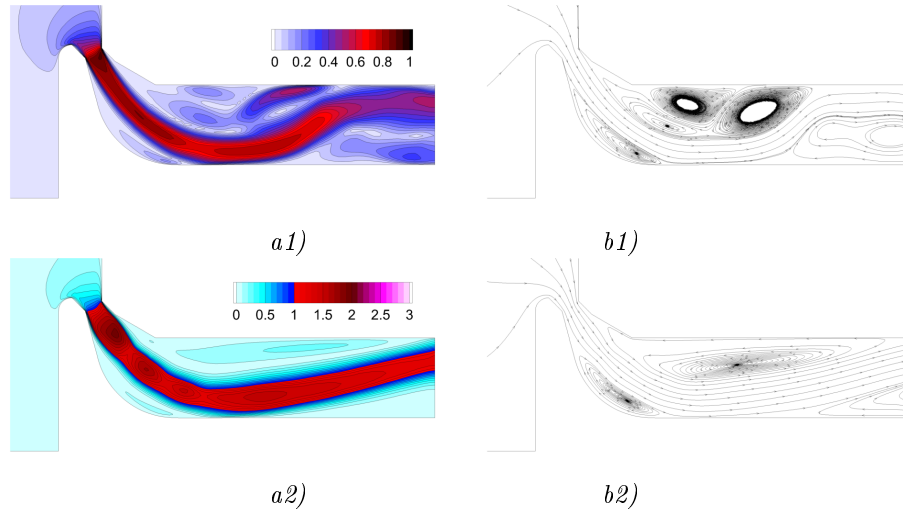


Figure 7.30: Laminar flow simulation, the MUSA solver, $Re/L=1500$. *a)* isolines of the Mach number, *b)* velocity streamlines. The pressure ratio *a1)*, *b1)* $p_2/p_0 = 0.656$, *a2)*, *b2)* $p_2/p_0 = 0.250$.

Similarly to results with the inviscid flow model, for both regimes a dominant flow beam is formed at the throat section. This beam reflects from the valve stem (note that the Coanda effect does not appear) and leaves the domain. Massive recirculation zones appear on both sides of the beam, on top of that one passing the outlet boundary.

For the lower pressure ratio the beam occurs more compact, not interfering with its vicinity. This hypothesis is intensified by the internal topology of the beam that reminds a jet similar to a nozzle exiting in a vessel.

The table 7.9 quantifies the results obtained.

Pressure ratio p_2/p_0	0.656	0.250
Max. Mach number	0.909	1.936
Avg. outlet Mach number	0.293	0.511
Mass flow rate	1.301	1.813

Table 7.9: Laminar flow simulation, $Re/L = 1500$. Influence of the pressure ratio.

7.4.2 Influence of Viscosity Parameter

At the given pressure ratio $p_2/p_0 = 0.656$ the magnitude of the viscosity parameter Re/L has been successively altered to 800, 1 500 and 10 000. Due to a non-specific geometry of the domain, the transition value of the viscosity parameter has been a priory unknown. The largest value tested ($Re/L = 10\,000$) has finally showed to be over this transition limit (discussed below), however the result is presented among the others in figure 7.31.

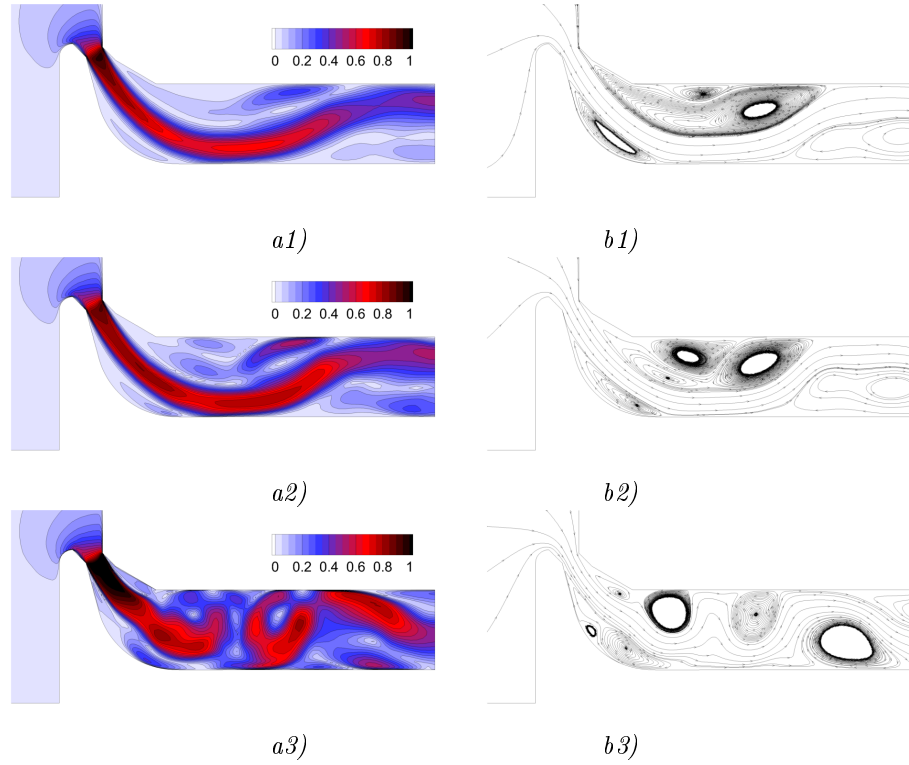


Figure 7.31: Laminar flow simulation, the MUSA solver, $p_2/p_0 = 0.656$. *a)* isolines of the Mach number, *b)* velocity streamlines. The viscosity parameter *a1)*, *b1)* $Re/L=800$, *a2)*, *b2)* $Re/L=1500$, *a3)*, *b3)* $Re/L=10\ 000$.

Viscosity parameter Re/L	800		1 500		10 000	
	Abs.	Diff [%]	Abs.	Diff [%]	Abs.	Diff [%]
Max. Mach number	0.974	7.2	0.909	0.0	1.184	30.3
Avg. outlet Mach number	0.224	-23.5	0.293	0.0	0.273	-6.8
Mass flow rate	1.438	10.5	1.301	0.0	1.606	23.4

Table 7.10: Laminar flow simulation, $p_2/p_0 = 0.656$. Influence of the viscosity parameter.

The results obtained correspond to the behaviour expected: with an increasing viscosity parameter (i.e. increasing effect of dynamic forces) the flow loses its stability. The flow beam starts to interact with the surrounding recirculations, which causes a significant dispersion, accompanied by the raise of complicated vortex structures.

At the same time, the solution loses its numerical stability and leads to serious convergence issues. The regime with a lower pressure ratio (for $Re/L=10\ 000$) hasn't converged even for an adaptively decreased CFL. Besides, the convergence history for the solution 7.31 *a3)* contains a periodic pattern of significant amplitude, indicating an unsteady behaviour.

Being only a transition step towards the turbulent flow model the issues mentioned have been described but not explored into further details.

7.4.3 Influence of Geometry

Although a simplified geometry without the valve casing has mainly been studied, the difference against the complete geometry has not been left without any interest.

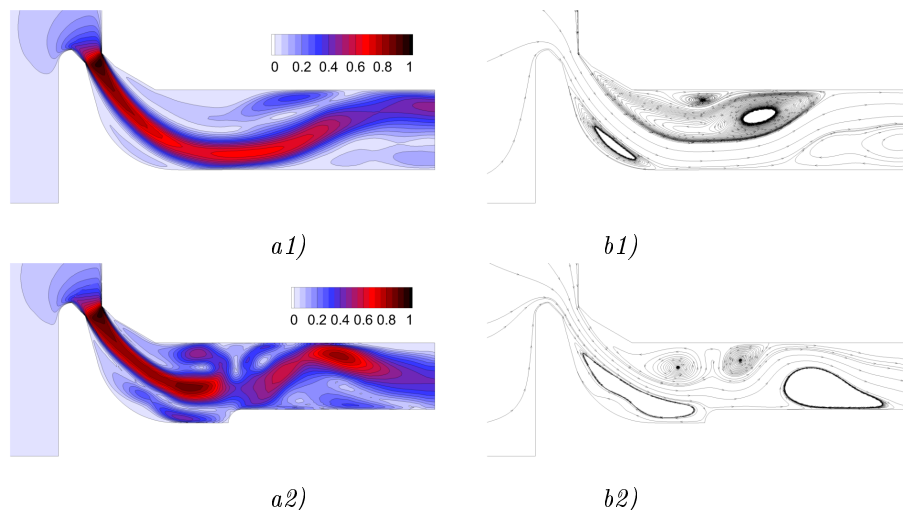


Figure 7.32: Laminar flow simulation, the MUSA solver, $p_2/p_0 = 0.250$, $Re/L = 800$. *a)* isolines of the Mach number, *b)* velocity streamlines. *a1)*, *b1)* geometry without valve casing, *a2)*, *b2)* complete geometry.

Geometry	without casing		complete	
	Abs.	Diff [%]	Abs.	Diff [%]
Max. Mach number	0.974	0.0	0.984	1.0
Avg. outlet Mach number	0.224	0.0	0.250	11.6
Mass flow rate	1.438	0.0	1.690	17.5

Table 7.11: Laminar flow simulation, $p_2/p_0 = 0.656$, $Re/L = 800$. Influence of the geometry.

As shown in figure 7.32 the contraction due to the casing affects the proportions of the recirculation zones, mainly along the valve stem. The impact of the main beam on the casing head causes a further flow dispersion. On the other hand, the narrower outlet helps reducing the recirculations in the rear part of the domain. The absence of the recirculation passing the outlet then affects the balance of the mass flow rate.

From the numerical point of view the complete geometry seems more delicate and sensitive due to the interferences with the recirculations.

7.4.4 Sensitivity to Gradient Discretization

The viscous terms in the Navier-Stokes equations contain the gradients of velocity and temperature. Section 5.6.1 describes two methods (exact and approximate) of computing the gradients on structured grids.

Because of its lower demands the *approximate* method is preferred and has been used in all the simulations. Figure 7.33 (resp. the table 7.12) visualizes (resp. quantifies) the differences due to the gradient discretization.

Both the flow fields look similar and only a detailed overlay of the isolines discovers minor differences near the outlet boundary. These discrepancies are probably caused by the higher sensitivity to the outlet boundary condition (note that the solution suffers by the recirculation zone passing the boundary, that is numerically inconsistent to the condition imposed). Besides, further upstream from the outlet boundary the overlay shows practically an excellent agreement.

The differences on the monitored outputs are also within the accuracy of the method, proving the commutability of the discretization techniques.

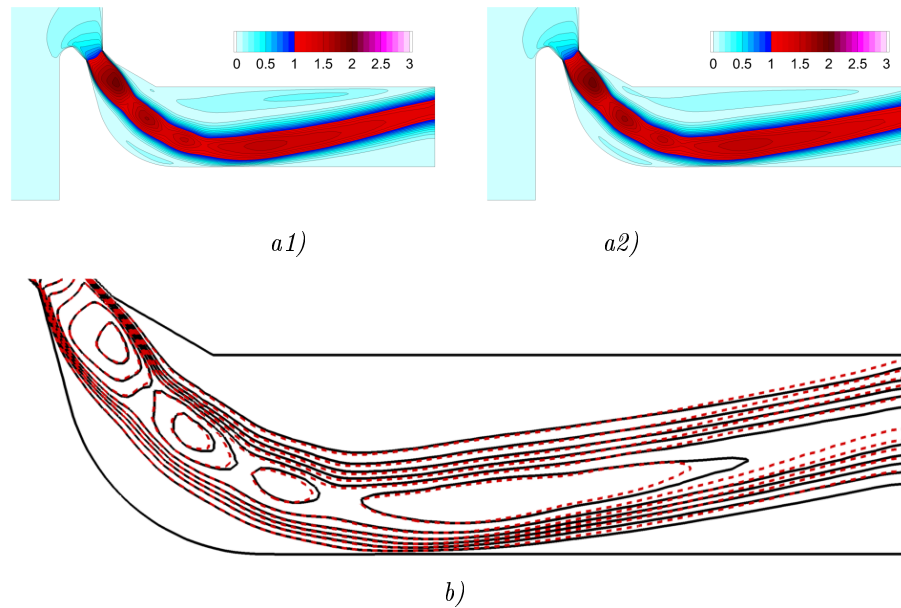


Figure 7.33: Laminar flow simulation, the MUSA solver, $p_2/p_0 = 0.250$, $Re/L = 1500$, isolines of the Mach number. Gradient discretization *a1)* approximate method, *a2)* exact method, *b)* isolines overlay.

Gradient discretization	approximate		exact	
	Abs.	Diff [%]	Abs.	Diff [%]
Max. Mach number	1.936	0.0	1.943	0.4
Avg. outlet Mach number	0.511	0.0	0.516	1.6
Mass flow rate	1.813	0.0	1.815	0.1

Table 7.12: Laminar flow simulation, $p_2/p_0 = 0.250$, $Re/L = 1500$. Influence of the discretization method for the variable gradients.

7.4.5 Summary for Laminar Flow Model

- The laminar flow model has confirmed the qualitative predictions of the inviscid flow model (size, position and importance of the recirculation zones).
- The results obtained are in a good agreement with the theoretical expectations (the successive loss of stability for an increasing Reynolds number).
- The low sensitivity of the solution to the different discretization techniques for the variable gradients has been proven.
- In order to simulate the real flow conditions in the exhaust channel, the laminar flow model remains only an intermediate step towards the turbulent flow computations.

Further conclusions would require some deeper investigations and/or more advanced numerical approaches, which have however not been a goal of this work.

7.5 Turbulent Flow Model

This section is subdivided into four main parts according to the geometry dimension and the movability of the exhaust valve during a simulation: *2D/3D* and *fixed/moving*.

The effect of the turbulence modelling on the solution has been studied for each part, together with the influence of the valve geometry (see section 7.2) and operating conditions (mainly for simulations with a moving valve). The effects of the individual attributes have been described through a qualitative comparison of the flow fields and the appraisal of the mass flow rate and the average outlet Mach number. For the sake of completeness (see section 7.3) the maximal Mach number across a domain is also monitored.

Computation Setup

All the results with the turbulent flow model have been acquired with the COOLFluiD solver. If not stated otherwise and according to the previous explorations of chapter 6, the *AUSM+up* scheme has been selected. The Barth limiter has been chosen to accompany the spatial reconstruction (section 5.5) and the ALE formulation has been used for the computations on moving grids.

Remaining parameters have either been uniquely defined in chapter 5 or have been subject to the influence testing and therefore being specified in the setup of respective simulations.

7.5.1 2D Geometry, Fixed Valve

Sensitivity to Domain Discretization

The first simulations have been aimed at the sensitivity to the domain discretization. In other words, how big would be the solution error for coarser/finer computational grids. This study is useful for respective future calculations and provides basic information about the requirements on the grid quality.

Three grids have been tested in particular: a regular grid and (roughly) a twice coarser and a twice finer alternative. Their description is in the table 7.13.

Grid no.	1	2	3
Size	8 820	21 680	42 480
Pts. across throat	40	70	100
Element type	triangle		

Table 7.13: Computational grids for 2D turbulent simulations.

For this exploration the SST turbulence model has been used. The outlet pressure has been set to $p_2 = 100$ kPa (simulating an atmospheric condition), the pressure ratio $p_2/p_0 = 0.400$ and the freestream temperature $T = 500$ K. For aerodynamically choked flow the mass flow rate is always determined by the critical section of the channel. In order to overcome this constraint the valve lift $L = 7$ mm has been used (usual lift for computations with fixed valve is $L = 4$ mm).

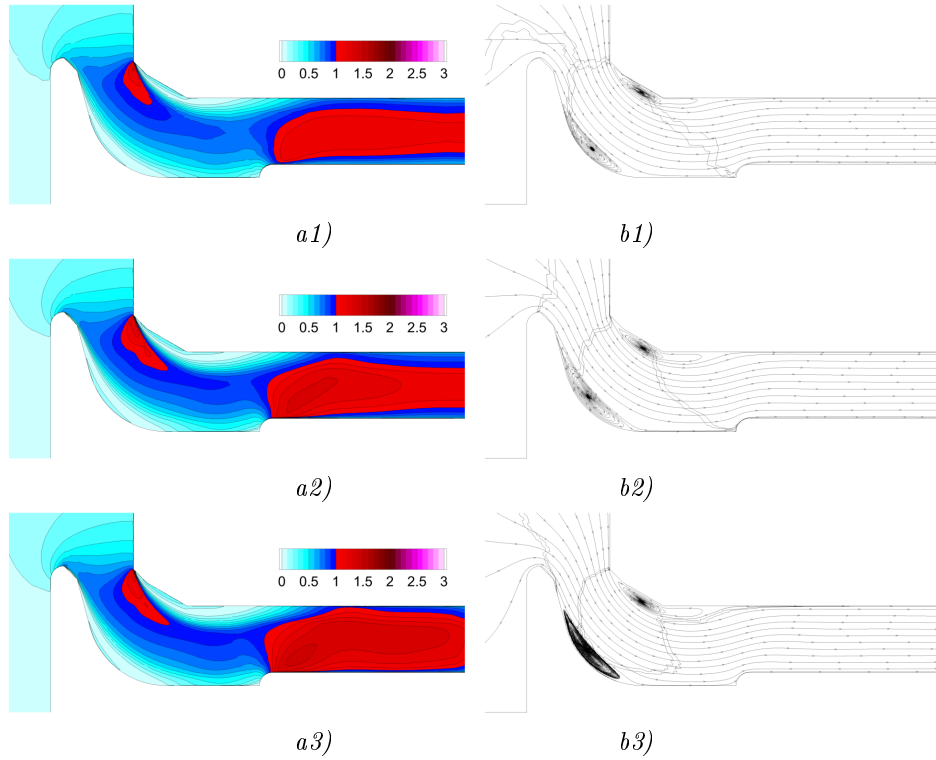


Figure 7.34: Sensitivity to grid coarseness. Turbulent flow simulation, SST turbulence model, $L = 7$ mm, $p_2/p_0 = 0.400$. *a)* isolines of the Mach number, *b)* velocity streamlines; According to the table 7.13: *a1) b1)* grid 1, *a2) b2)* grid 2, *a3) b3)* grid 3.

Figure 7.34 shows the comparison of the flow fields for all the grids tested. The most significant differences are visible for the coarse grid which predicts a lower supersonic expansion and smaller separation zones. Nonetheless, despite these imperfections even this solution can provide a reliable prediction of the flow topology.

For the finer grid the differences have become less evident - apart from the flow near the outlet. The summary of all the computations is tabulated in 7.14. According to this table an obvious accuracy improvement with the finer grid has been observed. All three computations have been run on the identical hardware environment (CPU, RAM, HW load) and with identical level of parallelization. The wall-clocktime measured then indicates that further grid refinements would lead to excessive growth of time demands which seems inadequate to the precision gained.

Grid no.	1		2		3	
Size [elements]	8 820		21 680		42 480	
	Abs.	Diff [%]	Abs.	Diff [%]	Abs.	Diff [%]
Max. M [-]	1.209	-9.3	1.333	0.0	1.349	1.2
Avg. outlet M [-]	0.996	-2.5	1.022	0.0	1.038	1.6
Mass flow rate [kg/s]	3.350	-0.7	3.374	0.0	3.386	0.4
Wall-clocktime [min]	190	-2.6	195	0.0	290	48.7

Table 7.14: Turbulent flow simulation. Sensitivity to grid coarseness.

Sensitivity to Numerical Scheme Parameter

As mentioned in the section 5.4, the numerical scheme used (AUSM+up) requires a user-defined parameter M_∞ . Regarding the theory this Mach number is likely related to the freestream velocity or the conventional compressibility limit. Because the usual flow field in the exhaust channel evinces no obvious reference (freestream) values, the three magnitudes of M_∞ have been tested: 0.01; 0.10; 0.30.

The SST turbulence model has been used, the pressure ratio $p_2/p_0 = 0.400$, $p_2 = 100$ kPa and the valve lift $L = 4$ mm.

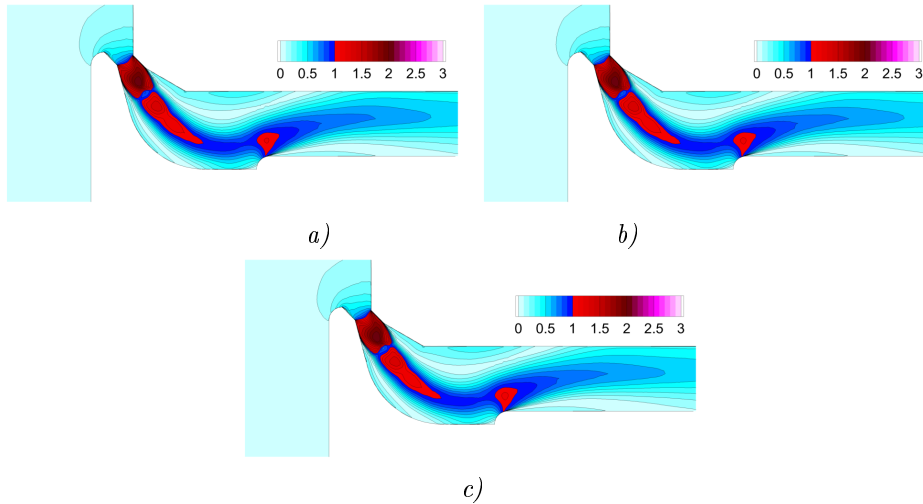


Figure 7.35: Sensitivity to numerical scheme parameter. Turbulent flow simulation, SST turbulence model, $L = 4$ mm, $p_2/p_0 = 0.400$. Isolines of the Mach number *a)* $M_\infty = 0.01$, *b)* $M_\infty = 0.10$, *c)* $M_\infty = 0.30$.

M_∞	0.01		0.10		0.30	
	Abs.	Diff [%]	Abs.	Diff [%]	Abs.	Diff [%]
Max. M [-]	2.071	-0.4	2.079	0.0	2.081	0.1
Avg. outlet M [-]	0.399	0.2	0.398	0.0	0.398	0.0
Mass flow rate [kg/s]	1.231	-0.0	1.231	0.0	1.232	0.1

Table 7.15: Turbulent flow simulation. Sensitivity to the parameter of the AUSM+up scheme.

According to the figure 7.35 and the table 7.15 negligible differences have been observed, proving the flow insensitivity to M_∞ (within the range tested). For all future computations, this parameter has been set to $M_\infty = 0.1$.

Influence of Turbulence Models

One of the important observations has been the impact of the turbulence model chosen on the solution. All the models implemented have been tested on the exhaust channel geometry with identical boundary conditions: the pressure ratio $p_2/p_0 = 0.400$, $p_2 = 100$ kPa, the temperature $T = 500$ K and the valve lift $L = 4$ mm.

The overview of the flow fields is shown in figures 7.36 and 7.37, the quantified parameters are in the table 7.16 (the SST model has been chosen as a reference).

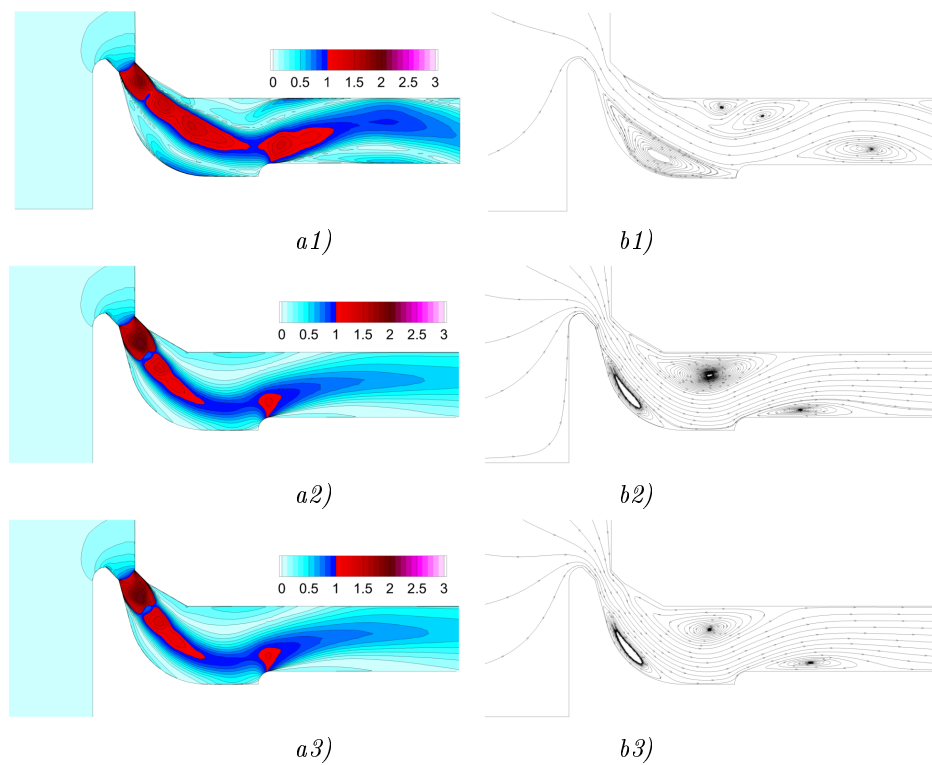


Figure 7.36: Influence of the turbulence model. $L = 4$ mm, $p_2/p_0 = 0.400$. a) isolines of the Mach number, b) velocity streamlines, a1, b1) Spalart-Allmaras, a2, b2) BSL, a3, b3) SST.

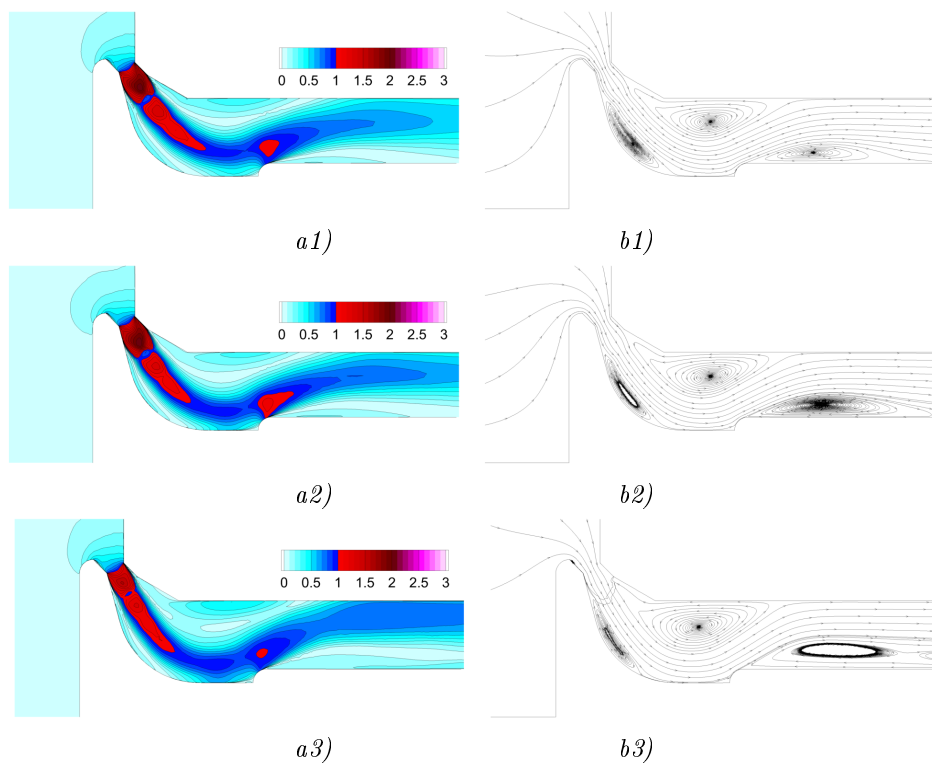


Figure 7.37: Influence of the turbulence model. $L = 4$ mm, $p_2/p_0 = 0.400$. a) isolines of the Mach number, b) velocity streamlines, a1, b1) Wilcox, a2, b2) TNT, a3, b3) EARSM.

Turbulence model	SST		S-A		BSL	
	Abs.	Diff [%]	Abs.	Diff [%]	Abs.	Diff [%]
Max. M [-]	2.079	0.0	1.941	-6.6	2.084	0.2
Avg. outlet M [-]	0.398	0.0	0.460	15.6	0.398	0.0
Mass flow rate [kg/s]	1.231	0.0	1.241	0.8	1.232	0.0
Turbulence model	Wilcox		TNT		EARSM	
	Abs.	Diff [%]	Abs.	Diff [%]	Abs.	Diff [%]
Max. M [-]	2.055	-1.2	2.067	-0.6	1.617	-22.2
Avg. outlet M [-]	0.401	0.8	0.414	4.0	0.452	13.6
Mass flow rate [kg/s]	1.230	-0.1	1.234	0.2	1.233	0.2

Table 7.16: Influence of the turbulence model.

The graphs 7.39 show the distribution of the pressure and the Mach number along the central streamline⁴ and the table 7.17 compares the size of the main recirculation zones.

The computations for all the models have converged to a qualitatively same result. For the pressure ratio given, the channel gets aerodynamically choked, forming a compact supersonic flow beam that passes the domain. As schematized in figure 7.38 on both sides of the beam the recirculation zones appear. The separation is either caused by the sharp corners (mainly on the upper wall) or induced by the shock wave which deflects the flow (mainly on the valve). Next significant recirculation appears along the valve casing. With a close zoom a couple of small recirculations can be found behind the valve seat and near the intersection of the valve stem and casing.

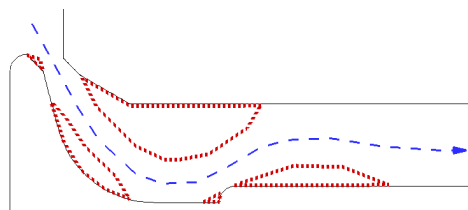


Figure 7.38: Scheme of the main recirculation zones, 2D model.

The large recirculations form a second aerodynamical throat inside the channel, that allows another weaker supersonic expansion. For most of the models the flow beam then spreads across the entire outlet section.

Due to the aerodynamical blockage of the channel, all the models have predicted (nearly) identical values of the mass flow rate. An overall closest agreement has been observed among the SST, BSL and the Wilcox models. The Spalart-Allmaras model has predicted the largest recirculation along the valve, that has affected the rest of the flow topology. The significant differences have also been observed for the EARSM model, that predicts the earliest separation on the upper wall. The evoked restriction of the active section then does not allow such a strong supersonic expansion behind the throat. For the S-A, TNT and the EARSM models a next recirculation passing the outlet boundary has been observed.

⁴The central streamline is released from the geometrical mid-point of the throat.

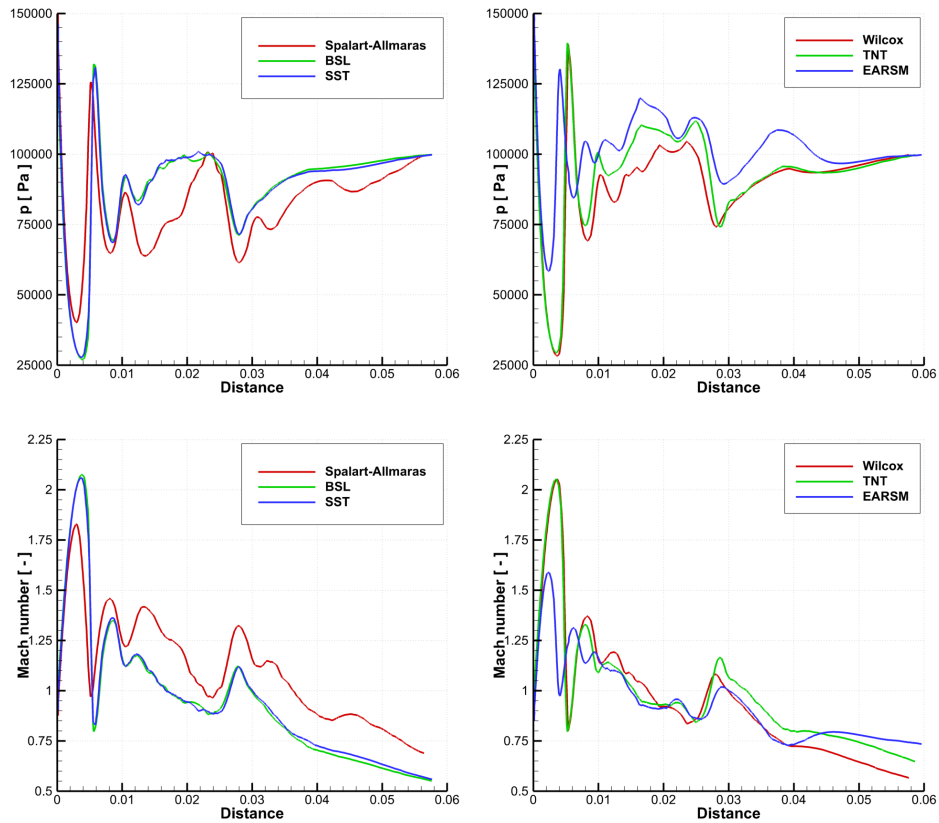
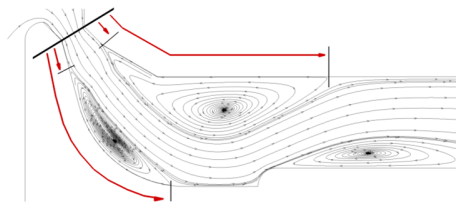


Figure 7.39: Distribution of the pressure and the Mach number along the central streamline for different turbulence models.



Turbulence model	Size of recirculation [mm]					
	Channel wall			Valve		
	start	end	length	start	end	length
Spalart-Allmaras	2.80	35.89	33.08	1.51	30.84	29.35
BSL	4.31	29.35	25.05	4.29	21.68	17.39
SST	4.28	29.16	24.88	3.91	21.52	17.61
Wilcox	3.18	28.97	25.79	3.93	20.56	16.64
TNT	4.11	28.60	24.49	3.89	19.07	15.18
EARS	0.37	29.35	29.53	2.62	16.45	13.83

Table 7.17: Influence of the turbulence models on the size of recirculation zones.

Influence of Pressure Ratio

In order to match better the pressure ratio of a real engine, for the two turbulence models selected, SST and EARS, the previous value of p_2/p_0 has been decreased to $p_2/p_0 = 0.250$. At the same time the influence of the valve casing has been tested. All the remaining parameters were kept the

same as in the section “Influence of Turbulence Models”.

The comparison of the flow fields with the complete geometry is shown in figure 7.40, for the simplified geometry (without the casing) in figure 7.41. The complete quantitative comparison is in the tables 7.18 and 7.19.

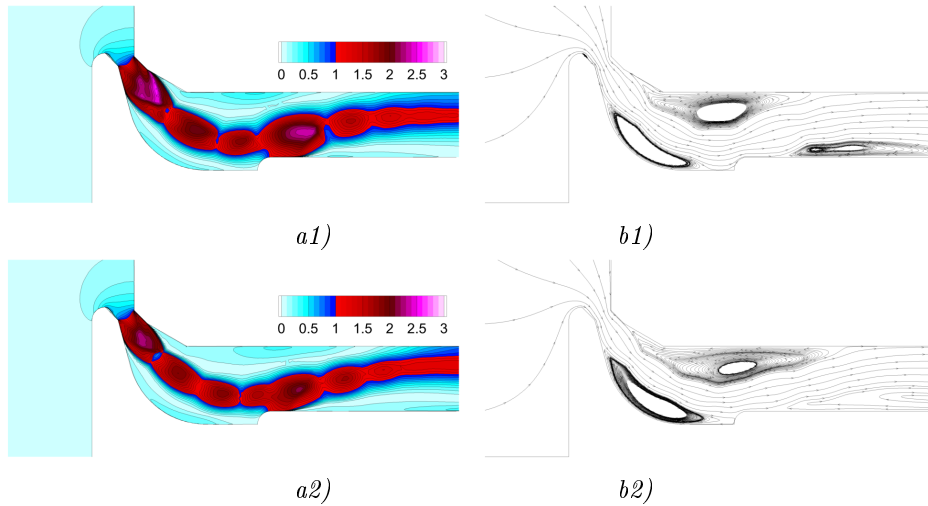


Figure 7.40: Influence of the turbulence model. $L = 4$ mm, $p_2/p_0 = 0.250$. *a)* isolines of the Mach number, *b)* velocity streamlines, *a1, b1)* SST, *a2, b2)* EARSM.

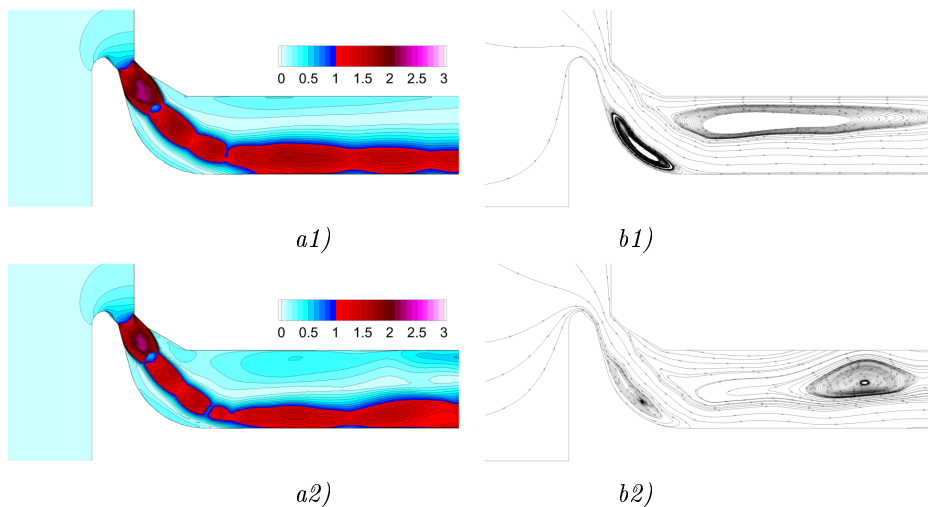


Figure 7.41: Influence of the turbulence model. Simplified geometry without the casing. $L = 4$ mm, $p_2/p_0 = 0.250$. *a)* isolines of the Mach number, *b)* velocity streamlines, *a1, b1)* SST, *a2, b2)* EARSM.

For the complete geometry the flow topology has remained the same as in the schematic figure 7.38. The flow is, however, distinctly faster, creating a series of the so-called supersonic shock-diamonds. Their pattern has also impressed into the recirculations (particular shock-diamonds can be clearly identified from the streamlines plot). The EARSM model predicts again an earlier separation on the upper wall, but the separation point predicted on the valve is the same with the SST model. For both models the recirculation along the casing elongates and leaves the domain.

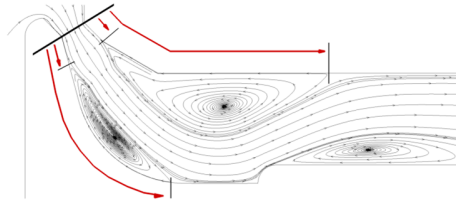
For the simplified geometry without casing the flow topology changes notably. Although still consisting of the similar shock-diamond pattern the flow does not reflect from the valve and remains

attached to the valve stem. This has resulted in a massive enlargement of the upper recirculation zone. From the quantitative point, both the turbulence models have reached a good agreement in the position of the separation points on both sides and the re-attachment point on the valve.

Turbulence model	SST		EARSM	
	Abs.	Diff [%]	Abs.	Diff [%]
Max. M [-]	2.617	0.0	2.293	-12.4
Avg. outlet M [-]	0.620	0.0	0.654	5.5
Mass flow rate [kg/s]	1.993	0.0	1.980	-0.6

Turbulence model	SST		EARSM	
	Abs.	Diff [%]	Abs.	Diff [%]
geometry without casing				
Max. M [-]	2.332	0.0	2.296	-1.5
Avg. outlet M [-]	0.557	0.0	0.628	12.8
Mass flow rate [kg/s]	1.982	0.0	1.984	0.1

Table 7.18: Influence of the turbulence model, $p_2/p_0 = 0.250$.



Turbulence model	Size of recirculation [mm]					
	Channel wall			Valve		
	start	end	length	start	end	length
SST	4.77	35.70	30.93	4.95	27.45	22.50
EARSM	4.12	37.76	33.63	4.86	30.84	25.98
SST (no casing)	3.74	-	-	4.30	24.48	20.18
EARSM (no casing)	3.36	-	-	3.89	24.67	20.78

Table 7.19: Influence of the turbulence models on the size of recirculation zones, $p_2/p_0 = 0.250$.

Due to the aerodynamical blockage of the channel, no significant differences regarding the mass flow rate could be observed for any of the cases.

Influence of Valve Geometry

The influence of the valve shape has been tested on three geometries (see figure 7.4):

- **original** geometry;
- **G1** with a bigger stem curvature;
- **G2** with a milder stem curvature.

In order to avoid an aerodynamical choking the valve lift has been increased to $L = 10$ mm. The SST turbulence model has been applied together with $p_2/p_0 = 0.400$, $p_2 = 100$ kPa and $T = 500$ K. The results comparison is shown in figure 7.42 and in the table 7.20.

For the regime tested a surprising gain of the mass flow rate has been observed for the alternative G2 with the narrowest *geometrical* cross-section. A thicker stem has however prevented the recirculation along the valve, which has led to a slightly wider *active* cross-section.

On the contrary, the alternative G1 hasn't led to any improvement from the original state. Its wider geometrical cross-section has been completely filled with a recirculation that has besides appeared even more restrictive than the original shape.

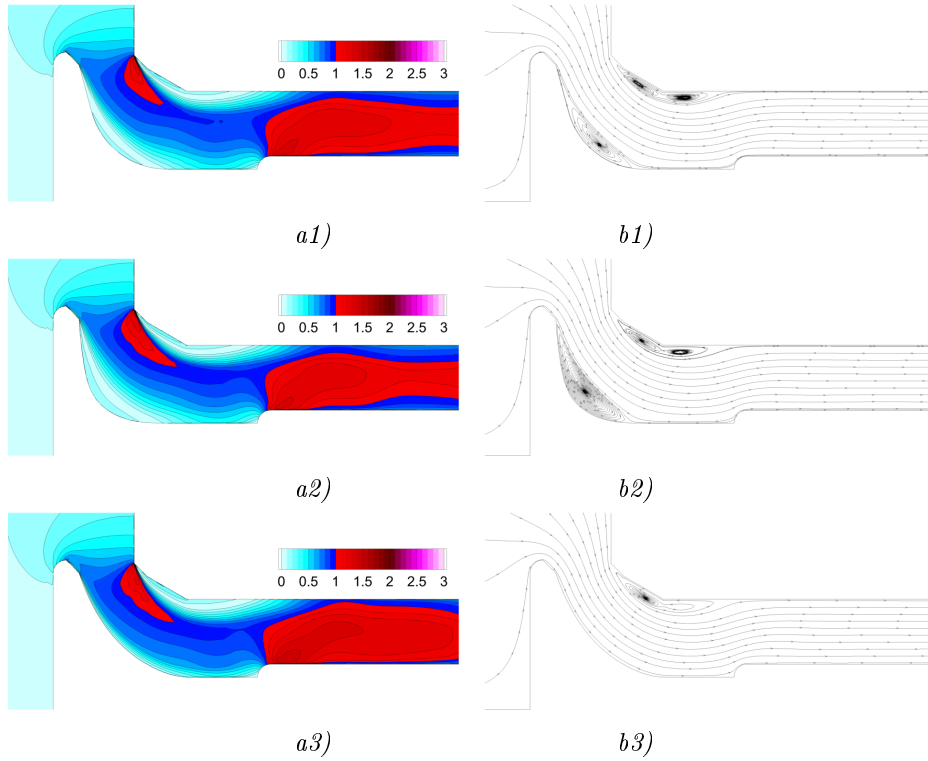


Figure 7.42: Influence of the valve geometry. $L = 10$ mm, $p_2/p_0 = 0.400$. *a)* isolines of the Mach number, *b)* velocity streamlines. Valve geometry *a1*, *b1)* original, *a2*, *b2)* G1, *a3*, *b3)* G2.

Valve geometry	original		G1		G2	
	Abs.	Diff [%]	Abs.	Diff [%]	Abs.	Diff [%]
Max. M [-]	1.351	0.0	1.348	-0.2	1.468	8.7
Avg. outlet M [-]	1.015	0.0	1.002	-1.4	1.061	4.5
Mass flow rate [kg/s]	3.427	0.0	3.418	-0.3	3.477	1.4

Table 7.20: Influence of the valve geometry.

7.5.2 3D Geometry, Fixed Valve

Sensitivity to Domain Discretization

Similarly to the planar computations the sensitivity to the domain discretization has been tested at first. Apart from the regular grid the coarser and finer alternatives have been tested. Note that the overall grid size grows substantially with respect to actual internal detail, shown in the table 7.21.

Grid no.	1	2	3
Size	89 740	439 218	1 504 050
Pts. across throat	42	70	110
Element type	hexahedron		
File* size [MB]	16.7	78.6	264.2

Table 7.21: Computational grids for 3D turbulent simulations.

*) Grid file in a neutral (solution-free, ASCII) format *.neu* .

The computations have been performed on the geometry with the lift $L = 10$ mm, with the SST turbulence model, $p_2/p_0 = 0.400$, $p_2 = 100$ kPa and $T = 500$ K.

The results are presented on three perpendicular planes as sketched in figure 7.43.

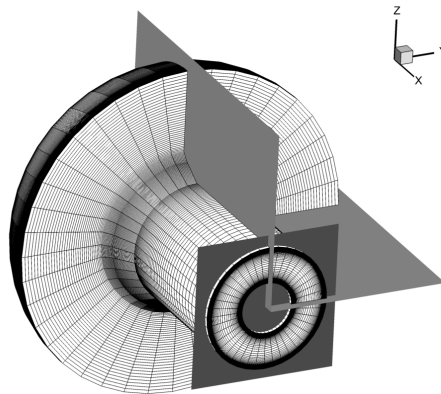


Figure 7.43: 3D grid. Planes for solution extraction.

The longitudinal cuts for the grids tested are shown in figure 7.44, the outlet transverse cut in figure 7.45.

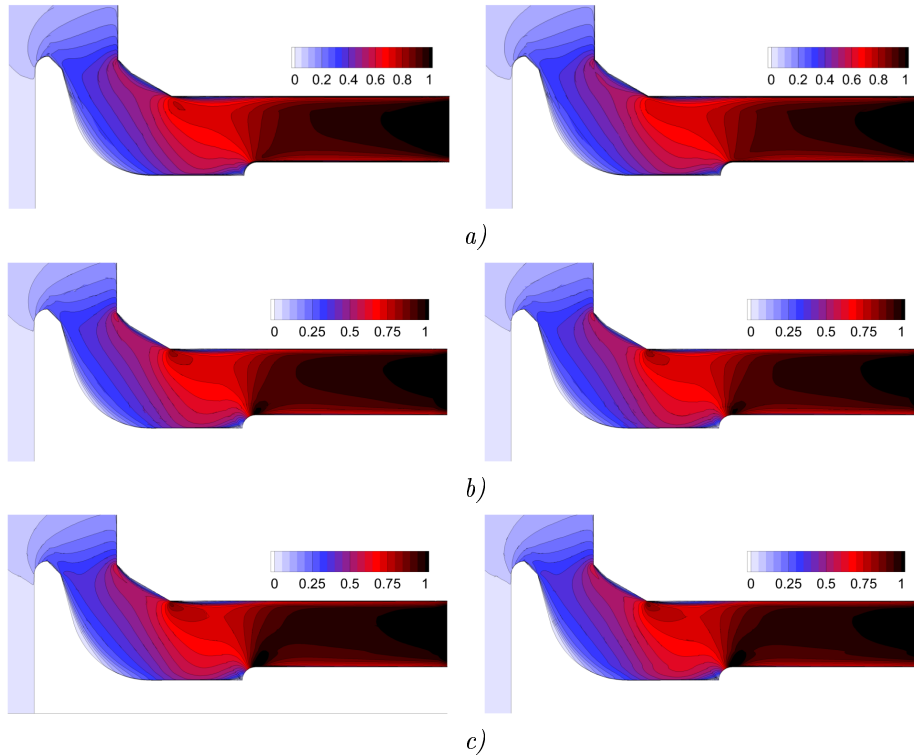


Figure 7.44: Sensitivity to grid coarseness. 3D turbulent flow simulation, SST turbulence model, $L = 10$ mm, $p_2/p_0 = 0.400$, contours of the Mach number, two longitudinal perpendicular cuts. According to the table 7.21: *a)* grid 1, *b)* grid 2, *c)* grid 3.

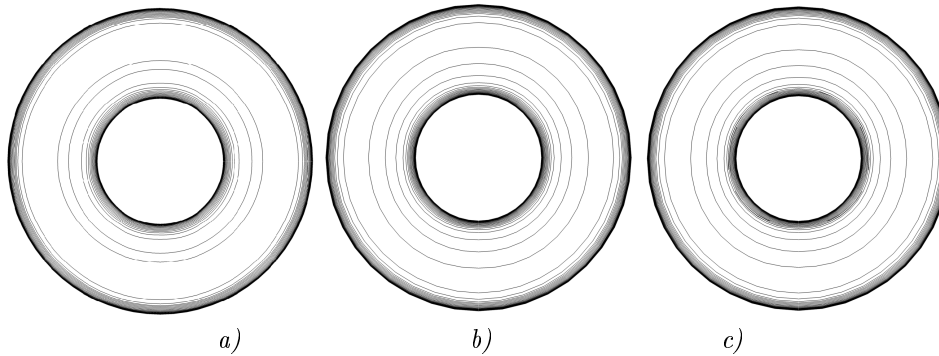


Figure 7.45: Sensitivity to grid coarseness. 3D turbulent flow simulation, SST turbulence model, $L = 10$ mm, $p_2/p_0 = 0.400$, isolines of the Mach number, outlet transverse cut. According to the table 7.21: *a)* grid 1, *b)* grid 2, *c)* grid 3.

Besides the differences in the flow resolution, no significant accuracy improvement has been observed. For all the three grids tested, the flow pattern is nearly symmetric, allowing to capture the main solution character by a single longitudinal cut. Furthermore, within the cut plane the velocity streamlines can be plotted, however some distortions (due to the negligence of the third velocity component in a planar cut) are possible.

The qualitative comparison of the results is in the table 7.22. Some differences can be observed between the grid 1 and 2 (coarse and normal) but almost no differences between 2 and 3 (normal and fine).

Grid no.	1		2		3	
Size [elements]	89 740		439 218		1 504 050	
	Abs.	Diff [%]	Abs.	Diff [%]	Abs.	Diff [%]
Max. M [-]	1.103	-3.9	1.148	0.0	1.148	0.1
Avg. outlet M [-]	0.973	-7.2	1.049	0.0	1.058	0.8
Mass flow rate [kg/s]	0.305	-0.5	0.306	0.0	0.306	0.0
1 iter. wall-clocktime [s]	12.9	-90.1	130.8	0.0	429.8	228.6

Table 7.22: 3D turbulent flow simulation. Sensitivity to grid coarseness.

Due to various parallelization the time demands have been converted to a theoretic wall-clocktime required for 1 iteration on 1 cpu.

As all the computations have been realized at a large valve lift with a relatively smooth solution, the grid quality corresponding to the grid 2 has been chosen also for all the oncoming simulations.

Influence of Turbulence Model

The computations have been performed at identical computational setup as in the 2D simulations: $p_2/p_0 = 0.400$, $p_2 = 100$ kPa, $T = 500$ K and $L = 4$ mm. Only three turbulence models have been tested: SST, Wilcox and EARSM - see figure 7.46 and the table 7.23.

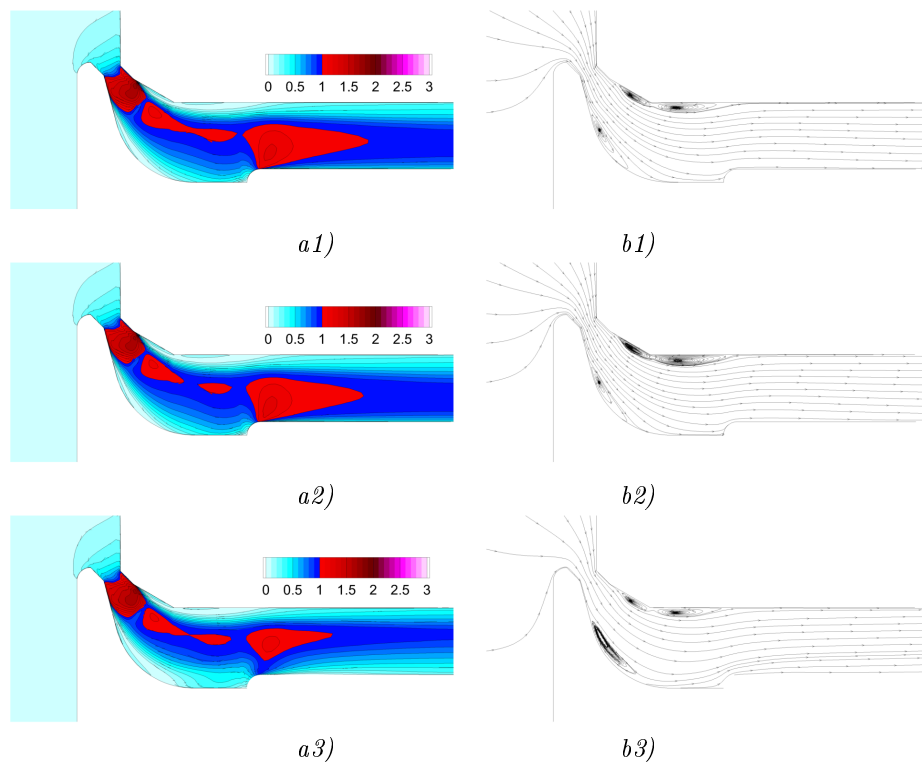


Figure 7.46: Influence of the turbulence model. $L = 4$ mm, $p_2/p_0 = 0.400$. a) isolines of the Mach number, b) velocity streamlines, a1, b1) SST, a2, b2) Wilcox, a3, b3) EARSM.

Turbulence model	SST		Wilcox		EARSM	
	Abs.	Diff [%]	Abs.	Diff [%]	Abs.	Diff [%]
Max. M [-]	1.757	0.0	1.743	-0.8	1.686	-4.0
Avg. outlet M [-]	0.758	0.0	0.750	-1.0	0.665	-12.2
Mass flow rate [kg/s]	0.180	0.0	0.179	-0.7	0.174	-2.2

Table 7.23: Influence of the turbulence model.

The computations with all the models have converged to a similar solution, schematized in figure 7.47.

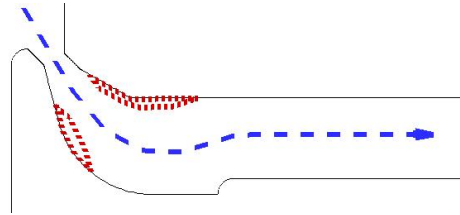
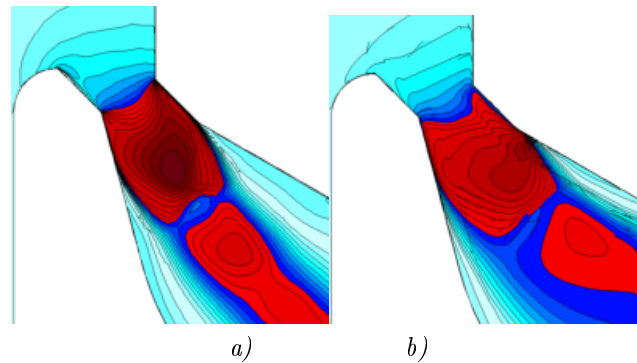


Figure 7.47: Scheme of the main recirculation zones, 3D model.

The large (and numerous) recirculations observed in the planar cases have been reduced to just two recirculation zones, both being induced by the shock-wave.

The dominant flow beam formed at the channel throat uniformly fills the exhaust pipe staying attached to the valve stem (SST and Wilcox models) or leaving through the centre of the channel (EARSM). The structure of the first supersonic pocket differs from the planar case, mainly in the shape of the sonic line and the shifted region with highest velocity, see figure 7.48.

Figure 7.48: Detail of the throat zone. *a)* 2D model, *b)* 3D model.

The quantitative comparison later shows a very good agreement between the SST and Wilcox models. The EARSM model predicts slightly lower values of all the outputs monitored.

Influence of Inlet Wall Inclination

In the section 7.3.1 an artificial geometry with an inclined inlet wall has been proposed, see figure 7.19. Its goal has been to control and/or reduce the recirculations inside the channel.

The modification has been tested on a channel with $L = 10$ mm, $p_2/p_0 = 0.400$, $p_2 = 100$ kPa and $T = 500$ K, with the SST turbulence model. See figure 7.49 and the table 7.24 for results.

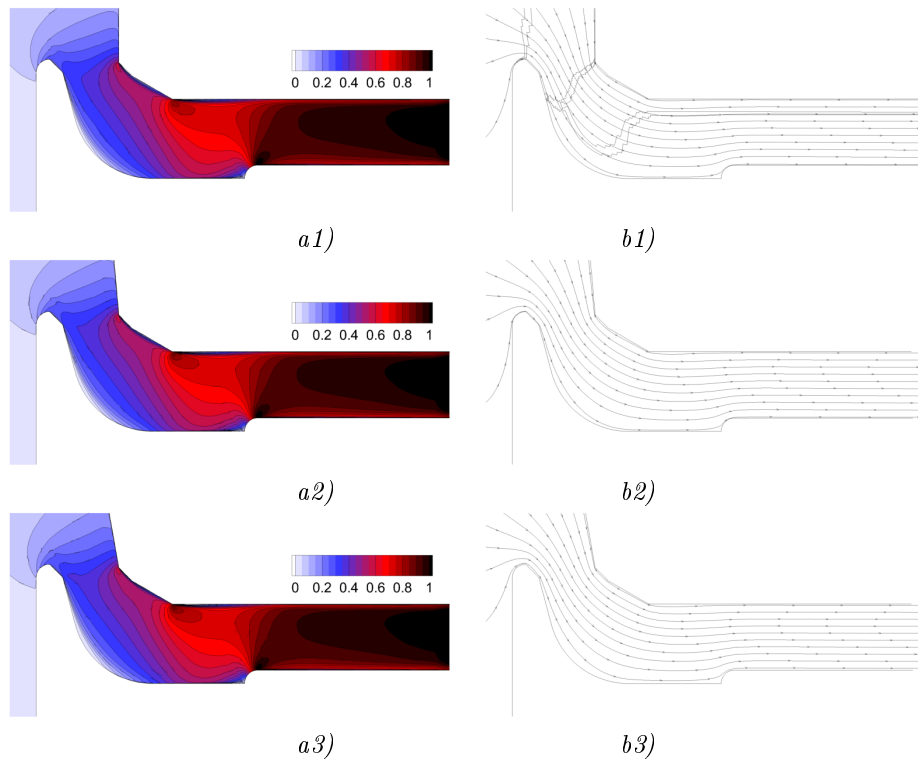


Figure 7.49: Influence of the inclined inlet wall. $L = 4$ mm, $p_2/p_0 = 0.400$. *a*) isolines of the Mach number, *b*) velocity streamlines, *a1*, *b1*) 0 degrees (original), *a2*, *b2*) 5 degrees, *a3*, *b3*) 10 degrees.

Inclination angle	0°		5°		10°	
	Abs.	Diff [%]	Abs.	Diff [%]	Abs.	Diff [%]
Max. M [-]	1.148	0.0	1.149	0.1	1.149	0.1
Avg. outlet M [-]	1.049	0.0	1.072	2.2	1.074	2.4
Mass flow rate [kg/s]	0.306	0.0	0.304	-0.7	0.305	-0.3

Table 7.24: The influence of the inclination angle.

For the regime given on a real (i.e. 3D) geometry, none of the streamline plots detects a recirculation, therefore the effect desired could not be reached. The quantitative comparison has also shown no significant gain (the mass flow rate has even dropped under the original value).

All the computations with an inclined inlet wall have therefore resulted in no substantial improvement against the status geometry. Hence, within the parameters monitored, this geometrical modification seems inefficient.

Influence of Inlet Boundary Condition

As described in the section 5.10, the inlet boundary condition imposes the total pressure, the total temperature and the incidence angle. For the (original) *radial* inlet, this angle is perpendicular to the inlet boundary (figure 7.50 *a*). The second alternative tested, the *tangential* inlet, has rotated the velocity vector by 90 degrees (indicated in figure 7.50 *b*).

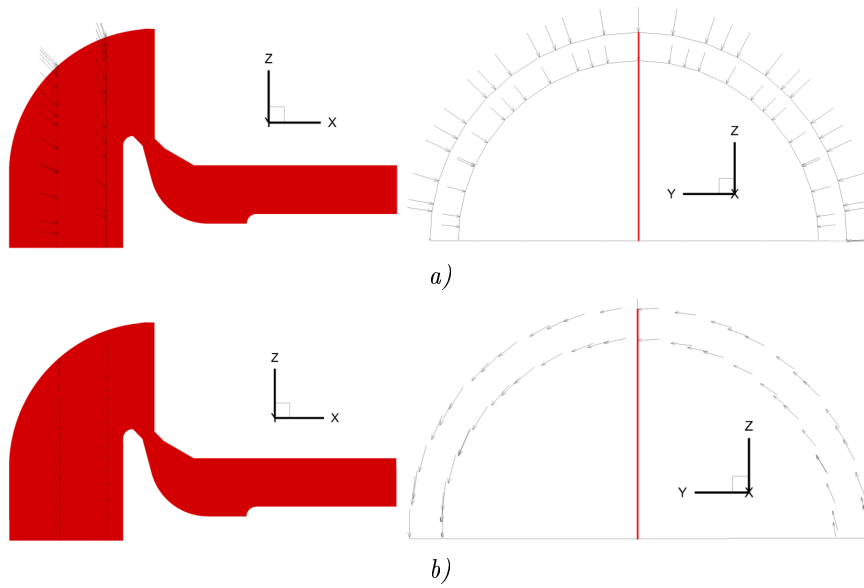


Figure 7.50: Schematic view of different inlet boundary conditions: *a)* radial inlet, *b)* tangential inlet.

Two valve lifts 4 and 10 mm have been tested. Figure 7.51 and the table 7.25 prove a large sensitivity on the tangential velocity component for both the lifts.

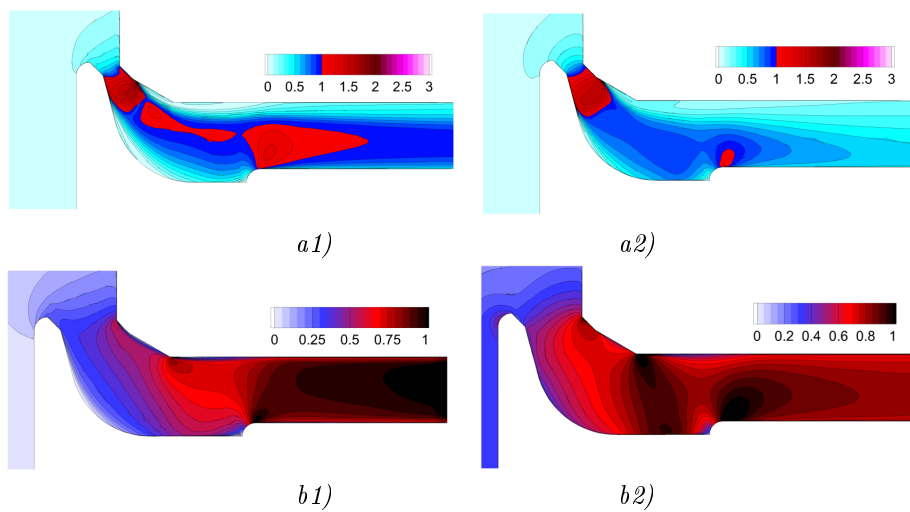


Figure 7.51: Influence of the inlet boundary condition, SST model, $p_2/p_0 = 0.400$. Contours of the Mach number. *a)* $L=4$ mm, *b)* $L=10$ mm; *a1)*, *b1)* radial inlet, *a2)*, *b2)* tangential inlet.

Inlet condition	radial		tangential	
L=4 mm	Abs.	Diff [%]	Abs.	Diff [%]
Max. M [-]	1.757	0.0	1.635	-6.9
Avg. outlet M [-]	0.758	0.0	0.485	-36.0
Mass flow rate [kg/s]	0.180	0.0	0.172	-4.4
Inlet condition	radial		tangential	
L=10 mm	Abs.	Diff [%]	Abs.	Diff [%]
Max. M [-]	1.148	0.0	1.179	2.7
Avg. outlet M [-]	1.049	0.0	0.733	-30.1
Mass flow rate [kg/s]	0.306	0.0	0.291	-4.9

Table 7.25: The influence of the inlet boundary condition.

For the lower lift the centripetal forces turn the supersonic expansion (and following flow) towards the valve stem, together with a reduction of further supersonic pockets. The substantial diversion of the incoming flow also affects the sonic line. The similar trends have been observed also for the bigger lift.

For the average outlet Mach number and the mass flow rate the differences of the same order have been found for both the lifts tested.

Influence of Valve Geometry

The three valve shapes tested were the *original*, *G1* (with a bigger stem curvature) and *G2* (with a milder stem curvature). In order to avoid an aerodynamical choking the valve lift has been set to $L = 10$ mm. The SST turbulence model has been applied together with $p_2/p_0 = 0.400$, $p_2 = 100$ kPa and $T = 500$ K.

The results comparison is presented in figure 7.52 and in the table 7.52.

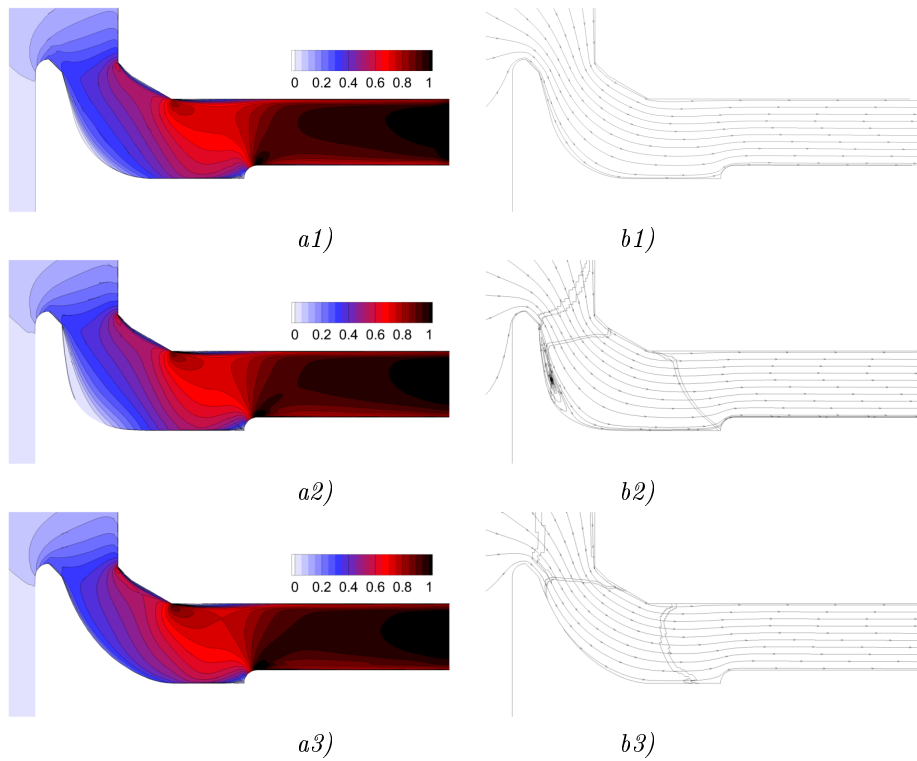


Figure 7.52: Influence of the valve geometry. $L = 10$ mm, $p_2/p_0 = 0.400$. *a)* isolines of the Mach number, *b)* velocity streamlines. Valve geometry *a1*, *b1)* original, *a2*, *b2)* G1, *a3*, *b3)* G2.

Valve geometry	original		G1		G2	
	Abs.	Diff [%]	Abs.	Diff [%]	Abs.	Diff [%]
Max. M [-]	1.148	0.0	1.128	-1.7	1.164	1.4
Avg. outlet M [-]	1.049	0.0	1.010	-3.7	1.013	-3.4
Mass flow rate [kg/s]	0.306	0.0	0.296	-3.3	0.301	-1.6

Table 7.26: Influence of the valve geometry.

Compared to the planar computations no altered shape provides a larger mass flow rate than the original valve. A surprising drop has been observed for the G1 geometry. The streamline plot has then discovered a separation zone which has arisen along the valve. For both the geometries remaining no recirculations have been registered.

This comparison has again confirmed that a slimmer valve does not always lead to an (intuitive) improvement of the exhaust efficiency, as the wider geometrical cross-section gets usually filled with a hollow recirculation.

7.5.3 2D Geometry, Moving Valve

Influence of Unsteady Approach

The first interest, after having developed the method for computations with moving valve, has been to study the actual influence of this unsteady approach. In order to avoid issues with the remeshing and the solution interpolation (discussed in the section 5.9.3) the first computation has been accomplished for an oscillating valve at a big valve lift.

The movement has been imposed by as sinusoidal ($L_0 = 10$ mm, amplitude 1 mm) and the boundary conditions have been fixed at constant values: $p_2/p_0 = 0.500$, $p_2 = 100$ kPa and $T = 500$ K, SST turbulence model. As indicated in figure 7.53 three cycle periods have been simulated.

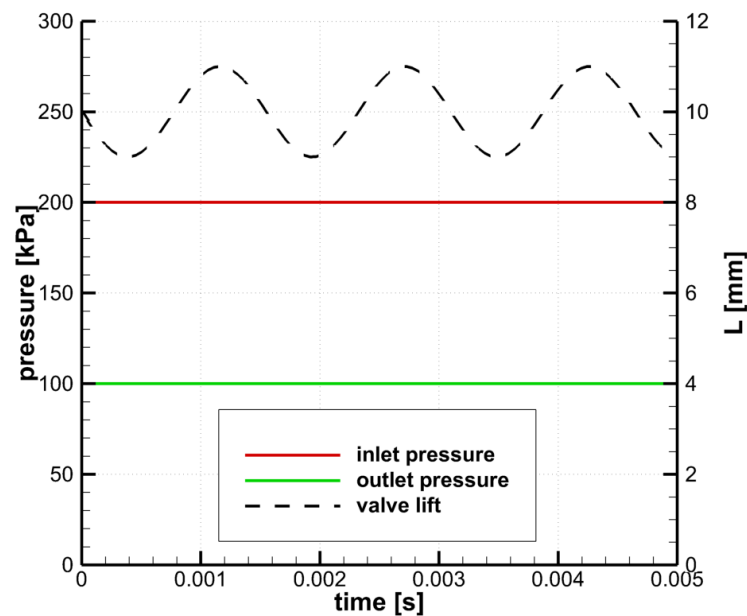


Figure 7.53: Setup of the boundary conditions and the valve movement for an initial unsteady simulation.

Figure 7.54 compares the initial solution (steady state simulation on the fixed geometry) with the solutions at the identical valve lift after three cycle periods (at opening and closing stage). The table 7.27 compares the the quantitative indicators.

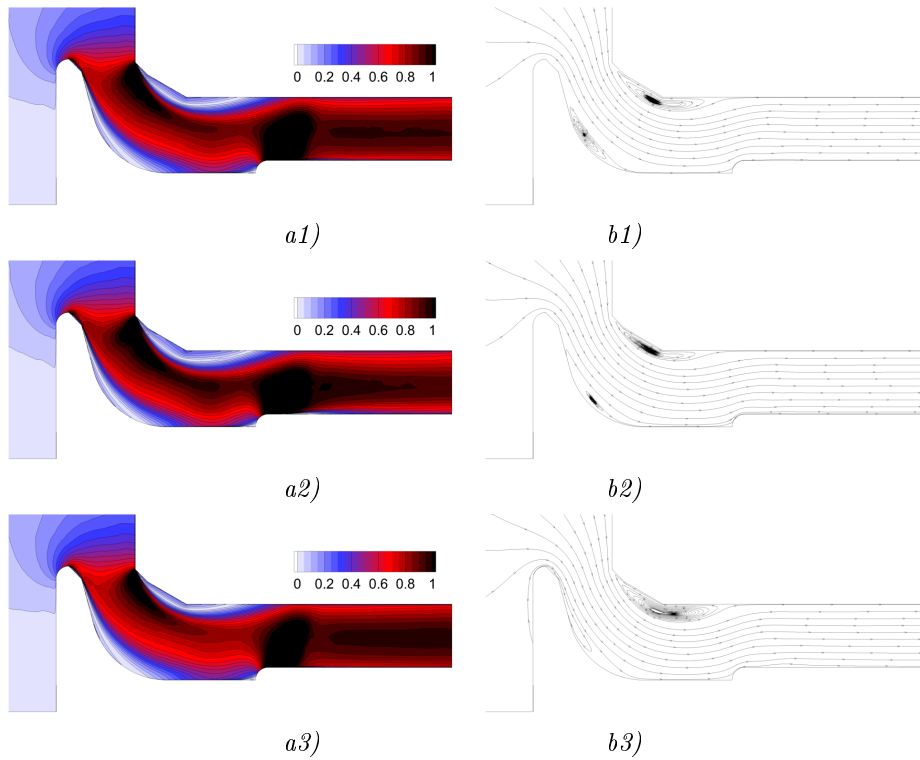


Figure 7.54: Influence of the unsteady approach, $L = 10$ mm, $p_2/p_0 = 0.500$. *a)* isolines of the Mach number, *b)* velocity streamlines, *a1, b1)* steady state solution, *a2, b2)* unsteady (opening stage), *a3, b3)* unsteady (closing stage).

	steady		unsteady			
	Abs.	Diff [%]	opening		closing	
Abs.			Diff [%]	Abs.	Diff [%]	
$L=10$ mm						
Max. M [-]	1.475	0.0	1.548	4.9	1.467	-0.5
Avg. outlet M [-]	0.824	0.0	0.784	-4.9	0.858	4.1
Mass flow rate [kg/s]	2.761	0.0	2.612	-5.4	2.893	4.8

Table 7.27: Influence of the unsteady approach.

Apparent differences have been found among all the results shown. The supersonic pocket near the seat reacts on the throat change, taking the flow inertia into account. The separation zone on the upper wall follows these fluctuations accordingly. The effect of the unsteady approach has also been observed on the second supersonic pocket near the casing.

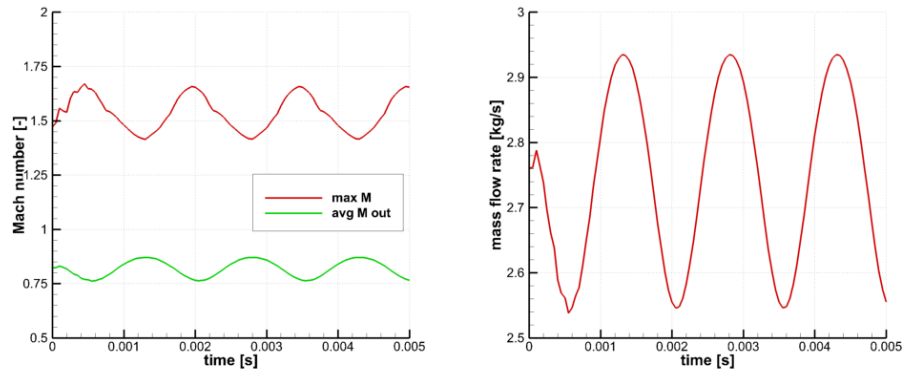


Figure 7.55: Evolution of the Mach number and the mass flow rate with time.

The graph 7.55 plots the time evolution of the parameters monitored. It has been found the solution needs (approximately) one period to stabilize on the periodic pattern. Both the mass flow rate and the average outlet Mach number then reproduce the movement imposed. The contour of the maximal Mach number has an opposite phase and indicates a small discontinuity during the opening stage. Altogether it underlines the non-negligible influence of the unsteady approach.

Simulation of Closing Stage - Influence of Inlet Inclination

Next results present a simulation of the complete closing stage at constant boundary conditions, as shown in figure 7.56. The valve movement is modelled by a quarter sinusoidal; the initial lift $L_0 = 10$ mm; the final lift (as close as possible to) $L_{final} = 0$ mm.

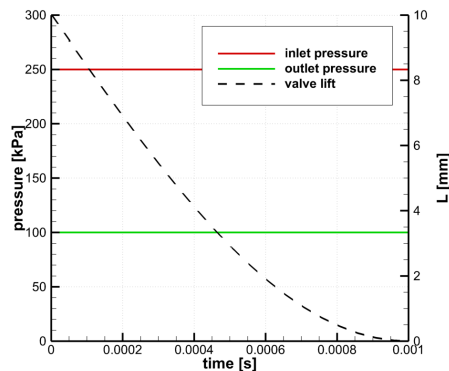


Figure 7.56: Setup of the boundary conditions and the valve movement for a closing stage simulation.

From the numerical point of view, this simulation enforces strong grid deformations which may corrupt the solution (see in the later figure 7.60). To eliminate this risk, a series of three computational grids have been used ($L=10, 6, 3$ mm), among which the respective solution has been interpolated (explained in the section 5.9.3). The interpolation is shown in figure 7.57.

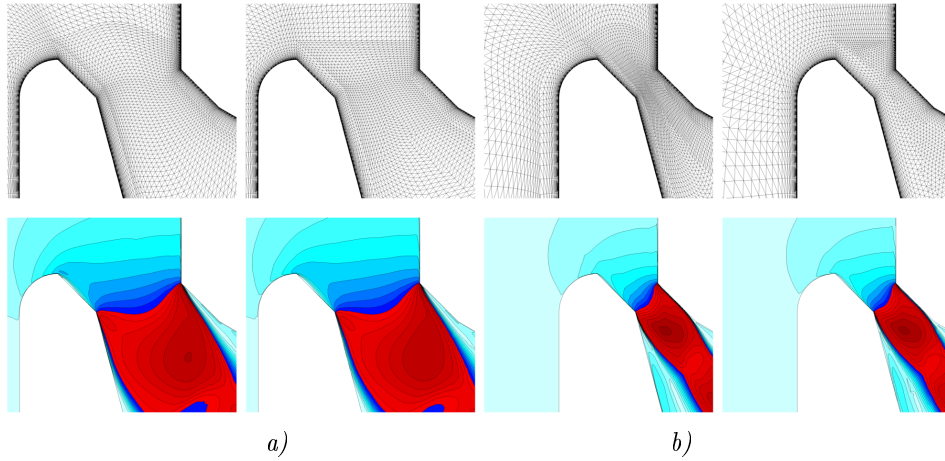


Figure 7.57: Solution interpolation. *a)* $L=6$ mm, *b)* $L=3$ mm. Left: detail of the original (deformed) grid and solution, Right: detail of the new grid, interpolated solution.

The final solution is shown in figure 7.58, the time evolution of the parameters monitored in figure 7.59. For the regime given (constant pressure ratio during entire closing stage) with a decreasing throat cross-section the flow accelerates to supersonic and chokes aerodynamically the channel. By doing so, the mass flow rate is bounded by its critical value and decreases together with the lift. This results to a growth of the recirculation zones.

Initially, the recirculations appear on both sides of the flow beam, however with a smaller lift this beam attaches to one of the walls and reduces the respective recirculation. Note that for very low lifts the flow alters between upper and lower wall.

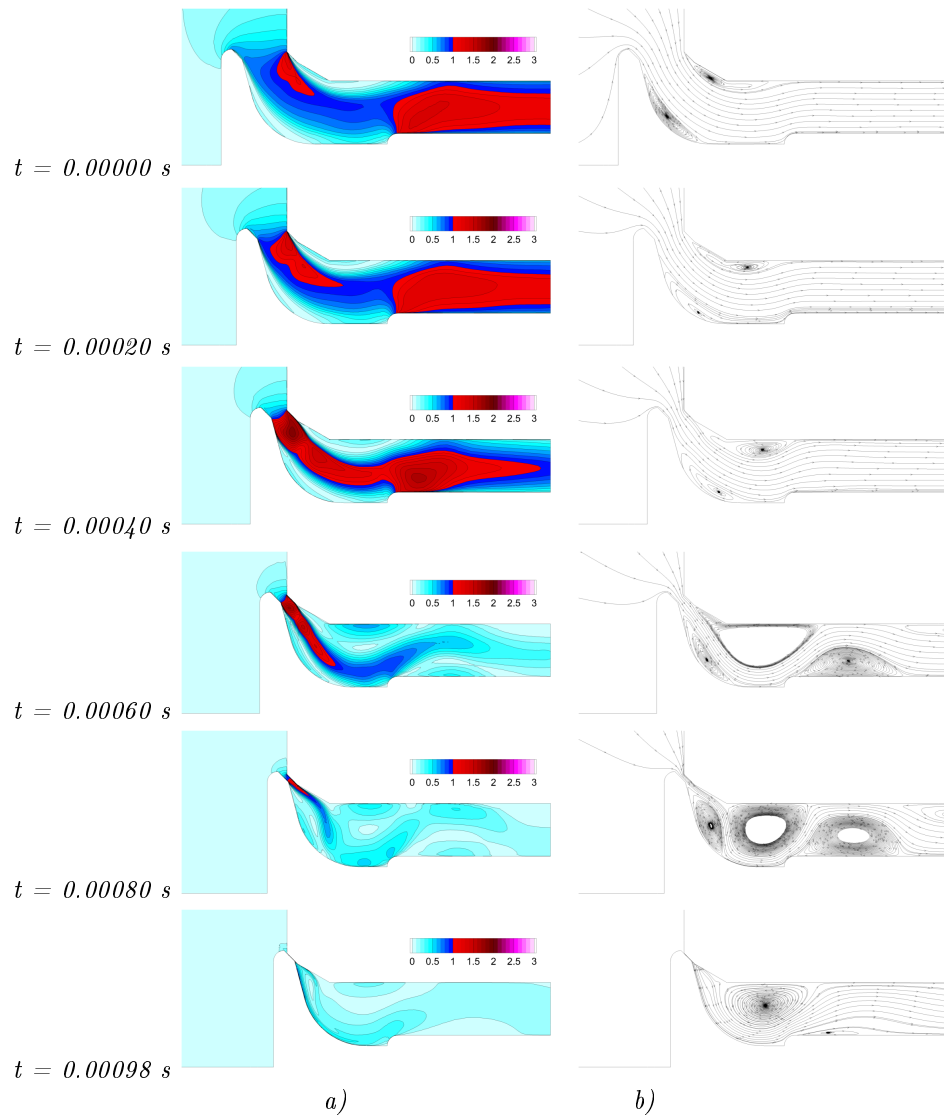


Figure 7.58: Closing stage. Solution development along time. *a)* isolines of the Mach number, *b)* velocity streamlines.

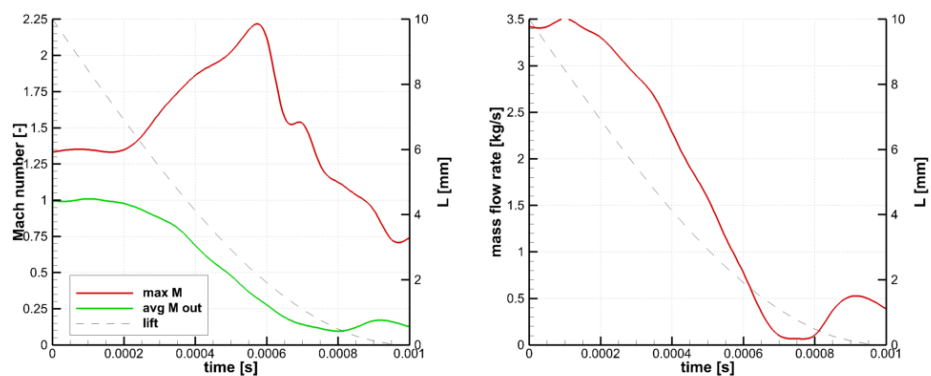


Figure 7.59: Evolution of the Mach number and the mass flow rate with time, closing stage.

Regarding the necessity of the grid interpolation, figure 7.60 shows the solution obtained on

a massively deformed grid. The initial grid with $L=10$ mm has been used till approximately $L=1$ mm. As shown on the solution, the excessively skewed elements have completely corrupted the solution.

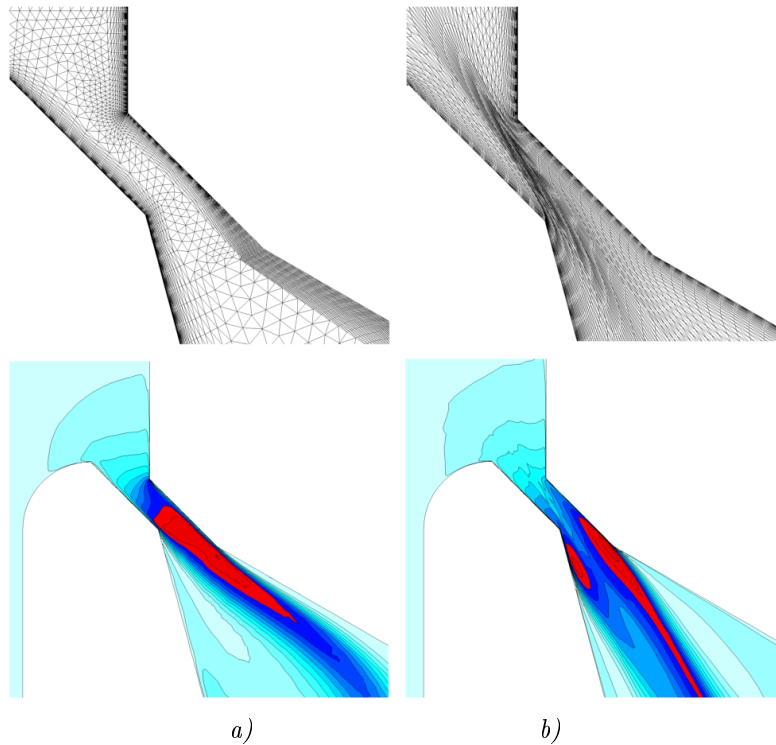


Figure 7.60: Influence of the grid deformation. *a)* detail of a proper grid and solution in the throat region; *b)* detail of an excessively deformed grid and its impact on the solution.

The computation setup has been used also for the geometries with an inclined inlet wall (see figure 7.19). Figure 7.61 shows the evolution of the parameters monitored for both the geometries tested (inclination angle 5° and 10°).

The graph 7.62 then superposes the mass flow rates for all the geometries. Despite the expectations, all the contours overlap in a single curve, indicating no significant effect of this modification. This is, however, consistent with all the previous conclusions (from steady state computations) observed on these geometries.

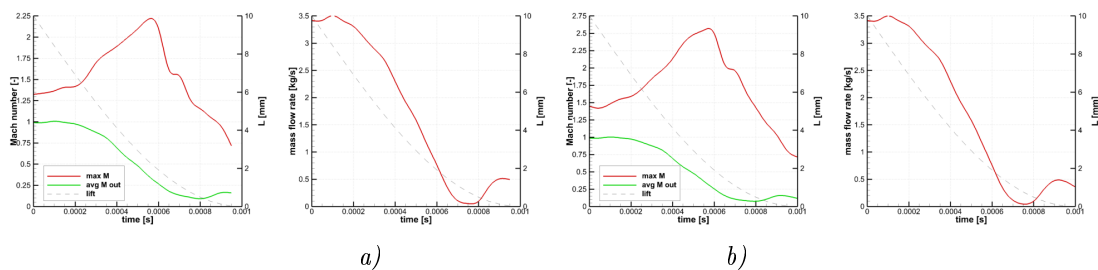


Figure 7.61: Evolution of the Mach number and the mass flow rate with time, closing stage. Inlet wall inclination *a)* 5° , *b)* 10° .

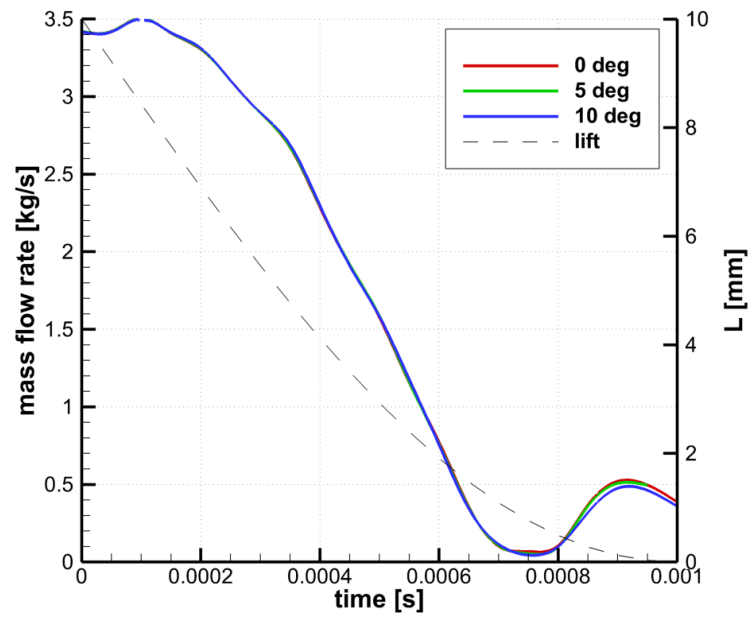


Figure 7.62: Evolution of the Mach number and the mass flow rate with time, closing stage. Influence of the Inlet wall inclination.

Simulation of Closing Stage - Influence of Valve Geometry

Using the computational setup from the previous simulation (see figure 7.56) three valve geometries have been tested: *original*, *G1* (with a bigger stem curvature) and *G2* (with a milder stem curvature).

Figures 7.63 and 7.64 present the flow fields for the lifts (approximately) $L=4$ mm and 2 mm. Figure 7.65 then shows the time evolution of the Mach number and the mass flow rate.

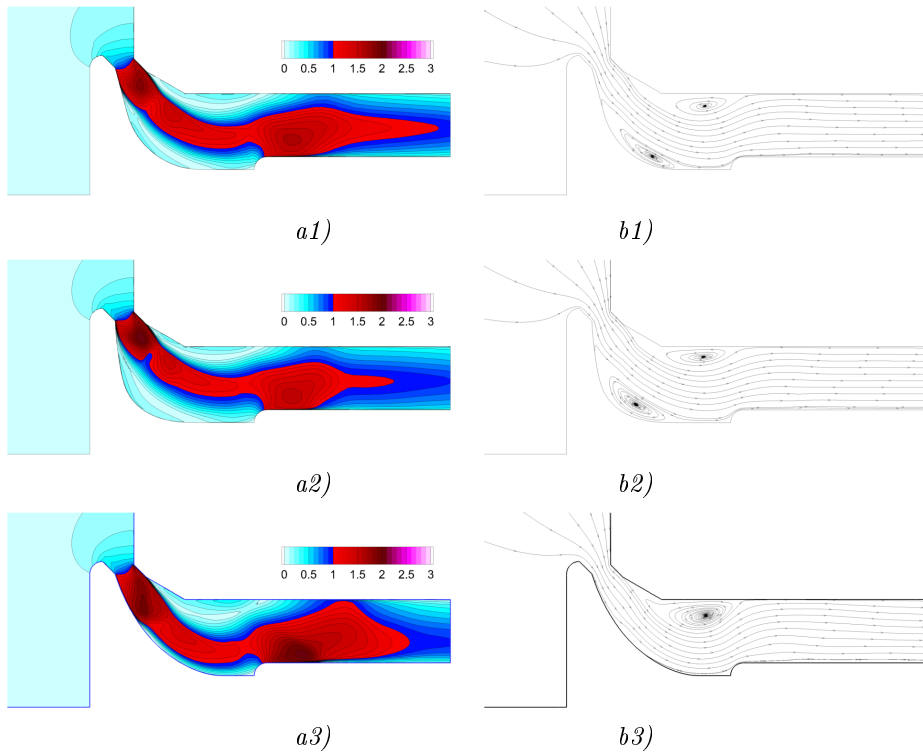


Figure 7.63: Closing stage. Influence of the valve geometry. $L=4$ mm. *a)* isolines of the Mach number, *b)* velocity streamlines; Valve shape *a1) b1)* original; *a2) b2)* G1; *a3) b3)* G2.

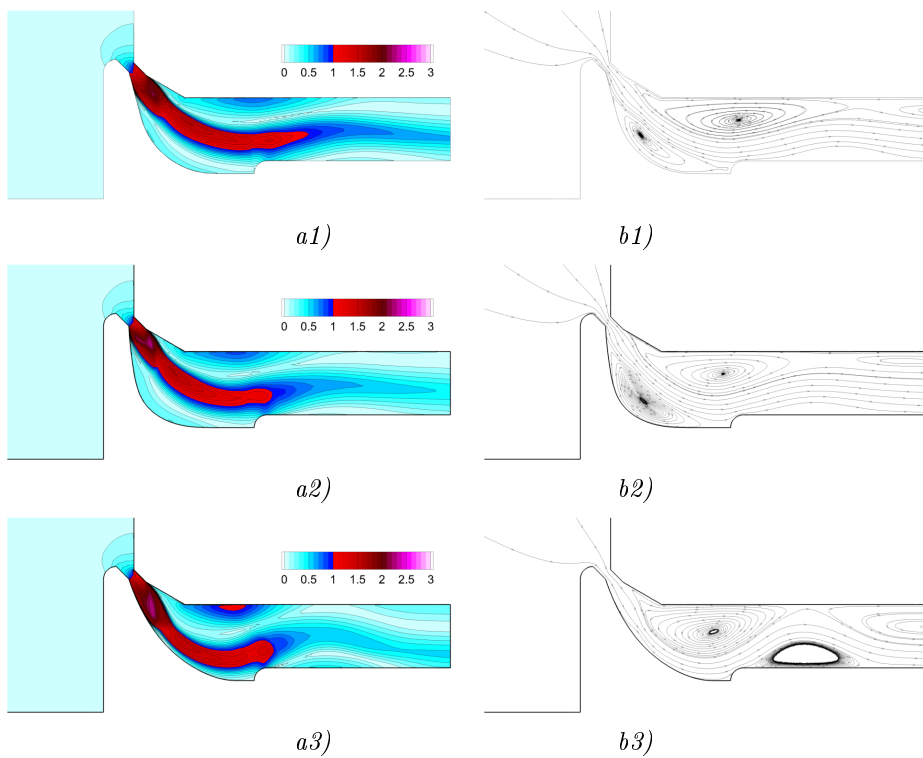


Figure 7.64: Closing stage. Influence of the valve geometry. $L=2$ mm. *a)* isolines of the Mach number, *b)* velocity streamlines; Valve shape *a1) b1)* original; *a2) b2)* G1; *a3) b3)* G2.

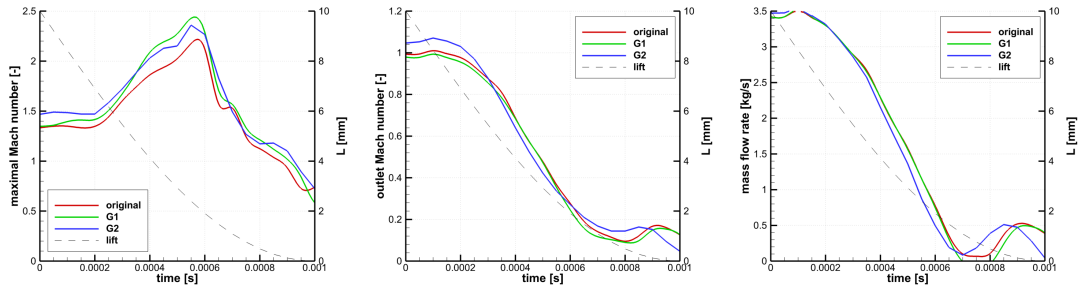


Figure 7.65: Evolution of the Mach number and the mass flow rate with time, closing stage. Influence of the valve geometry.

For the larger lift shown an agreement has been observed between the original and the G1 geometry. The extra space around the valve (due to bigger curvature) therefore remains void and filled with the recirculation. For the geometry G2 the flow stays attached to the valve stem, leading to an almost perpendicular impact on the casing, which then affects the later supersonic expansion.

For the smaller lift, the earlier separation on the G1 deflects the flow slightly downwards than the original geometry. However, as shown in the evolution graphs, these alternatives stay in a close agreement for most of the period. The G2 geometry evinces identical behaviour as for the bigger lift, giving arise to a large separation zone near the casing.

From the graph comparisons, the G2 geometry seems best performing in the initial phase of the cycle. With the decreasing lift its narrower throat spoils the performance below the original and G1 alternatives. This has been proven by an integral value of the mass flow rate over the period computed, which is shown in the table 7.28.

Valve geometry	original		G1		G2	
	mass flow rate [kg/s]	Abs.	Diff [%]	Abs.	Diff [%]	Abs.
L = 9 mm	3.507	0.0	3.523	0.4	3.543	1.1
L = 6 mm	3.105	0.0	3.113	0.3	3.102	-0.1
L = 3 mm	1.578	0.0	1.563	-0.9	1.391	-11.8
total mass flow [g]	1.707	0.0	1.675	-1.9	1.647	-3.5

Table 7.28: Influence of the valve geometry.

Real Cycle Simulation - Influence of Inlet Boundary Condition

Figure 7.66 schematizes the valve lift during a real cycle of a reciprocating engine for a chosen value of the engine revolutions: 3500 RPM.

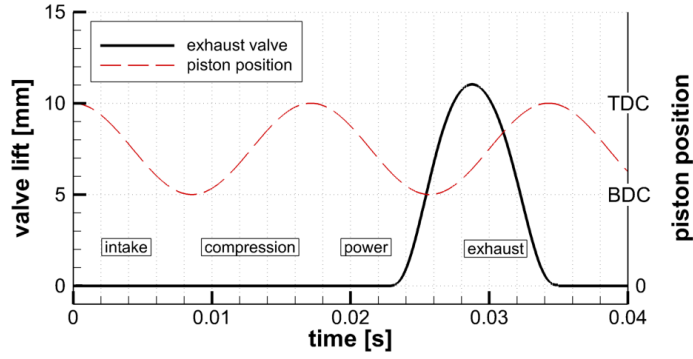


Figure 7.66: The valve lift evolution during a real cycle of a reciprocating engine.

The development of the pressure inside the cylinder and in the exhaust pipe (at the position of the outlet section) are plotted in figure 7.67. The values shown are taken from [41] and represent the inlet and outlet boundary values for the numerical simulations. For the inlet pressure two curves have been used in turn, corresponding to the pressure evolution for the compression ignition (CI) and the spark ignition (SI) engine (their basics have been described in the section 2.1).

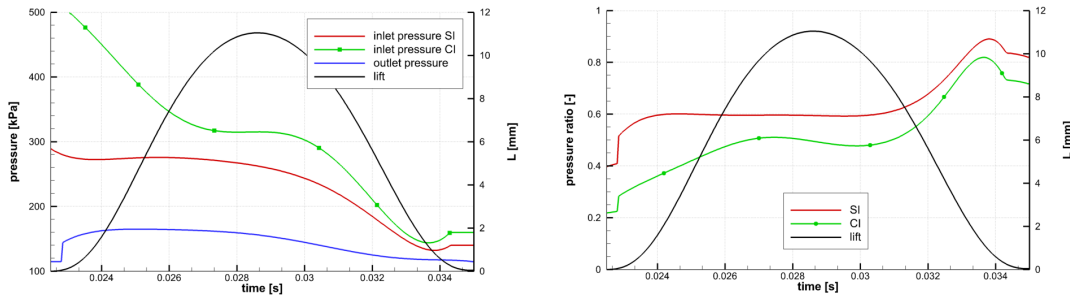


Figure 7.67: The evolution of the pressure in the cylinder and in the exhaust pipe during a real cycle of a reciprocating engine.

The influence of the inlet pressure (i.e. the curve chosen) has been studied in this subsection. All the results shown here have used the SST turbulence model.

According to figure 7.67, the numerical simulations have been performed between time 0.0225 s and 0.0350 s (corresponding to a yet/already fully closed valve) with a physical time-step $\Delta t = 10^{-6}$ s.

Because of a negligible mass flux and in order to avoid grid singularities for a fully closed valve, the minimal clearance gap $L_{min} = 0.40$ mm has been applied. The maximal valve lift has been $L_{max} = 11.05$ mm. To prevent excessive grid deformations a series of four grids with nominal lifts: 0.40; 1.51; 2.93 and 7.02 mm has been used, leading to four interpolation points, as indicated in the graph 7.68.

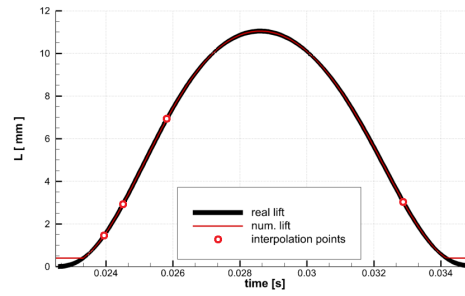


Figure 7.68: Numerical realization of the valve motion.

Figures 7.69, resp. 7.70 show the flow fields for the SI, resp. CI inlet conditions. The development of the parameters monitored is presented in the graph 7.71.

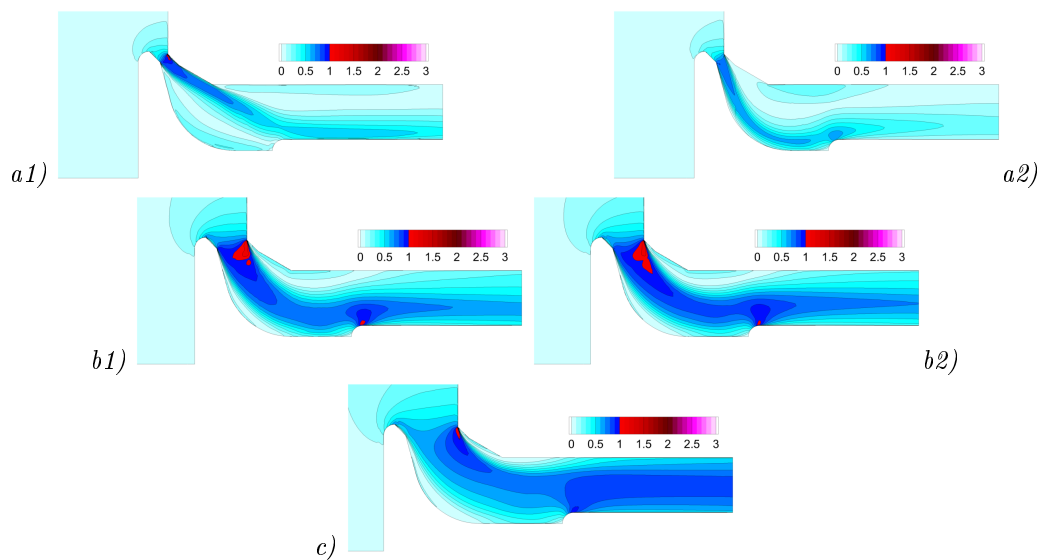


Figure 7.69: Real cycle simulation, SI inlet condition, contours of the Mach number. Valve lift: *a)* 3 mm, *b)* 7 mm, *c)* 11 mm; *a1, b1)* opening stage, *a2, b2)* closing stage.

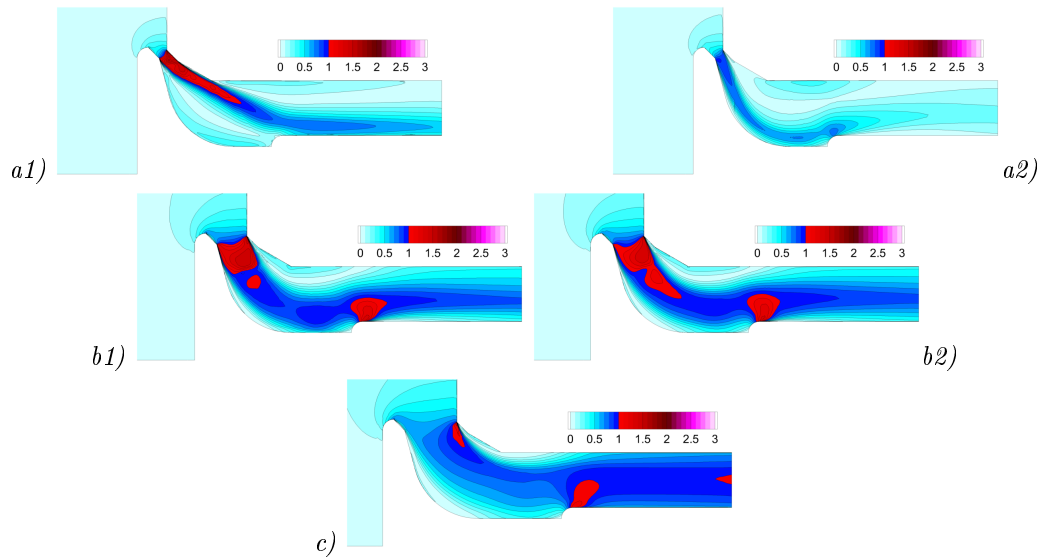


Figure 7.70: Real cycle simulation, CI inlet condition, contours of the Mach number. Valve lift: a) 3 mm, b) 7 mm, c) 11 mm; a1, b1) opening stage, a2, b2) closing stage.

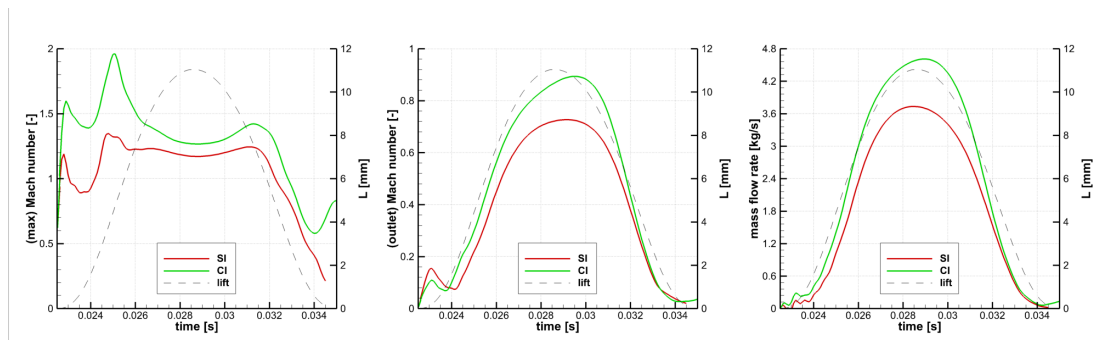
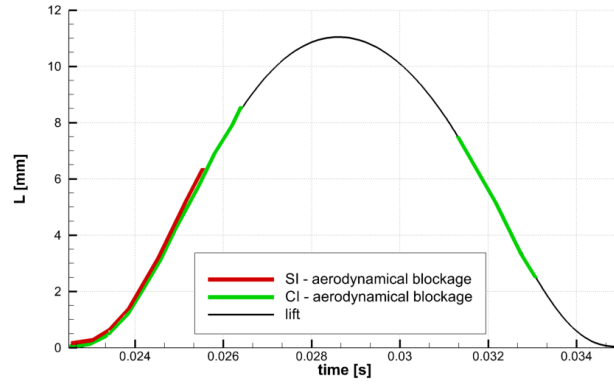


Figure 7.71: Evolution of the Mach number and the mass flow rate with time, closing stage. Real cycle simulation. Influence of the inlet boundary condition.

With the lower pressure ratio, the solution of the CI regime shows an aerodynamical blockage for nearly a twice longer period than for the SI regime, as summarized in the table 7.29.



Regime	Time [s]				Portion of cycle [%]
	Opening stage		Closing stage		
	Since	Till	Since	Till	
SI	0.0225	0.0257	-	-	25.6
CI	0.0225	0.0268	0.0313	0.331	48.8

Table 7.29: Period of aerodynamical blockage for different inlet boundary conditions.

The flow topology is, however similar for both the inlet conditions, with an offset of the velocity magnitude: for the lower lifts at opening stage the flow is attached to the upper wall, whereas at the closing stage it attaches to the valve stem. For larger lifts the flow beam passes through the middle of the channel, being surrounded by recirculations on both sides.

In order to illustrate the influence of an unsteady approach, two steady state simulations have been performed for the fixed lift $L = 7$ mm and the related boundary conditions of the CI regime (both the opening and closing stage). The flow field comparison is then showed in figures 7.72, 7.73 with the mass flow rate comparison in the table 7.30. The main differences have been observed in the size of the supersonic expansion and the positions of the separation zones. According to the table 7.30, it has been observed that neglecting the flow unsteadiness leads to differences of the order $\approx 10\%$.

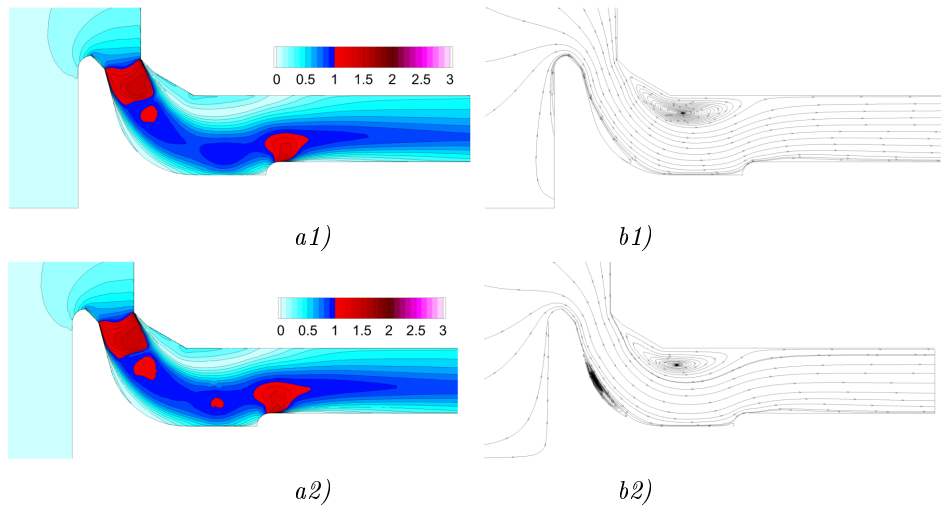


Figure 7.72: Influence of the unsteady approach, CI inlet condition, opening stage, $L=7$ mm. *a)* contours of the Mach number, *b)* velocity streamlines; *a1)* *b1)* unsteady, *a2)*, *b2)* steady.

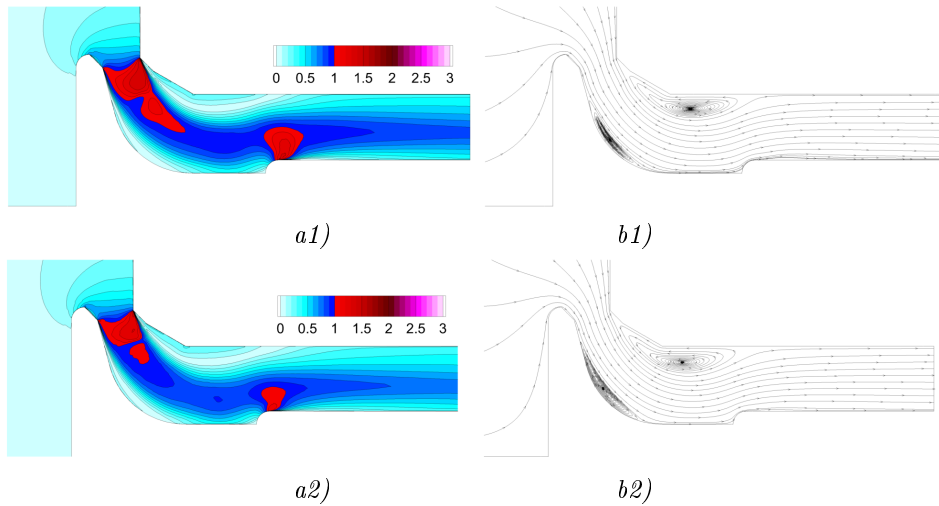


Figure 7.73: Influence of the unsteady approach, CI inlet condition, closing stage, $L=7$ mm. *a)* contours of the Mach number, *b)* velocity streamlines; *a1)*, *b1)* unsteady, *a2)*, *b2)* steady.

L=7 mm	mass flow rate [kg/s]			
	Unsteady		Steady	
	Abs	Diff [%]	Abs	Diff [%]
Opening stage	3.162	0.0	3.469	9.7
Closing stage	2.532	0.0	2.220	-12.3

Table 7.30: Differences between steady state and unsteady solutions.

Real Cycle Simulation - Influence of Valve Geometry

For an identical computational setup (both the SI and CI inlet conditions) the three valve geometries (original, G1 and G2) have been tested. Hence, the comparative results on the original geometry have been already shown in figures 7.69-7.70. The next figures present identically structured solution snapshots for the CI regime on the G1 (figure 7.74) and the G2 (figure 7.75) geometries.

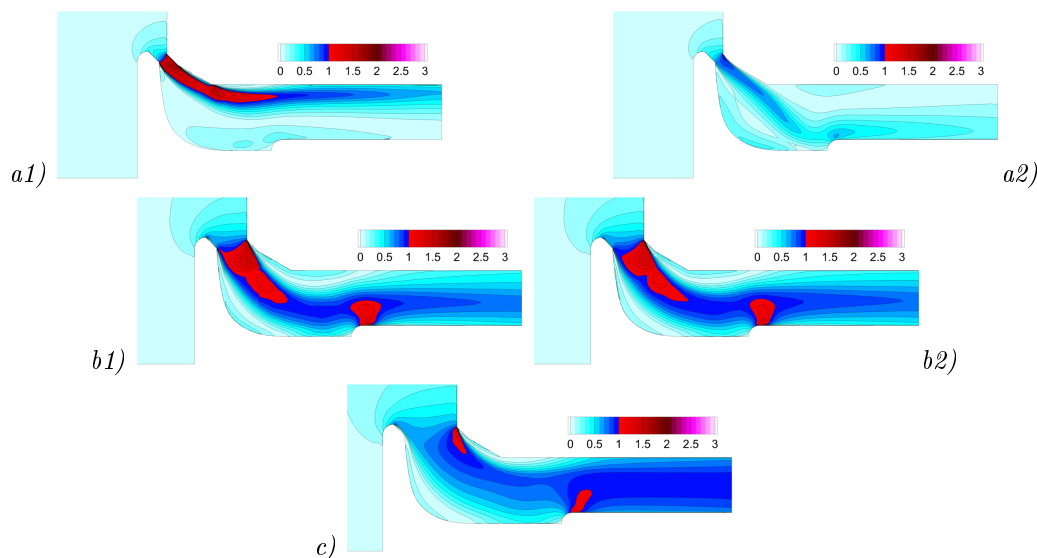


Figure 7.74: Real cycle simulation, CI inlet condition, G1 geometry, contours of the Mach number. Valve lift: *a)* 3 mm, *b)* 7 mm, *c)* 11 mm; *a1)*, *b1)* opening stage, *a2)*, *b2)* closing stage.

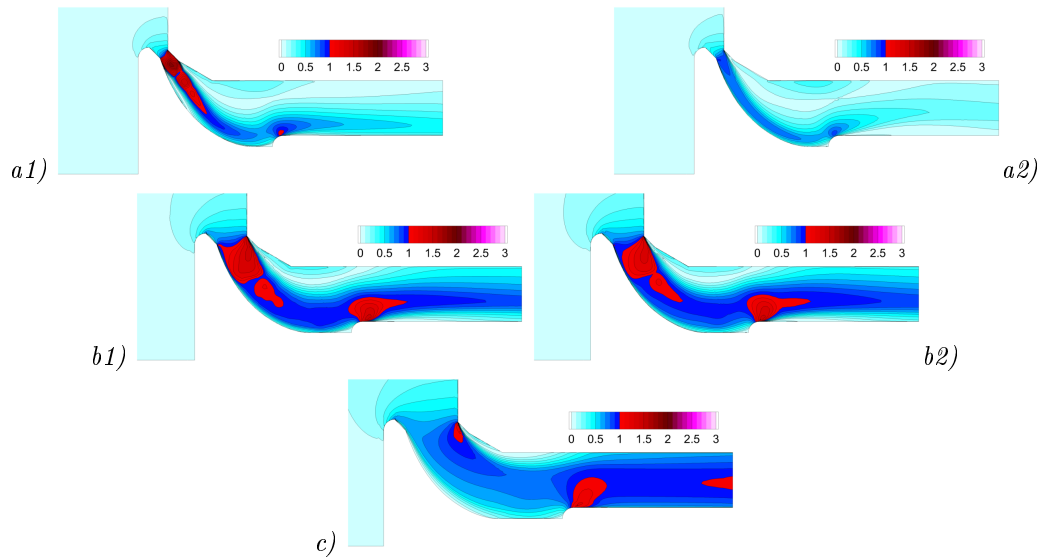


Figure 7.75: Real cycle simulation, CI inlet condition, G2 geometry, contours of the Mach number. Valve lift: a) 3 mm, b) 7 mm, c) 11 mm; a1, b1) opening stage, a2, b2) closing stage.

The graphs 7.76 and the table 7.31 summarize the effect of the valve geometry on the Mach number and the mass flow rate.

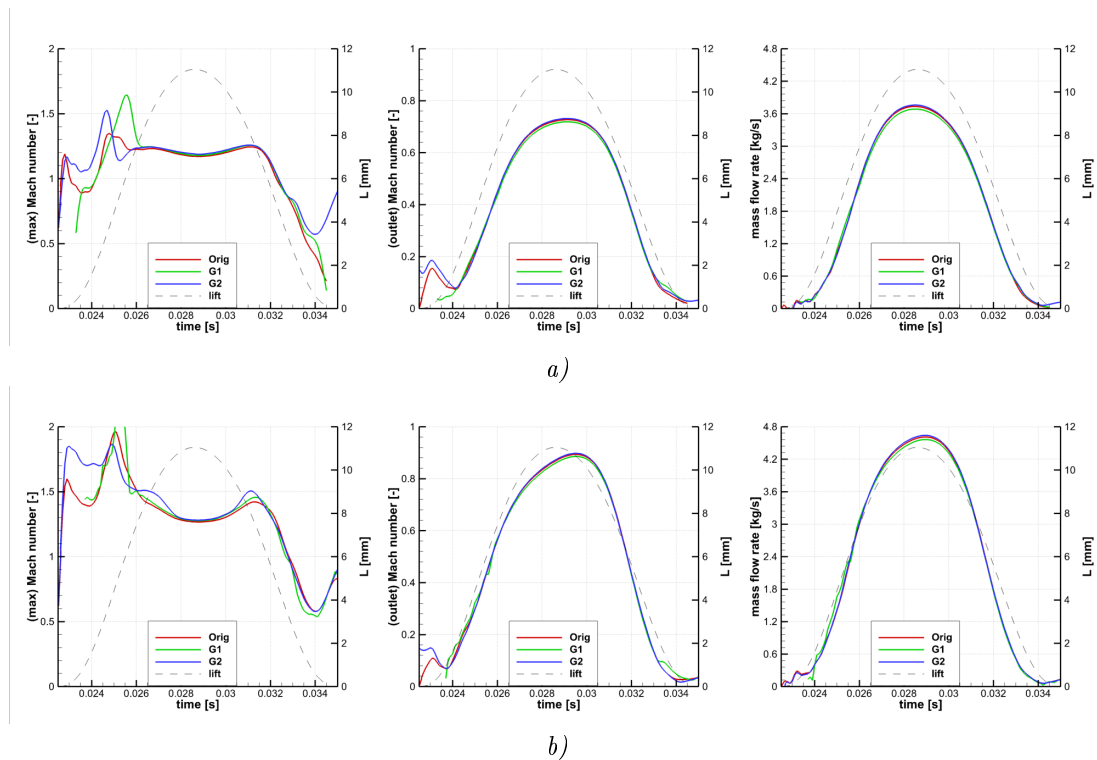


Figure 7.76: Evolution of the Mach number and the mass flow rate with time, closing stage. Real cycle simulation. Influence of the valve geometry. a) SI regime, b) CI regime.

Valve geometry	Total mass flow over one cycle [kg]					
	Original		G1		G2	
Regime	Abs.	Diff [%]	Abs.	Diff [%]	Abs.	Diff [%]
SI	0.0224	0.0	0.0221	-1.3	0.0225	+0.7
CI	0.0281	0.0	0.0278	-1.1	0.0284	+1.1

Table 7.31: Influence of the valve geometry on the total mass flow over one cycle.

According to all the previous (steady state) observations the exhaust channel gets aerodynamically choked, which sets the critical mass flow rate. Hence a wider geometrical cross-section (alternative G1) does not lead to an increase of the mass flux. By contrary, the void space along the stem always induces a strong recirculation which then restricts the active cross-section. Due to this strong recirculation the main flow beam stays attached to the upper wall even for a low lift at closing stage (as distinct to other geometries). In total, this geometry deteriorates the total mass flow over a cycle by $\approx 1\%$ from the original geometry.

On the other hand, the alternative G2 completely eliminates the separation on the stem. This has a positive effect on the flow stability and allows the main flow beam to stay attached to the stem for almost entire cycle. It also leads to a very light increase of the mass flow rate over a dominant part of the cycle. The overall performance is therefore $\approx 1\%$ better than the original geometry. Identical trends have been observed for both the inlet regimes tested.

Real Cycle Simulation - Influence of Turbulence Model

For one numerical simulation (with one regime selected) the EARSM has been used. The CI regime has been chosen, as its lower pressure ratio leads to more complex transonic effects, upon which the influence of the turbulence model can be better evinced. For convenience sake the original valve geometry has been used.

The comparative result of the SST model has been shown in figure 7.70. The results of the EARSM model are then shown in figure 7.77 and the graph 7.78.

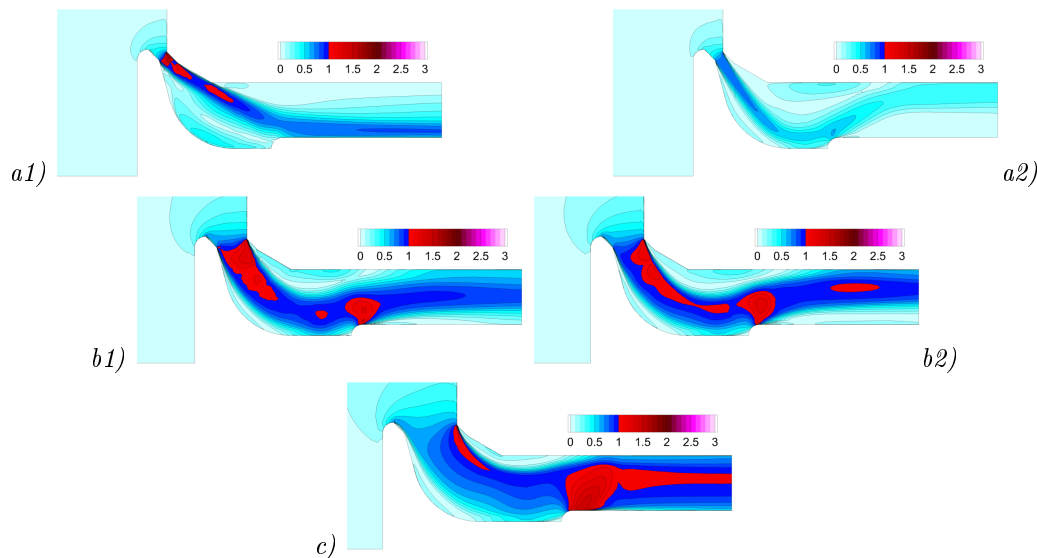


Figure 7.77: Real cycle simulation, CI inlet condition, EARSM turbulence model, contours of the Mach number. Valve lift: a) 3 mm, b) 7 mm, c) 11 mm; a1, b1) opening stage, a2, b2) closing stage.

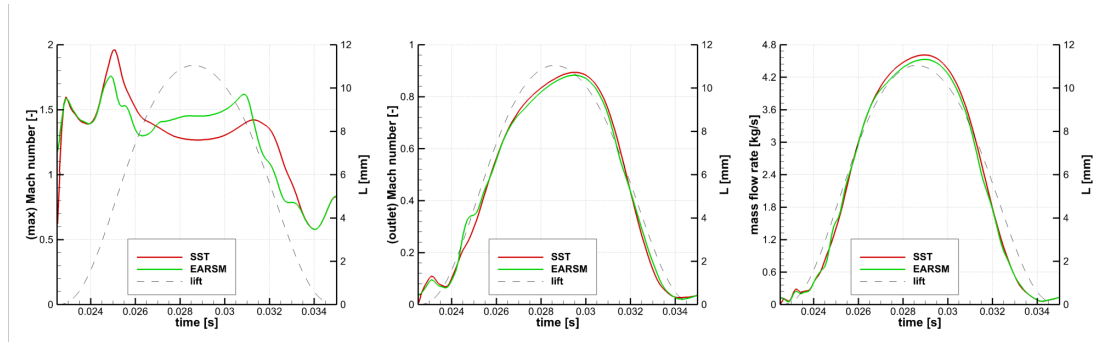
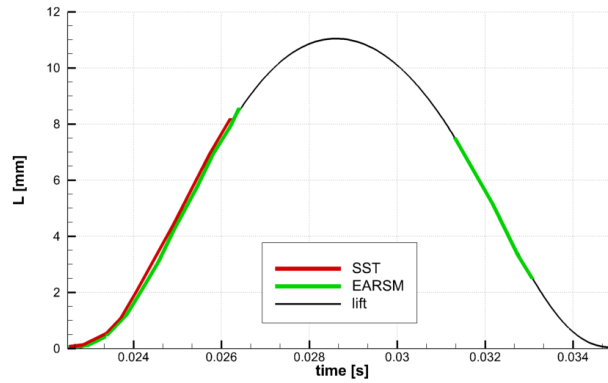


Figure 7.78: Evolution of the Mach number and the mass flow rate with time, closing stage. Real cycle simulation. Influence of the turbulence model.



Turb. model	Time [s]				Portion of cycle [%]
	Opening stage		Closing stage		
	Since	Till	Since	Till	
SST	0.0225	0.0268	0.0313	0.331	48.8
EARSM	0.0225	0.02623	-	-	30.4

Table 7.32: Period of aerodynamical blockage for different turbulence models.

Although the results are in a good qualitative agreement, the flow field comparison detects differences on the supersonic expansion. During the closing stage the EARSM model predicts longer and thinner supersonic pockets. Furthermore, for the lift $L=3$ mm (distinct to all the previous results) the flow has not attached to any wall yet. As indicated in the table 7.32, during this stage the EARSM model has not predicted an aerodynamical blockage.

On the other hand the initial phase of the opening stage is in a perfect agreement for all the parameters monitored. Later, the EARSM model predicts an earlier separation on the valve, leading to a weaker expansion (in terms of maximal Mach number). The table 7.32 also shows that the time of the aerodynamical opening of the channel is similar for both models.

As shown in the graph 7.78, for the non-choked period of the cycle ($t > 0.0270$ s) the EARSM model predicts slightly smaller mass flow rate. This fact significantly influences the total mass flow, as this period with the big lift is responsible for the largest transport of mass, see the table 7.33. However, for time $t > 0.0320$ s a perfect fit of the mass flow rate for both models has again been observed.

Total mass flow over one cycle [kg]				
Turbulence model	SST		EARSM	
Regime	Abs.	Diff [%]	Abs.	Diff [%]
CI	0.0281	0.0	0.0275	-2.1

Table 7.33: Influence of the turbulence model on the total mass flow over one cycle.

7.5.4 3D Geometry, Moving Valve

The computational setup from the previous section 7.5.3 for a real valve cycle has been re-used, with some obvious extensions due to the third dimension.

The boundary conditions and the valve movement have been again described by the plot 7.67, corresponding to the engine revolutions at 3500 RPM (the relations have been taken from a literature which actually refers to operating conditions of a real, i.e. 3D, engine). Besides, the SST turbulence model has been used.

The unsteady approach has again implied the need of a series of computational grids, in order to prevent excessive element deformations. A usual computational grid has contained approximately 500 000 elements, making the complete simulation setup (on available CPU resources) costly.

Extracting from the computations performed, an average runtime period of one valve cycle has been (scaled to 1 CPU) approximately 162 days. Assuming a common parallelization onto 8 cores, a necessary pre-processing (grid generation, solution interpolation), an ideal (snag-free) run and a post-processing, the current demands are about one month on a single simulation. Hence, the testing phase has been reduced to a minimum with a main focus on the real cycle simulations. To save some computational time, the stages with very low valve lifts (hence a very low mass flux) have been skipped for some simulations.

Real Cycle Simulation

The exhaust process has been studied on the original valve geometry for both alternatives of the inlet condition (SI and CI). Afterwards, the influence of the valve geometry has been tested in both regimes, leading to six computation campaigns in total.

Figures 7.79, 7.80 and 7.81 present the results on all three geometries for the SI regime. The solutions of the CI regimes are shown later in figures 7.83, 7.84 and 7.85⁵. All the solutions obtained have been nearly symmetric (no substantial asymmetrical flow pattern has been found), thus the results are represented by their respective planar cuts.

The time evolution of the parameters monitored (see the section 7.3) is shown in the graphs 7.82 (SI regime) and 7.86 (CI regime).

For the SI regime the flow velocity has been transonic only in the initial stage of a cycle for all the geometries tested. Besides, very similar flow topology has been observed for the original and the G1 geometry, implying no significant (aerodynamical) gain with the thinner valve stem. Consistently to all the previous observations, the extra volume gained by the stem thinning is occupied by a recirculation zone formed between the valve seat and the casing - creating an artificial valve shape in fact. The main flow beam stays attached to the upper wall during the entire cycle.

⁵A parallelization used has usually operated on 8 CPU cores. The COOLFluid solver does not merge the fractional solutions into one file, but stores them in (eight) separate files. The result visualization is then realized by an actual overlapping of these files inside a post-processing software Tecplot. Because of the internal overlap of each zone (according to the computational stencil), the solution plot often contains discontinuous (fraying) isolines. It is, however a purely post-processing imperfection and not a solution defect.

As distinct from the original and G1 shape, the contour of the G2 geometry (nearly) follows the border of the main flow beam. It reduces the recirculation along the stem, but generates another one on the upper wall, as the flow attaches to the stem.

From the quantitative point of view (graph 7.82 and table 7.35) the different geometries have however led only to minor differences. Compared to the planar simulations, the graph of the mass flow rate vs. time is biased towards the opening stage. The differences can also be seen in the plots of the average outlet velocity: the planar simulation predicts a smooth ascend and descend, whereas for the 3D simulation a long plateau can be found in the same period of large valve opening. The average velocity magnitude is also higher for the 3D simulation.

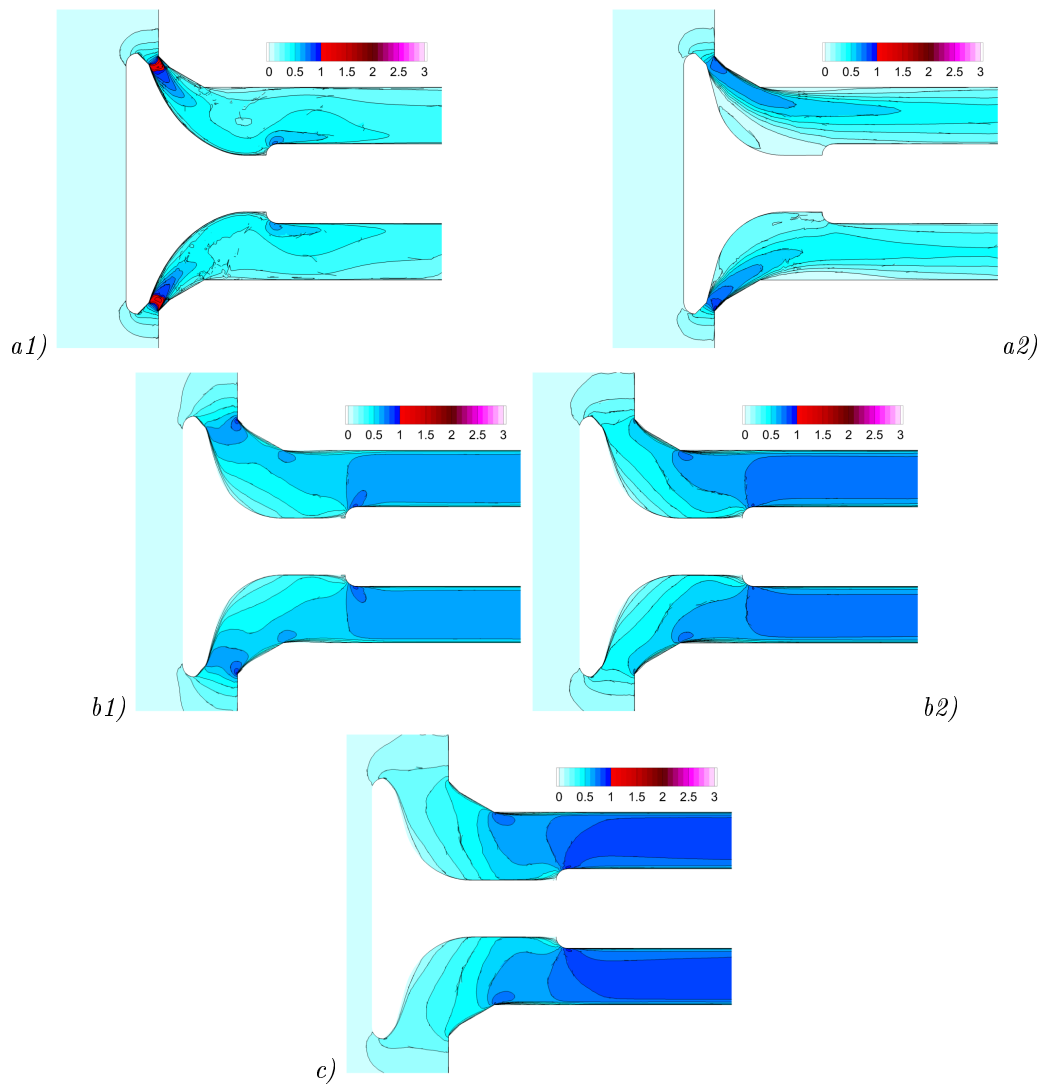


Figure 7.79: Real cycle simulation, original valve shape, SI inlet condition, contours of the Mach number. Solution cut $Z = 0$. Valve lift: *a)* 3 mm, *b)* 7 mm, *c)* 11 mm; *a1, b1)* opening stage, *a2, b2)* closing stage.

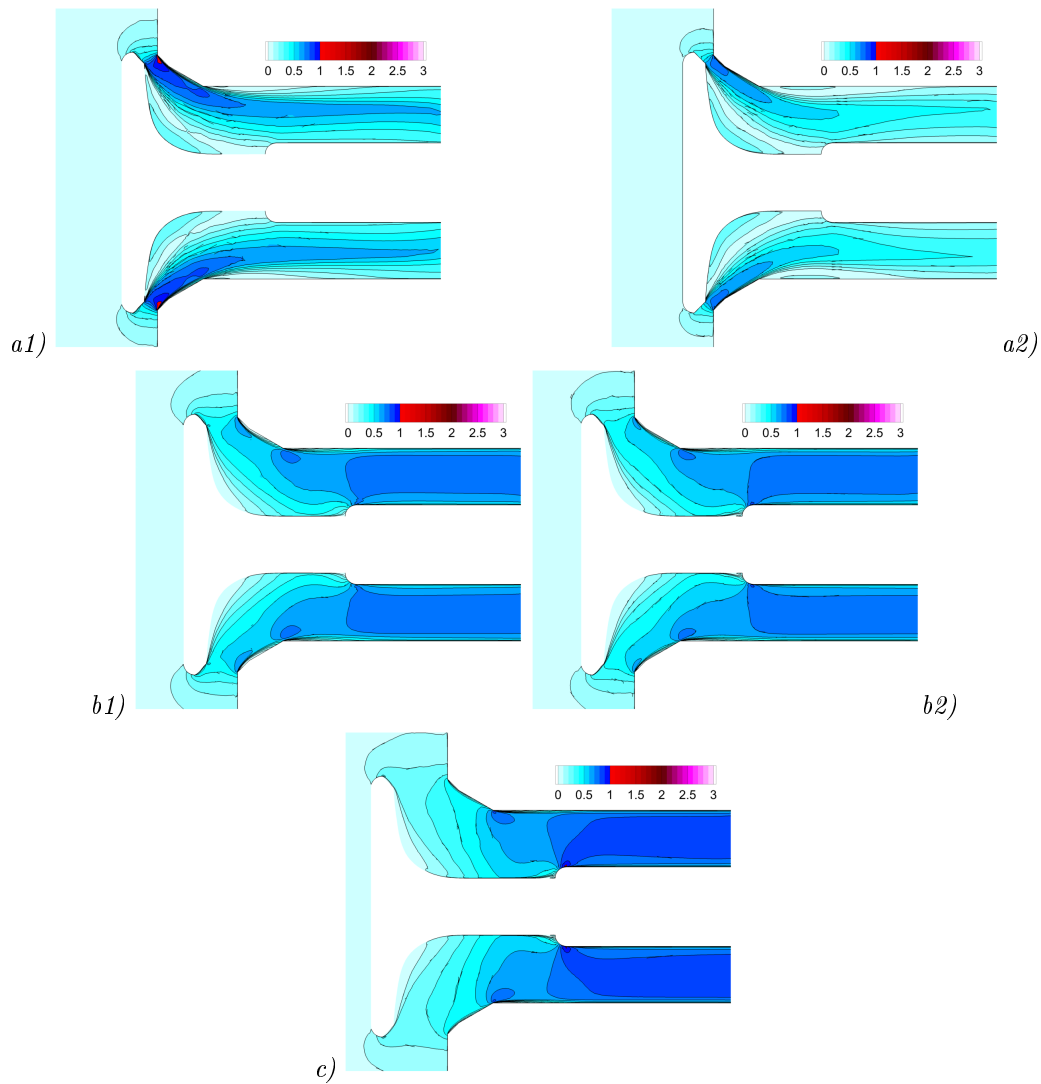


Figure 7.80: Real cycle simulation, G1 valve shape, SI inlet condition, contours of the Mach number. Solution cut $Z = 0$. Valve lift: a) 3 mm, b) 7 mm, c) 11 mm; a1, b1) opening stage, a2, b2) closing stage.

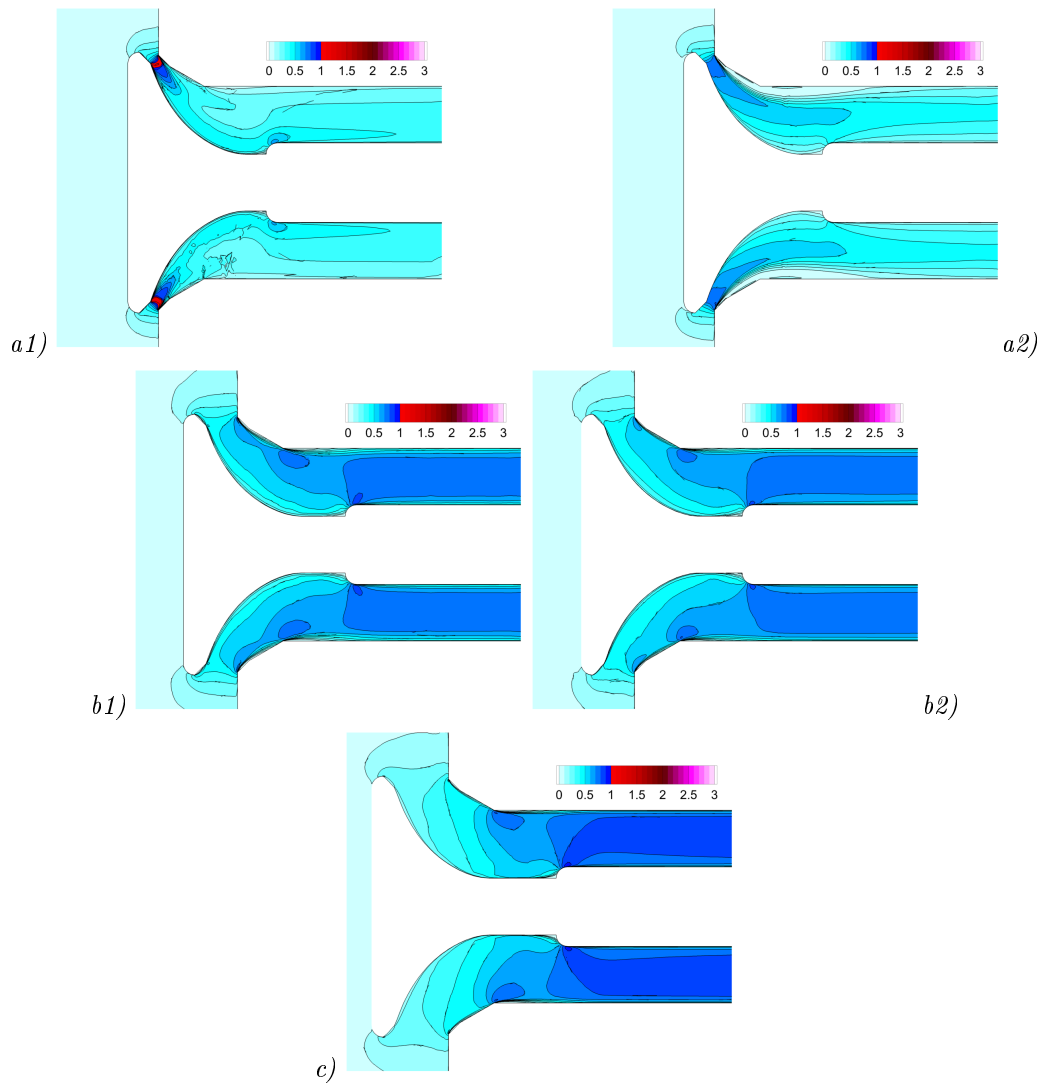


Figure 7.81: Real cycle simulation, G2 valve shape, SI inlet condition, contours of the Mach number. Solution cut $Z = 0$. Valve lift: a) 3 mm, b) 7 mm, c) 11 mm; a1, b1) opening stage, a2, b2) closing stage.

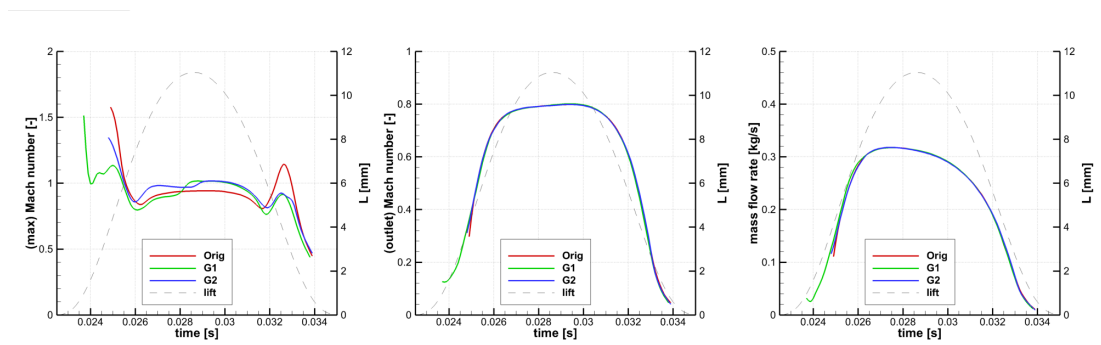


Figure 7.82: Evolution of the Mach number and the mass flow rate with time. Real cycle simulation. SI regime. Influence of the valve geometry.

The CI regime evinces longer period of the aerodynamical choking for all the geometries tested. The period of the blockage is, however, much shorter from the planar predictions and appears only

during the opening stage; compare the tables 7.34 and 7.29.

With a decreased pressure ratio p_2/p_0 the trends observed in the SI regime are further emphasized: the mass flow rate is more biased towards the opening stage and the significant plateau in the outlet velocity evolution is again identified. After relieving the aerodynamical blockage of the throat, the flow detaches from the upper wall and a smaller supersonic pocket appears on the casing. Other flow characteristics are similar to the SI regime.

Regarding the measurable outputs, the G1 geometry predicts smaller mass flow rate, as well as the outlet velocity. On the other hand the performance of the original and G2 geometry is very similar.

The results presented within this section have confirmed a necessity of a full 3D model and an unsteady approach to the problem, as the observations made could not be extrapolated from any simplified models (2D and/or steady). Further conclusions are left to the next chapter.

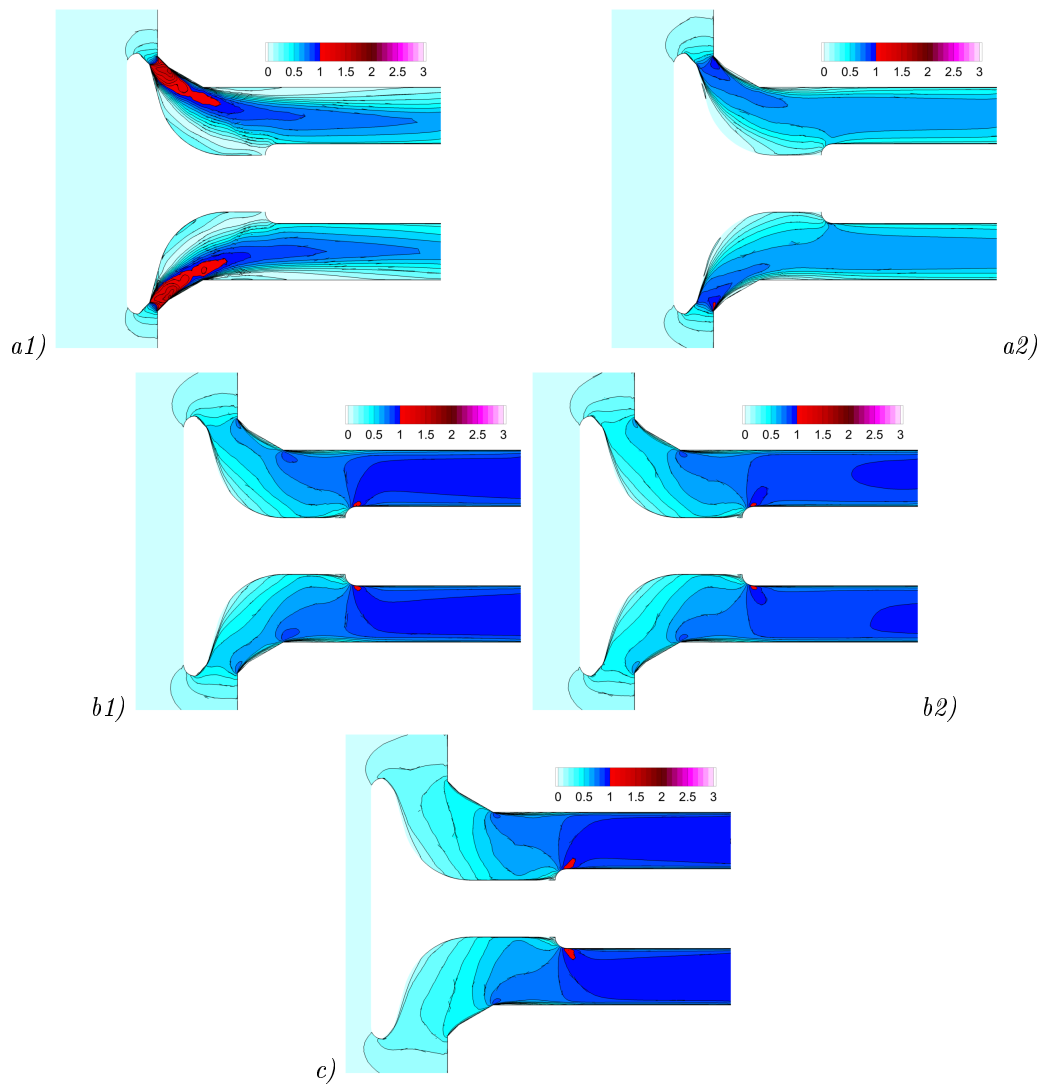


Figure 7.83: Real cycle simulation, original valve shape, CI inlet condition, contours of the Mach number. Solution cut $Z = 0$. Valve lift: a) 3 mm, b) 7 mm, c) 11 mm; a1, b1) opening stage, a2, b2) closing stage.

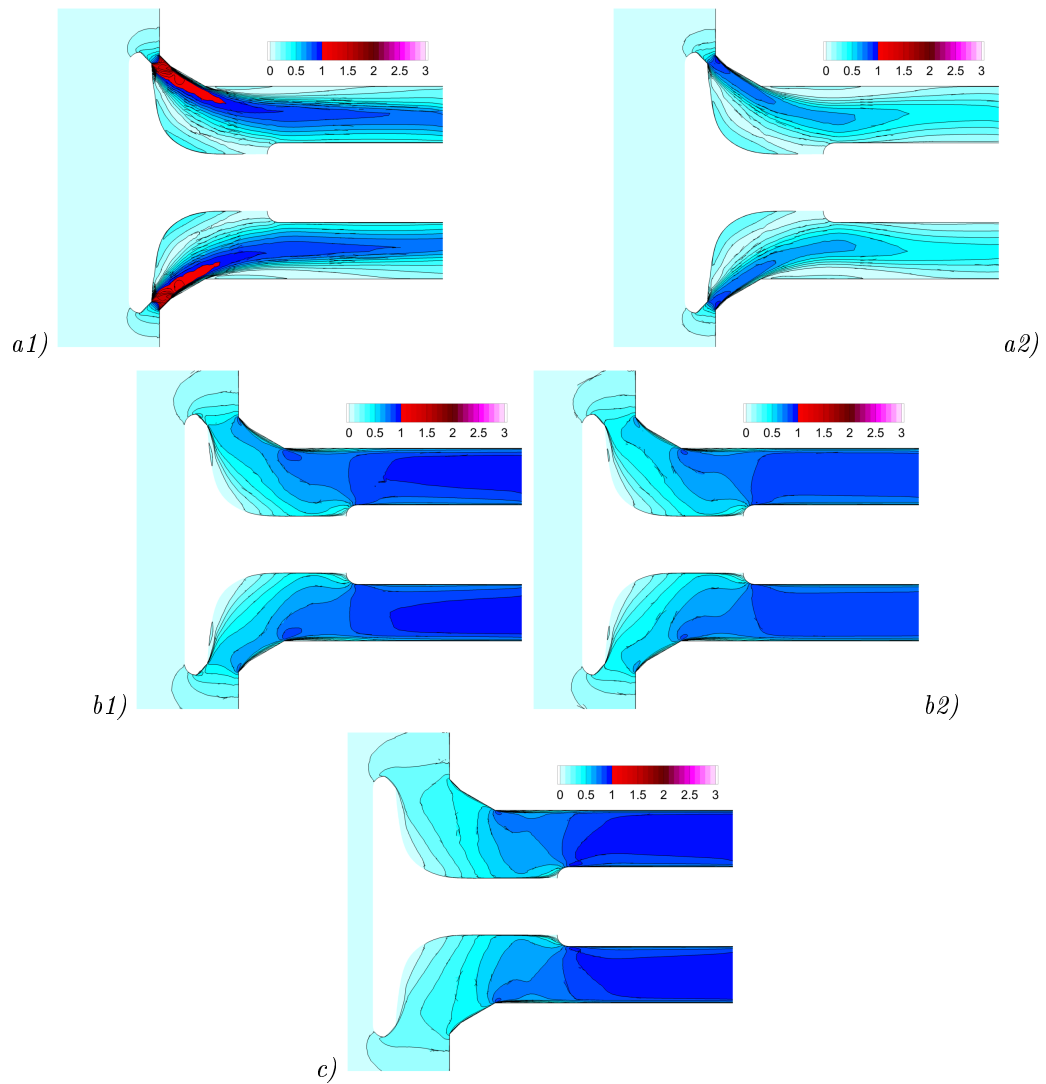


Figure 7.84: Real cycle simulation, G1 valve shape, CI inlet condition, contours of the Mach number. Solution cut $Z = 0$. Valve lift: *a*) 3 mm, *b*) 7 mm, *c*) 11 mm; *a1*, *b1*) opening stage, *a2*, *b2*) closing stage.

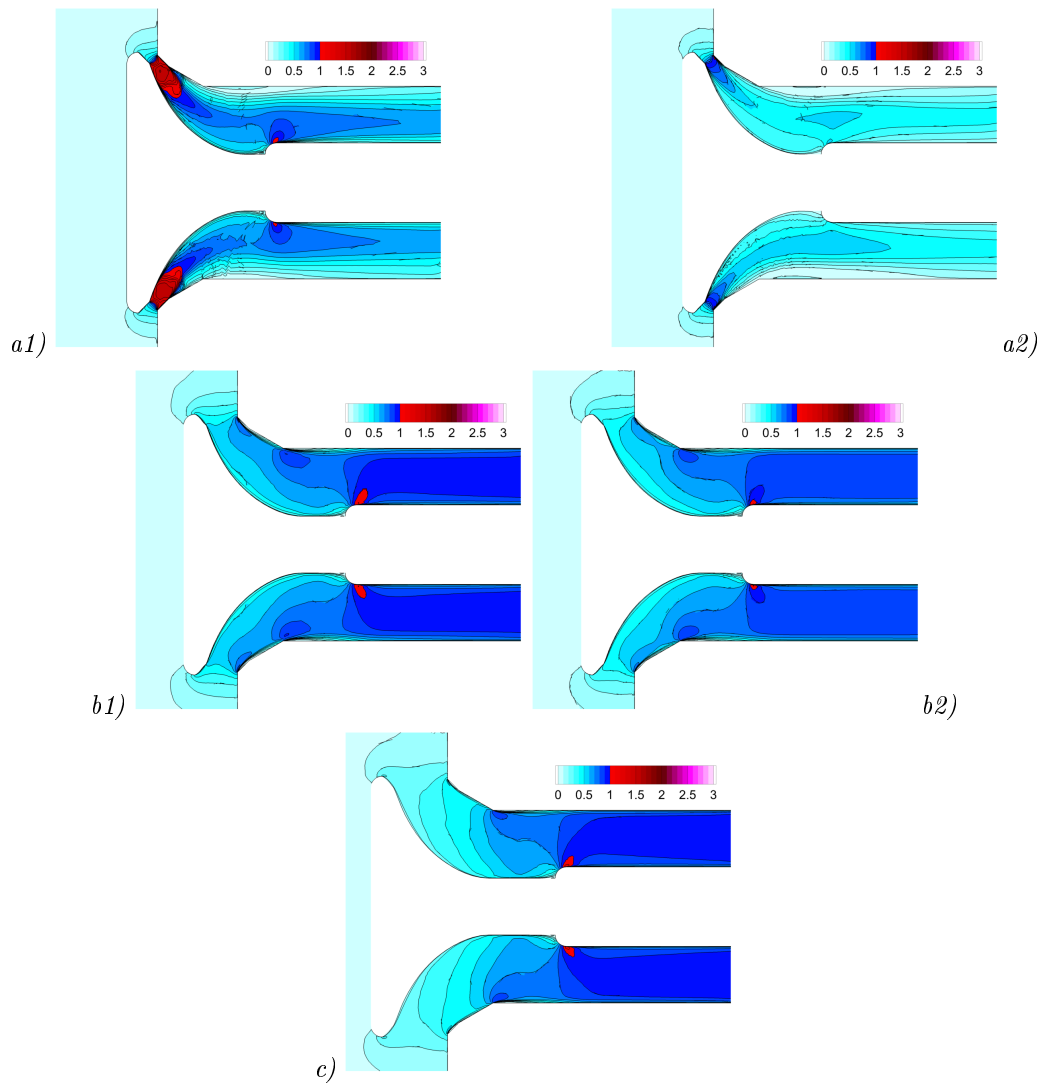


Figure 7.85: Real cycle simulation, G2 valve shape, CI inlet condition, contours of the Mach number. Solution cut $Z = 0$. Valve lift: a) 3 mm, b) 7 mm, c) 11 mm; a1, b1) opening stage, a2, b2) closing stage.

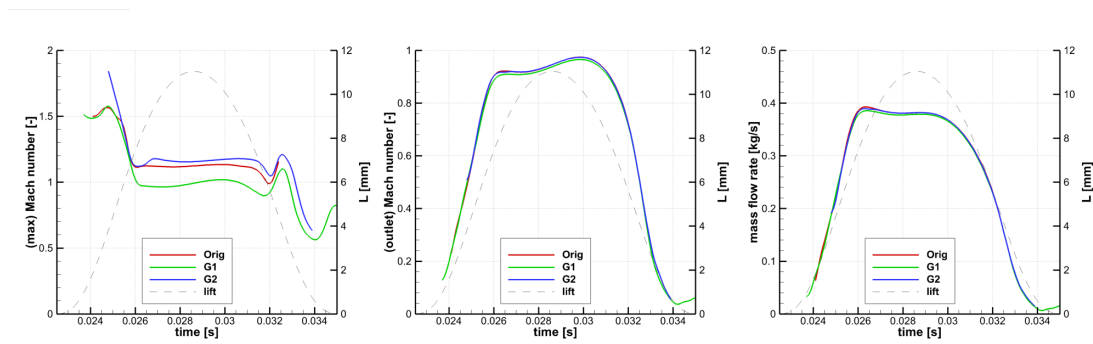
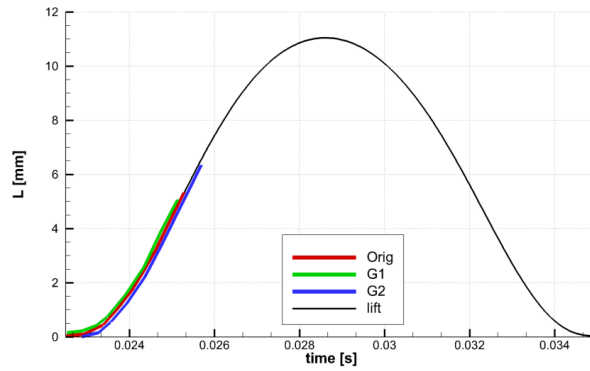


Figure 7.86: Evolution of the Mach number and the mass flow rate with time. Real cycle simulation. CI regime. Influence of the valve geometry.



Valve geometry	Time [s]				Portion of cycle [%]
	Opening stage		Closing stage		
	Since	Till	Since	Till	
Original	0.0225	0.0253	-	-	22.4
G1	0.0225	0.0252	-	-	21.6
G2	0.0225	0.0255	-	-	24.0

Table 7.34: Period of aerodynamical blockage for different inlet boundary conditions. 3D simulation, CI regime.

Valve geometry Regime	Total mass flow over one cycle [kg]					
	Original		G1		G2	
	Abs.	Diff [%]	Abs.	Diff [%]	Abs.	Diff [%]
SI	0.00228	0.0	0.00226	-0.7	0.00229	0.5
CI	0.00295	0.0	0.00285	-4.4	0.00293	-0.6

Table 7.35: Influence of the turbulence model on the total mass flow over one cycle.

Chapter 8

Conclusions

Several sub-projects have had to be accomplished along the whole research in order to fulfill the goals of this dissertation.

In the beginning, the mathematical formulation for a general case of a fluid motion on a moving domain using the finite volume method has been stated. The formulation has been based on the integral form of the conservation laws of mass, momentum and energy. Single-phase ideal gas has been assumed as the working medium.

This general set of equations has served as a basis for *all* computations made by the *MUSA* and the *COOLFluiD* solvers and (with specific extensions) for *all* flow models used.

Along the computations made, the turbulence modelling has occurred to be an important aspect. Thus, the entire fourth chapter has been dedicated to the description of turbulence. After making a general review of the models available, five different models have been selected to be used for the purposes of this thesis.

In the following chapter the numerical methods for discretization of the continuous mathematical equations are described. Due to the large extent of this chapter, only the key concepts are mentioned here: discretization of the convective (inviscid) fluxes by the AUSM-family schemes; discretization of the viscous fluxes and the source terms; the improvement of the solution spatial accuracy by a piece-wise linear reconstruction and a limiter; explicit and implicit time integration; adaptations for the time accurate computations on moving domains; proper initial and boundary conditions and the job parallelization. Some of these issues are commented further in this chapter.

Regarding the original state of both the platforms the following code extensions have been necessary to implement.

MUSA: the original code was able to solve the 2D inviscid flow on a single domain. Within this work the capabilities of the solver have been extended so to allow computations with the laminar and the turbulent (using the one-equation Spalart-Allmaras model) models in 2D. For 3D cases the code allows to choose between the inviscid and the laminar model. The code has also been re-structured to allow a usage of multi-block grids in a generic format. An original AUSM scheme has been replaced by its more advanced successors, among which the influence on the solution accuracy has been tested.

The code, however still uses the explicit time integration which is the main bottle-neck for the respective oncoming simulations (due to the time-step constrains the computations require excessive number of iterations).

COOLFluid: since the beginning the capabilities of this code have been more advanced compared to the solver MUSA, mainly thanks to the longer period of development and the larger team of developers. On the other hand, due to its bigger size and complexity, the code has been more difficult for adding new functionalities.

The code at its initial state (from the thesis standpoint) has required an implementation of first turbulence models which were represented by the classical $k - \epsilon$ and $k - \omega$ models. This step has been finished under a tutelage of the code founder T. Wuilbaut. The following developments have been subject to an independent research activity. In the scope of this activity the two-equations turbulence models have been implemented (both 2D and 3D), debugged and tested.

Next main developments have been related to the specific needs of the target test case: mesh deformation techniques; dual time stepping; radial and time dependent boundary conditions; internal conditions and several debugging interventions on various parts of the code.

The properties of both the codes have been continuously evaluated by monitoring the results on the series of reference test cases. Although playing an important role for proving the code reliability and accuracy, findings for each test case have been kept in their respective sections not to make the general conclusions excessively long.

The verified numerical codes have then been used for the main target - the flow through an exhaust channel with a moving valve. The flow structure has been revealed and described both qualitatively and quantitatively. The deeper evidences are elaborated in the following section.

8.1 Findings on the Exhaust Channel

The current work has modelled the flow around an exhaust valve using various numerical methods, flow regimes and geometrical modifications.

The *inviscid* flow model has occurred the simplest to implement but inappropriate with regards to the flow characteristics. The usual flow topology consists of a dominant flow beam formed between the seats. This beam transports the majority of the mass and is surrounded by the recirculation zones on both sides that form an artificial channel. The interaction among recirculations and the main beam then suppresses or stimulates further expansion, therefore requires an accurate modelling that cannot be provided by the inviscid flow model. For the 3D geometry the size of the recirculation zones is reduced. The 3D model also predicts different position of the main flow beam and the more uniform velocity profile (higher average magnitude but milder peaks) than in 2D.

The *laminar* flow model has confirmed the qualitative predictions of the inviscid flow model regarding the size, position and importance of the recirculations. The detailed conclusions for both the intermediate flow models (inviscid and laminar) have been captured in sections 7.3.4 and 7.4.5.

The main focus has therefore been on the *turbulent* flow model on which several properties have been tested. For usual operating conditions the channel gets aerodynamically choked, followed by a supersonic expansion, a drop back to subsonics and the re-acceleration near the casing due to the channel restriction. Hence, the general flow is transonic and sensitive to any (geometrical) changes.

The geometrical modifications tested have shown the following results:

- the flow is insensitive to the shape of the inlet region (original geometry with the horizontal inlet BC *vs.* reduced inlet with the radial BC, figure 7.2); the flow in the cylinder area has a negligible velocity; no impact has been observed on the transonic flow in the exhaust channel; the inlet computational domain can thus be reduced to the nearest vicinity of the valve;
- an inclination of the inlet wall (figure 7.19) has turned to be inefficient to control the flow character (recirculation zones) for most of the regimes tested. The improvements appear only for big lifts (channel already not choked), moreover only with a low potential gain.
- regarding the valve shape (figure 7.4) the modification G2 (milder stem curvature) has shown a comparable or better performance than the original valve in all the regimes tested; the thicker stem prevents the separation along the valve and allows for a better control of the (attached) flow beam;
- the modification G1 (larger stem curvature and the geometrical cross-section) deteriorates the exhaust performance due to the induced separation; at any regime the flow has not been able to fill up completely the void volume;
- all the 3D simulations have converged to solely symmetric solutions; the steep pressure ratio has prevented the formation of the non-symmetric patterns; both the qualitative and quantitative comparison to the planar solutions however justify the need of a fully 3D approach.

The appraisal of the different turbulence models has led to the following observations:

- all the turbulence models used have converged to a qualitatively similar solution;
- differences have been found with the Spalart-Allmaras and the EARSM models which both have predicted the earlier flow separation;
- all the remaining models (Menter's BSL, SST; TNT and Wilcox) have shown a very close agreement (<4% for all the outputs monitored) in both 2D and 3D.

Finally, the tuning of some numerical parameters has discovered:

- the tangential (swirling) component of the inlet velocity has a strong effect on the solution; the exhaust process seems therefore sensitive to the velocity distribution in the cylinder; according to the piston movement during the exhaust stroke (the volume compression damps the velocity fluctuations) the radial inlet is however much more likely;
- the response on the grid refinement has followed the trends expected; the finer grids have allowed for more accurate solutions; the accuracy improvement is however disproportionate, compared to the increase of the CPU and the increased wall-clocktime demands;
- the two different strategies of the dual cell construction have not led to any actual impact on the solution;
- the numerical scheme used (AUSM+up) has shown a low sensitivity on its free parameter M_∞ , proving its sufficient robustness for the flow fields with wide velocity range.

Some of these observations have been reviewed and presented at the various international conferences on fluid dynamics. Choosing from the most important references: mainly the steady state solutions have been published at [31, 32, 112, 113] and the solutions on the moving domain later at [21, 114].

All the computations done have confirmed the reliability and accuracy of the numerical solvers used. The current numerical methods are able to simulate the exhaust process based exclusively on the measurable variables of the cylinder pressure and temperature and the exhaust pressure. The numerical solution then provides a detailed insight to the typical aerodynamical effects during the exhaust stroke.

Considering the work statement, we can conclude that all the main objectives of this thesis have been successfully accomplished.

8.2 Future Work

Regarding the current experience the crucial bottle-neck is the computational time required for a single 3D simulation with a moving valve. A decent reduction of the computational time can be reached by the larger parallelization and/or an automation of the pre-processing (grid generation, solution interpolation) and the post-processing activities.

Preferably with a shortened time demands, also the remaining turbulence models shall be tested for the full-scale simulation. All the computations have assumed a constant inlet temperature. Although some literature seems sceptical about the influence of temperature, its actual effect could be verified.

Within a future research the experimental measurements shall be proposed in order to validate the numerical results and to evaluate the performance of the geometrical changes tested. Such experiment could also provide an accurate pressure evolution for different RPM to be used as boundary conditions for the numerical computations.

The numerical methods developed here for the exhaust stroke can later be coupled with some other numerical codes in order to accurately simulate the entire four-stroke engine cycle.

Bibliography

- [1] *COOLFluid homepage* [on-line], URL <http://coolfluidsrv.vki.ac.be>, Cited 28th Mar 2011.
- [2] *GT-Power User's Manual*, GT-Suite version 6.0, Gamma Technologies Inc., 2003.
- [3] Langley Research Center, *Turbulence Modelling Resource*, URL <http://turbmodels.larc.nasa.gov>, Cited 15th August 2011.
- [4] National Program for Applications-Oriented Research in CFD (NPACR), URL <http://www.grc.nasa.gov/WWW/wind/valid/raetaf/raetaf.html>, Cited 19th November 2011.
- [5] PETSc: Portable, extensible toolkit for scientific computations, URL <http://www-unix.mcs.anl.gov/petsc>, Cited 26th Apr 2011.
- [6] *Statistical Yearbook of the Czech Republic 2009*, Czech Statistical Office, www.czso.cz, e-0001-09, Cited 17th May 2011.
- [7] Antheaume, S. *Implicit Time Spectral Method for Time-Periodic Incompressible Flows*, Dissertation of Doctoral Degree, Université de Grenoble, 2010.
- [8] Baldwin, B. S. - Barth, T. J. *A one-equation turbulence transport model for high Reynolds number wall-bounded flows*, NASA TM 102847, 1990.
- [9] Barth, T. - Jespersen, D. *The Design of Application of Upwind Schemes on Unstructured Grids*, AIAA Paper 89-0366, 1989.
- [10] Baruzzi, G. *Finite Element Solutions of the Euler Equations in Primitive Variables Form*, Concordia University in Montreal, 1989.
- [11] Barth, T. *Numerical methods and error estimation for conservation laws on structured and unstructured meshes*, von Karman Institute Lecture Series on Computational Fluid Dynamics, 2003.
- [12] Bianchi, G. M. - Cantore, G. - Fontanesi, S. *Turbulence Modelling in CFD Simulation of ICE Intake Flows: The Discharge Coefficient Prediction*, SAE Technical Paper Series, Paper 2002-02-1118, 2002.
- [13] Billet, G. - Louedin, O. *Adaptive Limiters for Improving the Accuracy of the MUSCL Approach for Unsteady Flows*, Journal of Computational Physics, Vol. 170, 2001.
- [14] Blazek, J. *Computational Fluid Dynamics: Principles and Applications*, Elsevier Science Ltd, ISBN 008-043009-0, 2001.

- [15] Boussinesq, J. *Théorie de l'écoulement tourbillant*, Mem. Pres. Acad. Sci. Paris, 1877.
- [16] Bradshaw, P. - Ferriss, D. H. - Atwell, N. P. *Calculation of boundary layer development using the turbulent energy equation*, Journal of Fluid Mechanics 28, 1967.
- [17] Cai, X. C. - Sarkis M. *A Restricted Additive Schwarz Preconditioner for General Sparse Linear Systems*, CU-CS-843-97, Colorado, 1997.
- [18] Chapman, B. - Jost, G. - van der Pas, R. *Using OpenMP: portable shared memory parallel programming*, ISBN 978-0-262-53302-7, 2008.
- [19] Cook, P. H. - McDonald, M. A. - Firmin, M. C. P. *Aerofoil RAE 2822 - pressure distributions and boundary layer and wake measurements*, AGARD AR-138, 1979.
- [20] Darracq, D. - Champagneux, S. - Corjon, A. *Computation of Unsteady Turbulent Airfoil Flows with an Aeroelastic AUSM+ Implicit Solver*, AIAA Technical Report 98-2411, 1998.
- [21] Deconinck, H. - Fořt, J. - Źaloudek, M. *Unsteady Numerical Simulation of the Turbulent Flow Around an Exhaust Valve*, FVCA VI, Problems & Perspectives, Berlin: Springer-Verlag, 2011, ISBN 978-3-642-20670-2.
- [22] Degrez, G. *Three-Dimensional Boundary Layers and Separation*, Course Note 154, VKI, 1999.
- [23] Delanaye, M. *Polynomial reconstruction finite volume schemes for the compressible Euler and Navier-Stokes equations on unstructured adaptive grids*, Dissertation of Doctoral Degree, Université de Liège, 1996.
- [24] Delanaye, M. - Aftosmis, J. - Berger, M. J. - Liu, Y. - Pulliam, T. *Automatic hybrid-cartesian grid generation for high-Reynolds number flows around complex geometries*, AIAA Paper 99-0777, 1999.
- [25] Deléry, J. *Experimental investigations of turbulence properties in transonic shock/boundary layer interactions*, AIAA Journal 21(2), 1983.
- [26] Dieudonné, W. *Anisotropic Turbulence Modelling in Compressible Flows and Applications to Aerospoke Plug Nozzles*, Dissertation of Doctoral Degree, Université de Poitiers, 2000.
- [27] Dobeř, J. *Numerical Algorithms for the Computation of Steady and Unsteady Compressible Flow over Moving Geometries - Application to Fluid-Structure Interaction*, Dissertation of Doctoral Degree, Université Libre de Bruxelles, 2007.
- [28] Donea, J. - Huerta, A. - Ponthot, J. P. - Rodriguez-Ferran, A. *Arbitrary Lagrangian-Eulerian methods*, Encyclopedia of Computational Mechanics, John Wiley & Sons, Ltd., 2004.
- [29] Edwards, J. R. - Liou, M. S. *Numerical speed of sound and its application to schemes for all speeds*, AIAA Paper 99-3268, 14th AIAA CFD Conference, 1999.
- [30] Favre, A. *Equations des gaz turbulents compressibles*, Journal de Mécanique, Vol. 4, 361-421, 1965.
- [31] Fořt, J. - Źaloudek, M. *Numerical Simulation of Flow in an Exhaust Valve*, Colloquium FLUID DYNAMICS 2005, ŮT AV ŹR, 2005, ISBN 80-85918-94-3.

- [32] Fořt, J. - Fürst, J. - Žaloudek, M. *Numerical Solution of Compressible Flow in a Channel and Blade Cascade*, Flow, Turbulence and Combustion [online] 2006, vol. 76, no. 4, ISSN 1573-1987, 2006.
- [33] Fürst, J. *Numerické řešení transonického proudění užitím TVD a ENO schémat*, Dissertation of Doctoral Degree, ČVUT, Praha, 2000.
- [34] Fürst, J. - Janda, M. - Kozel, K. *Finite volume solution of 2D and 3D Euler and Navier-Stokes equations*, Mathematical Fluid Mechanics, Birkhäuser Verlag, 2001.
- [35] Fürst, J. - Kozel, K. *Numerické metody řešení problémů proudění I*, Editors center ČVUT, Praha, 2001.
- [36] Günther, C. - Hartmann, D. - Meinke, M. - Schröder, W. *A Level-Set Based Cut-Cell Method for Flows with Complex Moving Boundaries*, Proceedings of the V European Conference on Computational Fluid Dynamics ECCOMAS CFD 2010, Lisbon, ISBN: 978-989-96778-1-4, 2010.
- [37] Hanjalić, K. *Turbulence and transport phenomena: Modelling and simulation*, TU Darmstadt, 2005.
- [38] Hanjalić, K. - Launder, B. E. *A Reynolds stress model of turbulence and its application to thin shear flows*, Journal of Fluid Mechanics, Vol. 52, 1972.
- [39] Harlow, F. H. - Nakayama, P. I. *Turbulence transport equations*, Phys. Fluids, Vol. 10, 1967.
- [40] Harten, A. *On a class of high resolution total-variation-stable finite difference schemes*, SIAM Journal of Numerical Analysis, Vol. 21, 1984.
- [41] Heywood, J. B. *Internal Combustion Engine Fundamentals*, McGraw-Hill, ISBN 0-07-028637, 1988.
- [42] Hirt, C. W. - Amsden, A. A. - Cook, J. L. *An Arbitrary Lagrangian Eulerian Computing method for all Flow speeds*, Journal of Computational Physics, Vol. 14, 1974.
- [43] Huang, P. G. *Physics and Computations of Flows with Adverse Pressure Gradients*, Modeling Complex Turbulent Flows, Kluwer, Dordrecht, 1999.
- [44] Issman, E. *Implicit Solution Strategies for Compressible Flow Equations on Unstructured Meshes*, Dissertation of Doctoral Degree, Université Libre de Bruxelles, 1997.
- [45] Ježek, J. - Váradiová, B. - Adamec, J. *Mechanika tekutin*, Editors center ČVUT, Praha, 2000.
- [46] Kinsey, T. - Dumas, G. *Parametric Study of an Oscillating Airfoil in a Power-Extraction Regime*, AIAA Journal, Vol. 46, No. 6, 2008.
- [47] Kok, J. C. *Resolving the Dependence on Freestream Values for $k-\omega$ Turbulence Model*, AIAA Journal, Vol. 38, 2000.
- [48] Kolmogorov, A. N. *Local Structure of Turbulence in Incompressible Viscous Fluid for Very Large Reynolds Number*, Doklady Akademiyia Nauk SSSR, Vol. 30, 1941.
- [49] Kolmogorov, A. N. *Equations of Turbulent Motion of an Incompressible Fluid*, Izvestia Academy of Sciences, Vol. 1, 2, USSR, 1942.

- [50] Kozel, K. - Fořt, J. *Numerické metody řešení problémů proudění II*, Editors center ČVUT, Praha, 2003.
- [51] Kozel, K. - Louda, P. - Bodnár, T. - Beneš, L. - Sládek, I. *Numerická simulace proudění II*, Editors center ČVUT, Praha, 2004.
- [52] Lani, A. *An Object Oriented and High Performance Platform for Aerothermodynamics Simulation*, Dissertation of Doctoral Degree, Université Libre de Bruxelles, 2009.
- [53] Lepot, I. *A parallel high-order implicit finite volume method for three-dimensional inviscid compressible flows on deforming unstructured meshes*, Dissertation of Doctoral Degree, University of Liège, 2004.
- [54] LeVeque, R. *Numerical Methods for Conservation Laws*, Birkhauser Verlag, ISBN 3764327235, 1992.
- [55] Liou, M. S. - Steffen, C. *A New Flux Splitting Scheme*, Journal of Computational Physics, Vol. 107, 1993. AIAA 2003-4116
- [56] Liou, M. S. - Wada, Y. *A flux splitting scheme with high-resolution and robustness for discontinuities*, AIAA Paper 94-0083, 1994.
- [57] Liou, M. S. *A Sequel to AUSM: AUSM+*, Journal of Computational Physics, Vol. 129, 1996.
- [58] Liou, M. S. *Ten years in the Making - AUSM family*, AIAA Journal 2001-2521, 2001.
- [59] Liou, M. S. *A Further Development of the AUSM+ Scheme towards Robust and Accurate Solutions for All Speeds*, AIAA Paper 2003-4116, 2003.
- [60] Liou, M. S. *A Sequel to AUSM, Part II: AUSM+up - for all speeds*, Journal of Computational Physics, Vol. 214, 2006.
- [61] Macek, J. - Suk, B. *Spalovací motory I*, Editors center ČVUT, Praha, ISBN 80-01-02085-1, 2000.
- [62] Macek, J. *Program pro simulaci oběhu přepřínovaného motoru - OBEH*, version 00-I, Software repository of Department 220, ČVUT, 2000.
- [63] Mareš, B. - Hatschbach, P. - Baumruk, P. *Simulation of Steady Flow Through Inlet Port to Cylinder*, Proceedings of EAEC Congress [CD-ROM], Bratislava, Vol. 1, 2001.
- [64] Menter, F. R. *Two-equation eddy-viscosity turbulence models for engineering applications*, AIAA Journal 32, 1994.
- [65] Menter, F. R. - Rumsey, C. L. *Assessment of Two-Equation Turbulence Models for Transonic Flows*, AIAA Journal, 1994.
- [66] Michalak, K. - Gooch, C. O. *Limiters for Unstructured Higher-Order Accurate Solutions of the Euler Equations*, Advanced Numerical Simulation Laboratory, University of British Columbia, 2008.
- [67] Michalec, J. et al. *Pružnost a pevnost I*, Editors center ČVUT, Praha, 1995.
- [68] Nožička, J. *Základy termomechaniky*, Editors center ČVUT, Praha, ISBN 80-01-02865-8, 2001.

- [69] Pacheco, P. *Parallel Programming with MPI*, Morgan Kaufmann Publishers, Inc., ISBN 1-55860-339-5, 1997.
- [70] Paillère, J. - Carette, J.-C. - Deconinck, H. *Multidimensional upwind and supg methods for the solution of the compressible flow equations on unstructured grids*, von Karman Institute Lecture Series 94-5, VKI, 1994.
- [71] Panesi, M. - Lani, A. - Magin, T. - Pinna, F. - Chazot, O. - Deconinck, H. *Numerical investigation of the non-equilibrium shock-layer around the expert vehicle*, AIAA Paper 2007-4317, 2007.
- [72] Polášek, M. *Eulerovský zónový model spalovacího motoru*, Doctoral thesis, ČVUT, Praha, 1998.
- [73] Pope, S. B. *Turbulent Flows*, The Press Syndicate of the University of Cambridge, Cambridge, ISBN 0-521-59886-9, 2000.
- [74] Prandtl, L. *Über die ausgebildete Turbulenz*, ZAMM, Vol 5., 1925.
- [75] Příhoda, J. - Louda P. *Matematické modelování turbulentního proudění*, Editors center ČVUT, Praha, 2007.
- [76] Pulliam, T. *Efficient Solution Methods for the Navier-Stokes Equations*, von Karman Institute Lecture Series on Numerical Techniques for Viscous Flow Computation in Turbomachinery Bladings, 1985.
- [77] Punčochářová, P. *Výpočet stlačitelného proudění metodou konečných objemů*, Diploma thesis, ČVUT, Praha, 2005.
- [78] Quintino, T. *A Component Environment for High-Performance Scientific Computing - Design and Implementation*, Dissertation of Doctoral Degree, Katholieke Universiteit Leuven, 2008.
- [79] Reynolds, O. *On the Dynamical Theory of Incompressible Viscous Fluids and the Determination of the Criterion*, Philosophical Transactions of the Royal Society of London, Series A, Vol. 186, p. 123, 1895.
- [80] Reynolds, W. C. *Modeling on Fluid Motions in Engines - an Introductory Overview*, Combustion Modeling in Reciprocating Engines, pp 41-67, 1980, ISBN 0-306-40431-1.
- [81] Ricchiuto, M. *Construction and Analysis of Compact Residual Discretizations for Conservation Laws on Unstructured Meshes*, Dissertation of Doctoral Degree, Université Libre de Bruxelles, 2005.
- [82] Ripley, R. C. - Lien, F.-S. - Yovanovich, M. M. *Adaptive Mesh Refinement of Supersonic Channel Flows on Unstructured Meshes*, International Journal of Computational Fluid Dynamics, Vol. 18, 2004.
- [83] Rodi, W. *A new algebraic relation for calculating the Reynolds stress*, ZAMM Zeitung, 56, 1976.
- [84] Roe, P. L. *Characteristic-Based Schemes for the Euler Equations*, Annual Reviews of Fluid Mechanics, 18:337, 1986.

- [85] Rotta, J. *Statistische Theorie nichthomogener Turbulenz*, Z für Physik, 1951.
- [86] Saad, Y. - Schultz, M. *GMRES: A generalized minimal residual algorithm for solving non-symmetric linear systems*, SIAM Journal of Scientific Statistical Computations, Vol. 7, 1986.
- [87] Schmidt, F. *The Internal Combustion Engine*, Chapman and Hall, 4/0685/88, 1965.
- [88] Shepard, D. *An Two-Dimensional Interpolation Function for Regularly Spaced Data*, Proceedings of the 23rd National Conference of the Association for Computing Machinery, Princeton, 1968.
- [89] Smith, R. *AUSM(ALE): A Geometrically Conservative Arbitrary Lagrangian-Eulerian Flux Splitting Scheme*, Journal of Computational Physics, Vol. 150, 1999.
- [90] Spalart, P. R. - Allmaras S. R. *A one-equation turbulence model for aerodynamic flows*, AIAA paper 92-0437, 1994.
- [91] Speziale, C. G. - Abid, R. - Anderson, E. C. *A Critical Evaluation of Two-Equation Models for Near Wall Turbulence*, AIAA paper 90-1481, Seattle, 1990.
- [92] Stein, K. - Tezduyar, T. - Bennery, R. *Mesh Moving Techniques for Fluid-Structure Interactions with Large Displacements: Flow Simulation and Modelling*, Journal of Applied Mechanics, Vol. 70, 2003.
- [93] Šesták, J. - Rieger, F. *Přenos hybnosti, tepla a hmoty*, Editors center ČVUT, Praha, ISBN 80-01-01715-X, 1993.
- [94] Tennekes, H. - Lumley, J. L. *A first course in turbulence*, MIT Press, 1972.
- [95] van der Weide, E. *Compressible Flow Simulation on Unstructured Grids using Multi-dimensional Upwind Schemes*, Dissertation of Doctoral Degree, Technische Universiteit Delft, 1998.
- [96] van Leer, B. *Towards the ultimate conservation difference scheme. A new approach to numerical convection*, Journal of Computational Physics, Vol. 14, 361-370, 1979.
- [97] van Leer, B. *Flux vector splitting for the euler equations*, Proceedings of 8th International Conference on Numerical Methods in Fluid Dynamics, Springer Verlag, 1982.
- [98] Vítek, O. *Simulace dějů v pístovém motoru s vlivem turbulence*, Dissertation of Doctoral Degree, ČVUT, Praha, 2006.
- [99] Wallin, S. *Engineering turbulence modelling for CFD with focus on explicit algebraic Reynolds stress models*, Dissertation of Doctoral Degree, Norstedts Tryckeri AB, Stockholm, 2000.
- [100] Waterson N. P. *Simulation of Turbulent Flow, Heat and Mass Transfer using a Residual Distribution Approach*, Dissertation of Doctoral Degree, TU Delft, 2003.
- [101] Venkatakrishnan, V. *Convergence to steady state solutions of the Euler equations on unstructured grids with limiters*, Journal of Computational Physics, Vol. 118, 120-130, 1995.
- [102] Wilcox, D. C. *Reassessment of the scale-determining equation for advanced turbulence models*, AIAA Journal 26, 1988.

- [103] Wilcox, D. C. *Turbulence modelling for CFD*, La Canada, DCW Industries, Inc., second edition, ISBN 1-928729-10-X, 2000.
- [104] Wilcox, D. C. *Formulation of the $k - \omega$ Turbulence Model Revisited*, AIAA Journal, Vol. 46, 2008.
- [105] Wuilbaut, T. *Algorithmic Developments for a Multiphysics Framework*, Dissertation of Doctoral Degree, Université Libre de Bruxelles, 2009.
- [106] Yang, Z. - Mavriplis, D. *Unstructured Dynamic Meshes with High-Order Time Integration Schemes for the Unsteady Navier-Stokes Equations*, AIAA 2005-1222, 2005.
- [107] Zeithammer, K. *Vývoj techniky*, Editors center ČVUT, Praha, 1998.
- [108] Zhang, Z. - Gil, A. - Hassan, O. - Morgan, K. *The Simulation of 3D Unsteady Incompressible Flows with Moving Boundaries on Unstructured Meshes*, Computers and Fluids 37, 2008.
- [109] Zhao, Y. - Forhad, A. *A General Method for the Simulation of Fluid Flows with Moving and Compliant Boundaries on Unstructured Grids*, Computational Methods for Applied Mechanical Engineering 192, 2003.
- [110] Žaloudek, M. *Numerical Simulation of Flow in a Channel and a Blade Cascade*, Diploma thesis, ČVUT, Praha, 2005.
- [111] Žaloudek, M. - Fořt, J. *Numerical Solution of Compressible Flow Applied in Internal Aerodynamics*, Application of Experimental and Numerical Methods in Fluid Mechanics, University of Žilina, 2006, ISBN 80-8070-533-X.
- [112] Žaloudek, M. - Fořt, J. *Steady Simulation of Flow around an Exhaust Valve*, Topical Problems of Fluid Mechanics 2008, ÚT AV ČR, 2008, ISBN 978-80-87012-09-3.
- [113] Žaloudek, M. - Fořt, J. - Deconinck, H. *Numerical Solution of Gas Exhaustion from a Reciprocating Engine*, Computational Mechanics 2009, Nečtiny, 2009.
- [114] Žaloudek, M. - Deconinck, H. - Fořt, J. *Simulation of Gas Exhaustion from a Combustion Chamber of a Reciprocating Engine*, Proceedings of the V European Conference on Computational Fluid Dynamics ECCOMAS CFD 2010, Lisbon, ISBN: 978-989-96778-1-4, 2010.

Appendix A

Laval Nozzle - 1D Analysis

The Laval nozzle is a convergent-divergent channel, as shown in the figure A.1.

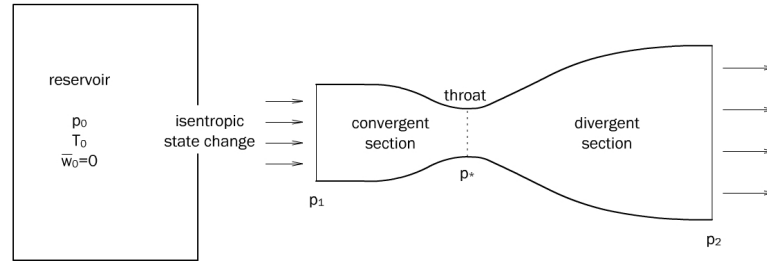


Figure A.1: Scheme of a Laval nozzle.

Note

- p_0 the reservoir pressure ($\vec{w}_0 \equiv 0$),
- p_1 the pressure at inlet section,
- p_* the pressure at the throat section,
- p_2 the pressure at the outlet section.

Assume a constant reservoir state and a fixed shape of the nozzle. According to ratio of pressure, 6 operating regimes can be distinguished:

1. $p_2 = p_0$, no pressure gradient, the medium inside the channel remains at rest.
2. $p_0 - p_2 = \epsilon$ (p_2 slightly smaller than p_0), velocity at convergent part increases (does not reach the critical speed of $M = 1$) and gradually decreases in the divergent part.
3. $p_2 = p_{c1}$ (first critical regime), the velocity reaches $M_* = 1$ only at the throat section and gradually decreases in the divergent section again. The velocity across whole channel remains subsonic. The value p_{c1} can be derived from the geometrical size of the throat and outlet sections.

$$\frac{A_2}{A_*} = \frac{M_* \cdot \left(1 + \frac{\kappa-1}{2} M_*^2\right)^{\frac{1}{1-\kappa} - \frac{1}{2}}}{M_2 \cdot \left(1 + \frac{\kappa-1}{2} M_2^2\right)^{\frac{1}{1-\kappa} - \frac{1}{2}}}, \quad (\text{A.1})$$

$$\frac{p}{p_0} = \left(1 + \frac{\kappa-1}{2} M^2\right)^{\frac{\kappa}{1-\kappa}}, \quad (\text{A.2})$$

with κ the ratio of specific heats, A and M the size and Mach number in respective sections.

4. $p_2 < p_{c1}$, the velocity at convergent part is subsonic, reaches the critical speed at the throat section and accelerates to supersonic down the divergent part. There the velocity suddenly changes to subsonic through a so-called shock-wave.
5. $p_2 = p_{c2}$ (second critical regime), the shock-wave appears right in the outlet section. The value p_{c2} represents the highest pressure for which the outlet section can still be subsonic. The value p_{c2} can be determined by the relations (A.1) and (A.2).
6. $p_2 < p_{c2}$, the velocity in the divergent part is exclusively supersonic, no shock-wave appears and the channel operates as a supersonic nozzle.

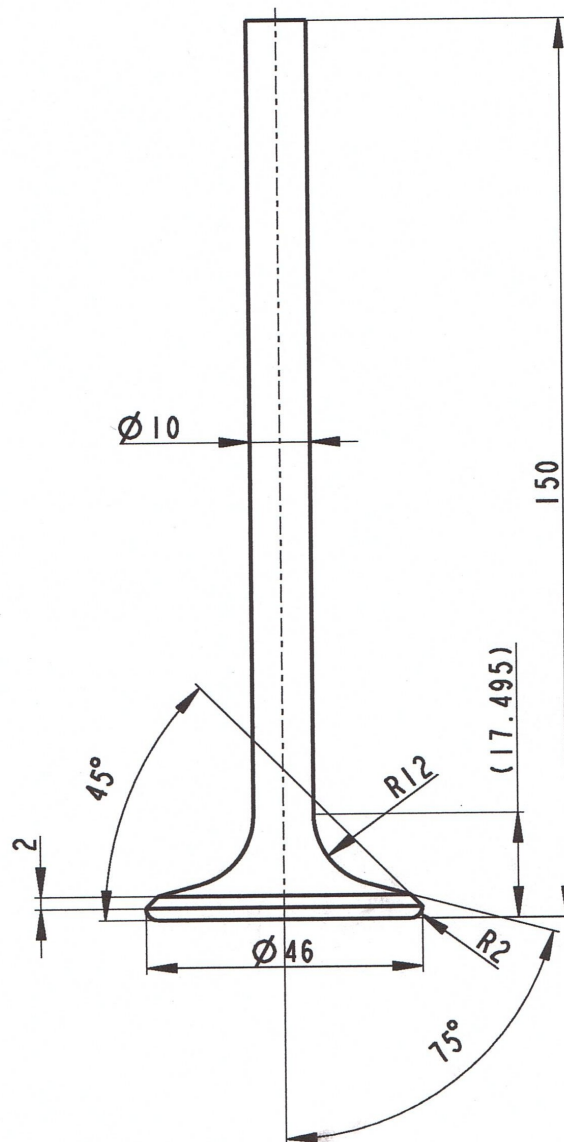


Figure B.2: Technical drawing of the exhaust valve.